

Vibrational imaging for chemical biology:
from label-free to molecular probes

Thesis by
Jiajun Du

In Partial Fulfillment of the Requirements for
the degree of
Doctor of Philosophy

The logo for the California Institute of Technology (Caltech), featuring the word "Caltech" in a bold, orange, sans-serif font.

CALIFORNIA INSTITUTE OF TECHNOLOGY
Pasadena, California

2024
Defended November 13, 2023

© 2023

Jiajun Du

ORCID: [0000-0003-2693-834X]

ACKNOWLEDGEMENTS

First and foremost, I extend my deepest gratitude to my advisor Prof. Lu Wei for not only accepting me as her first student but also for her unwavering support throughout the years. Lu is a remarkable individual who treats everyone with humility, irrespective of their title. Upon the first conversation with her at Columbia, I have decided to join with her. And now after more than six years when I look back, I still believe this is the rightest decision I made in my life. As a student with almost no background in microscopy, Lu taught me every detail of theory and experiments. She sets the role model to me in both research and character: being critical and creative in science, always embrace cross-disciplinary knowledge, going out of comfort zone while maintaining high standards, being strict with oneself but tolerant with others. I am especially grateful to Lu for granting me all the freedom to explore the topics I am interested in and providing me with all resources. The warm, relaxed and inspiring environment she creates in the group has nourished my enthusiasm to science and allowed me to immerse myself deeply into my research. At one moment, I even imagined that I could remain a part of this environment forever and never graduate.

Guided by Lu, the first couple of students including Chenxi Qian, Kun Miao, Dongkwan Lee and myself, worked together to set up the Wei lab from scratch. They are not only talented but also kind and warmhearted, and brought expertise from very different fields to the group. It is unforgettable of working with them every day, especially when we stayed together overnight to build our microscope and acquired the first image, which became the most beautiful image I have seen. I am also fortunate to work with Xiaotian Bi, Li-En Lin, Haomin Wang, Adrian Colazo, Rahuljeet Chadha, Yulu Cao, Ziguang Yang, Noor Naji, Philip Kocheril, Jia Gao, Amy Vo and Rona Yu in the Wei group.

In my first year when our lab was still under renovation, Prof. Brian Stoltz kindly hosted me work in his lab and had Chris Reimann train me as a synthetic chemist. I wanted to extend my heartfelt thanks to Brian for accepting me and treating me as a group member without any reservation. Chris is a very talented, responsive and patient mentor. The training I had with him lays the foundation for graduate work and helped me transit to be an independent

researcher. Following the training in organic chemistry, I had Yapeng Su as my mentor and had the opportunity to collaborate with Prof. James (Jim) Heath. Yapeng is the most hardworking student I have ever met at Caltech. He led several big projects simultaneously but still invested significant efforts in my training, effectively introducing me into the realm of biology. His patience, kindness and thoughtfulness motivated me to tackle real-world biological questions. Despite Jim's extensive commitments as the leader of a large research group and institute, he made valuable contribution to our collaboration with both intellectual input and practical support, dedicating extensive time to our monthly meetings and contributing substantially to our manuscript. I would also like to express my gratitude for the collaboration with exceptionally brilliant theoretical chemists, Xuecheng Tao and Tomislav Begušić. They were courageous to initiate the collaboration and talented enough to pilot the research and solved the fundamental problem in our field. Without my mentors and collaborators, I would not have made any contributions to research.

I am also deeply thankful to my mentees including Ziguang Yang, Jia Gao, Josh Signore, Hailan Yu, Meng (Stella) Luo. Throughout interacting with them, I got to know how to transfer my knowledge to them in an easy and convey complex concepts to individuals with diverse backgrounds. It's filled with pleasure to work with them. Their experiences and expertise enriched mine, and they made noteworthy contributions to my graduate research. In particular, I wish to acknowledge the exceptional intelligence and diligence of Ziguang, who contributed much to my last project.

I am privileged to have Prof David Tirrell, Prof. Brian M. Stoltz and Professor Linda Hsieh-Wilson in my thesis committee, and Prof. Jesse (Jack) Beauchamp in my candidacy committee. They provided invaluable time and suggestions to my thesis research, proposals and career. Their expertise and insightful comments provided me with the opportunity to examine my research and proposals within a broader context.

A significant reason that I didn't plan to graduate earlier is due to living with Shuoyan Xiong, Quan Gan and Zhihao Cui. Whatever failure I had from experiments, I got refreshed when

back home and stayed with them. I treasure every moment spent with them, especially during our board game Saturday night. I am grateful for their support from all aspects. The warmth and companionship that I have found at Caltech have left an indelible mark on me. I have had the privilege of getting to know many kind individuals who have become friends during my time here. They include but not limited to: Xinhong Chen, Yalu Chen, Weiting Deng, Hanwei Liu, Xiaoran Hu, Tian (May) Zeng, Zhen Liu, Guannan Dong, Mi Lei, Minghao Pan, Linqing Peng, Peng Liu, Shumao Zhang, Zhiyang Jin, Yuelin Shi, Chen Li, Yu-Ling (Debbie) Tseng, Yan Sun, Jinglin Huang, Yu Su, Xiaozhe Ding, Chong Sun, Shan Huang, Jeong Hoon Ko (JK), Hao Xie, Chenghan Li, Jiaming Li, Yang Yang, Juner Zhang, Yujia Tao, Guanya Shi, Yao Luo, Mingyao Guo, Ziyang Qin, Ruilin Qian, Shuai Wang, Lixue Cheng, Kaiwen Wang, Jianchun Wang, Alex Sun, Kai Chen, Weixuan Nie and Feng Zhong. They are warmer than the California sunshine.

In addition to my Caltech friends, I am grateful for the ongoing support and advice from friends outside of the institution. Although we don't have many chances to meet in person, just chatting with them is such a relief to me. I extend my appreciation to Yue Ma, Mingyang (Kafka) Xu, Yu Chen, Xiaoqian Wang, Haotian Liu, Kuang Shen, Binbin Luo, Ximing Li, Jun Lu, Jieyu Yao, Zhimeng Pan, Xin Pan, Shimin Gu, Minjie Shen, Shixiang Tang, Mingji Zhu, Chenyu Li, Jiawei Li, Xiaonan Zhang, Xiaofeng Chen, Lin Yuan, Xinyu Gu, Zhi Yang, Yingying Chen, Chen Chen, Yuchen Xing, Xuelin Sui, Yupeng Miao, Ruihan Li, Yijia Wang, Han Bao and many more.

My special thanks go to Dr. Scott Virgil from Center for Catalysis and Chemical Synthesis for sharing his facility with me and Dr. Mona Shahgholi for assistance with mass spectrometry. I would also like to express my appreciation for Gregory Rolette and Armando Villasenor, who deliver orders to our lab daily, and to division manager Joe Drew, who ensured the smooth operation of our lab. The administrative support provided by Alison Ross, Priscilla Boon and Ann Mao has been indispensable. I also extend my gratitude to Divina Bautista from the Health Center, who has cared for me as if I were her own.

Finally, my heartfelt thanks go to my parents and my family. Their unconditional love and support have shaped me into the person I am today. Their encouragement has given me the courage to face the challenges of scientific research and to remain dedicated to my work. I have not had the opportunity to see them for an extended period, and I owe them much family time and accompany. Amidst the pandemic, I suffered the loss of several family members, and I am determined to avoid any further regrets. It is now time for me to go back home.

Dedicated to my parents Kang Du and Hui Zhi

ABSTRACT

Since the invention of stimulated Raman scattering (SRS) microscopy in 2008, vibrational imaging is increasingly recognized as a powerful tool for biological investigation. As the most suitable far field vibrational imaging modality for live biological studies, SRS microscopy is taking the lead role within its vibrational counterparts with desired sensitivity and image quality. The totally different mechanism of generating vibration signals from fluorescence signals determines the special features of vibrational imaging. Bond vibration originating signals provide inherent optical contrast for every molecule and the quantitative manner allows straightforward quantification. Since the inception, SRS microscopy has achieved large success in label-free imaging. Label-free imaging avoids tedious labeling step and has the least perturbation to the biological samples but with limited sensitivity and specificity. The introducing of labeling starting about 10 years ago opens up a new avenue for SRS microscopy to tackle the fundamental limitations of label-free approaches. Whether to use label-free or molecular probes for SRS microscopy depends on the specific studies. This thesis aims to utilize SRS microscopy (both label-free and minimally labeling) for metabolic study and develop new molecular probes for SRS microscopy.

We start from comparing different vibrational imaging modality and fluorescence imaging and conclude that SRS is the best vibrational imaging technique for biological samples. Then we discuss the features of label-free, bioorthogonal labeling and super-multiplexed SRS imaging. The minimally perturbative triple bond tagging and isotope labeling makes SRS especially suitable for tracking metabolites and accessing metabolic pathways. Furthermore, we also summarize the design principles for functional Raman imaging probe development based on their spectroscopic signatures. (Chapter I)

Non-invasively probing metabolites within single live cells is highly desired but challenging. We explored Raman spectro-microscopy towards spatially-resolved single cell metabolomics, with the specific goal of identifying druggable metabolic susceptibilities from a series of patient-derived melanoma cell lines. The chemical composition analysis of single cell and single organelle lipid droplets identified the fatty acid synthesis pathway and lipid mono-unsaturation as druggable susceptibility. More importantly we revealed that inhibiting

lipid mono-unsaturation leads to cellular apoptosis accompanied by the formation of phase-separated intracellular membrane domains. (Chapter II)

Next, we established a first-in-class design of multi-color photoactivatable Raman probes for subcellular imaging and tracking. The fast photochemically generated alkynes from cyclopropenones enable background-free Raman imaging with desired photocontrollable features. After necessary molecule engineering to improve the biocompatibility and sensitivity, we generated organelle-specific probes for targeting mitochondria, lipid droplets, endoplasmic reticulum, and lysosomes. Multiplexed photoactivated imaging and tracking at both subcellular and single-cell levels was also demonstrated to monitor the dynamic migration and interactions of the cellular contents. (Chapter III)

Further improvement of the Raman signal with molecular probes is a central topic for Raman imaging. Recently developed electronic preresonance (epr) probes boost Raman signals and pushed SRS sensitivity close to that offered by confocal fluorescence microscopy. To guide the development of even stronger Raman probes and fill the final gap between epr-SRS probes and single molecule imaging, the structure-function relationship of epr-SRS probes is indispensable. We therefore used ab initio approach employing the displaced harmonic oscillator (DHO) model for calculating the epr-SRS signals, which proves to provide a consistent agreement between simulated and experimental SRS intensities of various triple-bond bearing epr-SRS probes. The theory also allows us to illustrate how the observed intensity differences between molecular scaffolds stem from the coupling strength between the electronic excitation and the targeted vibrational mode. Utilizing the discovered structure-function relationship of epr-SRS probes, we engineered MARS palette for higher sensitivity. With chemical modification to improve Raman mode displacement or enhance transition dipole moment or adjust detuning, we enhance the signal of alkynyl pyronins and nitrile pyronins, setting the current sensitivity records for small molecule far-field Raman probes. (Chapter IV&V)

PUBLISHED CONTENTS AND CONTRIBUTIONS

1. **Du, J.**[#], Tao, X.[#], Begušić, T.*^{*}, & Wei, L*^{*}. Computational Design of Molecular Probes for Electronic Preresonance Raman Scattering Microscopy. *J. Phys. Chem. B*, 2023, 127, 4979-4988.
#equal contribution. J.D. participated in designing the study, performing the experiments and preparing the manuscript.
2. **Du, J.**, Wang, H., & Wei, L*^{*}. Bringing Vibrational Imaging to Chemical Biology with Molecular Probes. *ACS Chem. Biol.*, 2022, 17, 7, 1621–1637.
J.D. participated in designing the study, raising proposals and writing the manuscript.
3. **Du, J.**, & Wei, L*^{*}. Multicolor Photoactivatable Raman Probes for Subcellular Imaging and Tracking by Cyclopropanone Caging. *J. Am. Chem. Soc.*, 2022, 144, 2, 777–786.
J.D. participated in designing the study, performing the experiments and writing the manuscript.
4. **Du, J.**[#], Su, Y.[#], Qian, C., Yuan, D., Miao, K., Lee, D., Ng, A., Wijker, R., Ribas, A., Levine, R., Heath, J.*^{*}, & Wei, L*^{*}. Raman-guided Subcellular Pharmacometabolomics for Metastatic Melanoma Cells. *Nat. Commun.*, 2020, 11, 4830.
#equal contribution. J.D. participated in designing the study, performing the experiments and preparing the manuscript.
5. Lee, D., **Du, J.**, Yu, R., Su, Y., Heath, J. R., & Wei, L*^{*}. Visualizing Subcellular Enrichment of Glycogen in Live Cancer Cells by Stimulated Raman Scattering. *Anal. Chem.*, 2020, 92(19), 13182-13191.
J.D. participated in designing the study, performing the experiments and preparing the manuscript.

TABLE OF CONTENTS

Acknowledgements	iii
Abstract.....	viii
Published contents and contributions.....	x
Table of Contents	xi
Chapter I: Introduction of stimulated Raman scattering microscopy.....	1
1.1 Stimulated Raman scattering microscopy: the chosen vibrational imaging modality for biological systems	1
1.2 Label-free vibrational imaging	4
1.3 Labeling with bioorthogonal probes	5
1.4 Small-molecule Raman tagging.....	7
1.5 Metabolic pathway analysis with deuterium labeling: from cell metabolism to microbiology	11
1.6 Raman probe palettes for highly sensitive and super-multiplexed imaging	14
1.7 Functional Raman Imaging Probes.....	17
1.8 Conclusion.....	23
1.9 Reference.....	24
Chapter II: Raman-guided subcellular pharmaco-metabolomics for metastatic melanoma cells.....	30
2.1 Introduction	30
2.2 Metabolic features are shown in both transcriptome and Raman	32
2.3 Differentiated cells are susceptible to fatty acid synthesis.....	35
2.4 Mesenchymal M381 accumulates selected lipids in lipid droplets....	39
2.5 Desaturases are involved lipid-droplet unsaturation of M381	43
2.6 Inhibiting SCD1 but not $\Delta 6$ desaturase induces apoptosis in M381..	45
2.7 SCD1 inhibition induces phase-separated membrane structures	46
2.8 Lipidomics suggest a reservoir role of lipid droplets	51
2.9 Supplying UFA rescues SCD1 induced apoptosis in M381	53
2.10 Conclusion.....	56
2.11 Methods.....	58
2.12 Supplementary Figures	66
2.13 Reference.....	81
Chapter III: Multicolor photoactivatable Raman probes for subcellular imaging and tracking by cyclopropanone caging.....	86
3.1 Introduction	86
3.2 Synthesis and Spectroscopic Characterizations of Model Cyclopropanone-caging Systems.....	90
3.3 Probe Engineering for Improved Chemical Stability and Enhanced Raman Sensitivity.....	92
3.4 Organelle-Targeted Probe Engineering for Live-cell Photoactivatable Raman Imaging.....	94

3.5 Live-cell Photoactivatable Multiplex Imaging	97
3.6 Intracellular Photoactivation and Multiplex Tracking.	99
3.7 Conclusion.....	102
3.8 Methods and supplementary figures.....	104
3.9 Reference.....	134
Chapter IV: Computational design of molecular probes for electronic preresonance Raman scattering microscopy.....	139
4.1 Introduction	139
4.2 Theory	142
4.3 Results and discussion	146
4.4 Conclusion.....	154
4.5 Methods.....	156
4.6 Supplementary Information	157
4.7 Reference.....	171
Chapter V: Second generation electronic preresonance Raman imaging probes	176
5.1 Introduction	176
5.2 Results	178
5.3 Discussion	187
5.4 Supplementary information	189
5.5 Reference.....	243

*Chapter 1*INTRODUCTION OF STIMULATED
RAMAN SCATTERING MICROSCOPY

The content of this chapter has been published in:

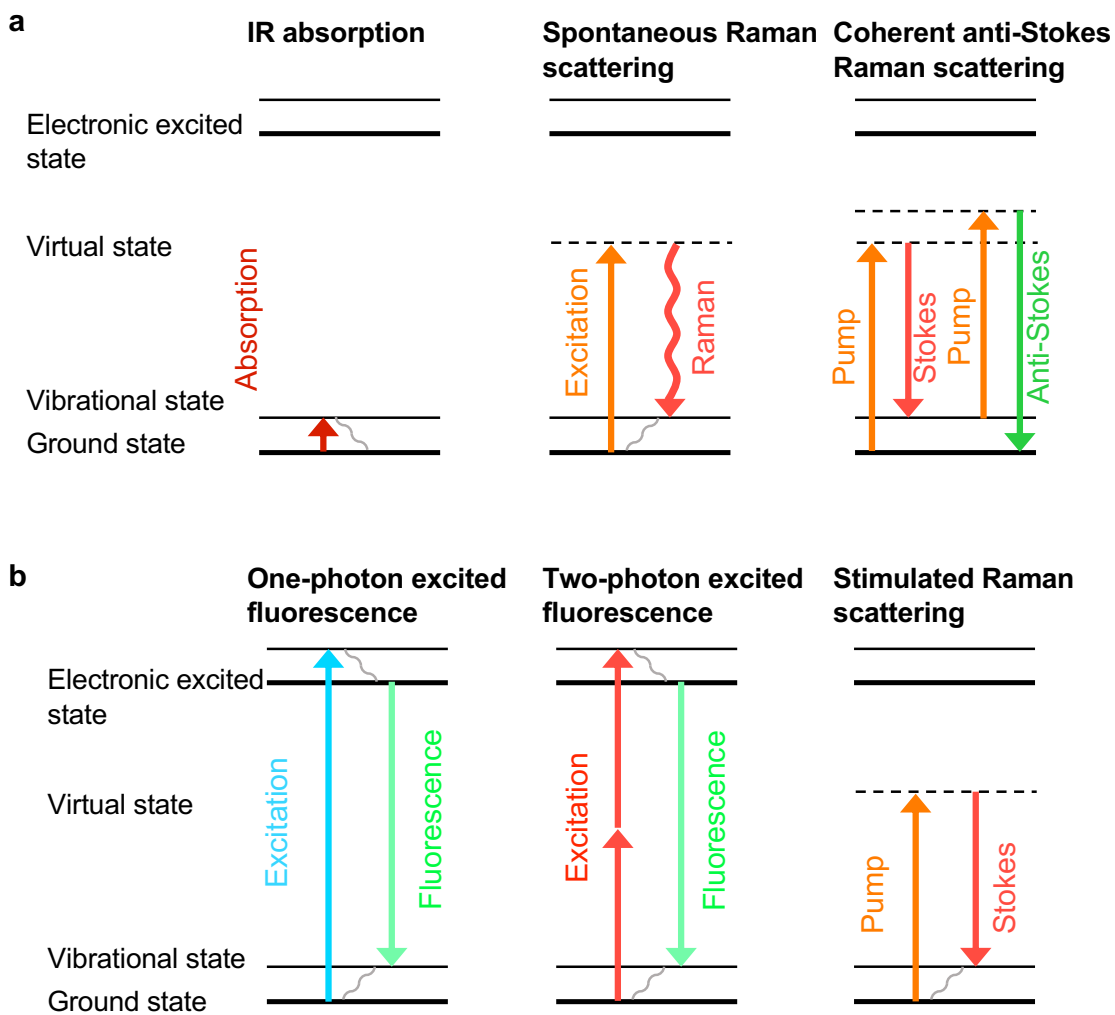
Du, J., Wang, H., & Wei, L. Bringing Vibrational Imaging to Chemical Biology with Molecular Probes. *ACS Chem. Biol.*, 2022, 17, 7, 1621–1637.

1.1 Stimulated Raman scattering microscopy: the chosen vibrational imaging modality for biological systems

Vibrational spectroscopy, including infrared (IR) absorption and Raman scattering, reveals molecular information through probing the inherent vibrations of chemical bonds. It has been extensively used for characterizing molecules¹, deciphering reaction mechanisms^{2,3}, and interpreting molecule-environment interactions^{4,5}. For subcellular biological investigations, Raman scattering is a better-suited technique. Raman spectroscopy was first discovered by the physicist Sir C.V. Raman in 1928, for which the inelastic Raman scattering shifts a very small portion of photons to lower frequency upon interacting with molecules⁶. The changes of the photon energy reflect the vibrational energy levels of the chemical bonds within the molecules and thus carrying rich chemical information. Although both IR and Raman spectroscopy contains vibrational information of the molecules, they have different selection rules. For example, water has very high IR absorption but weak Raman scattering. In addition, Raman typically utilizes UV to near-infrared light (200 - 1100 nm) while IR relies on infrared light (2500 – 50000 nm), thus the spatial resolution (scales inversely with the light wavelength) is much higher for Raman (Figure 1.1a). Both the subcellular spatial-resolution and the minimal water background laid the foundation for the biological Raman applications.

However, the utility of spontaneous Raman is largely limited by its feeble signals ($\sim 10^{10}$ smaller than fluorescence), which requires a long acquisition time and is easily overwhelmed by the auto-fluorescence background from the biological samples. To address both issues, the invention of the coherent Raman scattering, the coherent anti-Stokes Raman Scattering (CARS) microscopy (Figure 1.1a), significantly boosted the imaging sensitivity and speed and pushed Raman spectro-microscopy to be more compatible with biological imaging⁷. However, CARS signals suffer from the severe nonresonant background and has non-linear concentration dependence, which sacrifice imaging quality and add complexity for imaging annotation⁸. Around 2008, stimulated Raman scattering (SRS) microscopy was introduced that provided even better sensitivity than CARS and tackled both above issues inherently with CARS⁹⁻¹¹. SRS utilizes two spatially and temporally laser pulses (pump and Stokes), which could enhance the otherwise weak Raman transitions by up to 10^8 fold through the stimulated emission quantum amplification. This two-photon excitation feature yields SRS intrinsic 3D optical sectioning capability for deep tissue imaging. In addition, the technical implementation of the high-frequency modulation transfer scheme also pushed the detection sensitivity of SRS close to the theoretical limit and got rid of the auto-fluorescence background. The readers are encouraged to check more technical background of SRS in other reviews^{12,13}. It's now widely recognized that SRS is the most suitable far-field Raman imaging modality for biological studies by providing image quality comparable to fluorescence microscopy. Prominently, it also achieved a high imaging speed up to video-rate (110 frames/s)¹⁴⁻¹⁶ and a spatial resolution within 100 nm with recent instrumentation and sample-expansion strategies¹⁷⁻¹⁹. It would be informative to compare the key technical and application features of SRS microscopy with the popular one- and two-photon fluorescence microscopy. Below, we also provide the energy diagram and a table summarizing key imaging parameters for the three techniques (Figure 1.1b). The absence of electronic excitation provides SRS with general imaging capability without labeling and minimizes photobleaching or environmental quenching. Besides, SRS typically use near-infrared lasers (800-1100 nm) and thus has deeper penetration into thick tissues and less photodamage than one photon fluorescence. However relatively low signal level is still the fundamental problem with SRS. Recent efforts have shown probe engineering such as the

development of highly sensitive MARS and polyynes dyes could largely tackle this signal problem and even break the traditional color barrier in fluorescence microscopy with super-multiplexed imaging.



Imaging modality	Stimulated Raman scattering microscopy	One-photon fluorescence microscopy	Two-photon fluorescence microscopy
Contrast origins	Chemical bonds	Fluorophores	Fluorophores
Electronic excitation	No	Yes	Yes

Lasers	Picosecond or femtosecond pulsed laser	CW laser	Femtosecond pulsed laser
Power dependence	$\propto I_{\text{pump}}I_{\text{Stokes}}$	$\propto I_{\text{ex}}$	$\propto I_{\text{ex}}^2$
Compatible samples	Fixed or live samples	Fixed or live samples	Fixed or live samples
Pixel dwell time	μs	μs	μs
Spatial resolution	300-500 nm (lateral) ¹³ 1-2 μm (axial)	200-300 nm (lateral) $\sim 1 \mu\text{m}$ (axial)	300-600 nm (lateral) ²⁰ 1-2 μm (axial)
Sensitivity	mM for endogenous species; μM for triple-bond probes; nM for pre-resonance MARS dyes and the polyynes;	Up to single-molecule	Up to single-molecule
Intrinsic 3D sectioning capability	Yes	No	Yes
Imaging depth in Brain Tissues	200-500 μm ²³	50-100 μm ²¹	300-500 μm ²²
Probe quenching/photobleaching	Minimum	Yes	Yes
Hyperspectral information	Yes	Limited	Limited

Figure 1.1. Energy diagram of different vibrational micro-spectroscopy. (a) Energy diagram of IR absorption, spontaneous Raman scattering and coherent anti-Stokes Raman scattering spectroscopy. (b) Energy diagram and key parameters of SRS microscopy, one- and two-photon excited fluorescence microscopy.

1.2 Label-free vibrational imaging

Since Raman signals originate from chemical bonds instead of conjugated fluorophores, SRS offers general imaging applicability for versatile intrinsic molecules (Figure 1.1). From its invention, SRS microscopy has been established as a powerful label-free bioimaging

modality. Targeting the fingerprint region (500 - 1700 cm^{-1}) or high wavenumber carbon-hydrogen (C-H) stretching region (2800 - 3100 cm^{-1}), nucleic acids, proteins, lipids, carbohydrates, neuron-transmitters and other intrinsic biomolecules carrying O-P-O, C=O, C=C, C-H₂, C-H₃ bonds are readily imaged with subcellular resolution (Figure 1.2a). Additionally, hyperspectral SRS^{24,25} adds to another layer of information for subcellular spectral analysis. With these capabilities, the label-free SRS renders various applications, including sensing environmental cues²⁶, studying lipid metabolism and identifying druggable targets²⁷⁻³¹, tracking drug delivery and distribution^{10,32-34}, multicolor cell sorting^{35,36}, fast diagnosis of tumors^{37,38}, and investigations of amyloid plaques in neurodegenerative diseases^{39,40}. The current imaging speed, throughput and detection sensitivity are still being continuously improved with rapid instrumental innovations⁴¹⁻⁴³. In parallel, emerging data processing approaches, particularly the machine learning algorithms, further upgrade image quality and enable data mining with the rich chemical information^{18,29,43-45}.

Despite the success of label-free SRS imaging, there are several fundamental limitations. First, the specificity of targets is usually compromised since endogenous biomolecules tend to share many chemical bonds and therefore overlapping spectra. Second, the detection limit of SRS is still relatively low compared with fluorescence - at the scale of millimolar for most biomolecules. Thus label-free SRS are more suited to relatively abundant molecules including proteins, lipids, nucleic acids and carbohydrates. Third, label-free imaging is hard for tracking many dynamic processes such as uptake, synthesis, catabolism and intracellular to extracellular interaction. These limitations could be largely bypassed by labeling with Raman probes.

1.3 Labeling with bioorthogonal probes

Driven by the need of higher specificity, sensitivity, and functionality, which are fundamentally limited in the label-free approaches, Raman labels have been introduced to shift SRS imaging from the label-free to the labeling paradigm⁴⁶. Fortunately, the cell-silent spectral region (1800-2800 cm^{-1}), where there are no endogenous Raman signals from cells,

leaves spacious spectral room for background-free Raman labeling and imaging (Figure 1.2a). Bioorthogonal chemical bonds including alkynes ($C\equiv C$), nitriles ($C\equiv N$) and carbon-deuterium bonds (C-D) are small, nontoxic and Raman active in this clean region, thus are well suitable for tagging with low perturbation to the biological systems⁴⁶. As such, bioorthogonal SRS is especially beneficial for live-cell interrogations of small molecules including metabolites and drugs whose label-free vibrational signatures are normally overwhelmed by cellular background and whose physiological functions are easily perturbed by conventional fluorophore labeling.

Furthermore, by harnessing the narrow linewidth of Raman peaks (e.g. 50-100 times narrower than fluorescence peaks), the development of highly sensitive Raman probe palettes followed. The matching dye palettes enable super-multiplexed (more than 20 channels) optical imaging for organelles or protein profiling with sensitivity down to 250 nM, bridging the optical imaging's subcellular spatial resolution with system biology's high information throughput⁴⁷⁻⁴⁹. Moreover, chemically activatable and photochromic SRS probes have also been developed lately for intracellular sensing and multiplexed tracking, empowering the functional SRS imaging⁵⁰⁻⁵⁴.

All these recently established Raman probes have greatly expanded the application boundary of vibrational imaging. Efforts in the past decade have proven that probe development plays a central role in driving the next frontiers of SRS microscopy. The growing chemical biology toolbox inspires the development of new SRS imaging functionalities. In turn, the SRS platform also finds the unique niche for chemical biology studies. Exploring new opportunities for merging SRS imaging with chemical biology is worth brainstorming. In this perspective, we first review recent notable advances in the development of Raman probes and their biological applications. On this basis, we further provide an outlook to further expand multiplexity, enhance Raman signals and utilize SRS imaging to decipher new biology.

1.4 Small-molecule Raman tagging

Triple bonds (e.g. $C\equiv C$, $C\equiv N$) and stable-isotope-substituted chemical bonds (e.g. C-D, N-D, O-D) vibrate in the cell-silent region (Figure 1.2a). Among these chemical bonds, $C\equiv C$ have the highest Raman signals (Figure 1.2b). One representative molecule tagged by $C\equiv C$ is the well-adopted thymidine analogue 5-ethynyl-2'-deoxyuridine (EdU), it reached an SRS detection limit of 200 μM ,³² and is now frequently used as a benchmark for Raman intensity quantification. Pioneered by the click chemistry field, chemists have developed a suite of alkyne-tagged molecular handles for bio-labeling, many of which could now be directly detected by Raman without the subsequent click reactions. With these available and newly developed Raman-tailored alkyne probes (Figure 1.2c), the dynamic metabolic processes including DNA synthesis, choline and glucose uptake could be readily visualized in live cells and tissues (Figure 1.2d with the corresponding analog structures shown in Figure 1.2c)^{32,55-59}. Additionally, drugs bearing native alkynes (e.g. ponatinib) or nitriles (e.g. paxlovid) or upon proper alkyne derivatization such as diyne-ferrostatin (Figure 1.2c&d) could be quantitatively imaged for intracellular distribution with well-maintained pharmacokinetics^{32,59,60}. Inspired by the colorful fluorescent protein palette, alkyne “vibrational colors” are also tunable through an isotope-editing strategy based on the dependence of Raman frequency on the bond mass. A set of ^{13}C -edited probes were developed that enabled multicolor SRS imaging of DNA, RNA and lipids in the same set of live cells⁶¹ (Figure 1.2e).

Compared to $C\equiv C$, $C\equiv N$ has lower (about 40%) Raman cross-sections (Figure 1.2b). However, as the peak frequencies of $C\equiv N$ are sensitive to physical environment, particularly the electrostatic interactions^{4,62,63}, they provide additional functions as vibrational sensors. Moreover, the $C\equiv N$ vibration occupies the higher frequency region (2200 - 2300 cm^{-1}), which separates well from that of $C\equiv C$ (2100 – 2200 cm^{-1}). Therefore, nitriles with similar isotope-editing for frequency shifting could be combined with alkynes for expanded imaging multiplexity.

As the stable isotope of hydrogen, deuterium-labeled chemical bonds, exemplified by the C-D, have unmatched advantages. Most importantly, since stable isotopes have almost the same physicochemical properties as their counterparts, the labeled molecules could be processed by cells' natural machineries with minimal perturbation to the native biological functions. In addition, compared to the label-free imaging of C-H, C-D yields an improved SRS detection limit for the absence of the interfering cellular background. Although the Raman cross section of C-D is smaller than that of the triple bonds (Figure 1.2b), what is lacking in cross section could be compensated by the large labeling number. For example, palmitic acid, the most common long-chain saturated fatty acid in mammalian cells, could have 31 deuteriums per molecule as d_{31} -palmitic acid. Owing to these features, deuterium plays a significant role in Raman labeling and has been applied to interrogating a wide range of uptake and metabolic dynamics for targets including amino acids⁶⁴, glucose⁶⁵, fatty acids⁶⁶, choline⁶⁷, cholesterol⁶⁸, water⁶⁹, solvents³³ and drugs⁷⁰ (Figure 1.2f). For instance, the employment of deuterated amino acids allows imaging of complex protein metabolism, including synthesis, degradation, and analysis of temporally defined populations⁶⁴ (Figure 1.2g). Similarly, d_{31} -palmitic acid enabled quantitative SRS visualization of fatty acids uptake and their metabolic incorporation²⁹; and the deuteration of propylene glycol (PG) allowed the capture of real-time 3D penetration for this common pharmaceutical cosolvent/excipient across the mice stratum corneum⁷⁰ (Figure 1.2g).

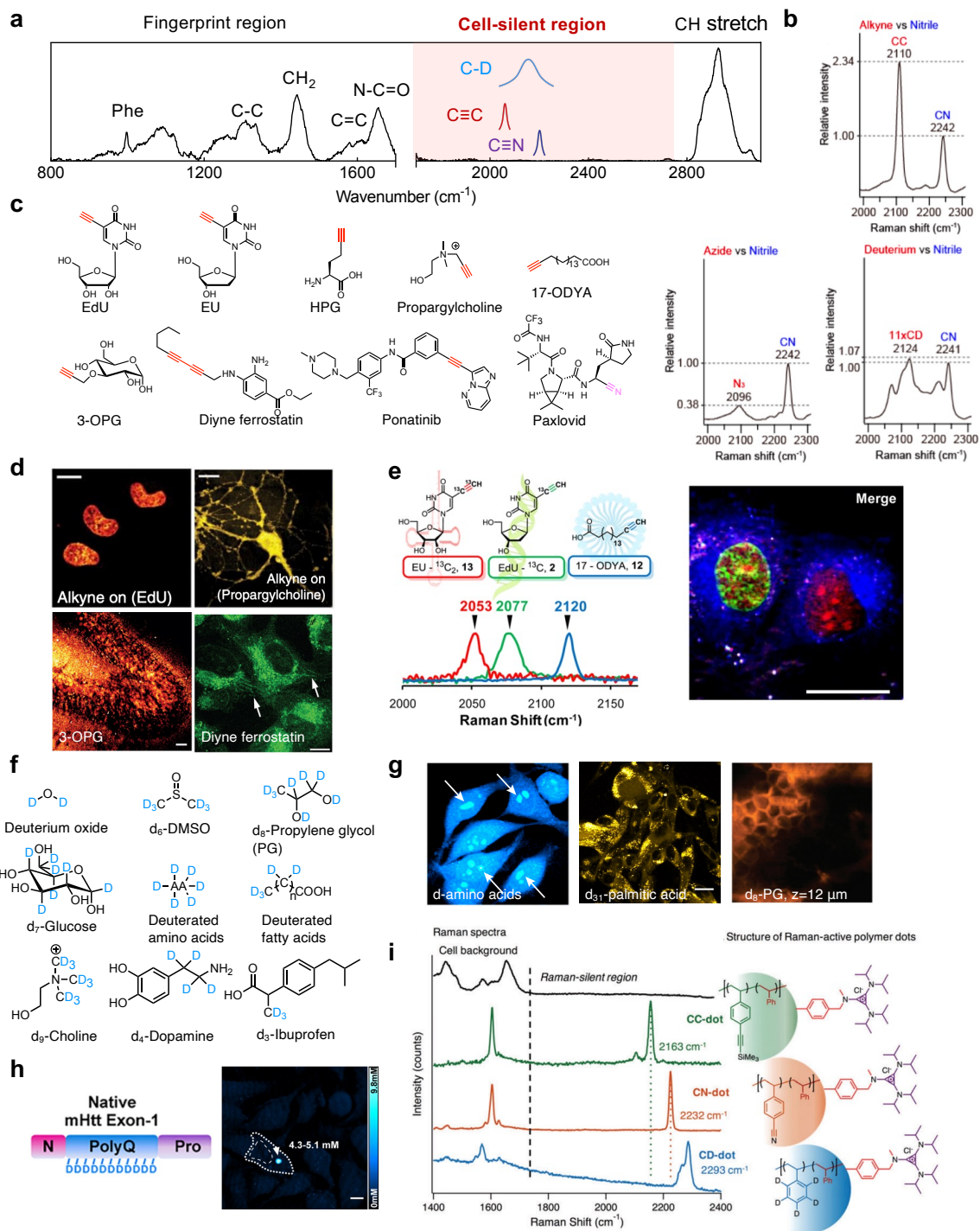


Figure 1.2. Small biorthogonal Raman tagging with $\text{C}\equiv\text{C}$, $\text{C}\equiv\text{N}$ and C-D . (a) A typical Raman spectrum of a mammalian cell (on glass slides) designating the crowded fingerprint region, the C-H stretch region, and the cell-silent region (pink). (b) Relative Raman peak intensities of common silent-

region Raman tags (i.e. C≡C, C≡N and C-D). Adapted in part with permission from ref⁷¹. Copyright 2010 American Chemical Society. (c) Representative triple-bond tagged small metabolites and drugs. (d) SRS Imaging targeting the alkyne vibrations for incorporation of thymidine-analogue EdU in live HeLa cells, choline-analogue propargylcholine in live neurons, glucose-analogue 3-OPG in cultured mouse brain tissue slices (Scale bar: 40 μm) and alkyne-tagged ferrostatin in live HT-1080 cells. Other scale bars: 10 μm. Adapted in part with permission from ref³², Copyright 2014 Nature publishing group. Adapted in part with permission from ref⁷², Copyright 2015 Wiley-VCH Verlag GmbH & Co. KGaA, Weinheim. Adapted in part with permission from ref⁵⁹. Copyright 2018 American Chemical Society. (e) ¹³C isotope editing enables three-color imaging of EdU, EU and 17-ODYA with alkyne probes. Scale bar, 25 μm. Adapted in part with permission from ref⁶¹. Copyright 2014 American Chemical Society. (f) Representative small molecules with deuterium tagging. (g) SRS imaging targeting the C-D vibration for the incorporation of deuterated amino acids in live HeLa cells, d₃₁-palmitic acid in melanoma cells (Scale bar: 20 μm) and d₈-PG in the mice stratum corneum at the depth of 12 μm after 124 min of treatment. Adapted in part with permission from ref⁶⁴, Copyright 2013 United States National Academy of Sciences. Adapted in part with permission from ref²⁹, Copyright 2020 Nature publishing group. Adapted in part with permission from ref⁷⁰. Copyright 2014 American Chemical Society. (h) SRS imaging of d₅-Gln-labeled mHtt-97Q aggregates in live HeLa cells. Quantifications for the local polyQ concentrations within the aggregates are also shown. Scale bars: 10 μm. Adapted in part with permission from ref⁷³. Copyright 2020 American Chemical Society. (i) C-D and triple-bond enriched polymer dots with amplified Raman signals. Adapted in part with permission from ref⁷⁴. Copyright 2017 The Royal Society of Chemistry.

Deuterium labeling could also obtain protein-specific imaging in live cells for certain targets. For example, aggregation-prone mutant Huntington (mHtt) protein harboring polyglutamine (polyQ) expansions has been shown to be specifically labeled by deuterated glutamine for their enrichment in the polyglutamine expansions⁷³ (Figure 1.2h). This design enabled first quantitative analysis of mHtt and non-mHtt proteins inside the same protein aggregates in live cells without the need of any fluorescent labels. To expand the library of labeled targets apart from proteins, similar selective labeling strategy may be developed, such as the selective labeling of glycogen by deuterated glucose in live cancer cells⁷⁵. The concept of harnessing such repeating units toward higher sensitivity is also adopted for C-D and triple-bond containing polymers, which could amplify the Raman signals by up to 10⁵ folds^{74,76–79}

(Figure 1.2i). The versatile applications of Raman-tagged cellular imaging are still expanding, which would also benefit from the easy synthetic accessibility to new vibrationally-tagged molecules. Toward this front, we envision that recent synthetic advances in late-stage functionalization⁸⁰⁻⁸² could provide convenient synthetic routes to deuterium or triple-bond tagged molecular targets beyond currently available pools.

1.5 Metabolic pathway analysis with deuterium labeling: from cell metabolism to microbiology

Various small Raman labels offer a wide range of applicability especially for investigating different aspects of cellular metabolism. To assay the uptake of metabolites (e.g. glucose), triple bonds are usually the top choice for their higher detectability^{57,72}. However, even triple-bond tagged metabolic analogs usually stop at the early catabolic steps in the metabolic pathway. In this case, stable isotope tagged metabolites are superior for tracing transformations into the downstream metabolic products from live cells to organisms with minimum toxicity¹³. For instance, with deuterated fatty acid labeling, lipid synthesis and mobilization could be non-invasively probed in live *Caenorhabditis elegans* by SRS with high throughput^{83,84} (Figure 1.3a). *C. elegans* with *daf-11* mutants were discovered to have no changes in the rate of lipid synthesis, but have a significant reduction in the rate of lipid catabolism⁸⁴.

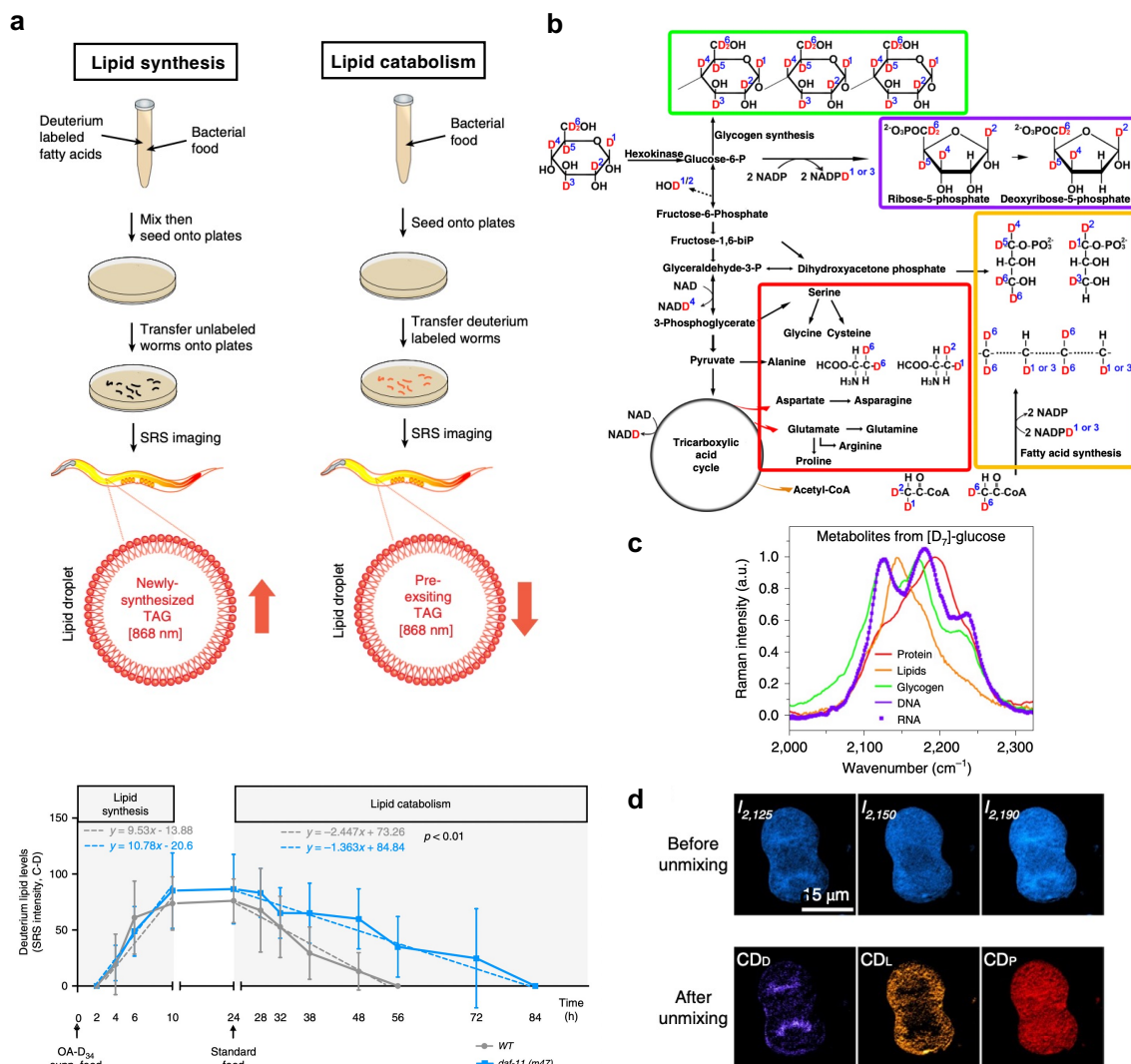


Figure 1.3. Metabolic pathway analysis with deuterium labeling. (a) Utilizing SRS imaging assays to determine the rate of lipid synthesis (left) and lipid mobilization (right) with deuterium-labeled fatty acids in *C. elegans*. Signals derived from deuterium-labeled lipids in intestinal lipid droplets were quantified (bottom). *daf-11* mutants have similar rate of lipid synthesis, but with reduced rate of lipid catabolism. Adapted in part with permission from ref^{83,84}, Copyright 2017, 2020 Nature publishing group. (b) The biological pathway from D_7 -glucose incorporation for spectral tracing of deuterium isotopes (STRIDE) of various metabolic products. Adapted in part with permission from ref⁸⁵, Copyright 2019 Nature publishing group. (c) Normalized C–D Raman spectra of five D_7 -glucose-derived biomolecules, including proteins, lipids, glycogen, DNA and RNA. Adapted in part with permission from ref⁸⁵, Copyright 2019 Nature publishing group. (d) Images of

a d₇-glucose metabolically labeled mitotic HeLa cell before and after spectral unmixing. Adapted in part with permission from ref⁸⁵, Copyright 2019 Nature publishing group.

Comprehensive cellular metabolism beyond metabolite uptake or distribution could be probed with suitable deuterium labeled probes. Glucose is the primary energy source for mammalian cells as well as an important precursor of downstream metabolites including amino acids, lipids, nucleic acids, glycogen and adenine dinucleotide phosphate (NADPH)⁸⁶. While 3-OPG (i.e. alkyne-tagged glucose, Figure 1.2d) is able to capture the glucose uptake in live cells and tissues, it stops at the phosphorylation step when going into the glucose metabolism pathway⁶¹. Recently, with deuterated glucose (i.e. d₇-glucose) labeling, diverse downstream products, such as DNA/RNA, proteins, lipids and glycogen, have been shown to be sparsely labeled with deuterium through each corresponding metabolic pathway⁸⁵ (Figure 1.3b). Meanwhile these sparsely labeled downstream products are spectrally separable with varied features due to altered chemical environment adjacent to the deuterium (Figure 1.3b&c)^{65,75,85}. A linear combination algorithm could then be utilized to quantitatively retrieve the relative C-D enrichment maps in each identified species^{75,85} (Figure 1.3d). Alternatively, site-specific deuterated glucose instead of d₇-glucose allows for tracing specific metabolic pathways. For example, 3-D-glucose ([3-D]Glc) was shown to monitor NADPH-mediated lipid synthesis through oxidative pentose phosphate pathway (oxPPP) by targeting lipid droplets⁸⁸.

Metabolic reprogramming serves as a unique hallmark for cancer and neurodegenerative diseases. This Raman-based imaging platform for complex glucose metabolism hence forms a live-cell spatially-resolved assay with subcellular resolution. Indeed, cancers cells have been shown to exhibit different levels of glucose uptake rate versus metabolism rate⁸⁷. Subcellular glycogen accumulation through d₇-glucose labeling was also discovered in cancer cells as potential indicators for their resistance to glucose deficiency⁷⁵. A similar spectral tracing strategy can be applied to cost-effective heavy water labeling (DO-SRS)⁶⁹. Since water is the most abundant molecule in biological systems, the incorporation of

deuterium from D₂O to C-D in macromolecules is highly efficient even at low and biologically-safe D₂O concentrations (e.g. 20% D₂O). The resulting distinct spectral signatures of C-D enable visualizing both lipid and protein metabolism in animals with long-term incubation (26 days)⁶⁹.

1.6 Raman probe palettes for highly sensitive and super-multiplexed imaging

Even with the signal amplification from SRS and the introduced Raman tags, there is still a sensitivity gap between the SRS and the fluorescence microscopy. The SRS detection limit of EdU is 200 μ M in live cells while the most sensitive fluorophores offer single molecule sensitivity (< 10 nM). One central drive in SRS imaging is to narrow this sensitivity gap. A promising way that has been proven successful and crucial is the development of highly sensitive Raman probes. As the Raman bands are inherently narrow (peak width about 10 cm^{-1} , ~ 50 -100 times narrower than that for fluorescent peaks), these Raman probes would enable high-throughput super-multiplexed (> 20 channels) imaging once the requirement for sensitivity is met. Therefore, Raman imaging holds the promise of breaking the color barrier of fluorescence imaging and should greatly benefit systematic biology investigations.

Two sets of highly sensitive and multiplexed Raman palettes have been developed for SRS imaging over the past five years. The first is xanthene-based electronic pre-resonance enhanced Manhattan Raman scattering (MARS) dyes^{47,48} (Figure 1.4a). By carefully tuning the absorption of the dyes (650 – 760 nm) to moderately close to the laser wavelength (~ 900 nm), SRS intensities of the nitrile vibration from these dyes could be pre-resonantly enhanced by up to 10^4 (detection limit up to 250 nM) with a well-maintained high signal-to-background ratio (Figure 1.4b). Taking advantage of the much narrower (78 times, 13 vs 1020 cm^{-1} of FWHM) SRS peak compared with fluorescence absorption peak and the multiplexity from isotope labeling as illustrated in the example of MARS2228 series dyes (Figure 1.4c), MARS dyes have the inherent capability for super-multiplexed imaging. With central atom (position 10) replacement, ring expansion and isotope editing, an SRS dye palette with up to 24 plex was created for super-multiplexed imaging⁴⁷ (Figure 1.4d). Through investigations in our

lab, we later found that different scaffolds could present vastly different pre-resonance SRS signals even with the same absorption wavelength, possibly due to the complicated electronic–vibrational coupling strength. This indicates that chemically finding a right scaffold is as important as physically modulating the absorption of the electronic structures. To facilitate the development of new palettes, theoretical models and computational tools are also urgently needed⁸⁹. While the construction of near-infrared chromophores is more challenging, the available electronic pre-resonance palettes could be largely expanded with freely tunable laser sources into the visible range^{90,91}.

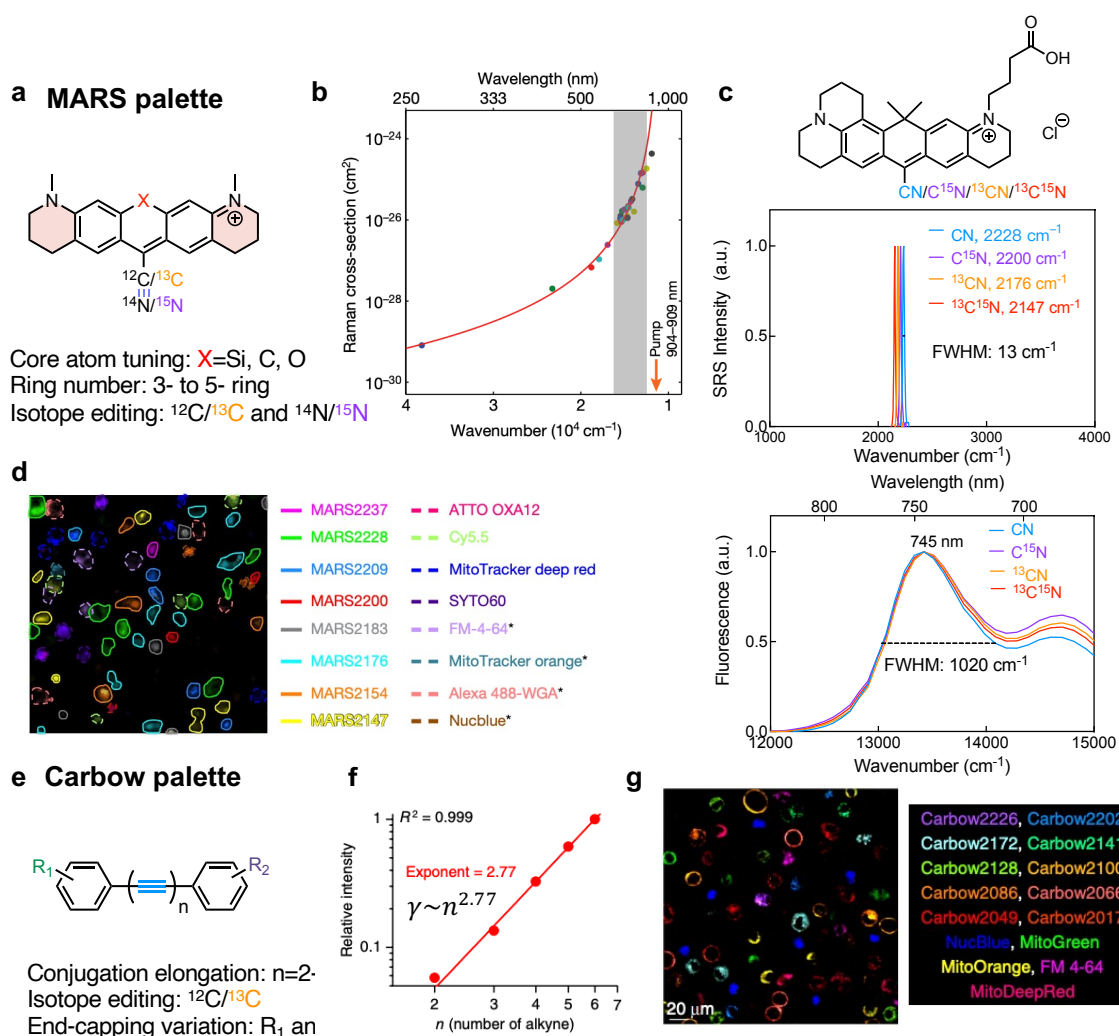


Figure 1.4. Physical principles for current strong and super-multiplexed Raman probes. (a) Construction of 24-color MARS xanthene palette. (b) The dramatical increase of SRS cross sections by electronic pre-resonance enhancing effects. Adapted in part with permission from ref⁴⁷, Copyright 2017 Nature publishing group. (c) The nitrile SRS peak (top) and the fluorescence absorption spectra (bottom) of a series of four isotope labeled MARS dyes (structure drawn at the top). The full width half maximum (FWHM) of the nitrile SRS peaks and the dominant absorption peak is listed. (d) Live-cell 16-color imaging with MARS and commercial dyes. Adapted in part with permission from ref⁴⁷, Copyright 2017 Nature publishing group. (e) Construction of 20-color Carbow polyynes palette. (f) The super-linear (an exponent of 2.77) SRS-signal growth with the number of conjugation alkynes. Adapted in part with permission from ref⁹², Copyright 2018 Nature publishing group. (g) Live-cell 15-color imaging with Carbow and commercial dyes. Adapted in part with permission from ref⁹², Copyright 2018 Nature publishing group.

The second established set of highly-sensitive Raman probes is the Carbow series, which is a set of linear conjugated alkynes with aromatic capping⁹² (Figure 1.4e). Different from electronic enhancement mechanism, the strong SRS signals of polyynes originate from the amplified second-order hyperpolarizability (γ) from conjugated alkynes. When the number of conjugated alkynes increases from 2 to 6, the Raman intensity grows super-linearly with an exponent of 2.77 (i.e. $\gamma \sim n^{2.77}$, Figure 1.4f), offering a desirable detectability down to 630 nM for 4-yne. The increase of conjugation length is also accompanied by the desirable Raman peak shifts, offering more spectral resolvability for multiplexed applications. Further combined with end-capping substitution and isotope editing, another 20-color CARBOW palette was created (Figure 1.4g). Without the involvement of electronic excitation, polyynes are free of photobleaching or environmental quenching. Although slightly smaller in cross sections compared to the MARS palette, Carbow palette has neutral scaffolds and is more suitable for live-cell targeted imaging with lower non-specific background. Theoretically, the longest conjugation length of polyynes could be over 6 with higher sensitivity than MARS, but at the risk of decreased stability. Going beyond polyynes structures, other oligomers such as polytriacetylenes, oligo(1,4-phenyleneethynylene)s⁹³, polydiacetylenes⁷⁷

have also been shown with exponential power-law relationship between the second-order hyperpolarizability (γ) and repeating units (n) with slightly increased sizes⁹⁴, thus are promising candidates for next-generation strong Raman probes.

1.7 Functional Raman Imaging Probes

Probing biological systems through chemical probes is a central topic for chemical biology study. Leveraging the live-cell compatibility, strict linear-concentration dependence and non-quenching nature of Raman signals, SRS probes are preferred for quantitative analysis. Although small vibrational probes have been extensively utilized for spectroscopic analysis of targeted cellular environment, such as electrostatic interactions, electrical currents and temperature^{4,62,63}, the development of highly sensitive Raman imaging probes for environmental sensing is still in its infancy. Benefiting from the unique super-multiplexed Raman features, functional SRS imaging probes should open the door for comprehensive investigations to elucidate the intricate intracellular and cell-to-cell interactions. Over the past four years, we witnessed the rapid growth of the development of such high-sensitivity SRS sensors. Based on their Raman spectroscopic features, we categorized these Raman sensors into four classes: sensing by peak shifts, peaks enhancement, peak generation and peak switching. Through the discussions, we aim to summarize systematic guidelines for designing new probes with tailored functions.

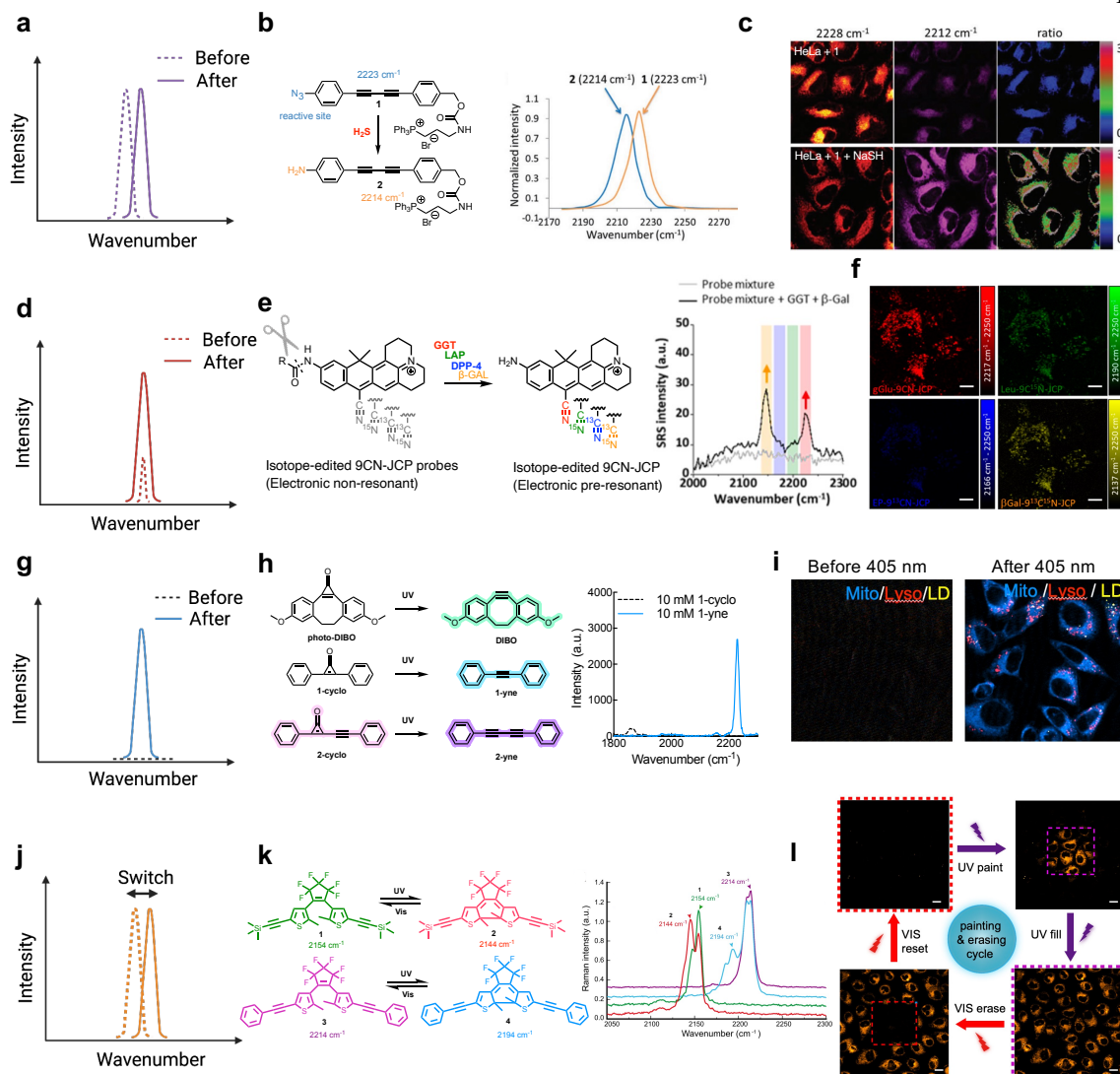


Figure 1.5. SRS probes for functional imaging with different spectroscopic signatures and their chemical designs. (a) SRS sensors based on peak shifts. (b) The conversion of $-\text{N}_3$ to $-\text{NH}_2$ induces a Raman peak shift of 9 cm^{-1} on the core of 2-yne. Adapted in part with permission from ref⁹⁵. Copyright 2018 The Royal Society of Chemistry. (c) Ratiometric imaging for NaSH sensing from the peak shift of the probe 1. Adapted in part with permission from ref⁹⁵. Copyright 2018 The Royal Society of Chemistry. (d) SRS sensors based on peak enhancements. (e) The electronic non-resonant 9CN-JCP probes undergo a large enzyme-induced red-shift in absorption to the electronic pre-resonant region with dramatic enhancement of SRS signals. Adapted in part with permission from ref⁵⁰. Copyright 2020 American Chemical Society. (f) The enhanced SRS signals enable multiplexed imaging for live-cell enzymes (GGT, LAP, DPP-4, and β -Gal) sensing. Scale bars: $10\text{ }\mu\text{m}$. Adapted

in part with permission from ref⁵⁰. Copyright 2020 American Chemical Society. (g) SRS sensors based on the peak generation. (h) The photoreactive conversion of cyclopropanones into alkynes generates strong SRS contrast with a sharp Raman peak. Adapted in part with permission from ref⁵⁴. Copyright 2022 American Chemical Society. (i) Engineered cyclopropanone probes enables three-color organelle-target photoactivatable SRS imaging in live HeLa cells (Mito: mitochondria channel; Lyso: lysosome channel; LD: lipid droplet channel). Adapted in part with permission from ref⁵⁴. Copyright 2022 American Chemical Society. (j) SRS sensors based on switchable peaks. (k) The Raman peak shifts reversibly upon photoisomerization of the diarylethene when irradiated by ultraviolet (UV) or visible light. Adapted in part with permission from ref⁵¹, Copyright 2021 Nature publishing group. (l) This photo-switchable peak shift enables SRS painting/erasing of cells with labelled alkyne-diarylethene. Scale bars: 20 μm . Adapted in part with permission from ref⁵¹, Copyright 2021 Nature publishing group.

Most of current Raman sensors are designed for sensing targeted chemical environment through Raman peak shifts (Figure 1.5a). The chemical reactions triggered by environmental stimuli are designed to change the chemical structures adjacent to the Raman reporters (e.g. alkynes or nitriles), therefore resulting in the distinct Raman peak shifts. For example, in a 2-yne scaffold, when the electron-withdrawing azide group on the end-phenyl cap is reduced to the electron donating amine in the presence of the reductive hydrogen sulfide species (such as H_2S and NaSH), the alkyne Raman peak shows a 9 cm^{-1} red shift⁹⁵ (Figure 1.5b), which is significant enough to be distinguished by SRS imaging (typical full-width-half-maximum (FWHM) for alkyne peak is 15 cm^{-1} and typical spectral width of SRS lasers are $\sim 12\text{-}15\text{ cm}^{-1}$). The demonstrated SRS ratiometric imaging indeed showed a strong response to NaSH level changes in the mitochondria of live cells (Figure 1.5c). With similar targeted reactions, triple-bond Raman probes with the peak-shift principles have also been rationally designed and developed for sensing pH⁹⁶, fluoride⁹⁷ and metal ions⁹⁸. Recently, the isotope exchange reactions especially the H/D exchange was harnessed on terminal alkynes for both two-color imaging and cellular environmental sensing applications^{99,100} taking advantage of the dramatic alkyne Raman peak shift of more than 130 cm^{-1} due to both the large mass

difference between D and H and the quantum coupling between the alkyne and the adjacent C-D. In addition to chemical reactions, Raman peak frequency could also be tuned by the surrounding physical environment. A well-known example is that the peak frequencies of triple bonds especially nitriles are highly sensitive to hydrogen-bonding and electrostatics, an effect known as vibrational solvatochromism. By specifically mapping the peak frequency of nitrile-bearing MARS Raman dyes in live cells, the bound-water percentage in cytoplasm was revealed to be around 60% while that in nucleus was about 30%^{101,102}. Recently, the SRS peak of voltage-sensitive rhodopsin has also been shown to shift upon voltage changes¹⁰³.

Intensity enhancement represents another category of design principle for SRS sensors (Figure 1.5d), but less explored. Recently, modulation of electronic pre-resonance SRS effect was implemented for intracellular enzyme activity sensing. The nitrile xanthene scaffold, once caged by amides structures (9CN-JCP probes), would absorb in the visible region (506 nm, electronic non-resonance) with almost invisible SRS signals. However, the enzymatic conversion of amides structures to amines structures (9CN-JCPs) would dramatically boost SRS signals by shifting the absorption to the near-infrared region (630 nm, electronic pre-resonance) (Figure 1.5e). With isotope editing on the nitrile to generate multiple colors, this elegant intensity-modulation principle was successfully exploited to create 4-color enzymatic sensing probes⁵⁰ (Figure 1.5e). In this case, simultaneous detecting the activities of 4 distinct enzymes were demonstrated for effective profiling of different cancer cell phenotypes (Figure 1.5f). With the super-multiplexed MARS dye palette, this enzyme-activatable sensor design holds high promises for profiling more than 10 enzymes simultaneously.

Peak generation allows background-free imaging and is highly beneficial for sensitive and multiplexed detection (Figure 1.5g). The Raman intensity activation does not solely come from the cellular or the chemical environment, but it could also originate from the photons. In a recent design, the first photoactivatable SRS imaging probes were developed based on the photocaged alkynes, the cyclopropenones (Figure 1.5h)⁵⁴. Such rationally designed

cyclopropanone structures were optimized with live-cell compatibility and have been proven to be well-suitable for multiplexed live-cell imaging and tracking⁵⁴ (Figure 1.5i). With high precision spatial-temporal control offered by photoactivation, these series of isotope editing probes was demonstrated for multiplexed tracking from the subcellular to the single-cell level. Upon further improvement of multiplexity, these new Raman sensors may illuminate complex cell-to-cell interactions and facilitate massive-parallel cell profiling. For example, combining photoactivatable SRS probes and single-cell RNA sequencing (scRNA-seq) could likely enable spatially-resolved transcriptomics profiling¹⁰⁴.

Raman peaks could also be reversibly switchable especially with light manipulations (Figure 1.5j). Such features are crucial to a variety of biological investigations including tracking protein dynamics, subcellular environment sensing and super-resolution imaging. In 2021, three groups independently reported photophysical or photochemical approaches to achieve photoswitchable SRS imaging⁵¹⁻⁵³. To name one example, the alkyne-tagged diarylethene showed impressive photo-switchable property in the cell-silent spectral window⁵¹ (Figure 1.5k). The UV induced photoisomerization converts diarylethene from the open-ring state to the closed-ring state while visible light would induce the reverse conversion, accompanied by the switching of SRS peak intensities. These alkynes-tagged diarylethenes were demonstrated for photo-rewritable patterning and mitochondria tracking (Figure 1.6l). It is noteworthy that the SRS readout lasers would induce the off-switch pathway, competing with the UV induced photo-cyclization, underscoring the careful choice of molecular absorption when designing the new probes.

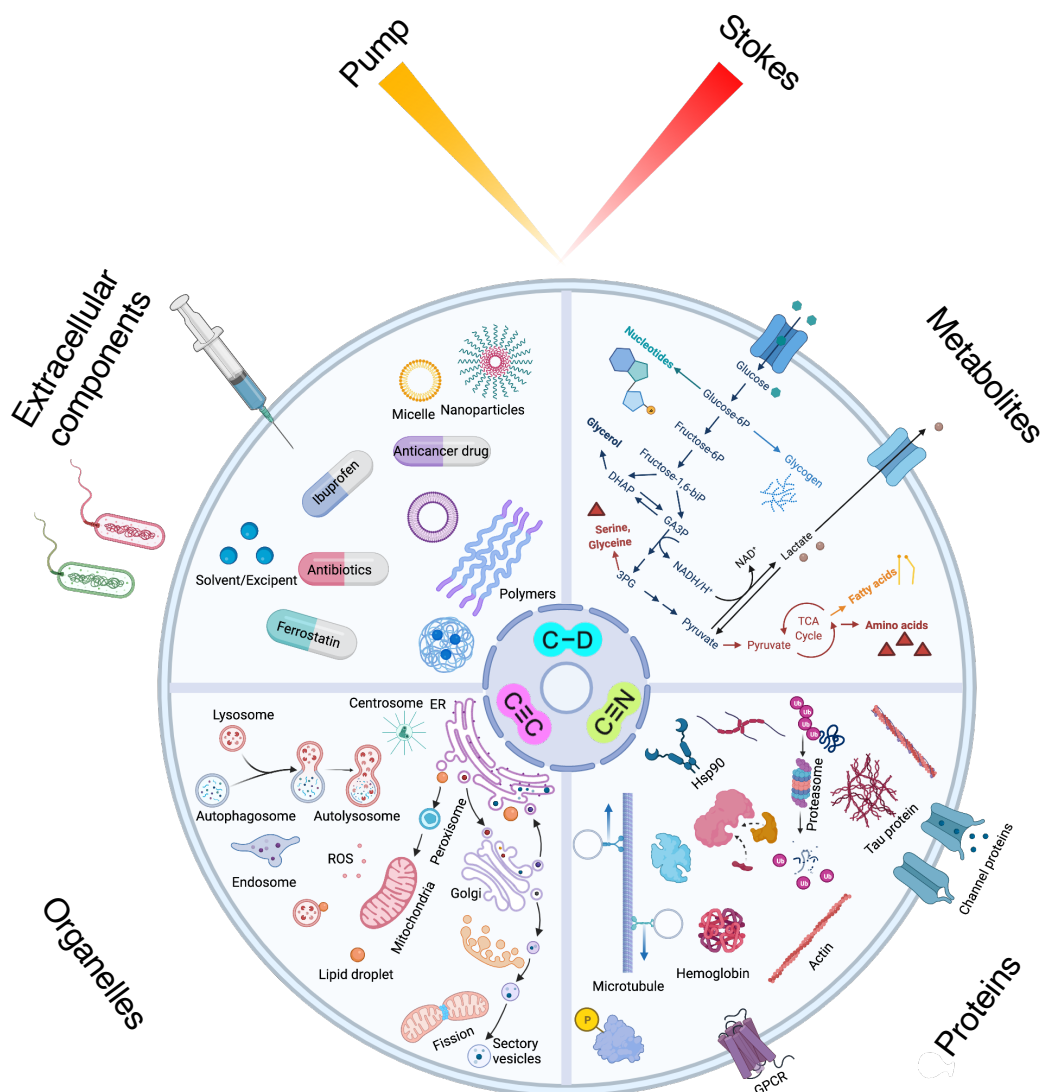


Figure 1.6. Representative and envisioned applications of SRS imaging, particularly with the development of Raman-tailored bioorthogonal chemical tags of $C\equiv C$, $C\equiv N$ and $C-D$. The dynamic processes of targets across different molecular scales, from small-molecule metabolites to proteins, organelles, and extracellular components, could be visualized with high specificity and low perturbation.

1.8 Conclusion

Through the past decade we have seen the SRS microscopy has transited from the initial technical demonstration into a powerful method with potentials to answer many biological questions in a way no other methods could (Figure 1.6). Such transformation is impossible without appropriate Raman probes. With small triple-bond or isotope tagging, SRS microscopy enables visualization and analysis of dynamic metabolism pathways in live cells and animals. From chemistry innovations, the construction of highly sensitive MARS and Carbow palettes realized the full potential of Raman for super-multiplexed imaging. The recently developed functional Raman sensors further expanded the applications for multiplexed cellular environment sensing and high precision spatial-temporal tracking. We also envision the design with further improved multiplexity and sensitivity of the Raman probes as a next step towards interrogating more complex biology.

As the development of Raman probes would continue to be a central topic for the SRS community, we also hope to invoke brainstorming to borrow the wisdom from the chemical biology field and to promote vibrational imaging to solve biological questions. In retrospect, many of the recent progress of SRS probes were inspired by other fields: deuterium and other isotope labeling are prevalent in mass spectrometry; alkynes are the most important biorthogonal chemical group handles; MARS dyes originate from commercially available fluorophores; diarylethene is a class of well-established photoswitchable chromophores, etc. The knowledge cross fields should hence largely accelerate the advances of SRS probes into higher selectivity, sensitivity, photostability, biocompatibility, and multiplexing capability. Together with the developments of instrumentation, biorthogonal chemistry, molecular delivery and labeling methods, data analysis and likely more, SRS microscopy should develop into an indispensable tool for chemical biology studies.

1.9 Reference

1. Kneipp, K., Kneipp, H., Itzkan, I., Dasari, R. R. & Feld, M. S. Ultrasensitive Chemical Analysis by Raman Spectroscopy. *Chem. Rev.* **99**, 2957–2975 (1999).
2. Fang, C., Frontiera, R. R., Tran, R. & Mathies, R. A. Mapping GFP structure evolution during proton transfer with femtosecond Raman spectroscopy. *Nature* **462**, 200–204 (2009).
3. Kukura, P., McCamant, D. W. & Mathies, R. A. Femtosecond stimulated Raman spectroscopy. *Annu. Rev. Phys. Chem.* **58**, 461–488 (2007).
4. Chattopadhyay, A. & Boxer, S. G. Vibrational Stark Effect Spectroscopy. *J. Am. Chem. Soc.* **117**, 1449–1450 (1995).
5. Thomas, G. J. Raman spectroscopy of protein and nucleic acid assemblies. *Annu. Rev. Biophys. Biomol. Struct.* **28**, 1–27 (1999).
6. Raman, C. V. & Krishnan, K. S. A new type of secondary radiation [11]. *Nature* **121**, 501–502 (1928).
7. Zumbusch, A., Holtom, G. R. & Xie, X. S. Three-dimensional vibrational imaging by coherent anti-stokes raman scattering. *Phys. Rev. Lett.* **82**, 4142–4145 (1999).
8. Min, W., Freudiger, C. W., Lu, S. & Xie, X. S. Coherent nonlinear optical imaging: Beyond fluorescence microscopy. *Annu. Rev. Phys. Chem.* **62**, 507–530 (2011).
9. Ploetz, E., Laimgruber, S., Berner, S., Zinth, W. & Gilch, P. Femtosecond stimulated Raman microscopy. *Appl. Phys. B Lasers Opt.* **87**, 389–393 (2007).
10. Freudiger, C. W. *et al.* Label-Free Biomedical Imaging with High Sensitivity by Stimulated Raman Scattering Microscopy. *Science* **322**, 1857–1861 (2008).
11. Ozeki, Y., Dake, F., Kajiyama, S., Fukui, K. & Itoh, K. Analysis and experimental assessment of the sensitivity of stimulated Raman scattering microscopy. *Opt. Express* **17**, 3651 (2009).
12. Cheng, J. X. & Xie, X. S. Vibrational spectroscopic imaging of living systems: An emerging platform for biology and medicine. *Science* **350**, (2015).
13. Hu, F., Shi, L. & Min, W. Biological imaging of chemical bonds by stimulated Raman scattering microscopy. *Nat. Methods* **16**, 830–842 (2019).
14. Saar, B. G. *et al.* Video-rate molecular imaging in vivo with stimulated Raman scattering. *Science* **330**, 1368–1370 (2010).
15. Camp, C. H. *et al.* High-speed coherent Raman fingerprint imaging of biological tissues. *Nat. Photonics* **8**, 627–634 (2014).
16. Wakisaka, Y. *et al.* Probing the metabolic heterogeneity of live *Euglena gracilis* with stimulated Raman scattering microscopy. *Nat. Microbiol.* **1**, (2016).
17. Bi, Y. *et al.* Near-resonance enhanced label-free stimulated Raman scattering microscopy with spatial resolution near 130 nm. *Light Sci. Appl.* **7**, 1–10 (2018).
18. Qian, C. *et al.* Super-resolution label-free volumetric vibrational imaging. *Nat. Commun.* **12**, 1–10 (2021).
19. Shi, L. *et al.* Super-resolution vibrational imaging using expansion stimulated Raman scattering microscopy. *bioRxiv* 2021.12.22.473713 (2021). doi:10.1101/2021.12.22.473713
20. Zipfel, W. R., Williams, R. M. & Webb, W. W. Nonlinear magic: Multiphoton microscopy in the biosciences. *Nat. Biotechnol.* **21**, 1369–1377 (2003).

21. Jonkman, J., Brown, C. M., Wright, G. D., Anderson, K. I. & North, A. J. Tutorial: guidance for quantitative confocal microscopy. *Nat. Protoc.* **15**, 1585–1611 (2020).
22. Miller, D. R., Jarrett, J. W., Hassan, A. M. & Dunn, A. K. Deep Tissue Imaging with Multiphoton Fluorescence Microscopy. *Curr. Opin. Biomed. Eng.* **4**, 32–39 (2017).
23. Hill, A. H., Manifold, B. & Fu, D. Tissue imaging depth limit of stimulated Raman scattering microscopy. *Biomed. Opt. Express* **11**, 762 (2020).
24. Fu, D., Holtom, G., Freudiger, C., Zhang, X. & Xie, X. S. Hyperspectral imaging with stimulated raman scattering by chirped femtosecond lasers. *J. Phys. Chem. B* **117**, 4634–4640 (2013).
25. Zhang, D. *et al.* Quantitative vibrational imaging by hyperspectral stimulated raman scattering microscopy and multivariate curve resolution analysis. *Anal. Chem.* **85**, 98–106 (2013).
26. Figueroa, B., Hu, R., Rayner, S. G., Zheng, Y. & Fu, D. Real-Time Microscale Temperature Imaging by Stimulated Raman Scattering. *J. Phys. Chem. Lett.* **11**, 7083–7089 (2020).
27. Yue, S. *et al.* Cholesteryl ester accumulation induced by PTEN loss and PI3KAKT activation underlies human prostate cancer aggressiveness. *Cell Metab.* **19**, 393–406 (2014).
28. Li, J. *et al.* Lipid desaturation is a metabolic marker and therapeutic target of ovarian cancer stem cells. *Cell Stem Cell* **20**, 303-314.e5 (2017).
29. Du, J. *et al.* Raman-guided subcellular pharmaco-metabolomics for metastatic melanoma cells. *Nat. Commun.* **11**, 4830 (2020).
30. Chen, T., Yavuz, A. & Wang, M. C. Dissecting lipid droplet biology with coherent Raman scattering microscopy. *J. Cell Sci.* **135**, (2022).
31. Shen, Y. *et al.* Metabolic activity induces membrane phase separation in endoplasmic reticulum. *Proc. Natl. Acad. Sci.* **114**, 13394–13399 (2017).
32. Wei, L. *et al.* Live-cell imaging of alkyne-tagged small biomolecules by stimulated Raman scattering. *Nat. Methods* **11**, 410–412 (2014).
33. Chiu, W. S. *et al.* Molecular diffusion in the human nail measured by stimulated Raman scattering microscopy. *Proc. Natl. Acad. Sci. U. S. A.* **112**, 7725–7730 (2015).
34. Fu, D. *et al.* Imaging the intracellular distribution of tyrosine kinase inhibitors in living cells with quantitative hyperspectral stimulated Raman scattering. *Nat. Chem.* **6**, 614–622 (2014).
35. Huang, K. C., Li, J., Zhang, C., Tan, Y. & Cheng, J. X. Multiplex Stimulated Raman Scattering Imaging Cytometry Reveals Lipid-Rich Protrusions in Cancer Cells under Stress Condition. *iScience* **23**, 100953 (2020).
36. Nitta, N. *et al.* Raman image-activated cell sorting. *Nat. Commun.* **11**, 1–16 (2020).
37. Ji, M. *et al.* Rapid, label-free detection of brain tumors with stimulated raman scattering microscopy. *Sci. Transl. Med.* **5**, (2013).
38. Hollon, T. C. *et al.* Near real-time intraoperative brain tumor diagnosis using stimulated Raman histology and deep neural networks. *Nat. Med.* **26**, 52–58 (2020).
39. Ji, M. *et al.* Label-free imaging of amyloid plaques in Alzheimer’s disease with stimulated raman scattering microscopy. *Sci. Adv.* **4**, 1–9 (2018).
40. Lin, L. E., Miao, K., Qian, C. & Wei, L. High spatial-resolution imaging of label-free in vivo protein aggregates by VISTA. *Analyst* **146**, 4135–4145 (2021).

41. Berto, P., Andresen, E. R. & Rigneault, H. Background-free stimulated raman spectroscopy and microscopy. *Phys. Rev. Lett.* **112**, 1–5 (2014).
42. Casacio, C. A. *et al.* Quantum-enhanced nonlinear microscopy. *Nature* **594**, 201–206 (2021).
43. Lin, H. *et al.* Microsecond fingerprint stimulated Raman spectroscopic imaging by ultrafast tuning and spatial-spectral learning. *Nat. Commun.* **12**, 1–12 (2021).
44. Kobayashi-Kirschvink, K. J. *et al.* Raman2RNA: Live-cell label-free prediction of single-cell RNA expression profiles by Raman microscopy. *bioRxiv* 2021.11.30.470655 (2021). doi:10.1101/2021.11.30.470655
45. Manifold, B., Men, S., Hu, R. & Fu, D. A versatile deep learning architecture for classification and label-free prediction of hyperspectral images. *Nat. Mach. Intell.* **3**, 306–315 (2021).
46. Wei, L. *et al.* Live-Cell Bioorthogonal Chemical Imaging: Stimulated Raman Scattering Microscopy of Vibrational Probes. *Acc. Chem. Res.* **49**, 1494–1502 (2016).
47. Wei, L. *et al.* Super-multiplex vibrational imaging. *Nature* (2017). doi:10.1038/nature22051
48. Miao, Y., Qian, N., Shi, L., Hu, F. & Min, W. 9-Cyanopyronin probe palette for super-multiplexed vibrational imaging. *Nat. Commun.* **12**, 4518 (2021).
49. Shi, L. *et al.* Highly-multiplexed volumetric mapping with Raman dye imaging and tissue clearing. *Nat. Biotechnol.* (2021). doi:10.1038/s41587-021-01041-z
50. Fujioka, H. *et al.* Multicolor Activatable Raman Probes for Simultaneous Detection of Plural Enzyme Activities. *J. Am. Chem. Soc.* **142**, 20701–20707 (2020).
51. Ao, J. *et al.* Switchable stimulated Raman scattering microscopy with photochromic vibrational probes. *Nat. Commun.* **12**, 1–8 (2021).
52. Shou, J. & Ozeki, Y. Photoswitchable stimulated Raman scattering spectroscopy and microscopy. *Opt. Lett.* **46**, 2176 (2021).
53. Lee, D. *et al.* Toward photoswitchable electronic pre-resonance stimulated Raman probes. *J. Chem. Phys.* **154**, 1–10 (2021).
54. Du, J. & Wei, L. Multicolor Photoactivatable Raman Probes for Subcellular Imaging and Tracking by Cyclopropanone Caging. *J. Am. Chem. Soc.* (2021). doi:10.1021/jacs.1c09689
55. Hong, S. *et al.* Live-cell stimulated Raman scattering imaging of alkyne-tagged biomolecules. *Angew. Chemie - Int. Ed.* **53**, 5827–5831 (2014).
56. Lee, H. J. *et al.* Assessing Cholesterol Storage in Live Cells and *C. elegans* by Stimulated Raman Scattering Imaging of Phenyl-Diyne Cholesterol. *Sci. Rep.* **5**, 1–10 (2015).
57. de Moliner, F. *et al.* A Palette of Minimally Tagged Sucrose Analogues for Real-Time Raman Imaging of Intracellular Plant Metabolism. *Angew. Chemie - Int. Ed.* **60**, 7637–7642 (2021).
58. Seidel, J. *et al.* Structure-activity-distribution relationship study of anti-cancer antimycin-type depsipeptides. *Chem. Commun.* **55**, 9379–9382 (2019).
59. Gaschler, M. M. *et al.* Determination of the Subcellular Localization and Mechanism of Action of Ferrostatins in Suppressing Ferroptosis. *ACS Chem. Biol.* **13**, 1013–1020 (2018).
60. Koike, K. *et al.* Quantitative drug dynamics visualized by alkyne-tagged plasmonic-

- enhanced Raman microscopy. *ACS Nano* **14**, 15032–15041 (2020).
61. Chen, Z. *et al.* Multicolor live-cell chemical imaging by isotopically edited alkyne vibrational palette. *J. Am. Chem. Soc.* **136**, 8027–8033 (2014).
 62. Waegele, M. M., Culik, R. M. & Gai, F. Site-specific spectroscopic reporters of the local electric field, hydration, structure, and dynamics of biomolecules. *J. Phys. Chem. Lett.* **2**, 2598–2609 (2011).
 63. Bakthavatsalam, S., Dodo, K. & Sodeoka, M. A decade of alkyne-tag Raman imaging (ATRI): applications in biological systems. *RSC Chem. Biol.* **2**, 1415–1429 (2021).
 64. Wei, L., Yu, Y., Shen, Y., Wang, M. C. & Min, W. Vibrational imaging of newly synthesized proteins in live cells by stimulated Raman scattering microscopy. *Proc. Natl. Acad. Sci. U. S. A.* **110**, 11226–11231 (2013).
 65. Li, J. & Cheng, J. X. Direct visualization of de novo lipogenesis in single living cells. *Sci. Rep.* **4**, 1–8 (2014).
 66. Zhang, D., Slipchenko, M. N. & Cheng, J. X. Highly sensitive vibrational imaging by femtosecond pulse stimulated raman loss. *J. Phys. Chem. Lett.* **2**, 1248–1253 (2011).
 67. Hu, F., Wei, L., Zheng, C., Shen, Y. & Min, W. Live-cell vibrational imaging of choline metabolites by stimulated Raman scattering coupled with isotope-based metabolic labeling. *Analyst* **139**, 2312–2317 (2014).
 68. Alfonso-García, A., Pfisterer, S. G., Riezman, H., Ikonen, E. & Potma, E. O. D38-cholesterol as a Raman active probe for imaging intracellular cholesterol storage. *J. Biomed. Opt.* **21**, 061003 (2015).
 69. Shi, L. *et al.* Optical imaging of metabolic dynamics in animals. *Nat. Commun.* **9**, (2018).
 70. Saar, B. G., Contreras-Rojas, L. R., Xie, S. X. & Guy, R. H. Imaging drug delivery to skin with coherent raman scattering microscopy. *Mol. Pharm.* **8**, 969–975 (2014).
 71. Yamakoshi, H. *et al.* Alkyne-tag Raman imaging for visualization of mobile small molecules in live cells. *J. Am. Chem. Soc.* **134**, 20681–20689 (2012).
 72. Hu, F. *et al.* Vibrational Imaging of Glucose Uptake Activity in Live Cells and Tissues by Stimulated Raman Scattering. *Angew. Chemie - Int. Ed.* **54**, 9821–9825 (2015).
 73. Miao, K. & Wei, L. Live-Cell Imaging and Quantification of PolyQ Aggregates by Stimulated Raman Scattering of Selective Deuterium Labeling. *ACS Cent. Sci.* **6**, 478–486 (2020).
 74. Hu, F., Brucks, S. D., Lambert, T. H., Campos, L. M. & Min, W. Stimulated Raman scattering of polymer nanoparticles for multiplexed live-cell imaging. *Chem. Commun.* **53**, 6187–6190 (2017).
 75. Lee, D. *et al.* Visualizing Subcellular Enrichment of Glycogen in Live Cancer Cells by Stimulated Raman Scattering. *Anal. Chem.* **92**, 13182–13191 (2020).
 76. Zhu, W. *et al.* Precise Encoding of Triple-Bond Raman Scattering of Single Polymer Nanoparticles for Multiplexed Imaging Application. *Angew. Chemie - Int. Ed.* **60**, 21846–21852 (2021).
 77. Tian, S. *et al.* Polydiacetylene-based ultrastrong bioorthogonal Raman probes for targeted live-cell Raman imaging. *Nat. Commun.* **11**, 1–9 (2020).
 78. Zhao, Z. *et al.* Ultra-bright Raman dots for multiplexed optical imaging. *Nat. Commun.* **12**, 1305 (2021).
 79. Jin, Q. Q. *et al.* Multicolor raman beads for multiplexed tumor cell and tissue imaging

- and in vivo tumor spectral detection. *Anal. Chem.* **91**, 3784–3789 (2019).
80. Farizyan, M., Mondal, A., Mal, S., Deufel, F. & Van Gemmeren, M. Palladium-Catalyzed Nondirected Late-Stage C-H Deuteration of Arenes. *J. Am. Chem. Soc.* **143**, 16370–16376 (2021).
 81. Zhao, D., Petzold, R., Yan, J., Muri, D. & Ritter, T. Tritiation of aryl thianthrenium salts with a molecular palladium catalyst. *Nature* **600**, 444–449 (2021).
 82. Porey, S. *et al.* Alkyne Linchpin Strategy for Drug:Pharmacophore Conjugation: Experimental and Computational Realization of a Meta-Selective Inverse Sonogashira Coupling. *J. Am. Chem. Soc.* **142**, 3762–3774 (2020).
 83. Yu, Y., Mutlu, A. S., Liu, H. & Wang, M. C. High-throughput screens using photo-highlighting discover BMP signaling in mitochondrial lipid oxidation. *Nat. Commun.* **8**, 1–11 (2017).
 84. Mutlu, A. S., Gao, S. M., Zhang, H. & Wang, M. C. Olfactory specificity regulates lipid metabolism through neuroendocrine signaling in *Caenorhabditis elegans*. *Nat. Commun.* **11**, 1–15 (2020).
 85. Zhang, L. *et al.* Spectral tracing of deuterium for imaging glucose metabolism. *Nat. Biomed. Eng.* **3**, 402–413 (2019).
 86. Deberardinis, R. J. & Thompson, C. B. Cellular metabolism and disease: What do metabolic outliers teach us? *Cell* **148**, 1132–1144 (2012).
 87. Long, R. *et al.* Two-color vibrational imaging of glucose metabolism using stimulated Raman scattering. *Chem. Commun.* **54**, 152–155 (2017).
 88. Hong, S. *et al.* Live-cell imaging of NADPH production from specific pathways. *CCS Chem.* **3**, 1642–1648 (2021).
 89. Miao, Y., Shi, L., Hu, F. & Min, W. Probe design for super-multiplexed vibrational imaging. *Phys. Biol.* **16**, 41003 (2019).
 90. Zhuge, M. *et al.* Ultrasensitive Vibrational Imaging of Retinoids by Visible Preresonance Stimulated Raman Scattering Microscopy. *Adv. Sci.* **8**, 1–11 (2021).
 91. Xiong, H., Qian, N., Miao, Y., Zhao, Z. & Min, W. Stimulated Raman Excited Fluorescence Spectroscopy of Visible Dyes. *J. Phys. Chem. Lett.* **10**, 3563–3570 (2019).
 92. Hu, F. *et al.* Supermultiplexed optical imaging and barcoding with engineered polyynes. *Nat. Methods* **15**, 194–200 (2018).
 93. Su, X. *et al.* Aggregation-Induced Emission-Active Poly(phenyleneethynylene)s for Fluorescence and Raman Dual-Modal Imaging and Drug-Resistant Bacteria Killing. *Adv. Healthc. Mater.* **10**, (2021).
 94. Lucotti, A. *et al.* Absolute Raman intensity measurements and determination of the vibrational second hyperpolarizability of adamantyl endcapped polyynes. *J. Raman Spectrosc.* **43**, 1293–1298 (2012).
 95. Zeng, C., Hu, F., Long, R. & Min, W. A ratiometric Raman probe for live-cell imaging of hydrogen sulfide in mitochondria by stimulated Raman scattering. *Analyst* **143**, 4844–4848 (2018).
 96. Wilson, L. T. *et al.* A new class of ratiometric small molecule intracellular pH sensors for Raman microscopy. *Analyst* **145**, 5289–5298 (2020).
 97. Tipping, W. J. *et al.* Ratiometric sensing of fluoride ions using Raman spectroscopy. *Chem. Commun.* **56**, 14463–14466 (2020).

98. Takemura, S., Watanabe, H., Nishihara, T., Okamoto, A. & Tanabe, K. Monitoring intracellular metal ion complexation with an acetylene-tagged ligand by Raman spectroscopy. *RSC Adv.* **10**, 36119–36123 (2020).
99. Egoshi, S., Dodo, K., Ohgane, K. & Sodeoka, M. Deuteration of terminal alkynes realizes simultaneous live cell Raman imaging of similar alkyne-tagged biomolecules. *Org. Biomol. Chem.* **19**, 8232–8236 (2021).
100. Bi, X., Miao, K. & Wei, L. Alkyne-Tagged Raman Probes for Local Environmental Sensing by Hydrogen – Deuterium Exchange. *J. Am. Chem. Soc.* **144**, 8504–8514 (2022).
101. Shi, L., Hu, F. & Min, W. Optical mapping of biological water in single live cells by stimulated Raman excited fluorescence microscopy. *Nat. Commun.* **10**, 1–8 (2019).
102. Lang, X. & Welsher, K. Mapping solvation heterogeneity in live cells by hyperspectral stimulated Raman scattering microscopy. *J. Chem. Phys.* **152**, (2020).
103. Lee, H. J. *et al.* Electronic Preresonance Stimulated Raman Scattering Imaging of Red-Shifted Proteorhodopsins: Toward Quantitation of the Membrane Potential. *J. Phys. Chem. Lett.* **10**, 4374–4381 (2019).
104. Tang, Q. *et al.* Optical Cell Tagging for Spatially Resolved Single-Cell RNA Sequencing. *Angew. Chemie Int. Ed.* **100730**, (2021).

*Chapter 2*RAMAN-GUIDED SUBCELLULAR
PHARMACO-METABOLOMICS FOR
METASTATIC MELANOMA CELLS

The content of this chapter has been published in:

Du, J.[#], Su, Y.[#], Qian, C., Yuan, D., Miao, K., Lee, D., Ng, A., Wijker, R., Ribas, A., Levine, R., Heath, J. *, & Wei, L*. Raman-guided Subcellular Pharmaco-metabolomics for Metastatic Melanoma Cells. *Nat. Commun.*, 2020, 11, 4830.

#equal contribution.

2.1 Introduction

Single-cell omics methods have revolutionized biology by resolving the heterogeneity that underlies population averages¹⁻⁵. One envisioned application is that of pharmaco-omics (i.e. pharmacogenomics), in which the genetic or functional composition of diseased tissues is harnessed to guide the deployment of custom therapeutic strategies for individual patient^{6,7}. Single-cell metabolomics has lagged behind other omics methods for the lack of proper toolsets for non-perturbative and targeted (analyte-specific) detection, but it has the potential to offer deep insights via shining light on the metabolic reprogramming that accompanies many disease states^{8,9}. Mass spectrometry metabolomics has recently advanced to the level where analyte labeling techniques can permit multiplex analysis from single cells^{10,11}, but it is intrinsically sample-destructive, so prohibits live-cell analysis. The fluorescence-based methods offer high sensitivity¹², but with poor multiplexing, and fluorophore labels can hinder metabolite processing⁸.

As a non-invasive optical tool, Raman spectroscopy probes the vibrational motions of chemical bonds, which allows detection of endogenous metabolites in a label-free manner. Multiple types of cellular metabolites have been identified by Raman fingerprinting, including nucleic acids, amino acids, lipids, glucose, neurotransmitters and etc¹³⁻¹⁵. In addition to spectroscopy, Raman microscopy further generates subcellular chemical maps by targeting pre-determined vibrational peaks. In particular, the recent emergence of stimulated Raman scattering (SRS) microscopy, utilizing stimulated emission quantum amplification, provides imaging quality comparable to fluorescence microscopy with resolution of ~ 450 nm and speed up to video-rate in live cells and tissues^{16,17}. By sweeping the laser across a designated wavelength range, hyperspectral-SRS (hSRS) rapidly produces Raman spectra of up to 600 cm^{-1} at subcellular locations¹⁸⁻²¹. Going beyond label-free analysis, Raman spectro-microscopy provides targeted detection and imaging of specific metabolites by recent strategies of stable-isotope labeling^{22,23}.

In this work, we explore Raman spectro-microscopy for subcellular pharmacometabolomics. We adopt a series of BRAF-mutant patient-derived melanoma cell lines as a model system. Metastatic melanoma is the most-deadly form of skin cancers, for which 66% of them harbor mutations in the BRAF kinase²⁴. We utilize Raman spectro-microscopy to characterize this series of related but distinct BRAF-mutant melanoma cancer cell phenotypes, each corresponding to a different level of cancer cell differentiation, from melanocytic (differentiated) to mesenchymal (de-differentiated)²⁵⁻²⁷. The associated biology of these and similar melanoma models has been deeply investigated, which informs our study here²⁷⁻³¹. The sensitivity of these cell lines to various targeted inhibitors and immunotherapies associates with de-differentiation status^{27,28,32}. Differentiated phenotypes exhibit higher sensitivity towards BRAF inhibitors, while the de-differentiated phenotypes exhibit an innate resistance^{27,33,34}. We hence mine the resulting spectroscopic information to identify phenotype specific, druggable metabolic susceptibilities.

We first establish a transcriptional relationship between cellular de-differentiation and metabolic reprogramming. We then integrate single-cell Raman data with transcriptomics analysis to establish that Raman-extracted trends in cellular chemical composition correlate with corresponding trends in gene expression. We identify and validate two druggable metabolic susceptibilities. One is specific to the differentiated melanoma cell lines studied, and is consistent with trends in gene expression. The second susceptibility is specific to the de-differentiated cell lines, and is uniquely extracted from the Raman analysis of subcellular lipid droplets. It is not detected through either bulk transcriptional analysis or bulk metabolomics, but can be validated by lipidomics. Raman analysis of single cells is thus shown as a potent pharmaco-metabolomics tool.

2.2 Metabolic features are shown in both transcriptome and Raman

Tsoi and coworkers recently published a pharmaco-genomic analysis of 53 patient-derived BRAF-mutant melanoma cell lines²⁷. Notably, they demonstrated that the expression profiles of these cell lines faithfully reflected what was seen in the corresponding patient tumors. Further, they adopted unsupervised clustering of those profiles and classified the cell lines into four groups based upon de-differentiation status: melanocytic (differentiated), transitory, neural-crest-like, and mesenchymal (de-differentiated). We first selected a subset of 30 of these cell lines for analysis, on the basis that they did not also contain RAS mutations. Similar to reported²⁷, the whole transcriptomic data of these 30 cell lines, when visualized within a two-dimensional space (see Methods), yielded a clear separation into four distinct phenotypes, separated by level of de-differentiation (Fig 1a, top panel). The nature of cancer cell de-differentiation means that energetic requirements, cellular morphology, etc., are all altered, suggesting that cellular differentiation is also accompanied by metabolic reprogramming³⁵. We tested this hypothesis by similarly analyzing the same 30 melanoma cell lines, but including in that analysis only ~1600 genes associated with metabolic processes. In fact, this calculation yielded an almost identical clustering (Figure 1a, bottom panel). Just like the well-reported phenotypic markers^{28,36}, metabolic genes also showed a

clear phenotype-dependent expression trend, with associated functions that span different metabolic processes (The representative (top 4 ranked) metabolic genes are shown in the bottom of Figure 2.1b, the complete heatmap and list of the top ranked metabolic genes are shown in Supplementary Figure 2.1 and Supplementary Table 2.1). This implies that metabolic susceptibilities that exist within these cell lines may well vary with cellular de-differentiation, similar to what is known for inhibitors that target oncogenic signaling³⁷.

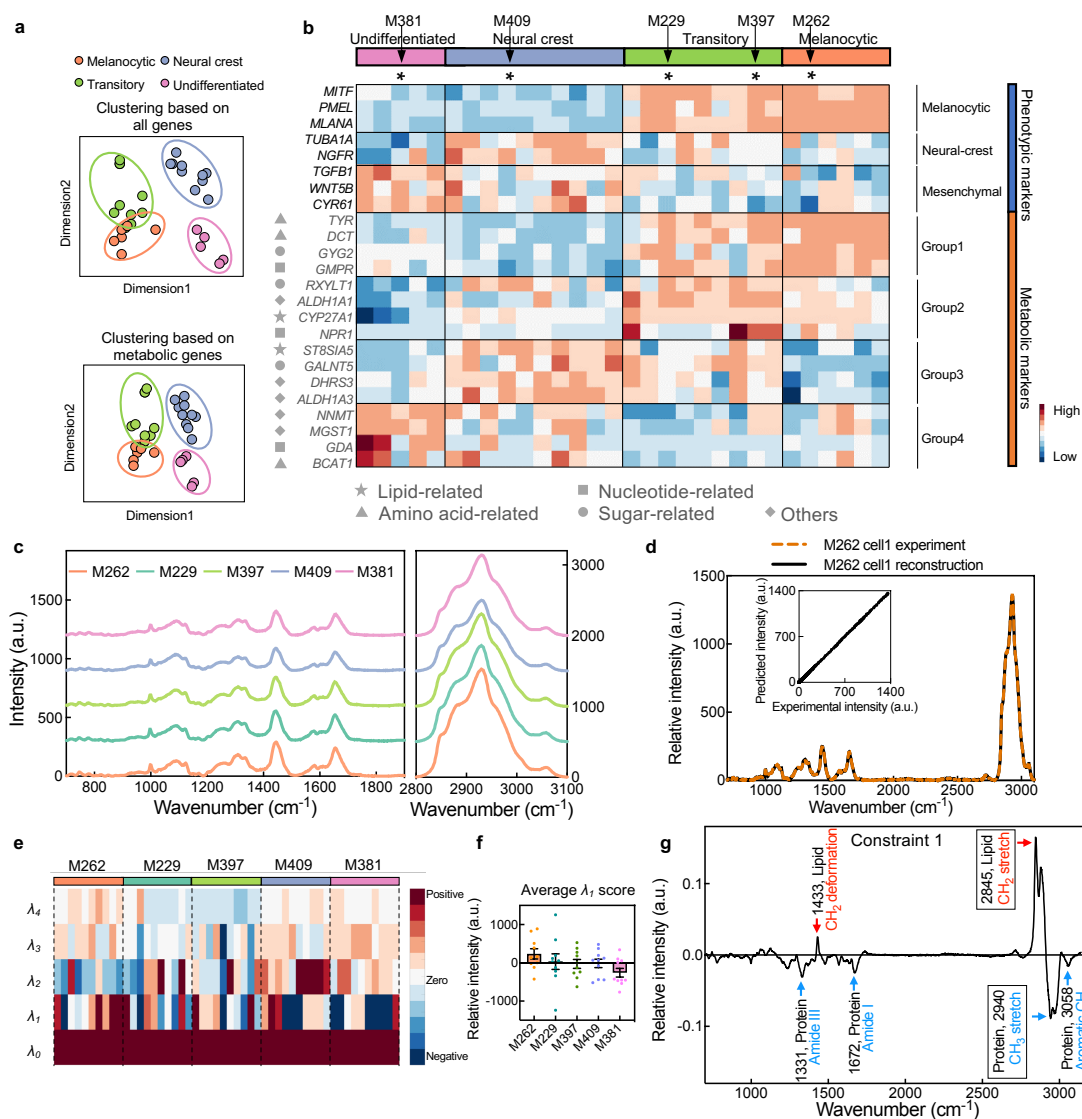


Figure 2.1. Transcriptomics and spontaneous Raman spectra analysis of metastatic melanoma

cell lines. (a) Dimensional reduction of bulk transcriptomics data of 30 melanoma cell lines yields a clear separation of four different melanoma phenotypes, based on either the expression of all genes (top panel) or ~ 1600 metabolic genes (bottom panel). (b) A heatmap of gene expression levels for representative genes involved in defining the cellular and metabolic phenotypes shown in (a). The black-font row labels are well-reported phenotypic marker genes for defining different subtypes. The grey-font row labels are top 4 ranked metabolic markers within each phenotype representing different processes, as identified by matching the symbol with the key at the bottom of the heatmap. The color-coded bars at the top of the heat map indicate the different cellular phenotypes for each cell line, while the arrows point to the 5 representative cell lines selected for Raman analysis. (c) Spontaneous Raman spectra of five selected cell lines (averaged over 50 spectra from 10 cells per cell line examined over 3 independent experiments). Each spectrum is offset apart in y-axis with no changes of absolute intensities. (d) A representative Raman spectrum of M262 cells reconstructed by summing the constraints $\lambda_0 - \lambda_4$ identified using surprisal analysis (SA). The inset plot shows the high correlation between the reconstructed and the measured spectrum. (e) Heatmap for scores of the top five constraints ($\lambda_0 - \lambda_4$) calculated by SA of the Raman spectra across the 5 cell lines (10 cells from each cell line). Each column represents SA scores across $\lambda_0 - \lambda_4$ from an individual cell. Each row represents the score of a given constraint across multiple single cells. (f) The average score of constraint 1 (λ_1) of 10 cells across all 5 cell lines. Data shown as mean \pm SEM. g, The spectrum of λ_1 , with Raman peak assignments. The most negative feature is from CH_3 vibration at 2940 cm^{-1} arising mainly from proteins (blue, boxed). The most positive feature is a CH_2 vibration at 2845 cm^{-1} mainly from lipids (red, boxed).

We selected five representative patient-derived cell lines based upon the single criteria that they collectively spanned the range of de-differentiation status (indicated at the top of Figure 2.1b with information listed in Supplementary Table 2.2), from M381 (undifferentiated) to M262 (differentiated). We acquired spontaneous Raman spectra at the single-cell level from all 5 cell lines (Supplementary Figure 2.2a) over the molecular fingerprinting spectral range of 700 cm^{-1} to 3100 cm^{-1} (Figure 2.1c). These spectral shapes are largely similar across four phenotypes. To extract differences between these spectra, we first utilized unsupervised surprisal analysis (SA) for dimension reduction³⁸. SA is similar to principal component analysis (PCA) in that it is an orthogonal transformation of the data, with the dominant

eigenvectors (also called constraints) capturing most of the variance observed in the Raman spectra of different cell lines. While SA has been successfully applied to analyzing gene expression data sets^{26,39}, an early application was for the analysis of molecular spectra⁴⁰. We first confirmed that the constraints and their respective weights obtained from SA could recapitulate the fine Raman spectral features (Figure 2.1d and Supplementary Figure 2.2b). We then generated a heatmap of the top 5 constraints, labeled in ascending order as $\lambda_0 - \lambda_4$, with each cell line represented by 10 individual cells (Figure 2.1e). The largest constraint, λ_0 , captures universally shared spectral features and is expected to be invariant across cell lines. This shared spectrum, with peak assignments, is provided in Supplementary Figure 2.3. The second largest constraint, λ_1 (Figure 2.1e) captures the greatest variance from spectra to spectra and exhibits an average score that obviously changes with cellular de-differentiation (Figure 2.1f). The remaining $\lambda_2 - \lambda_4$ are lower in amplitude and less revealing in spectral features (Figure 2.1e and Supplementary Figure 2.3). The spectral distribution of λ_1 exhibits positive contributions from CH_2 vibrational stretches (2845 cm^{-1} , largely arising from lipids), and negative contributions from CH_3 stretches (2940 cm^{-1} , mostly from proteins) (Figure 2.1g and Supplementary Figure 2.4). The λ_1 score declines from M262 to M381. This indicates that the lipid/protein (CH_2/CH_3) ratio decreases with the progression of de-differentiation in these melanoma cell lines (Figure 2.1g). We note here that the relative high variance in the λ_1 originates from the intracellular heterogeneity from relatively low sampling in spontaneous Raman acquisition (Supplementary Figure 2.2a). This issue is largely bypassed in SRS imaging, as shown below, with much higher resolution and sampling.

2.3 Differentiated cells are susceptible to fatty acid synthesis

After mining the metabolic-associated spectral features from the wide fingerprint region, we next turned to live, single-cell imaging investigations to capture intracellular heterogeneity. We utilized SRS imaging (Supplementary Figure 2.5a), with microsecond-level pixel dwell

time, subcellular resolution and linear-concentration dependence for straightforward metabolic quantifications^{16,17}, to interrogate how the overall trend shown in Figure 2.1f is reflected at the whole cell level. We targeted the lipid peak at 2845 cm^{-1} (attributed to CH_2 vibrations^{16,17}, Figure 2.1a, top) and the protein peak at 2940 cm^{-1} (from CH_3 vibrations⁴¹, Figure 2.1a, middle). The generated CH_2/CH_3 ratiometric images (Figure 2.2a, bottom) indeed nicely resolved a decreasing trend from melanocytic M262 cells toward mesenchymal M381 cells, implying that the more differentiated cells are relatively richer in lipids. SRS images on fixed cells yielded similar conclusions (Supplementary Figure 2.5b). After quantifying the averaged CH_2/CH_3 intensity ratios (Figure 2.2b and Supplementary Figure 2.5c), we then asked whether this trend extracted from Raman imaging could be correlated to transcriptomics data. Strongly correlating or anti-correlating gene expression patterns are shown in the heatmap of Figure 2.2c. In particular, several genes associated with lipid processing are identified with strong positive correlations, including fatty acid synthase (FASN), 3-hydroxyacyl-CoA dehydrogenase (HADH), and Malonyl CoA-acyl carrier protein transacylase, mitochondrial (MCAT). In fact, the gene ontology (GO) fatty acid synthetic processes exhibits a strong linear correlation with the CH_2/CH_3 Raman ratios (Figure 2.2d, top, $r = 0.93$, $p = 0.02$). Also notable are genes (Figure 2.2c) and biological processes that exhibit a negative-correlation with CH_2/CH_3 , such those associated with the cell migration pathway (Figure 2.2d, bottom, $r = -0.91$, $p = 0.03$). The high migratory nature is a known feature in mesenchymal phenotypes⁴². Similar relationships from features strongly related to melanocytic (Supplementary Figure 2.6a, top) or mesenchymal cell types (Supplementary Figure 2.6a, bottom) were also resolved. These data demonstrate that single-cell Raman imaging yields information consistent with transcriptional profiling.

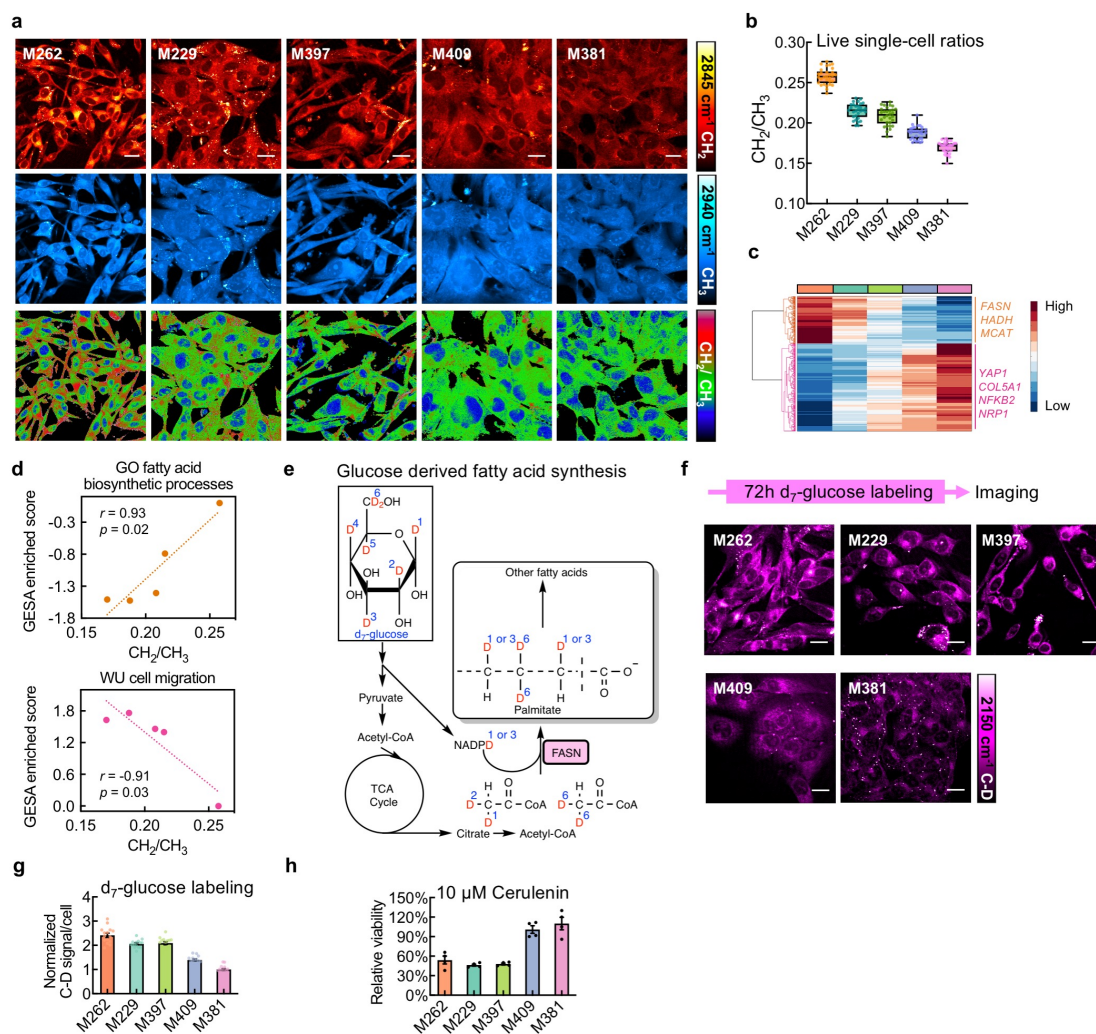


Figure 2.2. Live-cell SRS imaging and transcriptomics analysis reveal a differentiated-cell-specific susceptibility. (a) Representative live-cell SRS images targeted on the CH₂ (top, 2845 cm^{-1}) and CH₃ (middle, 2940 cm^{-1}) channels and the corresponding CH₂ to CH₃ ratio (bottom, CH₂/CH₃) images. (b) Average live single-cell CH₂/CH₃ values from the SRS ratio images for each cell line ($n = 30$ cells per cell line examined over 5 independent experiments). Data are plotted as boxplots: center line indicates median; box limits indicate upper and lower quartiles; whiskers indicate minimum and maximum. (c) Heatmap of genes with strong correlations or anticorrelations to the CH₂/CH₃ trends shown in (b). Representative genes involved in fatty acid metabolism (orange, positive correlation) and mesenchymal signature (purple, negative correlation) are indicated. (d) Two representative top biological functional processes from Gene Set Enrichment Analysis (GSEA) with GSEA scores that exhibit positive (top panel) or negative (bottom panel) correlations with the phenotype-dependent CH₂/CH₃ trends across different cell lines. (e) Illustration of the pathway for

deuterium transfer from deuterated glucose (d_7 -glucose) to de novo synthesized fatty acids through the major lipid biosynthetic pathways. (f) SRS imaging at the C-D channel (2150 cm^{-1}) for newly synthesized fatty acids in all 5 selected cell lines cultured with d_7 -glucose medium for 3 days. Labeling and imaging scheme shown on top. (g) Single-cell quantification of relative C-D signals in d_7 -glucose labeled cells ($n = 15$ cells examined over 3 independent experiments, the C-D signals of M381 cells are normalized to 1). (h) Relative viability of melanoma cells after treatment of FASN inhibitor cerulenin ($10\text{ }\mu\text{M}$, 3 days, $n = 4$ independent experiments). Scale bars, $20\text{ }\mu\text{m}$. Data shown as mean \pm SEM.

Elevated FASN expression (Supplementary Figure 2.6b) in the differentiated cell lines implies increased de novo fatty-acid synthesis. We first sought to further explore this biology through targeted SRS imaging. Elevated glucose catabolism is a characteristic of many cancers, and produces an excess of the glycolytic end-product, pyruvate, some of which can be converted to acetyl-CoA and then further converted, through an FASN mediated pathway, to fatty acids^{43,44} (Figure 2.2e). The relative importance of de novo fatty-acid synthesis in the various cell lines can be inferred by tracking the conversion of glucose into fatty acids (Figure 2.2e). Thus, we incubated the cells in media by replacing regular glucose with deuterated glucose (d_7 -glucose) for 3 days before SRS imaging (Figure 2.2f). The rationale is that an active de novo fatty-acid synthetic pathway will convert some of this d_7 -glucose into deuterated lipids, which exhibit a unique lipid associated C-D spectral signature around 2150 cm^{-1} , effectively yielding a live-cell assay of FASN activity⁴⁵. SRS images of the 5 cell lines, collected at 2150 cm^{-1} , are provided in Fig 2f. The measured cytoplasmic Raman spectrum (Supplementary Figure 2.6c) matches what is expected from deuterated lipids⁴⁵. The subsequent quantification of average C-D signals across multiples image sets (Figure 2.2g) implies that de novo fatty acid synthesis is most activated in the differentiated cell lines M262, M229, and M397 and remains relatively low in de-differentiated M409 and M381.

Elevated FASN activities in the more differentiated melanoma cell lines suggest that the FASN pathway may constitute a metabolic susceptibility in just those phenotypes. In fact,

interruption of this pathway has been previously studied for cancer drug development⁴⁶. We tested this hypothesis by treating the cells with FASN inhibitors, 10 μ M cerulenin⁴⁶ or 0.2 μ M TVB-3166⁴⁷, for 3 days. As hypothesized, the 3 most differentiated phenotypes exhibited the highest sensitivity to cerulenin and TVB-3166 while the two most undifferentiated cell lines are barely affected by such drug treatments (Figure 2.2h and Supplementary Figure 2.6d). This data demonstrates that single-cell Raman spectroscopy, integrated with transcriptional profiling, can uncover phenotype-specific druggable susceptibilities in cancer cells.

2.4 Mesenchymal M381 accumulates selected lipids in lipid droplets

The above results indicate that metabolic susceptibilities within BRAF mutant melanoma cell lines can be strongly dependent upon de-differentiation phenotype. A second relevant example is that of mesenchymal-specific GPX4-inhibitor-induced ferroptosis identified using pharmacogenomics by Tsoi and co-workers²⁷. That susceptibility is related to lipid peroxidation. Finding new druggable targets for the highly-invasive (Supplementary Figure 2.7a) and BRAFi innate-resistant phenotype (Supplementary Table 2.2) might facilitate the development of clinically relevant inhibitors. We thus hypothesized that a deep interrogation of the lipid biochemistries in these cell lines might reveal additional druggable susceptibilities that distinguish the mesenchymal phenotypes. To this end, we studied the role of lipid storage in lipid droplets. Lipid droplets are sub-micrometer-size lipid reservoir organelles^{48,49} that are comprised of a highly dynamic mixture of neutral lipids (i.e. triacylglycerides (TAG) and cholesteryl esters (CE)). They are increasingly recognized for their central roles in modulating the transport and oxidation of lipids through interaction with other organelles^{49,50}.

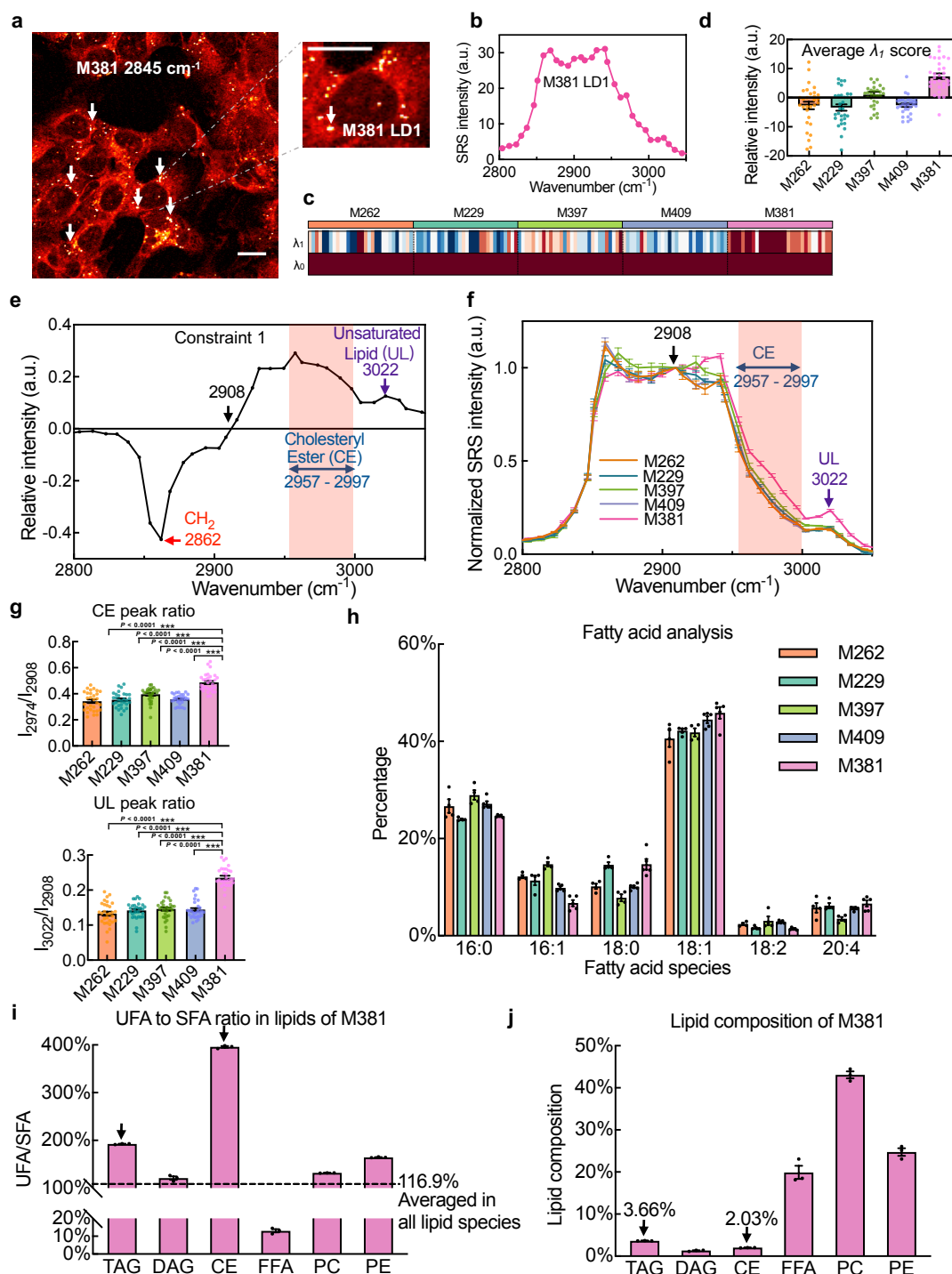


Figure 2.3. Accumulation of unsaturated lipids and cholesteryl esters in lipid droplets (LDs) of de-differentiated M381 cells. (a) A representative SRS image of M381 cells imaged in the CH₂ (2845 cm⁻¹) channel. LDs are indicated. A zoomed-in image at right highlights a single LD. (b) The

hSRS spectrum of the zoomed-in LD in (a) at the C-H stretch region (2800 cm^{-1} to 3050 cm^{-1}). (c) Heatmap for scores of the top two constraints ($\lambda_0 - \lambda_1$) by surprisal analysis of hSRS spectra on LDs across five cell lines ($n = 30$ LDs per cell line examined over 3 independent experiments). Each column represents an individual LD and each row represents the constraint scores. (d) The average score of λ_1 across five cell lines ($n = 30$ LDs). (e) Raman peak assignments for constraint 1 (λ_1). The pink shadowed range from 2957 cm^{-1} to 2997 cm^{-1} is assigned to cholesteryl esters (CE), and the 3022 cm^{-1} peak (violet arrow) is assigned to unsaturated lipids (=C-H, UL). (f) hSRS spectra (normalized at 2908 cm^{-1} , the zero point revealed in (e)) of LDs across each cell line ($n = 30$). (g) Quantification of relative CE ($2974\text{ cm}^{-1}/2908\text{ cm}^{-1}$, top panel) and UL ($3022\text{ cm}^{-1}/2908\text{ cm}^{-1}$, bottom panel) enrichment in LDs across cell lines from (f) ($n = 30$). (h) GC-MS measurement of fatty acids extracted from bulk melanoma cells. The percentages of 16:0, 16:1, 18:0, 18:1, 18:2, and 20:4 are normalized to all extracted fatty acids ($n = 4$ independent experiments for M262, M229, M397; $n = 5$ independent experiments for M409 and M381). (i) Average ratio of unsaturated fatty acids (UFA) to saturated fatty acids (SFA) in each lipid class from lipidomics of M381 cells ($n = 3$ independent experiments). j, Percentage of major lipid classes from lipidomics of M381 cells ($n = 3$). *** $p < 0.001$ from two-tailed unpaired t-tests. Scale bars, $20\text{ }\mu\text{m}$. Data shown as mean \pm SEM.

We used hSRS microscopy to analyze the composition of these sub-cellular lipid droplets at a spatial resolution of $\sim 450\text{ nm}$. Such live-cell compatible and non-perturbative subcellular quantification by hSRS is beyond what mass spectrometry and fluorescence analysis could offer. The unique spherical morphologies of lipid droplets are readily imaged by SRS. Since they are lipid-rich, they exhibit large CH_2 Raman scattering signals near 2845 cm^{-1} (Figure 2.3a). We generated Raman spectra on lipid droplets from each of the 5 cell lines, by acquiring SRS images across the C-H vibrational region from 2800 cm^{-1} to 3050 cm^{-1} with high spectral resolution of 8 cm^{-1} (Figure 2.3b). To extract the phenotype-dependent variations from these spectra, we again employed surprisal analysis (SA), which resolved a universal constraint λ_0 , and just a single additional constant λ_1 . As before, we confirmed that summing these two dominant constraints could recapitulate the measured hSRS spectra of lipid droplets (Supplementary Figure 2.7b). We then generated a heatmap of the weights of λ_0 and λ_1 for individual lipid droplets, grouped by their associated cell lines (Figure 2.3c).

Again, λ_0 is constant across cell lines (Figure 2.3c and Supplementary Figure 2.8a) while λ_1 exhibits a uniquely high positive amplitude for the mesenchymal M381 cell line (Figure 3c-d). Based on Raman spectra from reference pure lipid species (Supplementary Figure 2.8b), we annotated the spectral distribution of λ_1 . The 3022 cm^{-1} peak is assigned to the C-H stretch where the carbon is associated with a C=C double bond (i.e. =C-H). This spectral feature arises mostly from unsaturated lipids (UL)⁵¹. The broad band from 2957-2997 cm^{-1} largely originates from the C-H vibrations on the sterol rings of cholesterol ester (CE) (Figure 2.3e)^{52,53}. This spectral composition of λ_1 suggests that lipid droplets within M381 cells bear the highest level of UL and CE among the 5 cell lines. This is further verified by direct normalization of all hSRS spectra to 2908 cm^{-1} (Figure 2.3f-g), which is a zero point in λ_1 (Figure 2.3e).

The observation that the intracellular lipid droplets within the mesenchymal M381 cell line exhibit a relatively increased level of unsaturated lipids, relative to the other cell lines (Figure 2.3g, bottom), suggested a novel lipid regulation process within that cell line. We first examined whether this trend of lipid unsaturation was reflected in bulk analysis. We performed gas chromatography-mass spectrometry (GC-MS) based analysis of fatty acids from cell pellets (Figure 2.3h). For presentation, we follow the common lipid notation of xx:yy, where xx represents the number of carbon atoms in the lipid chain, and yy refers to the number of double bonds (Figure 2.3h). Although M381 cells show slightly enhanced level of 18:1 fatty acid (i.e. oleic acid) relative to the other cell lines, the heterogeneity of overall unsaturation across the cell lines is minor. Similarly, there is no clear trend for the expression levels of key desaturases in M381 compared to other cell lines (Supplementary Figure 2.8c). It is likely that the compositional variability of neutral lipids (i.e. TAG and CE) in lipid droplets is averaged out by other more abundant lipid species in the bulk GC-MS analyses. Therefore, we performed liquid chromatography-mass spectrometry (LC-MS) based lipidomics profiling with preserved lipid structures. Indeed, bulk lipidomics data for M381 cells clearly shows that while droplet-enriched species of TAG and CE have the highest unsaturated fatty acid composition among major lipid species (Figure 2.3i), they only

account for a small portion (in total < 6%) of all major lipid species (Figure 2.3j). Thus, M381 has elevated lipid unsaturation levels specifically within intracellular lipid droplets.

2.5 Desaturases are involved lipid-droplet unsaturation of M381

We next sought to trace the source of the enhanced lipid-droplet unsaturation in M381 cells. Such an increase may arise from either cellular uptake or de novo synthesis. Further, the unsaturated lipid signal could originate from either mono-unsaturated fatty acids (MUFA) or poly-unsaturated (multiple double bonds) fatty acids (PUFA). First, to assess lipid uptake, we adopted a labeled SRS imaging approach by incubating M381 cells in medium containing deuterated mono-unsaturated fatty acids (d_{33} -oleic acid) or saturated fatty acids (d_{31} -palmitic acid), the two most widely used fatty acids for assaying uptake. We found that M381 cells have the lowest uptake of extracellular fatty acids across all cell lines (Supplementary Figure 2.9), suggesting that de novo synthesized fatty acids may serve as major sources for M381. We next tested whether the MUFA or PUFA de novo synthesis pathway (Figure 2.4a) contributes to the elevated lipid-droplet unsaturation. In mammalian cells, $\Delta 9$ desaturase (Stearoyl-CoA desaturase-1, SCD1) is the rate-limiting enzyme for MUFA generation, specifically for producing oleic acids (OA, 18:1) and palmitoleic acids (PO, 16:1) from stearic (ST, 18:0) and palmitic (PA, 16:0) acids (Figure 2.4a). In addition, $\Delta 6$ and $\Delta 5$ desaturases contribute to generating functionally important PUFA, such as docosahexaenoic acid (DHA, 22:6) and arachidonic acid (AA, 20:4) by catalyzing the formation of additional double-bonds from essential fatty acids of linoleic acid (LA, 18:2) and alpha-linolenic acid (ALA, 18:3) (Figure 2.4a). We adopted pharmacological approaches to probe these pathways. CAY10566 (CAY) and SC 26196 (SC) are $\Delta 9$ (SCD1) and $\Delta 6$ desaturase inhibitors respectively (Figure 2.4a)⁵¹. Upon treatment with varying doses of CAY or SC on M381 for 3 days, our hSRS spectra revealed decreasing levels of unsaturation within lipid droplets (Fig 4b-c, 3022 cm^{-1}), demonstrating the involvement of both MUFA and PUFA in lipid droplets. This spectral response for decreased unsaturation upon drug treatment was

also well-reflected in the heatmap of constraint scores by SA (Supplementary Figure 2.10). In addition, the involvement of MUFA and PUFA in lipid droplets of M381 was supported by lipidomics of TAG and CE (Supplementary Figure 2.11), the main lipid-droplet species.

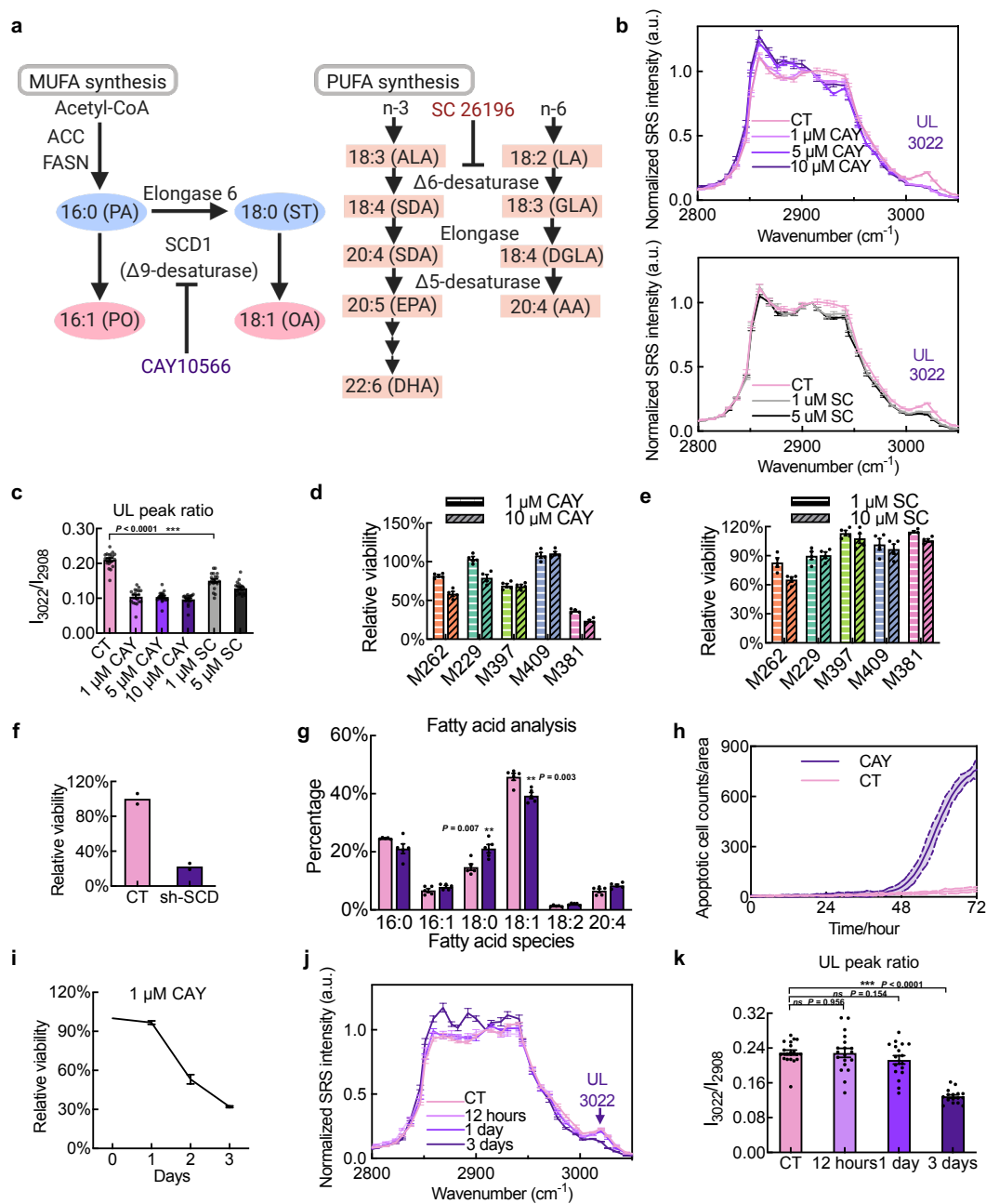


Figure 2.4. SCD1-dependent viability for the mesenchymal M381 cells. (a) (Left) De novo

synthesis pathway of monounsaturated fatty acids (MUFA) and (right) polyunsaturated fatty acids (PUFA) in mammalian cells. CAY10566 and SC 26196 are SCD1 ($\Delta 9$ -desaturase) and $\Delta 6$ -desaturase inhibitor respectively. (b) Normalized (to 2908 cm^{-1}) hSRS spectra of LDs in M381 cells without (CT) and with treatment of (top) 1 μM , 5 μM and 10 μM CAY ($n = 16, 18, 19, 19$ for CT, 1 μM , 5 μM and 10 μM CAY respectively), and (bottom) 1 μM and 5 μM SC ($n = 16, 19, 19$ for CT, 1 μM and 5 μM SC respectively) for 3 days. (c) Quantification of unsaturated lipid (UL) by intensity ratios of 3022 cm^{-1} /2908 cm^{-1} from (b). (d-e), Relative viability of all 5 cell lines after treatment of 1 μM and 10 μM CAY for 3 days ($n = 4$ independent experiments) (d) or 1 μM and 10 μM SC for 3 days ($n = 4$ independent experiments) (e). (f) Relative viability of M381 cells after shRNA knockdown of SCD1 gene compared to scrambled control (CT) ($n = 2$ independent experiments). (g) GC-MS measurements of fatty acids extracted from bulk M381 cells with (CAY, purple) and without (CT, pink) treatment of 1 μM CAY for 3 days. The percentages of 16:0, 16:1, 18:0, 18:1, 18:2, and 20:4 fatty acids are normalized to total extracted fatty acids ($n = 5$ independent experiments). (h) Time-lapse apoptotic cell counts of M381 cells with (purple, CAY) and without (pink, CT) treatment of 1 μM CAY ($n = 3$ independent experiments, data shown as mean \pm error with 95 % CI). (i) Time-dependent relative viability of M381 cells after treatment of 1 μM CAY for 0, 1, 2 and 3 days ($n = 4$ independent experiments). (j) Normalized (to 2908 cm^{-1}) hSRS spectra of LDs in M381 cells without (CT) and with 1 μM CAY treatment for 12 hours, 1 day and 3 days ($n = 20, 19, 17, 14$ for CT, 12 hours, 1 day and 3 days respectively). (k) Quantification of UL from intensity ratios of 3022 cm^{-1} /2908 cm^{-1} in (j). ** $p < 0.01$, *** $p < 0.001$, ns: not significant ($p > 0.05$) from two-tailed unpaired t-tests. Data shown as mean \pm SEM.

2.6 Inhibiting SCD1 but not $\Delta 6$ desaturase induces apoptosis in M381

Although both CAY and SC reduce the lipid-droplet unsaturation levels, CAY inhibition of SCD1 for MUFA synthesis leads to a more significant loss of viability for M381 cells relative to the other 4 cell lines (Figure 2.4d and Supplementary Figure 2.12), while SC treatment to block the $\Delta 6$ desaturase for PUFA synthesis pathway barely affects the viability of M381 (Figure 2.4e). It is worth noting that this specific susceptibility of SCD1 in M381 is not

indicated by bulk gene expression of SCD1 (Supplementary Figure 2.8c) or bulk fatty acid analysis (Figure 2.3h). The inhibitory function of SCD1 is further confirmed by small hairpin RNA (shRNA) based gene silencing of SCD1 (Figure 2.4f). This result illustrates that SCD1 inhibition could be a susceptibility of mesenchymal M381 cells and inspired us to develop a deeper understanding of SCD1 regulation in M381 cells. First, our bulk GC-MS analysis on major fatty acid species from cell pellets showed that SCD1 inhibitor mostly blocks the generation of the monounsaturated OA (18:1) from saturated ST (18:0) (Figure 2.4g). This is consistent with the knowledge that OA (18:1) is the principle product of SCD1⁵⁴. Second, a time-lapse apoptosis video assay demonstrated that CAY reduces the viability of M381 by inducing apoptosis (Figure 2.4h). Surprisingly, both the time-lapse apoptosis (Figure 2.4h) and the time-dependent viability assays (Figure 2.4i) revealed that the M381 cells don't initiate apoptosis program until 1-2 days treatment with CAY. A similar lagging effect is also observed for the decrease in the hSRS spectral signature for unsaturation within lipid droplets (Figure 2.4j-k). Taken together, the GC-MS and the kinetics data imply that the susceptibility of CAY may originate from the gradual depletion of OA (18:1) and/or the corresponding accumulation of ST (18:0).

2.7 SCD1 inhibition induces phase-separated membrane structures

Lipotoxicity from excessive saturated fatty acids (e. g. PA, 16:0 and ST, 18:0) is a well-documented effect that impairs cellular functions by inducing endoplasmic reticulum (ER) stress⁵⁵⁻⁵⁷, unfolded protein response (URP)⁵⁵⁻⁵⁷ and the formation of ceramides⁵⁵ and reactive oxygen species⁵⁷. Recently, it was found in live HeLa cells that supplying extra saturated fatty acids into the culture medium could convert the intracellular membranes from the regular liquid-disordered phase into an ordered-solid phase⁵⁸. This resulted in perturbed membrane functions and induced cell death. The conversion of a fluidic normal membrane (NM) into a rigid solid membrane (SM) can be characterized by detergent wash, in which the NM will be removed while the SM is not⁵⁸. Since CAY treatment of M381 mostly reduces intracellular OA (18:1) while increasing ST (18:0) levels by blocking the ST-to-OA

conversion (Figure 2.4a, g), we hypothesized that the resulting lipid imbalance would lead to phase-separated SM domains.

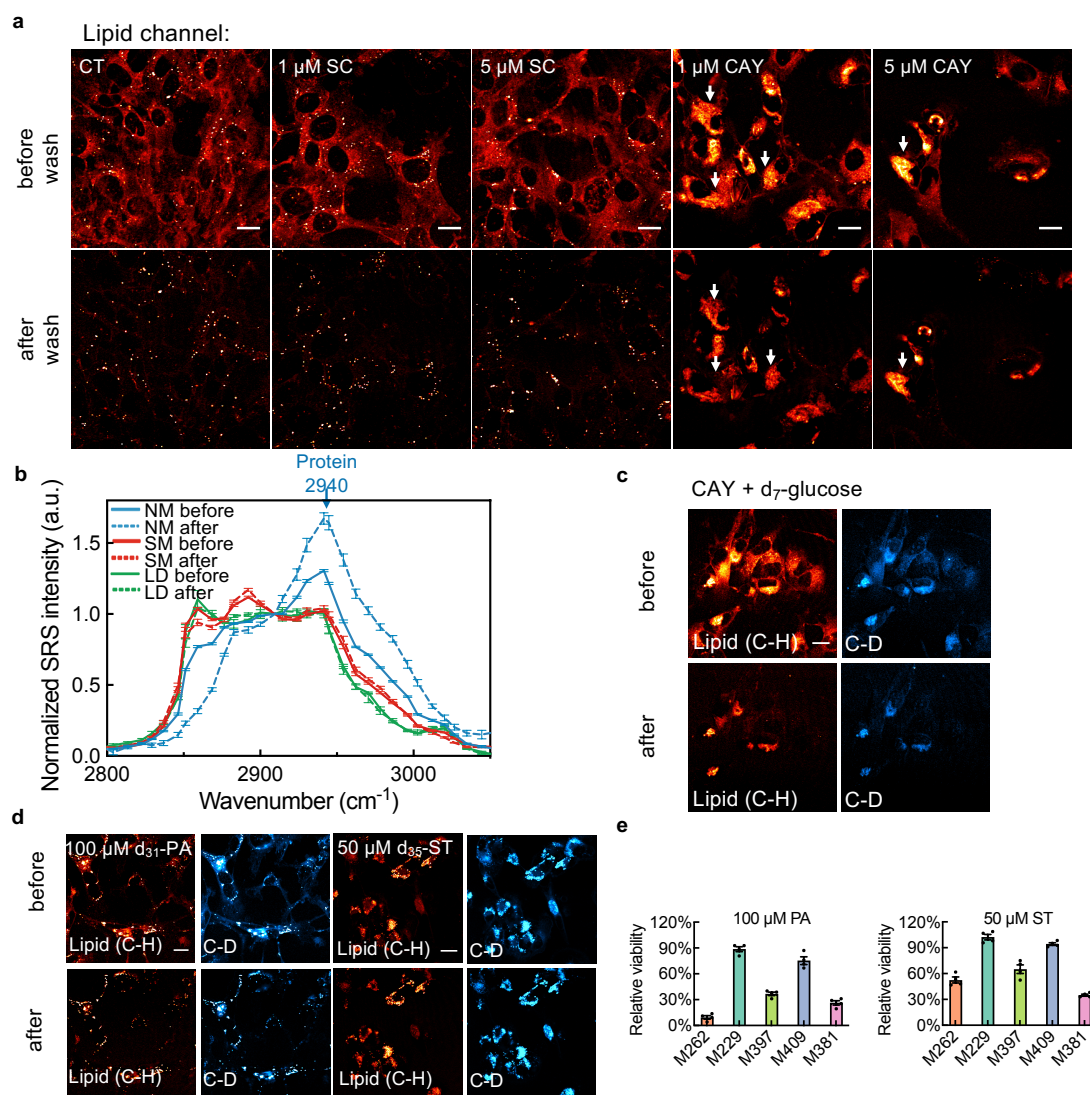


Figure 2.5. Formation of intracellular phase-separated solid membrane (SM) domains induced by mono-unsaturation inhibition. (a) Representative lipid-channel SRS images from the same set of M381 cells before (top) and after (bottom) detergent wash in control (CT), with SC or CAY treatment. Detergent-resistant SM structures are arrow indicated. (b) Normalized (to 2908 cm^{-1}) hSRS spectra on the same NM (normal membrane, blue), SM (red), and LDs (green) structures in M381 cells from before (solid-lined) and after (dash-lined) detergent wash. ($n = 7, 12, 6$ for NM, SM, LD

respectively, blue arrow indicates the protein peak at 2940 cm^{-1}). (c) SRS images at the lipid (C-H) and the C-D channels on the same set of M381 cells growing in d_7 -glucose medium with 1-day $5\text{ }\mu\text{M}$ CAY before (top) and after (bottom) detergent wash. (d) SRS images at the lipid (C-H) and the C-D channels on the same set of M381 cells with 3-day d_{31} -palmitic acid (d_{31} -PA) or d_{35} -stearic acid (d_{35} -ST) treatment before (top) and after (bottom) detergent wash. (e) Relative cellular viability with 3-day PA or ST treatment ($n = 4$ independent experiments). Scale bars, $20\text{ }\mu\text{m}$. Data shown as mean \pm SEM.

We used SRS imaging to characterize potential phase changes in M381 cell membrane after CAY treatment. Indeed, we observed that the membrane structures were clearly extracted by detergent wash in both control (CT) cells and cells treated with the $\Delta 6$ desaturase inhibitor SC ($1\text{ }\mu\text{M}$ and $5\text{ }\mu\text{M}$ for 3 days) (Figure 2.5a before vs after wash), indicating that these cells contain NM. By comparison, for cells treated with CAY ($1\text{ }\mu\text{M}$ and $5\text{ }\mu\text{M}$ for 3 days), the membrane structures were detergent-resistant, indicating the conversion of NM to SM structures (Figure 2.5a, before vs after wash). We next characterized the composition change of SM in situ by comparing the hSRS spectra on selected intercellular regions of detergent-extractable NM, detergent-resistant SM domains, and lipid droplets (LDs) (Figure 2.5b, normalized to 2908 cm^{-1} as previously indicated). First, comparing the spectra of NM from before and after wash, the greatly reduced peak at 2845 cm^{-1} confirmed the effective extraction of most lipid contents by detergent wash (Figure 2.5b, blue solid line vs blue dashed line). The maintained intensity at 2940 cm^{-1} after wash suggests that the NM is also enriched with proteins. In contrast, both SM and LD exhibit a largely maintained SRS spectral shape following detergent treatment (Figure 2.5b, red, SM before vs after and green, LD before vs after). This indicates that both structures are resistant to detergent wash. Interestingly, the overall Raman spectral shape of SM is very distinct from that of NM (Figure 2.5b, NM before vs SM before), but is similar to that from the LDs (Figure 2.5b, SM before vs LD before). The similarity indicates that the SM is highly lipid-rich. The difference between SM and NM suggests that the formation of phase-separated SM domains causes an exclusion of membrane-residing proteins, consistent with previous models that proteins or

peptides which are anchored in intracellular membranes by α -helix clearly prefer the liquid phase and would be excluded by the solid phase for dimerization^{56,59}. Thus, CAY inhibition on M381 cells indeed causes the formation of phase-separated intracellular solid-membrane structures that enrich lipids, but exclude proteins.

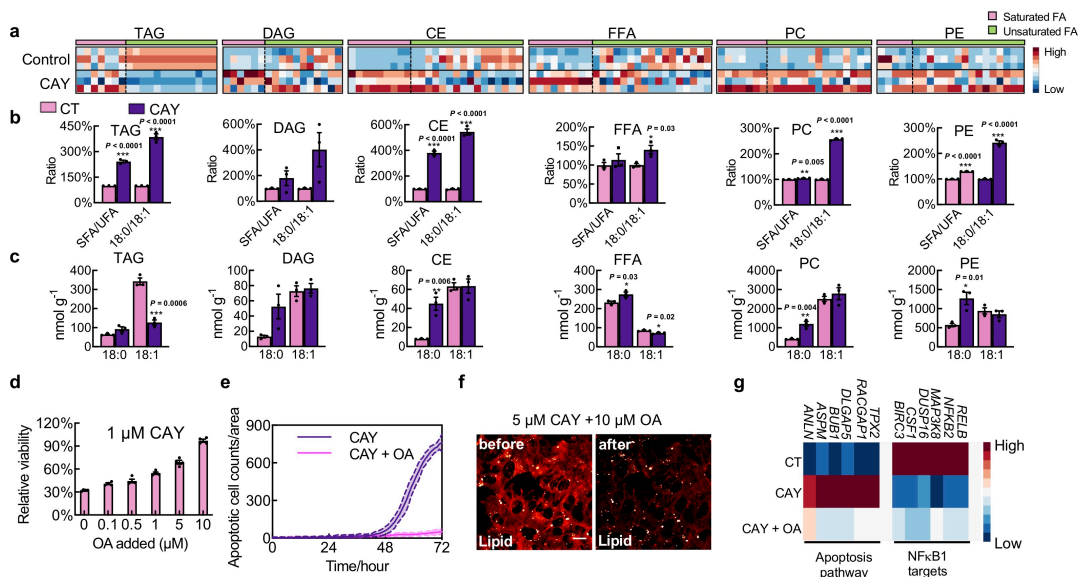


Figure 2.6. Lipid regulation upon mono-unsaturation inhibition and cellular rescue with oleic acid (OA) supplementation. (a) Heatmap for the relative fatty acid abundances in designated classes of lipids from lipidomics of bulk M381 cells with (CAY) and without (CT) CAY (1 μ M, 3 days) treatment. Each row represents a sample replicate and each column represents fatty acyl chains with increasing length and increasing double-bond numbers. SFA and UFA are categorized by pink and green respectively. The abundance of FA of different chain length is normalized as a Z-score across all 6 samples within each column. TAG: Triacylglycerol; DAG: Diacylglycerol; CE: Cholesteryl Ester; FFA: Free fatty Acids; PC: Phosphatidylcholine; PE: Phosphatidylethanolamine. (b) Overall concentration ratios between SFA to UFA (SFA/UFA), and between ST to OA (18:0/18:1) with CAY (purple) and without CAY (CT, pink, each value is shown as 100% reference) treatment from lipidomics of M381 cells in (a) ($n = 3$). (c) Concentration changes of 18:0 and 18:1 with CAY (purple) and without CAY (CT, pink) from lipidomics in (a) ($n = 3$ independent experiments). (d) Relative viability of M381 cells treated with 1 μ M CAY with supplement of OA (18:1) at indicated concentration for 3 days ($n = 4$ independent experiments). (e) Time-lapse apoptotic cell counts of

M381 cells after treatment of 1 μM CAY with (pink) or without (purple) 10 μM OA ($n = 3$ independent experiments, data shown as mean \pm error with 95 % CI). (f) SRS imaging at the lipid channel before (left) and after (right) detergent wash on the same set of M381 cells treated with CAY and OA for 3 days. (g) Ranked pathways from analysis of gene expression trends on control (CT), CAY-treated (middle row, CAY) and CAY plus OA (CAY + OA) M381 cells. Scale bars, 20 μm . Data shown as mean \pm SEM. * $p < 0.05$, ** $p < 0.01$, *** $p < 0.001$ from two-tailed unpaired t-tests.

Since CAY inhibition of SCD1 affects the de novo fatty-acid synthesis pathway (Figure 2.4a), the solid membranes should have a high accumulation of newly synthesized lipids. Having identified that de novo lipid synthesis in our melanoma cells traces back to glucose (Figure 2.2e-f), we again supplied M381 cells with d_7 -glucose, but this time together with CAY treatment for 3 days. We then used SRS imaging of C-D vibrations at 2150 cm^{-1} to visualize lipids that are synthesized specifically during the treatment period. As expected, we detected a formation of SM structures that were retained after detergent wash from C-D SRS images, which show similar patterns to that in the C-H channel (Figure 2.5c, before vs after wash). This observation confirms that the newly-synthesized saturated lipids contribute to the formation of SM upon SCD1 inhibition of CAY.

CAY treatment induces the formation of SM structures by blocking the cellular conversion of newly synthesized saturated fatty acids to unsaturated fatty acids. This imbalance of homeostasis between saturated and unsaturated fatty acids may also be caused by supplying cells with extra amount of saturated fatty acids in the medium, which could promote the formation of SM structures⁵⁸. Indeed, we observed the appearance of solid-membrane patterns by treating M381 cells with 100 μM palmitic acid (PA, 16:0) or 50 μM steric acid (ST, 18:0) (Figure 2.5d, before vs after). Interestingly, the viability assays with PA and ST

treatment (Figure 2.5e) exhibited a M-shaped trend across all 5 cell lines. This trend is similar to that with CAY treatment (Figure 2.4d), suggesting a similar toxicity effect between CAY and saturated fatty acid treatment. As a control, incubating cells with extra unsaturated fatty acids show negligible toxicity for all cell lines (Supplementary Figure 2.13a, PO, 16:1 and OA, 18:1). Additionally, in similar ways the invasiveness of M381 cells is impaired with either CAY, PA or ST treatments (Supplementary Figure 2.13b). The loss of invasiveness is likely because the formation of SM structures leads to a loss of membrane fluidity, which is required for metastatic cancer cells to invade through the dense basement membrane⁶⁰. We again validated the formation of intracellular solid-membrane structures and their associated cytotoxicity when cellular pool of saturated fatty acids exceeds that for the homeostatic level in M381 cells.

2.8 Lipidomics suggest a reservoir role of lipid droplets

To obtain a comprehensive picture of how SCD1 inhibition perturbs lipid homeostasis, we carried out bulk lipidomics analysis of M381 cells with and without CAY treatment (Figure 2.6a). We presented heatmaps on six major intracellular lipid species of triacylglyceride (TAG), diacylglycerol (DAG), cholesteryl sterol (CE), free fatty acid (FFA), phosphatidylcholine (PC) and phosphatidylethanolamine (PE) in control and CAY-treated cells (Figure 2.6a). Heterogeneous remodeling for saturated and unsaturated fatty acids is revealed across different lipid species (Figure 2.6a, pink, SFA, saturated fatty acids; green, UFA, unsaturated fatty acids of different acyl chain length and double-bond number). For quantification, we first plot the ratios of total saturated to total unsaturated fatty acids in each of six lipid species for control cells (CT, pink) and CAY-treated (1 μ M, 3 days, purple) cells (Figure 2.6b, SFA/UFA). Indeed, SFA/UFA ratios increase, although to a different extent, across all six lipid species in CAY-treated M381 samples. The increase is particularly

obvious for TAG and CE (Figure 2.6b), the main residents in lipid droplets. This again explains why hSRS spectroscopy and imaging on lipid droplets is so revealing. The difference between CT and CAY-treated cells becomes particularly obvious for the ST/OA (i.e. 18:0/18:1) ratios in each species (Figure 2.6b). This is consistent with our previous GC-MS results (Figure 2.4g) that the function of SCD1 is more strongly directed towards the generation of OA (18:1) from ST (18:0) relative to the generation of PO (16:1) from PA (16:0) (Supplementary Figure 2.13c). Further, the total concentrations of membrane lipids, PC and PE, increase by 40.2% and 38.6% after CAY treatment (Supplementary Figure 2.13d), which may explain the abnormally high lipid signals observed in solid membranes (Figure 2.5a). These species-dependent lipidomics heatmaps and ratio analysis confirm the relative increase of saturation level across all different lipid species and identify the more dominant changes in both TAG and CE under CAY treatment, consistent with our SRS data.

Further quantification of the absolute concentrations of ST (18:0) and OA (18:1) from lipidomics (Figure 2.6c) yields additional mechanistic insights into cellular behaviors under CAY inhibition. First, under CAY inhibition that blocks the conversion of ST (18:0) to OA (18:1), DAG, CE, FFA, PC and PE all show statistically significant increases in the levels of ST (18:0). This is likely due to the continuous synthesis and accumulation of new ST. Interestingly, the increase of ST (18:0) in TAG is not statistically significant. On the other hand, TAG presents a large drop in OA (18:1) level upon CAY treatment, while the other five lipid species have an approximately unchanged OA (18:1) level. This suggests that OA (18:1) in TAG may be hydrolyzed and released under CAY treatment. Taken with our previous kinetic SRS data that the unsaturation levels of lipid droplets, which are mainly comprised of TAG and CE, only decrease after 1-day of CAY treatment (Figure 2.4j-k), we suggest a possible reservoir role of TAG for unsaturated fatty acids in the lipid droplets of M381 cells. After SCD1 inhibition blocks the conversion of newly synthesized ST (18:0) to OA (18:1), the cytosolic saturation level increases. When the level of newly synthesized

saturated fatty acids in the cytosol reaches a threshold (in our case, after 1-day of CAY treatment), the TAG in the lipid droplets starts to release unsaturated fatty acids (e.g. OA) to restore the balance of cellular lipid unsaturation. With the continuous depletion of unsaturated fatty acids from TAG in lipid droplets under prolonged CAY treatment, this storage is eventually depleted. The imbalance of intracellular SFA/UFA ratios then leads to the formation of toxic solid membrane structures, as observed in Figure 2.5a.

2.9 Supplying UFA rescues SCD1 induced apoptosis in M381

We reasoned that supplying CAY-treated cells with extra unsaturated fatty acids, such as OA, may rescue the toxicity effect of the drug by restoring the balance between saturated and unsaturated fatty acids. Indeed, both cell viability (Figure 2.6d) and cell invasiveness (Supplementary Figure 2.13e) of CAY-treated M381 cells were restored by adding OA in the medium together with CAY in a dose-dependent manner. Our time-lapse apoptotic assay (Figure 2.6e) confirmed that high-dose (10 μ M) of OA fully rescues M381 cells from apoptosis under CAY (1 μ M) treatment. Further, with co-treatment of OA and CAY, the phase separated solid-membrane structures are absent, even at higher-concentration (5 μ M) CAY (Figure 2.6f, before vs after). It is known that OA supplementation can reduce lipotoxicity by channeling extra cytosolic saturated fatty acids into lipid droplets⁶¹. We hence performed a pulse-chase experiment to explore the possible rescue effect (Supplementary Figure 2.13f). We first pulse-treated M381 cells with 5 μ M CAY for 60 h. Verified the formation of solid-membrane structures in this condition (Supplementary Figure 2.13f, lipid, C-H), we then chased (i.e. rescued) the cells with 20 μ M of deuterated OA (d_{33} -OA) for another 10 h. We observed much less solid-membrane (Supplementary Figure 2.13f, set 1 & 2, C-H) and a significantly increased number of lipid droplets derived from deuterated OA (Supplementary Figure 2.13f, set 1 & 2, boxed, C-D). We also queried whether other UFA could have a similar rescue effect. At a low dose (1 μ M), OA is the most effective tested rescue agent (Supplementary Figure 2.13g). This may be due to the preference of the OA

substrate by the key enzymes, Diacylglycerol O-Acyltransferase 1 (DGAT1) and Diacylglycerol O-Acyltransferase 2 (DGAT2), involved in TAG formation^{62,63}. At higher concentration (5 μ M), other UFA (PO, 16:1; LA, 18:2; AA, 20:4) can reach similar rescue (Supplementary Figure 2.13h), showing that the key is to restore the cellular balance between saturated and unsaturated fatty acids.

To understand specific gene regulatory pathways involved in the saturated-lipid associated M381 susceptibility, we carried out RNA-seq transcriptomics analysis on control cells (CT), cells treated with 1 μ M CAY (CAY), and cells co-treated of 1 μ M CAY and 1 μ M OA (CAY+OA). We ranked the gene sets that either exhibit increased or decreased expression levels under CAY treatment relative to CT, and then exhibit restoration under CAY+OA treatment. Two pathways stand out (Figure 2.6g). First, the apoptosis pathway (Figure 2.6g, left and middle columns) is up-regulated with CAY treatment and recovers with CAY+OA. This observation is consistent with our functional assays (Figure 2.4h and 2.6e). Second, the NF κ B1-targets pathway exhibits decreased expression with CAY and recovers with CAY+OA. The high NF κ B transcriptional state in melanoma has been suggested to be BRAFi resistant, consistent with what is known for M381^{25,27,64}. In addition, the NF κ B pathway has been implicated in maintaining the stemness feature in ovarian cancer stem cells⁵¹, so it might play a similar role here in maintaining the mesenchymal nature of M381. In previous reported lipotoxicity studies, perturbation of cellular lipid composition through the use of either relatively high concentrations (\sim 0.5 mM) saturated lipid in the culture medium, or via SCD1 inhibitors, was shown lead to the activation of endoplasmic reticulum (ER) stress sensors and the unfolded protein response (UPR)⁵⁵⁻⁵⁷. In this study, transcriptional signatures associated with neither ER nor UPR stresses were significantly elevated following 1 μ M CAY treatment (Supplementary Figure 2.13i). One possibility is

that suppression of protein translocation into the solid membrane structures may trigger pro-apoptotic signaling.

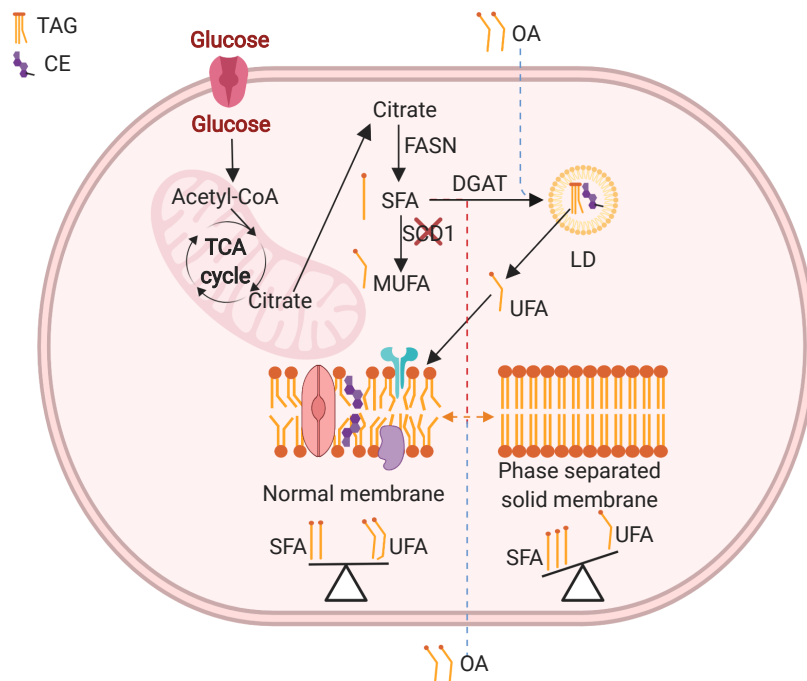


Figure 7 Schematic of the proposed cellular metabolic processes for M381 cells under SCD1 inhibition. SCD1 inhibition blocks *de novo* MUFA synthesis from SFA, which leads to an imbalance of intracellular SFA and UFA. This imbalance drives the release of UFAs stored in M381 lipid droplets, which act as reservoirs of unsaturated lipids, to restore the balance between SFA and UFA. Prolonged SCD1 inhibition eventually depletes the stored UFA. The resulting imbalance between SFA and UFA transforms fluid normal membrane domains into phase-separated solid membranes. The accompanied loss of membrane fluidity and exclusion of membrane-residing proteins are associated with an induced apoptosis - a cell fate that can be rescued by supplying excess UFA in the culture medium.

2.10 Conclusion

Single-cell metabolomics is challenging because there is neither a general amplification strategy, such as PCR, nor a general capture agent approach, such as antibodies, to facilitate the detection of specific metabolites with required sensitivity. Here, we demonstrated that Raman spectro-microscopy opens up the ability to spatially resolve and quantitatively analyze particular classes of metabolites, as well as specific targeted metabolites, in live and fixed cells. Raman imaging and spectral analysis essentially serves as a multiplex functional assay for metabolites that rapidly respond to environmental stimuli, and so provides a powerful complement to mass spectrometry and fluorescence detection methods. We showed the value of metabolic analysis by imaging a series of patient-derived, BRAF mutant melanoma cell lines, representing different de-differentiation phenotypes. The subcellular metabolic heterogeneity across these cell lines is effectively captured by Raman and used to mine for phenotype-dependent, druggable metabolic susceptibilities. We termed this approach as subcellular pharmaco-metabolomics.

In many cancers, mesenchymal-like cells exhibit invasive characteristics, as well as innate drug-resistance to targeted or even immune-therapies^{32,65-67}. We hypothesized that the maintenance of such characteristics required lipid biochemical processes that could be mined for druggable susceptibilities. To this end, we utilized a comparative analysis of Raman spectro-imaging on intracellular lipid droplets to identify that lipid-unsaturation associated metabolic activities were uniquely upregulated in the mesenchymal M381 phenotype, as depicted in Figure 2.7. This picture is supported by several findings. First, from SRS imaging of deuterated fatty acids and glucose, M381 cells exhibited the lowest relative activities for both lipid uptake (e.g. OA, 18:1) and de novo fatty acid synthesis. Such low metabolic activity might contribute towards making M381 cells insensitive to BRAFi⁶⁸. Second, incubation with SCD1 inhibitor, CAY, which blocks the conversion of saturated fatty acids (SFA) to mono-unsaturated fatty acids (MUFA), led to an imbalance of intracellular SFA

and UFA. This imbalance drives the release of UFA stored in M381 lipid droplets to restore the balance. This suggests an intracellular UFA reservoir function for these droplets. Prolonged SCD1 inhibition eventually depletes these lipid droplets of UFA, leading to an excess of SFA in M381. This excess, in turn, contributes towards a type of lipotoxicity through the formation of a phase-separated solid membrane domain. The accompanying loss of membrane fluidity and exclusion of membrane-residing proteins are then associated with an induced apoptosis – a cell fate that can be avoided by supplying extra MUFA in the culture medium. The susceptibility of SCD1 is uniquely revealed by subcellular Raman analysis, but is not reflected in the bulk transcriptomics (Supplementary Figure 2.8c) or bulk metabolomics (Figure 2.3h). Both the mechanism and applicability underlying reported susceptibilities in our work are distinctly different from previous reports that mainly relied on bulk analysis^{69–71}. This demonstration thus emphasizes the unique value of subcellular pharmaco-metabolomics as a revelatory tool for uncovering new cell biology.

The work here provides an important proof of concept for the use of Raman spectro-microscopy in identifying phenotype-dependent metabolic susceptibilities in cancer cells. It is likely that we are just beginning to mine for how different metabolites are processed and utilized within different cellular sub-compartments. Our current subcellular investigations focus on the spectral region of 2800-3100 cm^{-1} , but can be readily extended to additional windows within the fingerprint spectral region to permit the identification of additional metabolite classes^{19–21}. Other subcellular structures could be probed similarly to how the lipid droplets were analyzed here, to resolve a more comprehensive intracellular picture of the organelle network, such as the membrane-bound organelles of ER and the Golgi apparatus⁴⁶. Another aspect that worth exploration is the generality of the cell line specific results reported here. For example, whether the susceptibility of SCD1, as revealed in the mesenchymal M381 cells, applies more generally across mesenchymal BRAF mutant melanoma tumors, is both intriguing and important, given the challenges in drugging such tumors. A second challenge will be to extend these Raman tools, in conjunction with surprisal analysis, to characterize the metabolic heterogeneity within intact tissues, and more

physiologically relevant environments¹⁷. Such studies will further validate the general applicability of specific targets identified here and perhaps open up avenues for clinical translation.

2.11 Methods

Cell lines, chemicals and cell culture.

Patient-derived melanoma cell lines used in this study were generated under UCLA IRB approval # 11–003254. Cells were cultured in RPMI 1640 (Gibco, 11875119), supplemented with 10% fetal bovine serum (Omega, FB-12), and 0.2% MycoZap Plus-CL antibiotics (Lonza, VZA-2011). Cultures were incubated in a water-saturated incubator at 37°C with 5% CO₂. Cells were maintained and tested for mycoplasma using kit (Lonza, LT07-118).

Cerulenin (Sigma, C2389-5MG), TVB 3166 (Sigma, SML1694-5MG), CAY10566 (Cayman, 10012562), SC 26196 (Cayman, 10792) were dissolved in DMSO (ATCC, 4-X) at designated concentrations before adding to cell culture media. To conduct cell viability assay, 30k to 50k cells were seeded into six well dishes (Corning, 3516). After culturing for 2 days, growth medium was replaced with fresh medium containing drugs with indicated concentration, and the incubation continues for another 3 days. Cell viability was measured by counting cell numbers of each well. Cell number in vehicle (with DMSO as vehicle) well was used as normalization.

Stimulated Raman scattering microscopy.

The configuration is shown in Supplementary Figure 2.5a. An integrated laser (picoEMERALD, Applied Physics and Electronics, Inc.) was used as a light source for both pump and stokes beams. It produces 2 ps pump (tunable from 770 nm – 990 nm, bandwidth 0.5 nm, spectral bandwidth $\sim 7 \text{ cm}^{-1}$) and stokes (1031.2 nm, spectral bandwidth 10 cm^{-1}) beams with 80MHz repetition rate. Stokes beam is modulated at 20 MHz by an internal

electro-optic modulator. The spatially and temporally overlapped pump and stokes beams are introduced into an inverted multiphoton laser scanning microscopy (FV3000, Olympus), and then focused onto the sample by a 25X water objective (XLPLN25XWMP, 1.05 N.A., Olympus). Transmitted pump and stokes beams are collected by a high N.A. condenser lens (oil immersion, 1.4 N.A., Olympus) and pass through a bandpass filter (893/209 BrightLine, 25 mm, AVR Optics) to filter out stokes beam. A large area (10×10 mm) Si photodiode (S3590-09, Hamamatsu) is used to measure the remaining pump beam intensity. 64 V DC voltage was used on the photodiode to increase saturation threshold and reduce response time. The output current is terminated by a 50 Ω terminator and pre-filtered by an 19.2-23.6-MHz band-pass filter (BBP-21.4+, Mini-Circuits) to reduce laser and scanning noise. The signal is then demodulated by a lock-in amplifier (SR844, Stanford Research Systems) at the modulation frequency. The in-phase X output is fed back to the Olympus IO interface box (FV30-ANALOG) of the microscope. Image acquisition speed is limited by 30 μ s time constant set for the lock-in amplifier. Correspondingly, we use 80 μ s pixel dwell time, which gives a speed of 8.5 s frame⁻¹ for a 320-by-320-pixel field of view. For 2150 cm⁻¹ (C-D, d₇-glucose), 2109 cm⁻¹ (C-D, d₃₁-palmitic acid, d₃₃-oleic acid, d₃₅-stearic acid), 2845 cm⁻¹ (CH₂) and 2940 cm⁻¹ (CH₃), the wavelengths of pump laser are 844.1, 847.0, 797.3, and 791.3 nm, respectively. Laser powers are monitored through image acquisition by an internal power meter and power fluctuation are controlled within 5% by the laser system. 16-bit grey scale images are acquired by Fluoview software. SRS spectra were acquired by fixing the stokes beam at 1031.2 nm and scanning the pump beam through the designated wavelength range point by point. SRS spectra were processed and presented by Excel and GraphPad. Lipid-channel (C-H) image was processed from a linear combination algorithm of $5 \cdot [\text{CH}_2] - 0.4 \cdot [\text{CH}_3]$ from the CH₂ and CH₃ images⁵⁸. We recommend that at least three biological replicates with at least five cells in each replicate are acquired for analysis.

Spontaneous Raman spectroscopy.

Fixed cell pellets were washed two times with pure water, and then resuspended into water to be cell solution to avoid influence from salt crystals after drying. The cell solution

containing 5k cells was added dropwisely on a glass slide. After air dry, glass slides with cells were then used to take Raman spectra. Spontaneous Raman spectra were acquired using an upright confocal Raman spectrometer (Horiba Raman microscope; Xplora plus). A 532 nm YAG laser is used to illuminate the sample with a power of 12 mW on sample through a 100 x, N.A. 0.9 objective (MPLAN N; Olympus) with 100 μm slit and 500 μm hole. Spectro/Raman shift center was set to be 2000.04 cm^{-1} . With a 1200 grating (750 nm), Raman shift ranges from 690.81 cm^{-1} to 3141.49 cm^{-1} was acquired to cover whole cellular Raman peaks. Acquisition time for one spectrum was set to be 5 s, and then averaged for 5 times. The target cell was chosen randomly and spectra of five points (center, top, bottom, left, right) on individual cell were acquired. The acquired spectra were processed by the LabSpec 6 software for baseline correction. Spontaneous Raman spectra were organized and presented by Excel and GraphPad respectively. To reduce spectral variance for spontaneous Raman spectra caused by intracellular heterogeneity, we recommend that at least three biological replicates with at least ten cells in each replicate are acquired for analysis.

Coating of imaging dish.

Imaging dish (MatTEK, P35G-1.5-14-C) was coated with 2% sterile gelatin solution (Sigma, G1393) for 30 minutes, then the coating solution was removed and the dish was left for air dry for another 30 minutes before using.

Metabolic deuterium labeling.

Deuterated glucose RPMI 1640 medium was made by supplying d_7 -glucose (Cambridge Isotope Laboratories, DLM-2062-1) into glucose deficient RPMI 1640 medium (Gibco, 11879020), then completed with 10% fetal bovine serum (Omega, FB-12), and 0.2% MycoZap Plus-CL antibiotics (Lonza, VZA-2011). d_{31} -Palmitic acid (Cambridge Isotope Laboratories, DLM-215), d_{35} -stearic acid (Cambridge Isotope Laboratories, DLM-379) and d_{33} -oleic acid (Cambridge Isotope Laboratories, DLM-1891) were coupled to bovine serum albumin (Sigma, A9418) in 2:1 molar ratio and added to RPMI 1640 complete medium to designated concentration. The resulting solutions was sterile filtered by 0.22 μm low protein

binding filter system. The filtered solutions were completed by the addition of 10% FBS and 0.2% MycoZap Plus-CL antibiotics. Cultured melanoma cells were seeded onto an imaging dish to optimal confluency. The cells were then grown in the corresponding deuterated medium (e. g. 11.1 mM d-glucose used in Figure 2.2f, 50 μ M d₃₁-palmitic acid and d₃₅-stearic acid used in Supplementary Figure 2.9a and Supplementary Figure 2.9c) for 3 days before fixation and imaging.

Ratio image processing and data analysis.

Images are analyzed and assigned color by ImageJ. For CH₂/CH₃ ratio imaging, a threshold (mask) image was first generated by adjusting threshold using Huang method, then non-zero values were normalized to one. CH₂ images were then divided by the same set of CH₃, and the resulting ratio image multiplied with mask image to create the final CH₂/CH₃ ratio image.

Fatty acid analysis.

5 million cells were harvested, frozen, and lyophilized overnight. Fatty acid methyl esters (FAMES) were produced from biomass in a combined extraction, hydrolysis, and derivatization procedure based on previous methods⁷². For each sample, dried biomass was mixed with 2 ml of methylation mixture (20:1 v/v anhydrous methanol/acetyl chloride) and 1 ml hexane and reacted in sealed VOA vials at 100 °C for 10 minutes. After cooling, 2 mL deionized water was added to the mixture followed by 3 times extraction with 2 ml hexane. The hexane solution was then treated with anhydrous Na₂SO₄ to remove residual water and concentrated under a stream of N₂ to a final volume of 0.5 ml. FAMES were identified via gas chromatography/mass spectrometry (GC/MS) on a Thermo Fisher Scientific ISQ by injecting 1 μ l of sample in splitless mode. Chromatographic separation was achieved on a ZB-5ms capillary column (30 m by 0.25 mm; film thickness, 0.25 μ m). Peaks were identified by comparing the mass spectra and retention times to the authentic standards and library data. Quantification was achieved by a flame ionization detector. To avoid complications from sample loss at sample preparation stage, we used the relative abundance of each species of fatty acids for data interpretation. Relative abundances were calculated by dividing the peak

area for each of the six most abundant fatty acids (16:0, 16:1, 18:0, 18:1, 18:2, and 20:4) to the sum of peak areas of all six species. Data were processed by Excel. The signals of other species are too low and mostly buried in noise.

Detergent wash.

PBS solution containing 0.5% Triton X-100 (Sigma, T8787), short as PBS-T solution, was used to wash cells in imaging dish⁵⁸. Gently add 1 ml PBS-T detergent solution (above) into imaging dish and place the dish in 4 °C for 10 minutes. Then the PBS-T washing solution was gently removed and the samples were washed with PBS for two times before imaging.

RNA extraction, library construction, and sequencing.

Total RNA was extracted from frozen cells pellets (~ 1 million cells) using the RNeasy Micro Kit (Qiagen, 74004) according to the manufacturer's protocol. Then the RNA sequencing (RNA-seq) was performed using BGISEQ-500 platform at BGI Genomics (Wuhan, China). The library preparation was followed by BGI's standard procedure.

RNA-seq data dimension reduction and clustering analysis.

Sequencing reads were mapped and aligned to Human Reference Genome (UCSC hg 19) with TopHat. Assembled transcripts for each sample were generated from mapped reads using Cufflinks. All assemblies were combined into a single assembly by Cuffcompare for differential expression analysis. Expression levels in fragments per kilobase of exon per million fragments mapped (FPKM) were generated using Cuffdiff as normalized read counts.

Heatmap and clustering analysis of transcriptomic dataset was performed via MATLAB. Hierarchical clustering was performed with average linkage and Euclidean distance metric. Transcriptomic data of 30 BRAF but not NRAS mutated melanoma patient derived cell lines from the Gene Expression Omnibus database (GEO)²⁷ were chosen for dimension reduction

and clustering analysis. Gene expression of the whole transcriptome or metabolic subset (with all metabolic genes defined from reference⁷³) were project onto the top two most dominant constraints defined from surprisal analysis³⁸. This way, cell lines with similar whole transcriptomic profiles or metabolic-related gene expression profiles were projected nearby to each other. Cell lines were color-coded based on their respective phenotypes. Top 100 cell phenotype-specific metabolic genes for each of the phenotype are selected based on gene's contribution score towards each phenotype as listed in Table. S1. Contribution score of each gene to each phenotype are calculated based on gene's contribution score towards the X-axis ($G1$) and Y-axis ($G2$) in the two-dimensional map ($G1$ and $G2$ values from surprisal analysis). Detailed equations are listed as the following: contribution score of melanocytic phenotype, $S_{melanocytic}(S_1) = -G1 - G2$; contribution score of transitory phenotype, $S_{transitory}(S_2) = -G1 + G2$; contribution score of neural-crest phenotype, $S_{neural-crest}(S_3) = G1 + G2$; contribution score of undifferentiated phenotype, $S_{undifferentiated}(S_4) = G1 - G2$. Heatmap of all 400 phenotypic-specific metabolic genes are plotted in Supplementary Figure 2.1 and heatmap for a few representative phenotype markers and phenotypic-specific metabolic genes are shown in Figure 2.1b.

For CH₂/CH₃ correlation analysis across five cell lines, spearman correlation was calculated between each gene and the measured CH₂/CH₃ ratio across all five cell lines, where genes that displayed the highest positive or negative correlation with CH₂/CH₃ ratio (Spearman bigger than 0.95 or less than -0.95) were further mined for their function through enrichment analysis.

Gene set enrichment analysis (GSEA)⁷⁴ was performed using GSEA v4.0.1 with 1,000 geneset permutations. Normalized enrichment score (NES) was assessed across the curated Molecular Signatures Database (MSigDB) Hallmark, C2 curated gene sets, C4 computational gene sets and C5 gene ontology gene sets. To identify biological processes and pathways most correlated with CH₂/CH₃ ratio, we first ranked the genes based on the

Spearman correlation between their expression and CH₂/CH₃ ratio across all five melanoma cell lines and then performed the pre-ranked option of GSEA with 1000 permutations.

Surprisal analysis of Raman spectra.

Surprisal analysis was applied as previously described³⁸. Briefly, the measured Raman peak signal at certain wavenumber i at cell c , $\ln X_i(c)$, is expressed as a sum of a steady state term $\ln^0 X_i(c)$, and several constraints (modules) $\lambda_j(c) \times G_{ij}$ representing deviations from the steady state. Each deviation term is a product of a cell-dependent weight (influence score) of the constraint $\lambda_j(c)$, and the cell-independent contribution of the wavenumber peak to that constraint G_{ij} . Peaks i with high positive or negative G_{ij} values are the ones that are positively or negatively correlated with constraint (module) j , which can be used to infer the meaning of each module. To implement surprisal analysis, we first utilized singular value decomposition, which factors this matrix $\ln X_i(c)$ in a way that determines the initial estimate of the two sets of parameters that are needed in surprisal analysis: the Lagrange multipliers (λ_j) for all constraints at a given cell, and for all cell the G_{ij} (cell-independent) analyte patterns for all analyte i at each constraint j . Further interaction is implemented when necessary to stabilize the steady state and refining the constraints.

Incucyte Cell Apoptosis Assay.

Cells were seeded and monitored using an IncuCyte® S3 live-cell imaging system (Essen BioScience). Cells were exposed to drug treatments for up to 72 hours in the presence of IncuCyte® Caspase-3/7 Green apoptosis dye (Essen BioScience, Cat. No. 4440). Images were taken at 20-min intervals from 9 separate regions per well using a 20x objective. Apoptotic cell counts per well at each time point were quantified using the IncuCyte Basic Analyzer.

Migration and invasion assays.

Transwell chambers coated with and without matrigel respectively (Corning, 354480, 354578) were utilized to conduct the invasion and migration assays according to manufacturer's protocol. Briefly, cells received indicated treatments three days before the assays. At the start of the assays, cells were harvested and counted, and $50 \times 10^3 \text{ ml}^{-1}$ cells suspension was prepared. 0.5 ml of cell suspension was added to the upper chamber of the 24-well chambers. The media in lower chamber contains 10% FBS. Cells were allowed to migrate for 22 hours at 37 °C. The transwell membranes were then fixed and stained with 0.05% crystal violet solution. A cotton swab was used to remove cells that had not migrated or invaded through the chamber. Then, a fluorescence microscope was used to image the migrated or invaded cells, and 4 fields were independently counted from each migration or invasion chamber. Two or four biological replicates of experiments were conducted.

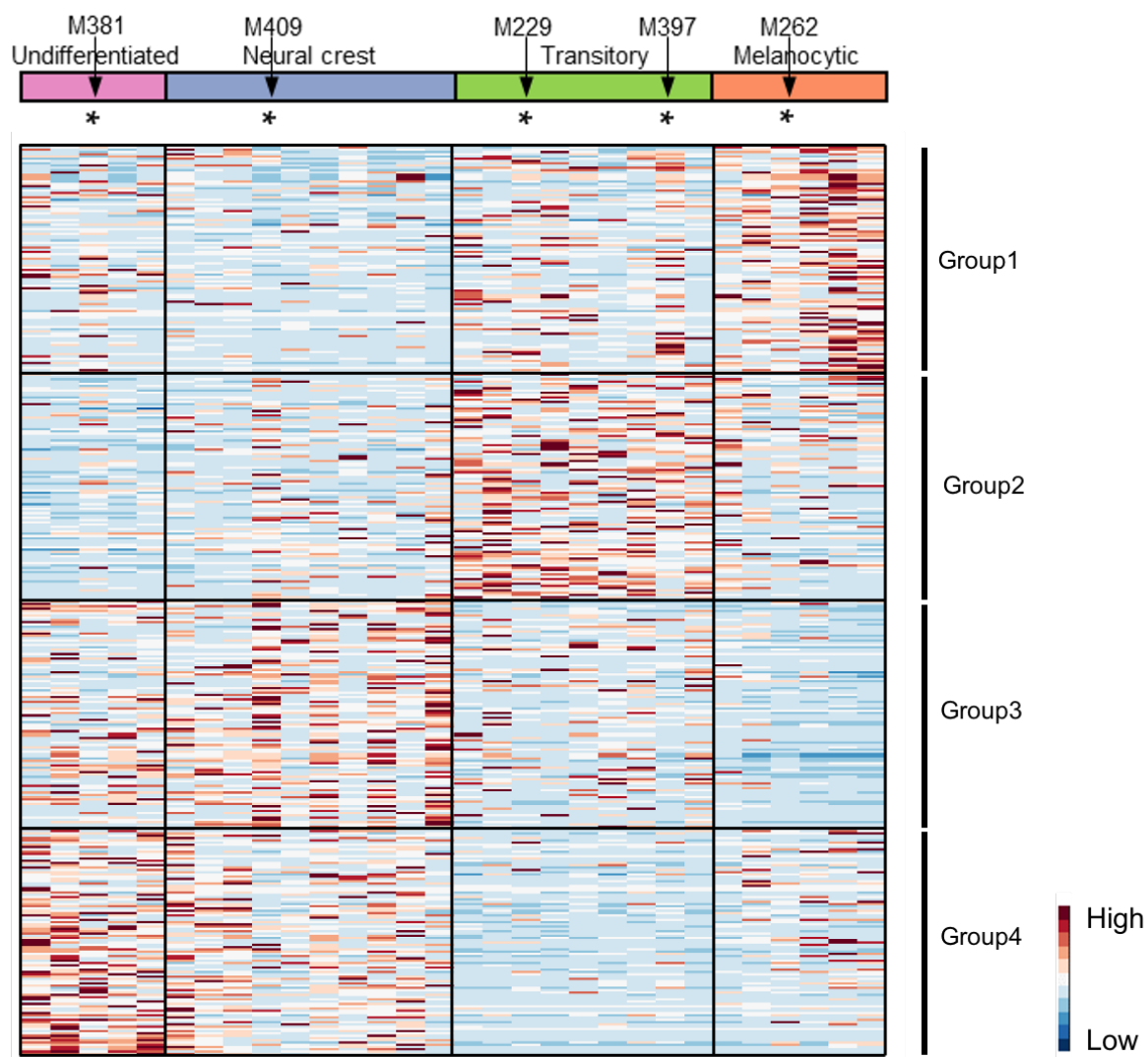
Generation of SCD1 stably knockdown cells.

M381 cells were transfected with shRNA lentiviral particles targeting SCD1 (Santa Cruz, sc-36464-V) following the manufacturer's protocol. Scrambled shRNA lentiviral particles (Santa Cruz, sc-108080) were used as a control. Stably transfected cells were selected with $1 \mu\text{g ml}^{-1}$ puromycin (Thermo Fisher, A1113803).

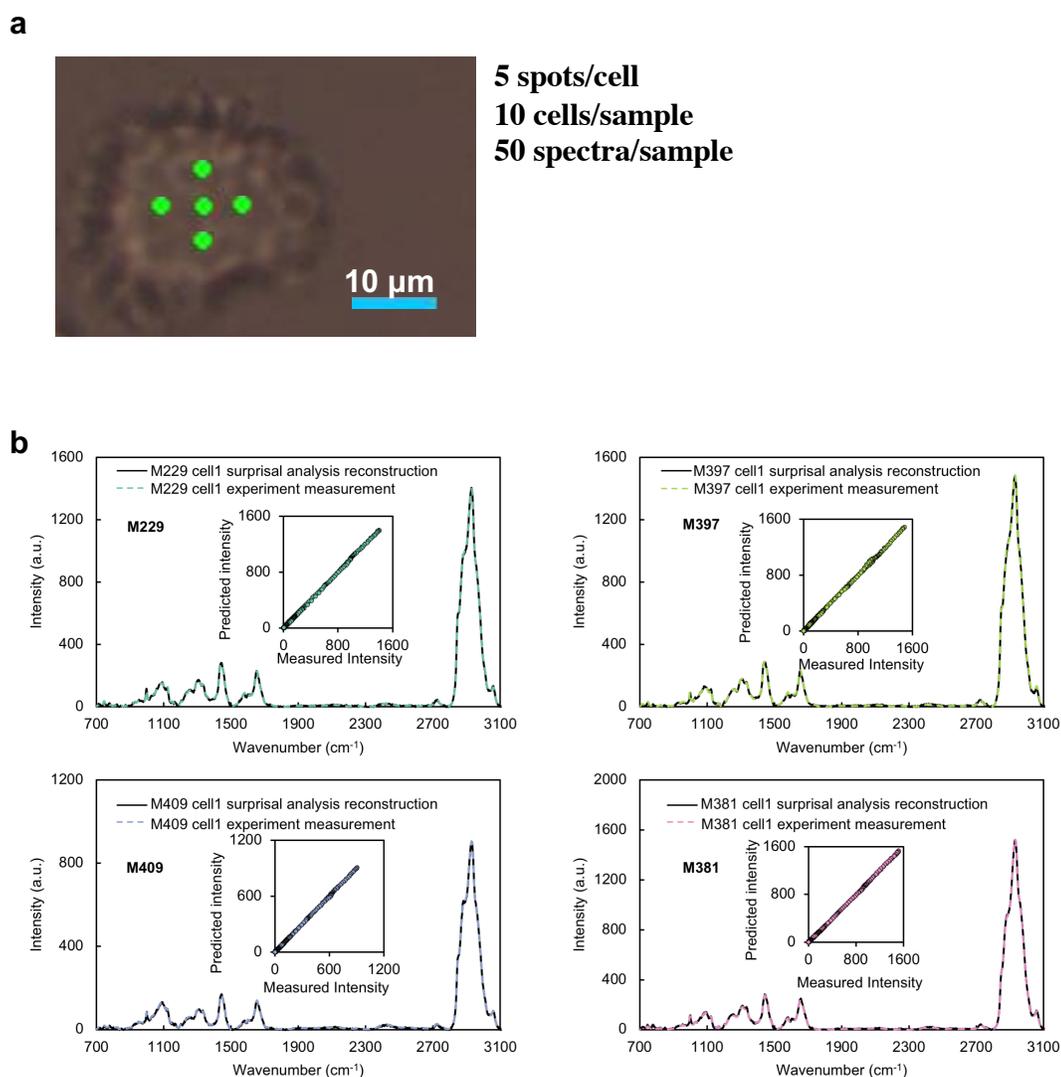
Lipidomics profiling: Liquid chromatography-mass spectrometry (LC-MS) analysis of lipids.

Cells going through indicated treatments were harvested as frozen pellets. Lipids were extracted using methyl tert-butyl ether (MTBE)/methanol after the addition of 54 isotope labeled internal standards across 13 lipid classes. The extracts were concentrated under nitrogen and reconstituted in 10 mM ammonium acetate in dichloromethane:methanol (50:50). Lipids were analyzed using the Sciex Lipidyzer platform consisting of a Shimadzu LC and AB Sciex QTRAP 5500 LC-MS/MS system equipped with SelexION for differential mobility spectrometry (DMS). Multiple reaction monitoring (MRM) was used to target and quantify over 1000 lipids in positive and negative ionization modes with and without DMS.

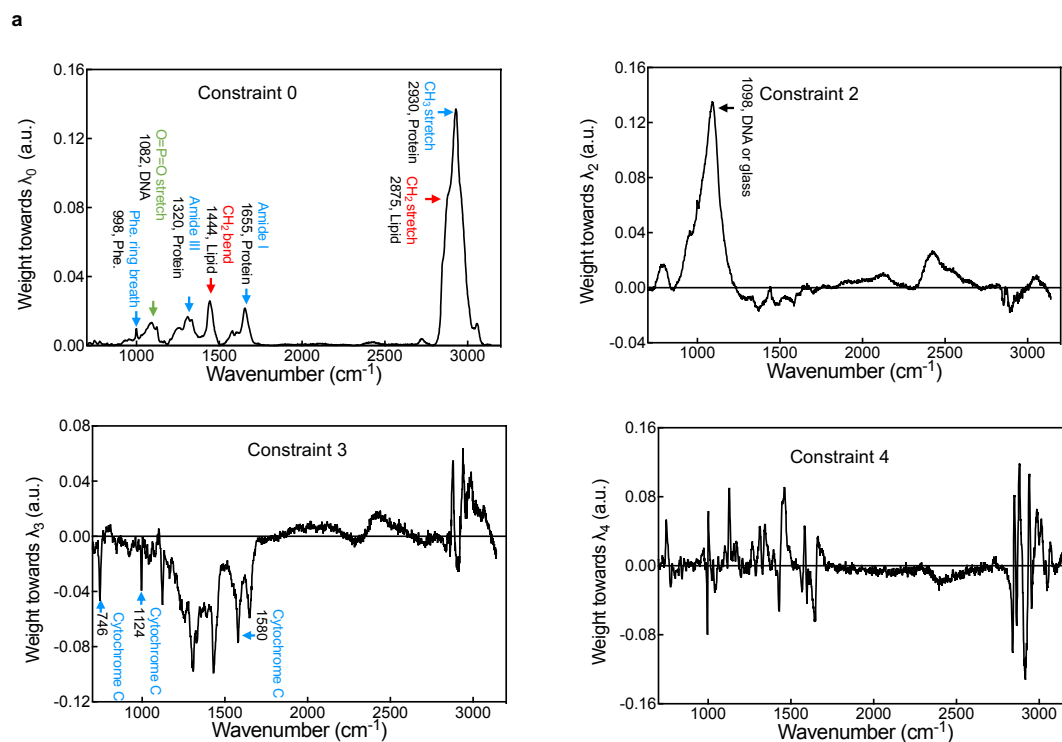
2.12 Supplementary Figures



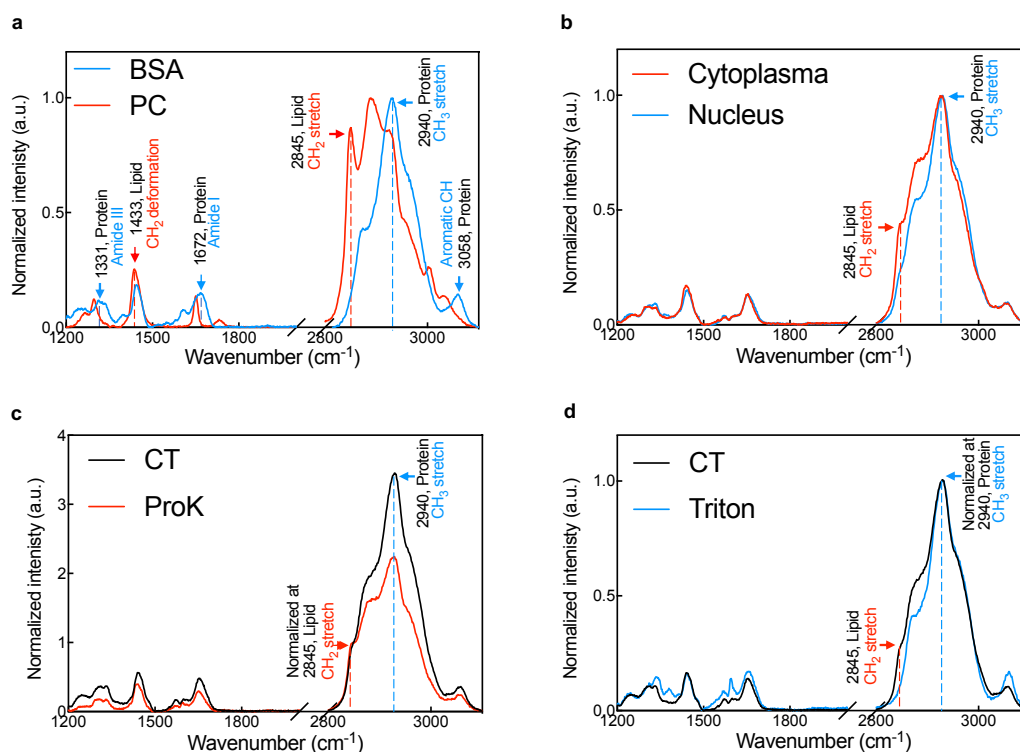
Supplementary Figure 2.1. Heatmap of the top 100 metabolic genes that are upregulated in each phenotype.



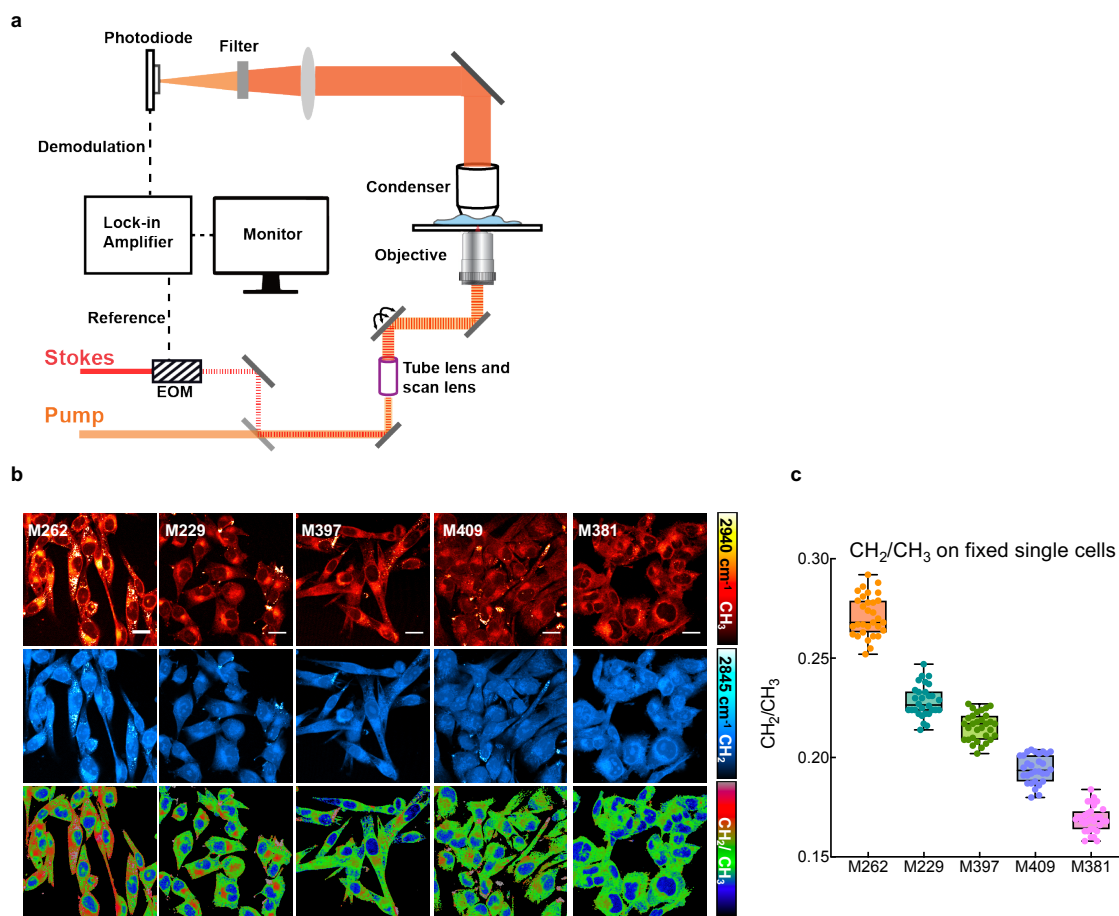
Supplementary Figure 2.2. Acquisition and surprisal analysis (SA) of spontaneous Raman spectra across the cell lines. (a) Illustration of laser focal spots on a representative cell under widefield mode during spontaneous Raman spectra acquisition. Green points indicate the laser focal points on cells. We selected 5 points (center, top, bottom, left, right) on each cell to acquire Raman spectra and averaged them for one cell. We randomly chose 10 cells to represent one cell line. (b) The comparison between SA reconstructed and experimentally obtained Raman spectra for individual M229, M397, M409, M381 cells. The SA plots are constructed by summing the spectral distribution and amplitudes of the first five resolved constraints ($\lambda_0 - \lambda_4$). The inset plots show the correlation between the predicted and calculated Raman spectra.



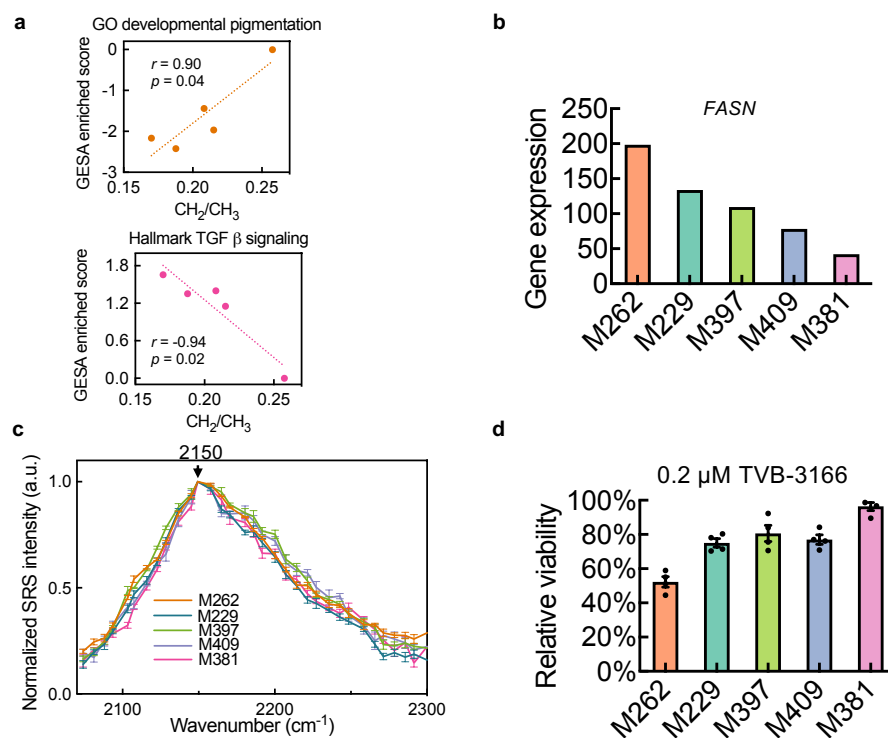
Supplementary Figure 2.3. Raman peak assignments of the shared constraint (constraint 0, λ_0) and lower amplitude constraints (constraints 2-4, $\lambda_2 - \lambda_4$).



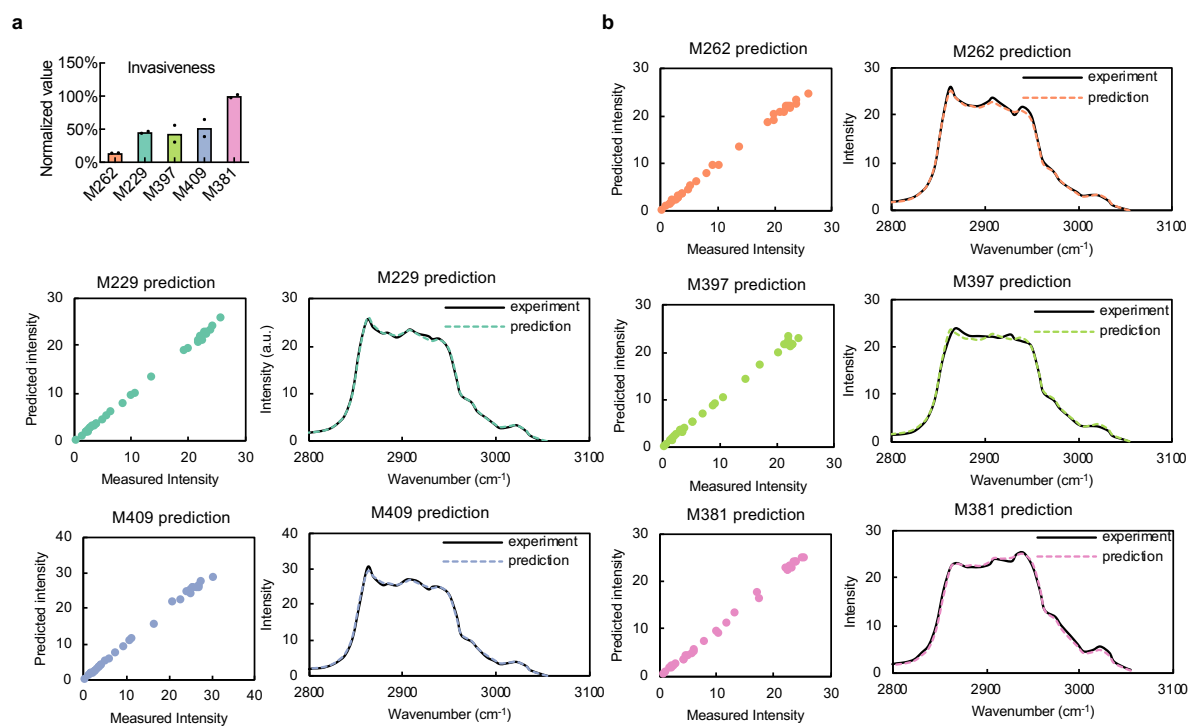
Supplementary Figure 2.4. Validation of the assignments for the 2845 and 2940 cm^{-1} Raman peaks to lipids and proteins in Fig. 2.1g. (a) Raman spectra of pure proteins (bovine serum albumin, BSA, blue) and lipids (1,2-dioleoyl phosphocholine, the highest abundant lipid in M381 cells from lipidomics, PC, red). 2845 cm^{-1} and 2940 cm^{-1} peaks are dash-line highlighted (the same for all sub-figures). (b) Raman spectra from cytoplasm (red, more lipid rich) and nucleus (blue, more protein rich) of M381 cells. (c) Raman spectra of M381 cells before (CT, control, black) and after protease k (ProK, red) treatment to digest most of the proteins. (d) Raman spectra of M381 cells before (CT, black) and after triton (Triton, red) treatment to wash away most lipids. Spectra in a) and b) are self-normalized, in c) and d) are normalized to 2845 cm^{-1} and 2940 cm^{-1} , respectively.



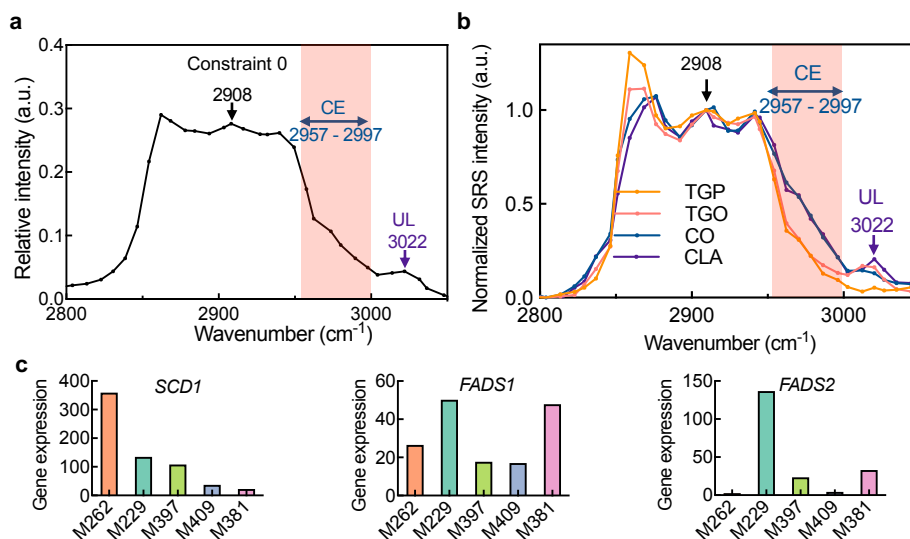
Supplementary Figure 2.5. SRS imaging of fixed melanoma cells. (a) Illustration of SRS configuration. (b) Representative SRS imaging of fixed melanoma cells at CH₂ (top, 2845 cm⁻¹) and CH₃ (middle, 2940 cm⁻¹) channels. Ratiometric images (bottom, CH₂/CH₃) were generated from the same sets of CH₂ and CH₃ images. Scale bar: 20 μm. (c) Average single-cell CH₂/CH₃ values from fixed cells for 5 cell lines (n = 30 cells per cell line examined over 3 independent experiments). Data are plotted as boxplots: center line indicates median; box limits indicate upper and lower quartiles; whiskers indicate minimum and maximum.



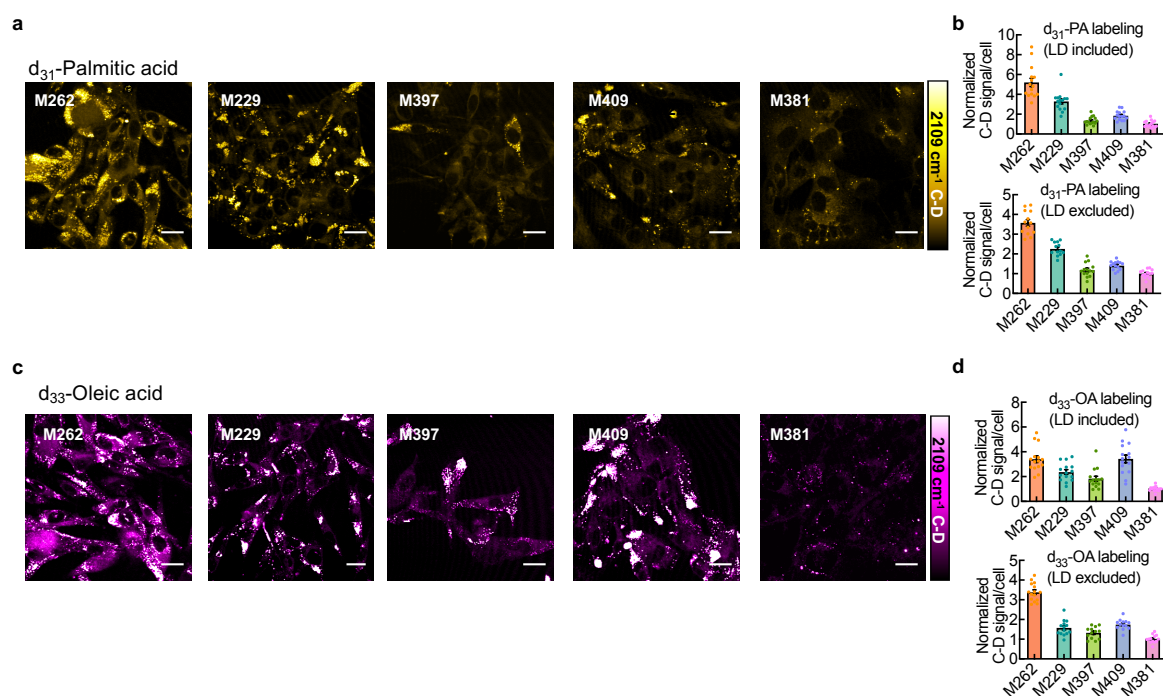
Supplementary Figure 2.6. The identification of de novo fatty acid synthesis as a druggable susceptibility for more differentiated melanoma cells. (a) Top panel: cell line-dependent correlation between GSEA scores for the GO developmental pigmentation pathway and CH_2/CH_3 ratios. Bottom panel: cell line-dependent correlation between GSEA scores for TGF beta signaling pathway and CH_2/CH_3 ratios. Each dot represents a two-dimensional relationship for one cell line. (b) Expression level of FASN across the five different melanoma cell lines ($n = 1$). (c) C-D region hyperspectral SRS (hSRS) spectra on cytoplasm in each single d_7 -glucose labeled melanoma cells for five cell lines ($n = 6, 8, 6, 8, 9$ for M262, M229, M397, M409, M381 respectively, data shown as mean \pm SEM, spectra are self-normalized). (d) Viability tests of melanoma cell lines under $0.2 \mu\text{M}$ TVB-3166 (FASN inhibitor) treatment for 3 days ($n = 4$ independent experiments, data shown as mean \pm SEM).



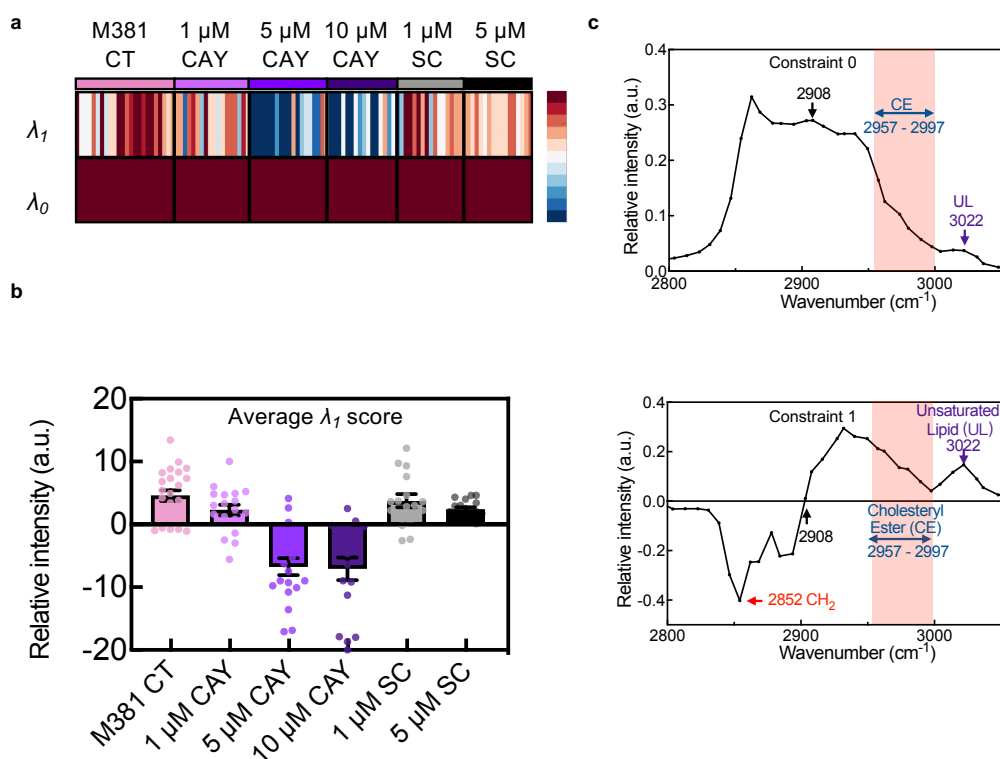
Supplementary Figure 2.7. Invasiveness assay and validation of SA of hSRS spectra from lipid droplets (LDs). (a) Relative invasiveness of different melanoma cell lines quantified by trans-well assay ($n = 2$ independent experiments). (b) The comparison between SA reconstructed and experimentally obtained Raman spectra for randomly selected individual lipid droplets from M262, M229, M397, M409, M381 cells. The SA reconstructions utilized only the first two constraints λ_0 and λ_1 .



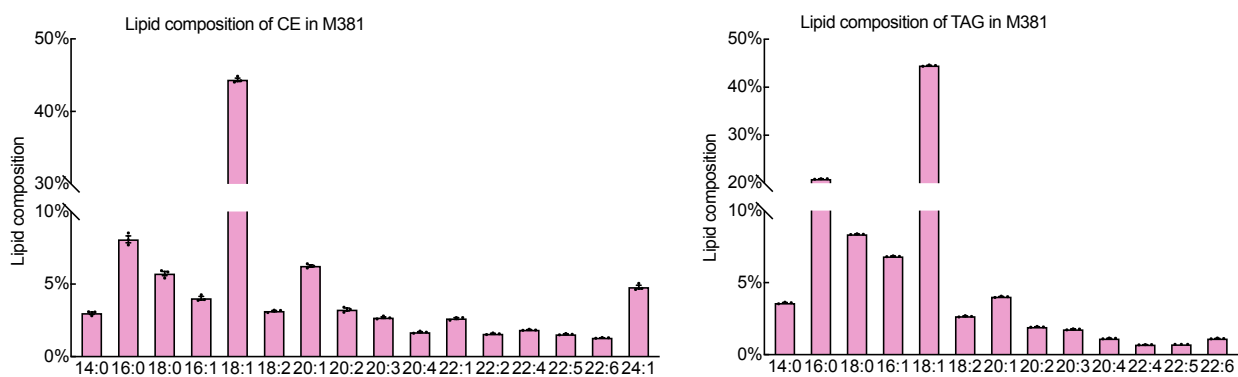
Supplementary Figure 2.8. Validation of peak assignments in Fig. 3e, and gene expression of fatty acid desaturases across cell lines. (a) Peak assignments of constraint 0 (λ_0). The 2908 cm^{-1} reference peak, cholesteryl esters band (CE, 2957 cm^{-1} to 2997 cm^{-1}) and unsaturated lipids peaks (UL, 3022 cm^{-1}) are indicated. (b) SRS spectra for pure references of glyceryl tripalmitate (TGP), glyceryl trioleate (TGO), cholesteryl oleate (CO), cholesteryl linoleate (CLA) after normalization at 2908 cm^{-1} . The broad band (indicated by pink shadow) ranging from 2957 cm^{-1} to 2997 cm^{-1} features CO and CLA, and is therefore assigned to cholesteryl esters. The 3022 cm^{-1} peak (indicated by violet arrow) is assigned to unsaturated lipid (=C-H), distinct in TGO, CO, CLA. (c) Gene expression levels of desaturase SCD1, FADS1 and FADS2 across cell lines (n = 1).



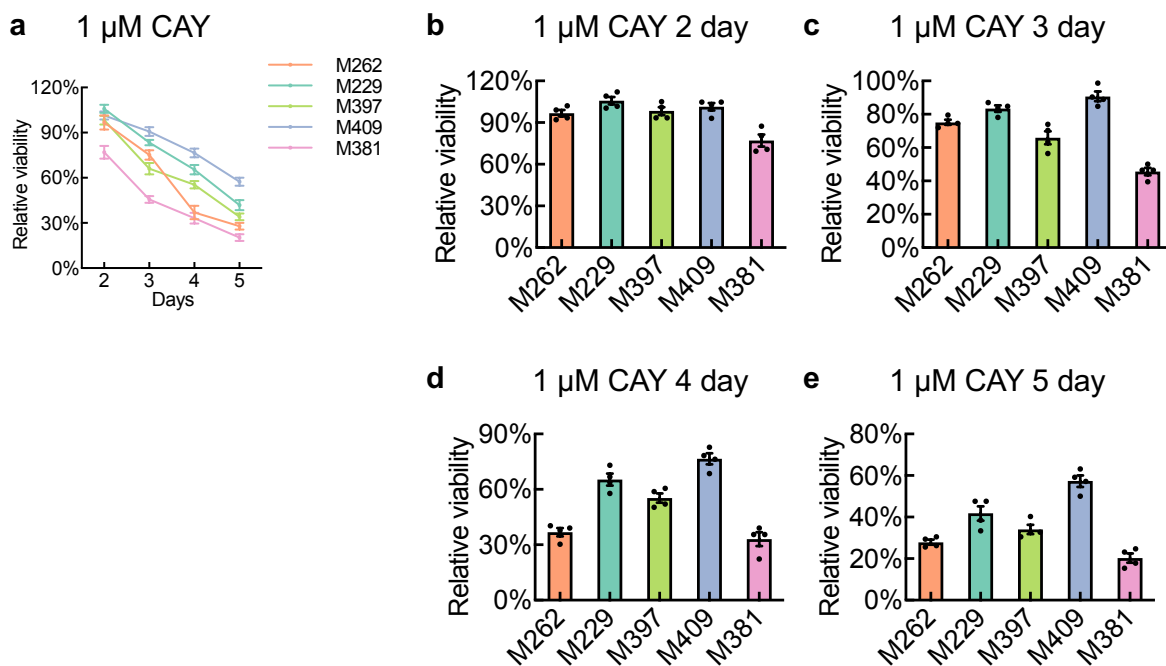
Supplementary Figure 2.9. Deuterated fatty acids uptake across cell lines. (a) Representative C-D channel (at 2109 cm^{-1}) SRS imaging of melanoma cells by incubating cells with d_{31} -palmitic acid ($50\text{ }\mu\text{M}$, 3 days). (b) Quantification of relative C-D signals in d_{31} -palmitic acid labeling cells at the single-cell level including or excluding LDs ($n = 15$ cells examined from 3 independent experiments, the C-D signal of M381 cells is normalized to 1). (c) Representative C-D channel (at 2109 cm^{-1}) SRS imaging of melanoma cells by incubating cells with d_{33} -oleic acid ($50\text{ }\mu\text{M}$, 3 days). (d) Quantification of relative C-D signals in d_{33} -oleic acid labeling cells at the single-cell level including or excluding LDs ($n = 15$ cells examined over 3 independent experiments. The C-D signal of M381 cells is normalized to 1. Scale bar, $20\text{ }\mu\text{m}$. Data shown as mean \pm SEM.



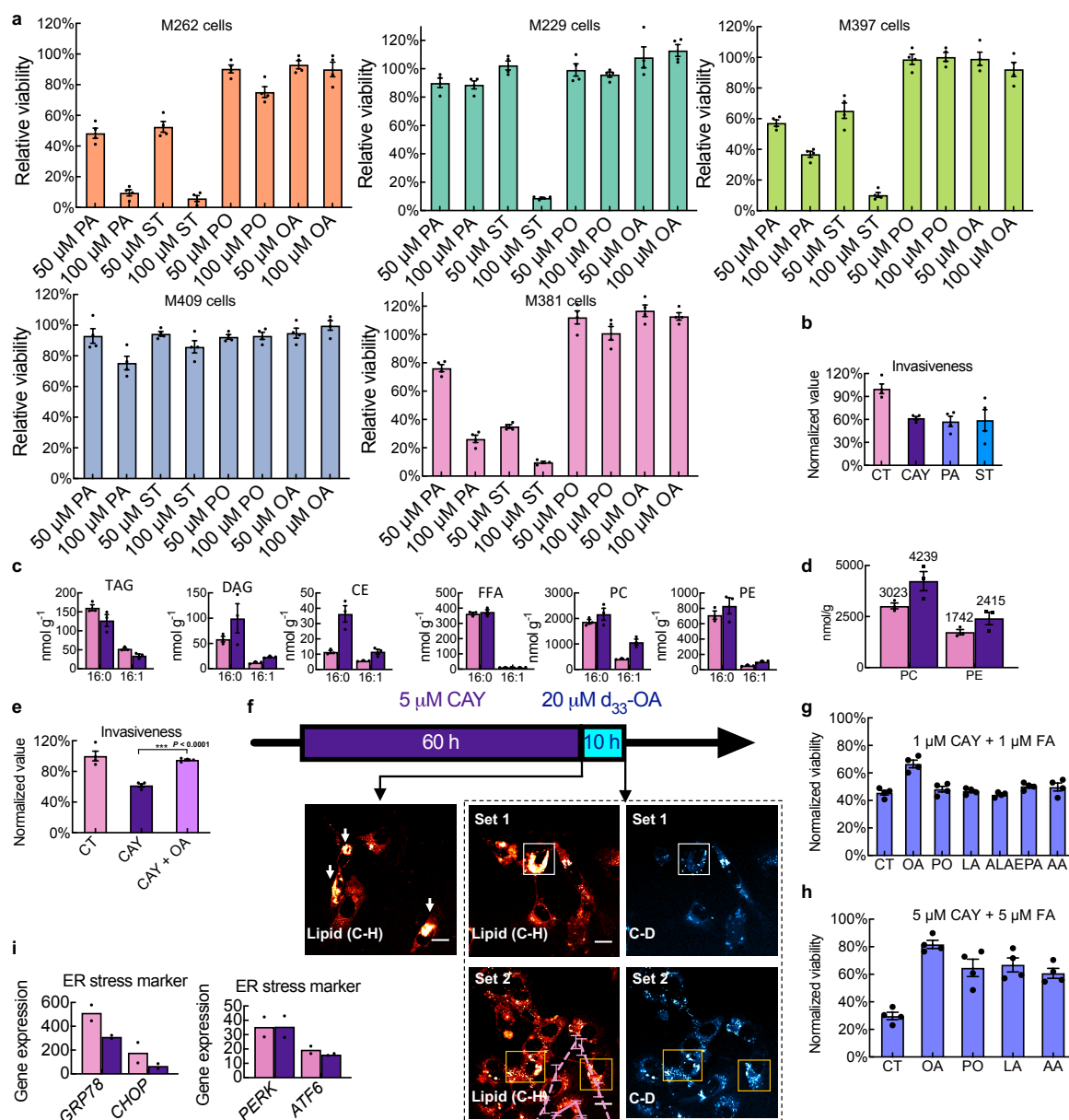
Supplementary Figure 2.10. SA of hSRS spectra on single LDs in M381 cells with drug treatment. (a) Heatmap for scores of the top two constraints (constraint 0 (λ_0) – constraint 1 (λ_1)) by surprisal analysis of hSRS spectra on LDs in M381 cells at different treatment conditions, i.e. M381 control (CT), 1 μ M CAY, 5 μ M CAY, 10 μ M CAY, 1 μ M SC, 5 μ M SC. Each column represents an individual LD and each row represents the constraint scores. $n = 24, 18, 19, 17, 16, 16$ for M381 CT, 1 μ M CAY, 5 μ M CAY, 10 μ M CAY, 1 μ M SC, 5 μ M SC respectively, examined over 3 independent experiments. (b) The average score of λ_1 in a) across six treatment conditions. Data shown as mean \pm SEM. (c) Raman peak assignments for λ_0 and λ_1 . The 3022 cm^{-1} peak (violet arrow) is assigned to unsaturated lipids (UL) and the pink shadowed range from 2957 cm^{-1} to 2997 cm^{-1} is assigned to cholesteryl esters (CE). 2908 cm^{-1} is the zero point in λ_1 .



Supplementary Figure 2.11. Lipidomics of CE and TAG from M381 cells show the involvement of both MUFA and PUFA. Bulk lipidomics of M381 cells with relative percentages of different fatty acid chains in CE (n = 3 independent experiments, left) and in TAG (n = 3 independent experiments, right). Data shown as mean \pm SEM.



Supplementary Figure 2.12. Viability assays of melanoma cell lines under different days of 1 μ M CAY treatment. (a) Dependence of viability for cell lines on the treatment length with 1 μ M CAY. (b-e) Bar-chart plot for comparing viability in (a) across five cell lines after 2-day (b), 3-day (c), 4-day (d), and 5-day (e) of CAY treatment. $n = 4$ independent experiments, Data shown as mean \pm SEM.



Supplementary Figure 2.13. The mesenchymal M381 is sensitive to saturated fatty acids (SFA) related lipotoxicity. (a) Relative viability of cells treated with major SFAs (PA, 16:0 and ST, 18:0), and major MUFAs (PO, 16:1 and OA, 18:1) at indicated concentration for 3 days (n = 4 independent experiments). (b) Relative invasiveness of control M381 cells (normalized to 100%) and M381 cells after treating with 1 μM CAY, 50 μM PA or 50 μM ST for 3 days. n = 4 independent experiments. (c) Concentration changes of PA (16:0) and PO (16:1) fatty acid chains in the 6 main species of lipids with (3 days, CAY, purple) and without (CT, pink) CAY treatment from lipidomics (n = 3

independent experiments). (d) Concentration changes of PC and PE with (3 days, CAY, purple) and without (CT, pink) CAY treatment from lipidomics (n = 3 independent experiments). (e) Relative invasiveness of control M381 cells (normalized to 100%) and M381 after treating with 1 μ M CAY, 1 μ M CAY plus 5 μ M OA for 3 days (n = 4 independent experiments). (f) Two color pulse-chase experiments. Top scheme: M381 cells were firstly incubated in medium containing 5 μ M CAY for 60 h (pulse), then the medium was changed to fresh medium containing 20 μ M d33-OA but not CAY for 10 h (chase). Representative SRS images at the C-H lipid channel and the C-D channel were shown at two time points of 60 h (1 set, i.e. only pulsed) and 70 h (2 sets, i.e. pulse-chased representative cells are squared). (g) Relative viability of 1 μ M CAY treated M381 cells without (CT) or with rescue of 1 μ M indicated unsaturated fatty acid (UFA) for 3 days (n = 4 independent experiments). PO: Palmitoleic acid; LA: Linoleic acid; ALA: Alpha-linoleic acid; EPA: Eicosapentaenoic acid; AA: Arachidonic acid. (n = 4 independent experiments). (h) Relative viability of 5 μ M CAY treated M381 cells without (CT) or with rescue of 5 μ M indicated UFA for 3 days (n = 4 independent experiments). (i) Representative ER stress marker expression with (3 days, purple) and without (pink) CAY treatment (n = 2 independent experiments). Scale bars, 20 μ m. Data shown as mean \pm SEM.

Rank	S ₁ top 100	S ₂ top 100	S ₃ top 100	S ₄ top 100	Rank	S ₁ top 100	S ₂ top 100	S ₃ top 100	S ₄ top 100
1	TYR	RXYLT1	ST8SIA5	NNMT	51	PDE6B	GLUD2	HS6ST3	TYMP
2	DCT	ALDH1A1	GALNT5	MGST1	52	HSD17B8	LPL	NPR2	RDH10
3	GYG2	CYP27A1	DHRS3	GDA	53	QDPR	CERS1	BST1	PNMT
4	GMPPR	NPR1	ALDH1A3	BCAT1	54	GCNT3	GUCY2C	BHMT2	AGPAT4
5	PNPLA4	ATP6V0A4	CYB5R2	MGAT5B	55	PFKFB2	PDE7B	CSGALNACT1	PDE9A
6	QPR1	GALNT5	NT5E	HS6ST3	56	CYP19A1	ASAH1	PDE7B	ALDOC
7	RENBP	TYRP1	PLA2G7	MTAP	57	ST8SIA1	LDHD	GSTM3	PDE1C
8	ADCY2	UROC1	CHST1	GALNT14	58	GSTO2	FMO4	CYP27C1	CYP24A1
9	GALNT3	FOLH1	ACOX2	B3GALNT1	59	NAT8L	CKMT1B	PDE9A	NME7
10	GAPDHS	GAL3ST1	PDE1C	ANPEP	60	MGST1	EPHX2	AK5	MFNG
11	TYRP1	ST8SIA1	B3GNT7	PTGS2	61	RDH8	CSGALNACT1	AK6	DSE
12	PRDM7	B3GAL1	GALNT13	CHST15	62	GALNT12	TPK1	INMT	TXNRD1
13	ADCY1	TYR	B3GNT5	HS3ST3A1	63	HSD3B7	ALDH1A3	DDO	B3GNT3
14	PIP5K1B	DGKI	B3GALT2	HS3ST3B1	64	PIK3C2B	BAAT	ACSS3	PCK1
15	ALDOC	ENPP2	MGLL	CYP2S1	65	CKMT1A	PCYT1B	P4HA3	CA2
16	ATP6V0D2	ACP5	DPYD	PTGES	66	INPP4B	PDE2A	ABHD17C	NME3
17	BAAT	B3GNT7	AKR1C3	GUCY1A2	67	MAOA	SCD5	DGKA	B4GALT1
18	LPIN3	ALDH2	AKR1C1	NMNAT2	68	LFNG	ELOVL2	PLCE1	PGM2L1
19	PLB1	DCT	ST6GALNAC5	LFNG	69	ATP8	CRYL1	SYNJ2	CYP26A1
20	CA14	NT5E	TBXAS1	DPYD	70	CHAC1	B3GALT2	HSY17B3	SYNJ2
21	CHSY3	ST6GAL1	ELOVL4	ALPP	71	ALDH3B2	CKMT1A	NMRK1	PLCD3
22	PTGDS	ST8SIA5	ABAT	CYP1B1	72	PLCG2	CA12	PDE10A	ACOT4
23	LDHC	COLGALT2	MGST2	CDS1	73	NAT8	ENPP1	GFPT2	UGCG
24	TKTL1	CYP7B1	AKR1B10	GALNT6	74	NAT8B	ACOT12	COX7A1	AMPD3
25	OGDHL	ASPA	UGT8	AOX1	75	PDE11A	CYP19A1	ME1	GGT5
26	PKLR	POLR2F	PIK3CG	ASS1	76	GALM	PIK3CG	GAD1	KYNU
27	ACP5	EXTL1	HS3ST5	AKR1C3	77	ARG2	PRDM7	ACSM4	RRM2
28	CA8	RENBP	PHGDH	PLA2G16	78	GSTA1	CNDP1	OPLAH	NMNAT3
29	UGT2B7	XYL1	LPL	B3GALT5	79	CKB	ABAT	DSE	NQO1
30	GLUL	ST3GAL6	EXTL1	ST6GAL2	80	PLD1	INPP5F	PLA2G4C	HS6ST2
31	PDE3B	MAN1C1	HEPH	GPX3	81	HSD17B6	GPD1	B3GAT1	EXT1
32	GUCY1A2	LARGE1	GPX7	MAN1A1	82	ACOT4	IL4I1	PIGZ	MBOAT7
33	CKMT1B	LARGE2	NMNAT2	XDH	83	PIP4K2A	MGAT5	HS3ST3A1	PDE6B
34	SELENOI	GAPDHS	CHST2	AK5	84	ST6GALNAC3	FADS2	AMT	PDE4D
35	ACSBG1	TBXAS1	PCYT1B	AK6	85	ISYNA1	DGKG	TUSC3	GLUL
36	GALC	PDE3B	ALDH2	INPP5J	86	ST6GALNAC1	HYAL1	FADS2	NSD1
37	PIK3CD	PDE3A	A4GALT	CPT1C	87	MAT1A	CHST11	ENPP4	NSD2
38	CYP1A1	CHST6	B4GALNT1	ENPP4	88	CYP24A1	BBOX1	UXS1	NSD3
39	ATP6V0A4	GSTM1	CHST7	CA8	89	RDH12	ACOX2	NOS2	ENTPD8
40	NPL	MAT1A	ANPEP	ACSL5	90	ACER2	GDPD1	ALDH3B1	TCIRG1
41	HNMT	MGAM	AOX1	PDE11A	91	PDE5A	ADCY2	XDH	CYP27C1
42	MGAT4A	MGAM2	FOLH1	HSD17B2	92	HYAL1	PIGZ	MFNG	HACD1
43	NMRK2	GALNT3	ETHE1	DGKE	93	HSD3B2	GLDC	IDS	PLOD2
44	B3GALT4	CA14	RXYLT1	PIK3CD	94	B3GALNT1	DDO	PLCH1	GCK
45	MTAP	ENPP3	VNN1	GBGT1	95	ASAH1	GNS	INPP5F	GSTM3
46	ST3GAL6	CHST7	PLOD2	GALC	96	MTMR8	PDXP	BCAT1	BDH1
47	FHIT	GSTA4	TPH1	PDE5A	97	LDHD	ACSL1	PGM3	ALDH1L2
48	PNLIPRP3	UGT2B7	CHST3	MOCOS	98	PDE4D	FHIT	GCNT1	ADK
49	HOGA1	HS3ST1	GALNT18	SPTLC3	99	HS6ST2	HOGA1	PTGES	IPMK
50	DGKE	MOGAT1	HS3ST1	ALPG	100	GSTO1	PNPLA4	A3GALT2	MARS

Supplementary Table 2.1. The genes list in Supplementary Figure 2.1. S₁-S₄ columns each indicates the top 100 ranked metabolic genes uniquely upregulated in the melanocytic (S₁), transitory (S₂), neural crest (S₃) and undifferentiated (S₄) phenotypes in Supplementary Figure 2.1.

Melanoma cell line	Phenotype	IC50 to vemurafenib (nM)	Mutational status
M262	melanocytic	150	BRAFV600E mutant 2 copies BRAF AKT1 mutation& CDKN2A deletion
M229	transitory	282	BRAFV600E mutant 4 copies BRAF MITF amplification AKT1 amplification PTEN deletion
M397	transitory	132	BRAFV600E mutant
M409	neural-crest-like	1018	BRAFV600E mutant
M381	mesenchymal	>100000	BRAFV600E mutant

Supplementary Table 2.2. Basic backgrounds of the five selected melanoma cell lines used in this study.

2.13 Reference

1. Camp, J. G., Platt, R. & Treutlein, B. Mapping human cell phenotypes to genotypes with single-cell genomics. *Science* 365, 1401–1405 (2019).
2. Tang, F., Lao, K. & Surani, M. A. Development and applications of single-cell transcriptome analysis. *Nat. Methods* 8, (2011).
3. Tirosh, I. et al. Dissecting the multicellular ecosystem of metastatic melanoma by single-cell RNA-seq. *Science* 352, 189–196 (2016).
4. Patel, A. P. et al. Single-cell RNA-seq highlights intratumoral heterogeneity in primary glioblastoma. *Science* 344, 1396–1401 (2014).
5. Budnik, B., Levy, E., Harmange, G. & Slavov, N. SCoPE-MS: mass spectrometry of single mammalian cells quantifies proteome heterogeneity during cell differentiation. *Genome Biol.* 19, 1–12 (2018).
6. Shalek, A. K. & Benson, M. Single-cell analyses to tailor treatments. *Sci. Transl. Med.* 9, 1–4 (2017).
7. Hauser, A. S. et al. Pharmacogenomics of GPCR drug targets. *Cell* 172, 41-54.e19 (2018).
8. Zenobi, R. Single-cell metabolomics: analytical and biological perspectives. *Science* 342, 1243259 (2013).
9. Fessenden, M. Metabolomics: Small molecules, single cells. *Nature* 540, 153–155 (2016).
10. Thiele, C., Wunderling, K. & Leyendecker, P. Multiplexed and single cell tracing of lipid metabolism. *Nat. Methods* 16, (2019).
11. Duncan, K. D., Fyrestam, J. & Lanekoff, I. Advances in mass spectrometry based single-cell metabolomics. *Analyst* 144, 782–793 (2019).

12. Taniguchi, Y. et al. Quantifying E. coli proteome and transcriptome with single-molecule sensitivity in single cells. *Science* 329, 533–539 (2010).
13. Clemens, G., Hands, J. R., Dorling, K. M. & Baker, M. J. Vibrational spectroscopic methods for cytology and cellular research. *Analyst* 139, 4411–4444 (2014).
14. Wu, H. et al. In vivo lipidomics using single-cell Raman spectroscopy. *Proc. Natl. Acad. Sci. U. S. A.* 108, 3809–3814 (2011).
15. Fu, D., Yang, W. & Xie, X. S. Label-free imaging of neurotransmitter acetylcholine at neuromuscular junctions with stimulated Raman scattering. *J. Am. Chem. Soc.* 139, 583–586 (2017).
16. Freudiger, C. W. et al. Label-free biomedical imaging with high sensitivity by stimulated Raman scattering microscopy. *Science* 322, 1857–1860 (2008).
17. Saar, B. G. et al. Video-rate molecular imaging in vivo with stimulated Raman scattering. *Science* 330, 1368–1370 (2010).
18. Fu, D., Holtom, G., Freudiger, C., Zhang, X. & Xie, X. S. Hyperspectral imaging with stimulated raman scattering by chirped femtosecond lasers. *J. Phys. Chem. B* 117, 4634–4640 (2013).
19. Zhang, D. et al. Quantitative vibrational imaging by hyperspectral stimulated raman scattering microscopy and multivariate curve resolution analysis. *Anal. Chem.* 85, 98–106 (2013).
20. Ozeki, Y. et al. High-speed molecular spectral imaging of tissue with stimulated Raman scattering. *Nat. Photonics* 6, 845–851 (2012).
21. Figueroa, B. et al. Broadband hyperspectral stimulated Raman scattering microscopy with a parabolic fiber amplifier source. *Biomed. Opt. Express* 9, 6116 (2018).
22. Cheng, J. X. & Xie, X. S. Vibrational spectroscopic imaging of living systems: An emerging platform for biology and medicine. *Science* 350, (2015).
23. Wei, L. et al. Live-cell bioorthogonal chemical imaging: stimulated Raman scattering microscopy of vibrational probes. *Acc. Chem. Res.* 49, 1494–1502 (2016).
24. Davies, H. et al. Mutations of the BRAF gene in human cancer. *Science* 417, 949–954 (2002).
25. Su, Y. et al. Single-cell analysis resolves the cell state transition and signaling dynamics associated with melanoma drug-induced resistance. *Proc. Natl. Acad. Sci.* 114, 13679–13684 (2017).
26. Su, Y. et al. Phenotypic heterogeneity and evolution of melanoma cells associated with targeted therapy resistance. *PLoS Comput. Biol.* 15, 1–22 (2019).
27. Tsoi, J. et al. Multi-stage differentiation defines melanoma subtypes with differential vulnerability to drug-induced iron-dependent oxidative stress. *Cancer Cell* 33, 890–904 (2018).
28. Müller, J. et al. Low MITF/AXL ratio predicts early resistance to multiple targeted drugs in melanoma. *Nat. Commun.* 5, (2014).
29. Berger, M. F. et al. Integrative analysis of the melanoma transcriptome. *Genome Res.* 20, 413–427 (2010).
30. Yu, Y. et al. Targeting the senescence-overriding cooperative activity of structurally unrelated H3K9 demethylases in melanoma. *Cancer Cell* 33, 322–336 (2018).
31. Su, Y. et al. Kinetic inference resolves epigenetic mechanism of drug resistance in melanoma. Preprint at <https://www.biorxiv.org/content/10.1101/724740v1> (2019).

32. Hugo, W. et al. Genomic and transcriptomic features of response to anti-PD-1 therapy in metastatic melanoma. *Cell* 165, 35–44 (2016).
33. Hugo, W. et al. Non-genomic and Immune Evolution of Melanoma Acquiring MAPKi Resistance. *Cell* 162, 1271–1285 (2015).
34. Rambow, F. et al. Toward minimal residual disease-directed therapy in melanoma. *Cell* 174, 843–855 (2018).
35. Ward, P. S. & Thompson, C. B. Metabolic reprogramming: a cancer hallmark even Warburg did not anticipate. *Cancer Cell* 21, 297–308 (2012).
36. Su, Y. et al. Multi-omic single-cell snapshots reveal multiple independent trajectories to drug tolerance in a melanoma cell line. *Nat. Commun.* 11, 1–12 (2020).
37. Bollag, G. et al. Vemurafenib: The first drug approved for BRAF-mutant cancer. *Nat. Rev. Drug Discov.* 11, 873–886 (2012).
38. Remacle, F., Kravchenko-Balasha, N., Levitzki, A. & Levine, R. D. Information-theoretic analysis of phenotype changes in early stages of carcinogenesis. *Proc. Natl. Acad. Sci.* 107, 10324–10329 (2010).
39. Zadrán, S., Arumugam, R., Herschman, H., Phelps, M. E. & Levine, R. D. Surprisal analysis characterizes the free energy time course of cancer cells undergoing epithelial-to-mesenchymal transition. *Proc. Natl. Acad. Sci.* 111, 13235–13240 (2014).
40. Levine, R. D. Information theory approach to molecular reaction dynamics. *Annu. Rev. Phys. Chem.* 29, 59–92 (1978).
41. Wei, L., Yu, Y., Shen, Y., Wang, M. C. & Min, W. Vibrational imaging of newly synthesized proteins in live cells by stimulated Raman scattering microscopy. *Proc. Natl. Acad. Sci. U. S. A.* 110, 11226–11231 (2013).
42. Hoek, K. S. et al. In vivo switching of human melanoma cells between proliferative and invasive states. *Cancer Res.* 68, 650–656 (2008).
43. Currie, E., Schulze, A., Zechner, R., Walther, T. C. & Farese, R. V. Cellular fatty acid metabolism and cancer. *Cell Metab.* 18, 153–161 (2013).
44. Intlekofer, A. M. & Finley, L. W. S. Metabolic signatures of cancer cells and stem cells. *Nat. Metab.* 1, 177–188 (2019).
45. Zhang, L. et al. Spectral tracing of deuterium for imaging glucose metabolism. *Nat. Biomed. Eng.* 3, 402–413 (2019).
46. Röhrig, F. & Schulze, A. The multifaceted roles of fatty acid synthesis in cancer. *Nat. Rev. Cancer* 16, 732–749 (2016).
47. Ohol, Y. M., Wang, Z., Kemble, G. & Duke, G. Direct inhibition of cellular fatty acid synthase impairs replication of respiratory syncytial virus and other respiratory viruses. *PLoS One* 10, 1–20 (2015).
48. Tobias C. Walther, Jeeyun Chung, R. V. F. J. Lipid droplet biogenesis. *Annu. Rev. Cell Dev. Biol.* 33, 491–510 (2017).
49. Olzmann, J. A. & Carvalho, P. Dynamics and functions of lipid droplets. *Nat. Rev. Mol. Cell Biol.* 20, 137–155 (2019).
50. Valm, A. M. et al. Applying systems-level spectral imaging and analysis to reveal the organelle interactome. *Nature* 546, 162–167 (2017).
51. Li, J. et al. Lipid desaturation is a metabolic marker and therapeutic target of ovarian

- cancer stem cells. *Cell Stem Cell* 20, 303–314.e5 (2017).
52. Yue, S. et al. Cholesteryl ester accumulation induced by PTEN loss and PI3K/AKT activation underlies human prostate cancer aggressiveness.pdf. *Cell Metab.* 19, 393–406 (2014).
 53. Fu, D. et al. In vivo metabolic fingerprinting of neutral lipids with hyperspectral stimulated raman scattering microscopy. *J. Am. Chem. Soc.* 136, 8820–8828 (2014).
 54. Nakamura, M. T. & Nara, T. Y. Structure, function, and dietary regulation of $\Delta 6$, $\Delta 5$, and $\Delta 9$ desaturases. *Annu. Rev. Nutr.* 24, 345–376 (2004).
 55. Wei, Y., Wang, D., Topczewski, F. & Pagliassotti, M. J. Saturated fatty acids induce endoplasmic reticulum stress and apoptosis independently of ceramide in liver cells. *Am. J. Physiol. - Endocrinol. Metab.* 291, 275–281 (2006).
 56. Volmer, R., Van Der Ploeg, K. & Ron, D. Membrane lipid saturation activates endoplasmic reticulum unfolded protein response transducers through their transmembrane domains. *Proc. Natl. Acad. Sci. U. S. A.* 110, 4628–4633 (2013).
 57. Borradaile, N. M. et al. Disruption of endoplasmic reticulum structure and integrity in lipotoxic cell death. *J. Lipid Res.* 47, 2726–2737 (2006).
 58. Shen, Y. et al. Metabolic activity induces membrane phase separation in endoplasmic reticulum. *Proc. Natl. Acad. Sci.* 114, 13394–13399 (2017).
 59. Van Meer, G., Voelker, D. R. & Feigenson, G. W. Membrane lipids: Where they are and how they behave. *Nat. Rev. Mol. Cell Biol.* 9, 112–124 (2008).
 60. Hagedorn, E. J. & Sherwood, D. R. Cell invasion through basement membrane: The anchor cell breaches the barrier. *Curr. Opin. Cell Biol.* 23, 589–596 (2011).
 61. Listenberger, L. L. et al. Triglyceride accumulation protects against fatty acid-induced lipotoxicity. *Proc. Natl. Acad. Sci.* 100, 3077–3082 (2003).
 62. Yen, C.-L. E., Stone, S. J., Koliwad, S., Harris, C. & Farese, R. V. DGAT enzymes and triacylglycerol biosynthesis. *J. Lipid Res.* 49, 2283–2301 (2008).
 63. Cases, S. et al. Cloning of DGAT2, a second mammalian diacylglycerol acyltransferase, and related family members. *J. Biol. Chem.* 276, 38870–38876 (2001).
 64. Konieczkowski, D. J. et al. A melanoma cell state distinction influences sensitivity to MAPK pathway inhibitors. *Cancer Discov.* 4, 816–827 (2014).
 65. Viswanathan, V. S. et al. Dependency of a therapy-resistant state of cancer cells on a lipid peroxidase pathway. *Nature* 547, 453–457 (2017).
 66. Fischer, K. R. et al. Epithelial-to-mesenchymal transition is not required for lung metastasis but contributes to chemoresistance. *Nature* 527, 472–476 (2015).
 67. Landsberg, J. et al. Melanomas resist T-cell therapy through inflammation-induced reversible dedifferentiation. *Nature* 490, 412–416 (2012).
 68. Delgado-Goñi, T. et al. Increased inflammatory lipid metabolism and anaplerotic mitochondrial activation follow acquired resistance to vemurafenib in BRAF-mutant melanoma cells. *Br. J. Cancer* 122, 72–81 (2020).
 69. Talebi, A. et al. Sustained SREBP-1-dependent lipogenesis as a key mediator of resistance to BRAF-targeted therapy. *Nat. Commun.* 9, 1–11 (2018).
 70. Wu, S. & Näär, A. M. SREBP1-dependent de novo fatty acid synthesis gene expression is elevated in malignant melanoma and represents a cellular survival trait. *Sci. Rep.* 9, 1–17 (2019).

71. Pisanu, M. E. et al. Inhibition of Stearoyl-CoA desaturase 1 reverts BRAF and MEK inhibition-induced selection of cancer stem cells in BRAF-mutated melanoma. *J. Exp. Clin. Cancer Res.* 37, 1–17 (2018).
72. Rodríguez-Ruiz, J., Belarbi, E. H., Sánchez, J. L. G. & Alonso, D. L. Rapid simultaneous lipid extraction and transesterification for fatty acid analyses. *Biotechnol. Tech.* 12, 689–691 (1998).
73. Xiao, Z., Dai, Z. & Locasale, J. W. Metabolic landscape of the tumor microenvironment at single cell resolution. *Nat. Commun.* 10, 1–12 (2019).
74. Subramanian, A. et al. Gene set enrichment analysis: A knowledge-based approach for interpreting genome-wide expression profiles. *Proc. Natl. Acad. Sci. U. S. A.* 102, 15545–15550 (2005).

Chapter 3

MULTICOLOR PHOTOACTIVATABLE
RAMAN PROBES FOR
SUBCELLULAR IMAGING AND
TRACKING BY CYCLOPROPENONE
CAGING

The content of this chapter has been published in:

Du, J., & Wei, L*. Multicolor Photoactivatable Raman Probes for Subcellular Imaging and Tracking by Cyclopropenone Caging. *J. Am. Chem. Soc.*, 2022, 144, 2, 777–786.

3.1 Introduction

Photoactivation, which allows for precise spatial-temporal control of target molecules, has found wide applications in biological research, such as for the delivery of therapeutic agents¹ and the modulation of cellular chemistry and physiology²⁻⁴. For microscopy, the invention of photoactivatable fluorescent probes, which can be converted from the non-fluorescent to the fluorescent state by light with photolabile groups⁵⁻⁷, has facilitated the development of ground-breaking localization-based super-resolution microscopy, such as photoactivated localization microscopy (PALM)⁸⁻¹². In addition, these fluorescent probes have opened new ways to study the dynamics of cell migration^{13,14} and the interactions of biomolecules at the targeted subcellular locations and time periods¹⁵⁻¹⁷.

Complementary to fluorescence, Raman microscopy also offers superior optical imaging capabilities. Notably, the recent coupling of the nonlinear stimulated Raman scattering (SRS) imaging¹⁸ with Raman probes, has helped address several fundamental challenges in fluorescence microscopy, such as for imaging small biomolecules¹⁹ and for super-multiplex

imaging^{20,21} in live cells. Compared to fluorescence, Raman microscopy has several unique advantages due to its nature of detecting vibrational motions of chemical bonds instead of probing the electronic state transitions of conjugated fluorophores. First, the sizes of Raman probes are usually much smaller than those of fluorophores. This introduces much less physical perturbation when tagging biomolecules²². Second, the Raman peak linewidth is about 50-100 times narrower compared to the broad absorption and the emission peaks from fluorophores²⁰. Third, Raman signals don't involve electronic excitation, and are resistant to photobleaching or environmental quenching, and hence are better suited for quantifications. These features allow for super-multiplexed optical imaging with high information throughput for interrogating the complex biology. The designed matching polyynes and electronic pre-resonance Raman dye palettes (e.g. the CARBOW and the MARS dye palettes) have achieved more than 20-plex SRS imaging with reported sensitivity close to what is offered by confocal fluorescence^{20,21,23,24}.

Essentially, light-activatable Raman probes would enable photoactivatable Raman imaging while preserving multiplexity and small-size features. This new functional Raman imaging would be highly beneficial to multi-component imaging and tracking. However, this category of Raman probes remains unexplored. Recently, electronic pre-resonance SRS dye based enzyme-activatable²⁵ and photoswitchable²⁶⁻²⁸ Raman probes have been reported, demonstrating the remarkable multiplexable or photo-controllable features for functional cellular imaging, respectively. However, enzyme-activatable probes lack the photo-controllable features. While reversibly switchable Raman probes share certain imaging functions with photoactivatable probes, their additional off-switching pathway was shown to be triggerable by the SRS imaging lasers²⁶. Additionally, their off-channel signals may also limit the resolvable Raman colors²⁶⁻²⁸. Therefore, photoactivatable Raman probes should offer superior quantification and multiplexity for tracking complex cellular dynamics and interactions.

Here, we report the first general design of photoactivatable Raman probes for live-cell multiplexed imaging and tracking. We adopt the photo-releasable alkyne scaffold since

alkynes are small and highly Raman-sensitive in the cell silent spectral region (1800 – 2800 cm^{-1})²⁹. In addition, alkynes could readily offer multiplexable Raman colors through proper isotope editing³⁰ or chemical-group capping²¹. The photoreaction that generates alkyne bonds is therefore a valuable platform for constructing photoactivatable Raman imaging probes. In the search for such probes, cyclopropenones stood out for their facile synthesis, highly efficient and fast photoconversion to alkynes^{31–33}. To explore the potential of cyclopropenones for photoactivatable Raman imaging, we first synthesized and spectroscopically characterized a series of model compounds. We then identified the suitable light-activating scaffold with combined features of quick activation, small sizes and desirable Raman selectivity and sensitivity. Next, we chemically engineered the selected cyclopropenone scaffold to substantially improve its chemical stability in the cellular environment and obtained enhanced Raman signals. After further derivatizations of the probes, we successfully achieved photoactivatable imaging of multiple organelles including mitochondria, lysosomes, lipid droplets and endoplasmic reticulum (ER) in live cells, with further demonstrations of subcellular and single-cell tracking. We envision that this rationally-designed novel toolset of photoactivatable Raman probes will help push the frontiers of Raman-based quantitative functional imaging, especially for multi-component and precisely-controlled interrogations in live biological systems.

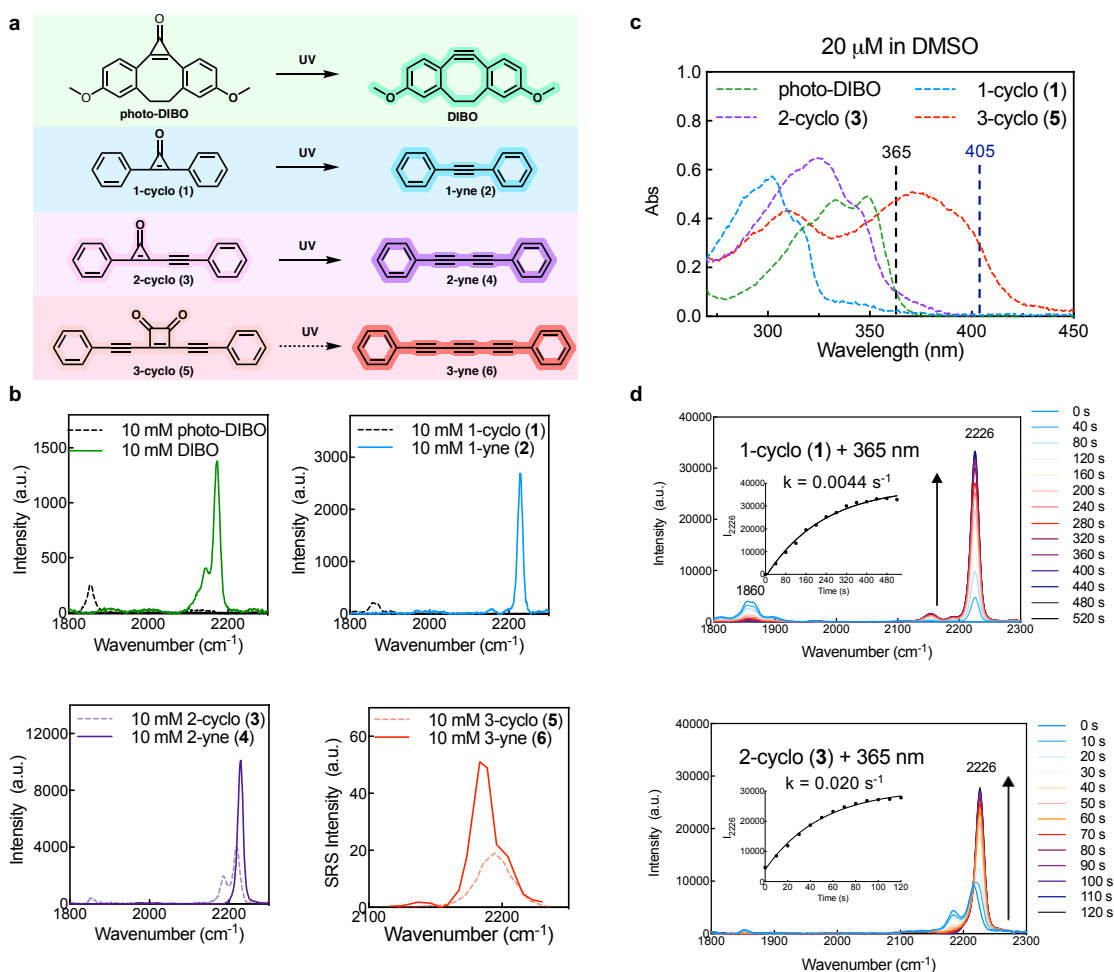


Figure 3.1. Characterizations of model systems for photoactivatable generation of alkynes. (a) Structures and reactions for four precursors of alkynes, including photo-DIBO, 1-cyclo (1), 2-cyclo (3) and 3-cyclo (5) that could potentially undergo UV-activated alkyne generation. (b) Spontaneous Raman and hyperspectral SRS spectra for 10 mM precursors and products shown in (a). (c) UV-Vis absorption spectra of all four precursors shown in (a) (20 μM , in DMSO). Vertical lines indicate the positions of 365 nm and 405 nm, which we used for photoactivation. (d) Times-series spontaneous Raman spectra for monitoring the photoactivation kinetics for 1-cyclo (1, top) and 2-cyclo (3, bottom) under 365 nm illumination (15 mW/cm^2). Inserts show the increase kinetics of alkyne peaks (2226 cm^{-1}).

Species	Photo-DIBO	DIBO	1-cyclo (1)	1-yne (2)	2-cyclo (3)	2-yne (4)	3-cyclo (5)	3-yne (6)	9	10
Peak (cm ⁻¹)	1851	2171	1860	2226	2218	2226	2194	2185	1850	2205
RIE	0.34	1.8	0.37	4.0	7.5	19.4	12.7	31.3	0.89	7.7
Abs (nm)	333	323	302	283	324	310	371	337	339	323
ϵ (M ⁻¹ cm ⁻¹)	23900	24200	28600	32300	32400	35700	25500	28100	13300	36800

Table 3.1. Photophysics characterization of molecules in model systems

3.2 Synthesis and Spectroscopic Characterizations of Model Cyclopropenone-caging Systems.

Cyclopropenone caging has been previously adopted for photoactivation and subsequent biorthogonal labeling of fluorophores in fluorescence microscopy^{34,35}. For examples, copper-free click labeling of dibenzocyclooctynes (DIBO) released from photoactivated diarylcyclopropenones (photo-DIBO)³⁶ has been demonstrated for surface³⁷ and cellular labeling and imaging³⁴. We herein first measured the alkyne Raman signal generation from photo-DIBO light-activation (Figure 3.1a). In the cell silent region, photo-DIBO only has a weak Raman peak around 1851 cm⁻¹ while photochemically generated DIBO by UV shows a characteristic alkyne peak at 2171 cm⁻¹ with significantly enhanced Raman intensity (Figure 3.1b, dashed black vs solid green spectra). Compared to 5-ethynyl-2'-deoxyuridine (EdU), the well-adopted benchmark for Raman intensity quantification, the relative Raman intensity to EdU (RIE) of the strained alkyne DIBO is only 1.8 (Table 3.1). Compared with DIBO, the planar diphenylacetylene (1-yne, **2**, Figure 3.1a) exhibits larger alkyne Raman signals²⁹. Given this, we reasoned that diphenylcyclopropenone (1-cyclo, **1**, cyclopropenone-caged 1-yne, Figure 3.1a) should be a better photoactivatable Raman scaffold with higher Raman sensitivity after uncaging. Indeed, UV-uncaging of 1-cyclo (**1**), which started from a similarly weak Raman peak at 1860 cm⁻¹ from photo-DIBO, produced an intense sharp peak for 1-yne (**2**) at 2226 cm⁻¹ (Figure 3.1b, dashed black vs solid blue spectra) with an improved RIE values to about 4 (Table 3.1).

Polyynes are an established palette of highly sensitive and multiplexable Raman probes²¹.

We next sought to explore whether we could construct polyynes-based cyclopropenones to obtain even higher after-conversion Raman intensity. We synthesized cyclopropenone-caged 2-yne (i.e. 2-cyclo, **3**, Figure 3.1a) and found that it also possesses superb UV-uncaging photochemistry similar to that of 1-cyclo (**1**). Photoconversion from 2-cyclo (**3**) to 2-yne (**4**) indeed generated a sharp alkyne peak with an RIE of 19 (Table 3.1). However, the spectra of 2-cyclo (**3**) and 2-yne (**4**) present a partial overlap (Figure 3.1b, dashed vs solid purple spectra), which is less desirable for background-free detection. We further attempted to synthesize 3-yne (**6**) based cyclopropenone, but the product was highly unstable at room temperature and decomposed quickly during concentrating. As an alternative, we next chose thermally stable 3,4-Bis(phenylethynyl)-3-cyclobutene-1,2-dione as our target molecule for caged 3-yne (i.e. 3-cyclo, **5**, Figure 3.1a), which was reported to yield 3-yne (**6**) by pyrolytic loss of two carbonyl groups, and was suggested to also undergo photolysis process to give the same product³⁸. However, we did not observe any activated Raman signals from synthesized 3-cyclo (**5**) after illuminations from our handheld UV-lamp (254 nm and 365nm) or 405 nm continuous-wave (CW) laser. Additionally, our characterizations from synthesized pure 3-cyclo (**5**) and 3-yne (**6**) showed that they also present an undesirable partial spectral overlap (Figure 3.1b, dashed vs solid red spectra, the SRS spectra are shown instead of spontaneous Raman spectra due to the large autofluorescence background of 3-cyclo, **5**).

Based on our spectroscopy characterizations on photo-DIBO and 1- to 3-cyclo (**1**, **3**, **5**) model compounds, 1-cyclo (**1**) and 2-cyclo (**3**) present as better candidates judging from photo-conversion capabilities and uncaged alkyne intensity (Table 3.1). The sizes of 1-cyclo (**1**) and 2-cyclo (**3**) are also small, thus would only exhibit minor labeling perturbation to biological targets. Moreover, the uncaged 1-yne (**2**) and 2-yne (**4**) are immune to photobleaching, making quantification more straightforward and reliable²¹. We next aimed to compare the photo-uncaging kinetics for both 1-cyclo (**1**) and 2-cyclo (**3**). The absorption spectra of all four caged model compounds are shown in Figure 3.1c. Although both 365 nm and 405 nm excitations only fall around the tails of the spectra, either handheld 365 nm UV-

lamp or 405 nm CW laser illumination can effectively uncage both 1-cyclo (**1**) and 2-cyclo (**3**). With 365 nm lamp illumination, the characteristic peaks of cyclopropenones ($\sim 1860\text{ cm}^{-1}$) continue to drop while the alkyne peaks (2226 cm^{-1}) gradually increase for both molecules (Figure 3.1d). 2-cyclo (**3**, $k = 0.020\text{ s}^{-1}$) showed uncaging kinetics about 5-fold faster than that of 1-cyclo (**1**, $k = 0.0044\text{ s}^{-1}$, with a reported quantum yield of 0.78³²), consistent with its higher molar extinction coefficient at 365 nm (Figure 3.1c). The progression of the UV-activation reactions could also be confirmed by the change in the corresponding absorption spectra (Supplementary Figure 3.1)³⁷.

3.3 Probe Engineering for Improved Chemical Stability and Enhanced Raman Sensitivity.

After spectroscopic study of the probes' photochemistry, we next sought to derivatize the probes for live-cell photoactivatable Raman imaging. Although 2-cyclo (**3**) has higher uncaged Raman signals and faster uncaging kinetics than 1-cyclo (**1**), our attempts to functionalize 2-cyclo (**3**) were not successful due to the instability of 2-cyclo core under the reaction conditions. Additionally, the background Raman signal from 2-cyclo (**3**) before photoactivation also complicates imaging analysis (Figure 3.1b, dashed vs solid purple spectra). We hence focused on derivatizing 1-cyclo (**1**) as functional imaging probes in live cells.

Nonetheless, we found that 1-cyclo (**1**) significantly suffers from instability in the cellular environment. Either 1-cyclo (**1**) or functionalized 1-cyclo with a mitochondria targeting group (i.e. Cyclo-Mito, **7**) did not produce any observable uncaging signals in labeled live cells (Supplementary Figure 3.2). We hypothesized that this was likely because the cyclopropenone structures are susceptible to nucleophilic attack, leading to ring-opened α,β -unsaturated acids derivatives^{39,40}. Cysteines, glutathione, and other biological thiols are strong nucleophiles and could easily deactivate cyclopropenones. We hence tested the

stability of 1-cyclo (**1**) in 10 mM cysteine phosphate-buffered saline (PBS) at 37 °C, mimicking physiological conditions⁴¹. HPLC analysis showed that both 1-cyclo (**1**) and Cyclo-Mito (**7**) completely decomposed within 30 minutes (Figure 3.2a & Supplementary Figure 3.3). The coupled mass spectrometry indicated that the byproduct was cysteine adduct, consistent with previous report⁴⁰.

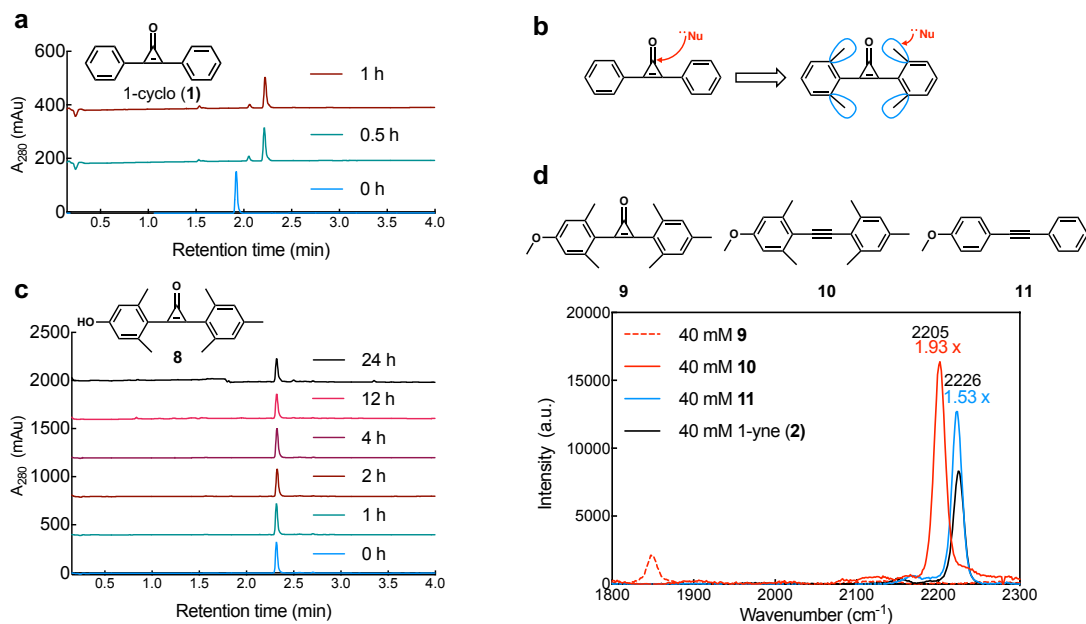
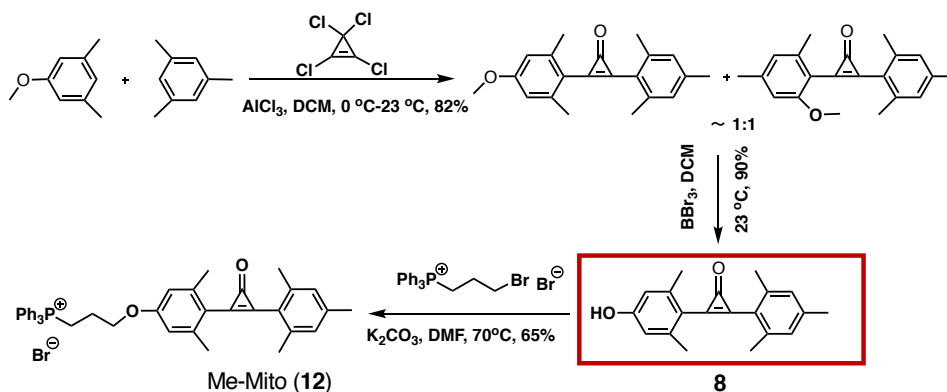


Figure 3.2. Molecular engineering of 1-cyclo (1**).** (a) HPLC trace of 1-cyclo (**1**) after incubating in 10 mM cysteine (PBS) for designated time at 37 °C. (b) Design principles of incorporating methyl groups to shield cyclopropanones from nucleophilic attack. (c) HPLC trace of **8** after incubating in 10 mM cysteine (PBS) for designated time at 37 °C. (d) Spontaneous Raman comparisons for 40 mM solutions of **9** (red dashed), **10** (red solid, generated by illuminating **9** with 365 nm), **11** (blue solid) and 1-yne (**2**, black solid).

We speculated that incorporating alkyl groups around cyclopropanones might shield the strained ketones from nucleophilic attack and improve the stability of 1-cyclo (**1**) inside cells (Figure 3.2b). To test this hypothesis, we synthesized methyl-shielded 1-cyclo with Friedel-Crafts alkylation of aromatic compounds (Scheme 3.1)³². The phenol alcohol handle was

introduced to link cellular targeting groups. HPLC trace confirmed that the methylated 1-cyclo (i.e. **8**, Scheme 3.1) presented substantially improved stability to cysteine attack even for incubation up to 24 hours (Figure 3.2c). We further found that methylated cyclopropanones not only have improved stability to nucleophiles, but also have enhanced uncaging Raman signals. Figure 3.2d shows that methylation and phenolation of the aromatic rings introduced an intensity increase (1.93 times) and a slight peak red-shift (21 cm^{-1}) to 2205 cm^{-1} for the activated alkyne peak compared with the unfunctionalized 1-cyclo (the solid black spectrum from 1-yne vs the red solid spectrum from **10**). In addition to the Raman spectral shift, the absorption spectrum of **9** also undergoes a red-shift to close to that from 2-cyclo (**3**), implying improved UV photoactivation kinetics (Supplementary Figure 3.4).



Scheme 3.1. Synthesis of methyl-shielded 1-cyclo (8**) and the corresponding organelle targeting probes (e.g. the mitochondria targeting probe, Me-Mito, **12**)**

3.4 Organelle-Targeted Probe Engineering for Live-cell Photoactivatable Raman Imaging.

After establishing the methylated phenyl capped 1-cyclo as a suitable uncaging scaffold for intracellular investigations, we then synthesized organelle-targeted cyclopropanone probes and applied them to live-cell imaging. The Me-Mito (**12**) probe uses positively charged

triphenylphosphonium (TPP⁺) as a mitochondria targeting group (Scheme 3.1 & Figure 3.3a). We first confirmed via HPLC that the synthesized Me-Mito (**12**) was stable in 10 mM cysteine solution for over 48 hours (Supplementary Figure 3.5). We next co-incubated cells with Me-Mito (**12**) and a commercial mitochondria fluorescence marker (Mitotracker deep red) and performed live-cell imaging. We validated that the caged Me-Mito (**12**) presented a clean background in cells before UV-activation (Figure 3.3a, Before 405, 2205 cm⁻¹; the CH₃ SRS image at 2940 cm⁻¹ outlines the cell morphology for the same set of cells). After two minutes of 405 nm laser illumination, a bright mitochondria pattern was observed by SRS imaging at the alkyne channel (Figure 3.3a, After 405, 2205 cm⁻¹), implying a high signal-to-background ratio. The labeling specificity by Me-Mito (**12**) was further verified by the co-localization with the fluorescence marker (Figure 3.3a, Fl marker and Merge; the magnified images, additional sets of activation and correlation images, and Pearson's R values are shown in Supplementary Figure 3.6). It is worth pointing out that, we found that high-power SRS lasers could very slowly activate the Me-Mito (**12**, Supplementary Figure 3.7), likely due to multi-photon activation from the pump (~ 800 nm, 2 ps) or Stokes (1031 nm, 2ps) laser alone and also from their combined excitation based on a series of activation-power relationship characterizations (Supplementary Table 3.1 and Supplementary Figure 3.8a). We confirmed that the activation by SRS lasers is independent of probe concentration (Supplementary Figure 3.8b) and selected 25 mW and 60 mW as suitable SRS imaging powers for the pump and Stokes beam respectively (Supplementary Figure 3.8a), which is high enough to maintain a decent imaging quality, but low enough to both yield a low side photoactivation rate by SRS lasers (close to one percent per frame with 80 μs pixel dwell time) and maintain minimum photo-toxicity. We also envision that the photoactivation rate from SRS lasers would be much-lowered with a faster scanning rate (i.e. lower pixel dwell time). Similarly, we designed the lysosomes imaging probe (Me-Lyso, **13**, Figure 3.3b), by introducing a basic dimethylamine group for acidic organelle targeting through similar chemistry as shown in Scheme 1 (detailed reaction conditions listed in Methods). We also confirmed the clean background (Figure 3.3b, Before 405, 2205 cm⁻¹), the achievable high photoactivation ratio (Figure 3.3b, After 405, 2205 cm⁻¹), and desired co-localization (Figure 3.3b, Merge) for proper lysosomes targeting from Me-Lyso (**13**) and the commercial

Lysoview 488 fluorophore co-labeled live cells (Figure 3.3b & Supplementary Figure 3.9). Furthermore, we designed the endoplasmic reticulum imaging probe (Me-ER, **14**, Figure 3.3c) by adding the methyl sulphonamide group and confirmed highly specific targeting, photoactivation and imaging performances (Figure 3.3c & Supplementary Figure 3.10). Unexpectedly, when we set out to design a HaloTag⁴² ligand carrying cyclopropenone probe for protein imaging, we instead found that this probe showed high-specificity for staining lipid droplets with preserved photoactivation properties. Interestingly, it quickly stained lipids droplets within 15 minutes, much faster than previously reported carboxylate-terminated C12 alkyl polyynes Raman probe, which requires overnight labeling²¹. We hence named the probe Me-LD (**15**, Figure 3.3d), after confirming its specificity in reference to fluorescence co-localization of lipid droplets marker Lipid Spot 610 (Figure 3.3d & Supplementary Figure 3.11). Through the above demonstrations, we hence showed that the methylated cyclopropenone is a well suitable motif for general design of live-cell compatible photo-uncaging Raman probes.

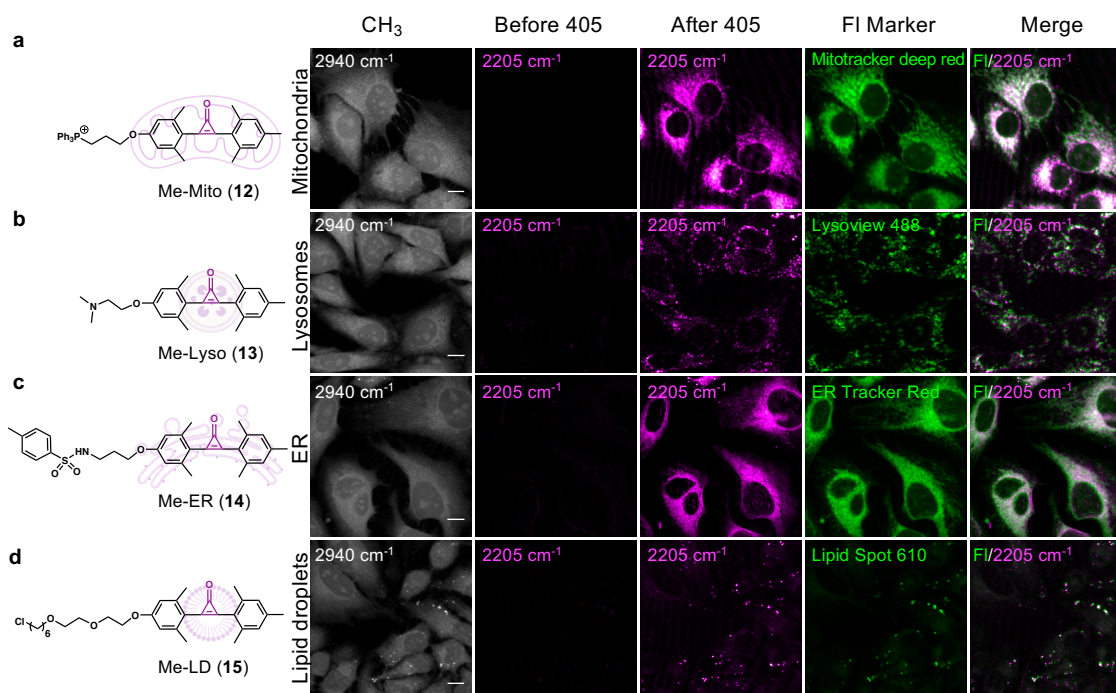


Figure 3.3. The structures and images of methylated cyclopropenone probes for photoactivated SRS imaging of organelle targets including mitochondria (Me-Mito, **12**, a), lysosomes (Me-Lyso, **13**, b), endoplasmic reticulum (Me-ER, **14**, c) and lipid droplets (Me-LD, **15**, d) in live HeLa cells. Fluorescence imaging with co-stained commercial markers were used to validate the labeling specificity of SRS probes via co-localization. Scale bar: 10 μm .

3.5 Live-cell Photoactivatable Multiplex Imaging.

After developing photoactivatable organelle-targeting Raman probes with the methylated 1-cyclo scaffold, we further derivatized them for photoactivatable multiplex imaging. We first adopted the isotope editing strategy for Raman color shift³⁰. With bis-¹³C isotope substitution on the Me-Mito (**12**) probe, the Me-Mito-¹³C (**16**) showed a drastic peak shift from the original 2205 cm^{-1} to 2125 cm^{-1} after uncaging (Figure 3.4a & 3.4b, blue color-coded). Therefore Me-Mito-¹³C (**16**) provided a well-resolvable color in addition to that offered by the non-isotope-edited probe such as Me-Lyso (**13**, Figure 3.4a & 3.4b, magenta color-coded). While we fully expect that mono-¹³C substitution would likely offer additional resolvable colors within the 80 cm^{-1} spectral gap similar to previously reported³⁰, the synthetic challenges and costs are also higher, and we are still exploring along this line.

To generate more photoactivatable Raman colors, we next explored the utility of the 21 cm^{-1} peak shift from unmethylated cyclopropenone (Figure 3.2d, **11** vs **10**). We revealed that the unmethylated cyclopropenone, once functionalized as the hydrophobic Cyclo-LD probe (**17**, Figure 3.4a, green color-coded), showed a much-increased stability to thiol-containing buffers (Supplementary Figure 3.12a & 3.12b) and preserved the fast lipid droplets labeling property. Its suitability for live-cell lipid droplet imaging is also confirmed by fluorescence co-staining (Supplementary Figure 3.12c). Together with the un-edited Me-Lyso (**13**) and the Me-Mito-¹³C (**16**), Cyclo-LD (**17**) could be adopted as the third photoactivatable color for intracellular multiplex imaging with minimal spectral cross-talk (Figure 3.4b & 3.4c). After confirming the minimal cytotoxicity of all cyclopropenone imaging probes (Supplementary Figure 3.13), we further demonstrated three-color co-labeling for

mitochondria (Me-Mito- ^{13}C , **16**), lysosomes (Me-Lyso, **13**) and lipid droplets (Cyclo-LD, **17**) on the same set of live cells (Figure 3.4d). The photoactivatable multiplex imaging of these intracellular targets presents clear contrast from each individual channel without the need of linear unmixing (Figure 3.4d). The well-maintained cellular morphology throughout photoactivation and multiplex imaging also proved the superior live-cell compatibility of this strategy.

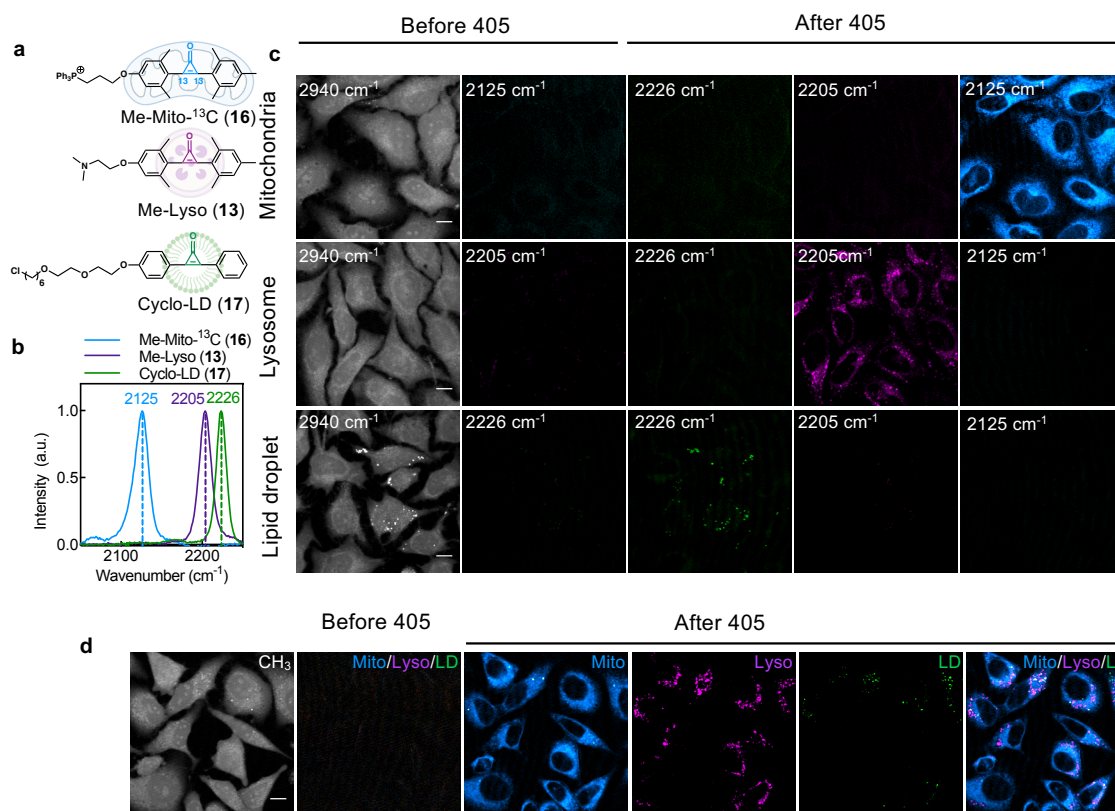


Figure 3.4. Three-color photoactivatable organelle imaging with Me-Mito- ^{13}C (16**), Me-Lyso (**13**) and Cyclo-LD (**17**) on live HeLa cells.** (a) Chemical structures of Me-Mito- ^{13}C (**16**), Me-Lyso (**13**) and Cyclo-LD (**17**). (b) The normalized spontaneous Raman spectra of Me-Mito- ^{13}C (**16**), Me-Lyso (**13**) and Cyclo-LD (**17**) after UV-uncaging. (c) SRS images of live HeLa cells before and after 405 nm illumination, labeled with Me-Mito- ^{13}C (**16**, 2125 cm^{-1}), Me-Lyso (**13**, 2205 cm^{-1}) or Cyclo-LD (**17**, 2226 cm^{-1}), respectively. 2940 cm^{-1} images for CH₃ outline the cell morphology. (d) Three-

color photoactivatable Raman imaging of the same set of live HeLa cells co-labeled with Me-Mito-¹³C (**16**), Me-Lyso (**13**) and Cyclo-LD (**17**). Scale bar: 10 μ m.

3.6 Intracellular Photoactivation and Multiplex Tracking.

Taking advantage of the high spatial-temporal control feature, tracking subcellular structures and single cells could realize the full potential of photoactivatable imaging. In addition, multiplex activation of single cells would illuminate complex cell-to-cell interactions and facilitate cell profiling^{14,43}. Our non-invasive multiplex SRS imaging with photoactivatable probes would be highly appealing for such applications.

Here, we showcased that our approach could illuminate subcellular and single-cell dynamics with pulse-chase photoactivation and imaging. We first confirmed high mitochondria-labeling specificity of our mitochondria probe for relatively long-term pulse-chase tracking applications. More than 85 % of activated Me-Mito-¹³C (**16**) signals retained in live HeLa cells after 2 hours of chasing (Supplementary Figure 3.14a) with well-maintained mitochondria labeling pattern (Supplementary Figure 3.14b). In live HeLa cells labeled with Me-Mito-¹³C (**16**), 405 nm laser was first used to pulse-activate the selected region of a single cell for 20 seconds (Figure 3.5a, CH₃, the white dashed box indicates the activation area). Immediately after photoactivation, SRS imaging at 2125 cm⁻¹ well resolved the distribution of mitochondria only from this activated subcellular region (Figure 3.5a, Mito_{0 min}, Pulse), implying high spatial selectivity. After only a 10-minute chase period, SRS imaging at the same channel (2125 cm⁻¹) captured fast redistribution of activated mitochondria signals (Figure 3.5a, Mito_{10 min}, Chase). The merged image of these two time spots (Figure 3.5a, Merge) clearly showed the quick diffusion of mitochondria, indicating dynamic mitochondria fission and fusion in live cells, consistent with the recent report^{26,44,45}.

In another set of live HeLa cells co-labeled with Me-Mito-¹³C (**16**) and Me-LD (**15**) for activation and multiplex tracking, similar pulse-chase experiments were carried out (Figure 3.5b). After activating a single cell (Figure 3.5b, CH₃, the outline of the cell was indicated by white dashed box), two-channel SRS imaging of mitochondria (Figure 3.5b, Mito, at 2125 cm⁻¹) and lipid droplets (Figure 3.5b, LD, at 2205 cm⁻¹) was immediately acquired (0 h).

Subsequent chase imaging was performed at an interval of one hour for up to two hours (1 h, 2 h). In the mitochondria channel (Figure 3.5b, Mito), it captured a likely material transfer from the photoactivated cell to the neighboring cell (indicated by the white arrow in the magnified images, the relative signals of the neighboring cell increased from 5 % to 32 % after 2 hours). In the parallel droplet channel (Figure 3.5b, LD), the chase images also demonstrated that the lipid droplets in the left side of the photoactivated cell (indicated by the yellow arrow in the magnified images) were approaching each other and were probably in the process of merging. We envision a covalently labeling probe (e.g. Me-Mito modified with a chloromethyl anchoring group) would allow unequivocal long-term tracking in more complicated biological systems. Our multiplex tracking with high spatial-temporal control hence present promises to understand complex intra- and inter- cellular interactions.

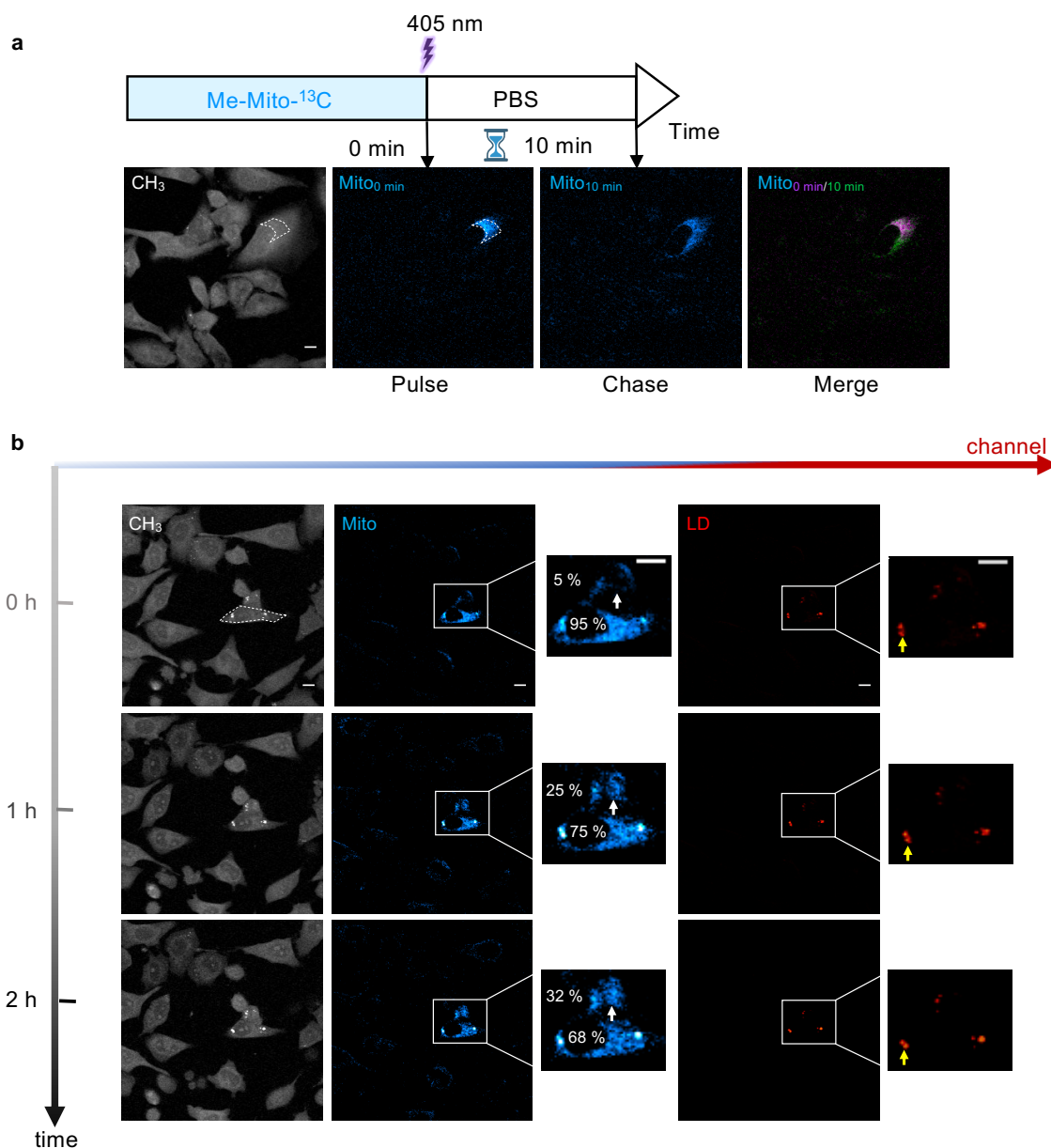


Figure 3.5. Subcellular and single-cell multiplex tracking with pulse-chase photoactivatable imaging. (a) Pulse-chase photoactivation and tracking for a selected subcellular region of a single cell (indicated by white dashed box) from Me-Mito- ^{13}C (16) labeled live HeLa cells. Pulse (Mito $_{0\text{ min}}$) shows SRS imaging at 2125 cm^{-1} immediately after 405 nm photoactivation, and chase (Mito $_{10\text{ min}}$) presents the distribution from the same field-of-view imaged after 10 minutes. The overlay of pulse (magenta) and chase (green) is shown in Merge (Mito $_{0\text{ min}}/10\text{ min}$). (b) Pulse-chase SRS images for the selectively activated single cell (CH $_3$, indicated by white dashed box) from live HeLa cells co-labeled

with Me-LD (**15**) and Me-Mito-¹³C (**16**). Two-color SRS images (2125 cm⁻¹ for mitochondria, Mito; 2205 cm⁻¹ for lipid droplets, LD) present the pulse (0 h) and chase (1 h, 2 h) distributions with the magnified images showing the selected cell together with its neighboring cell. The numbers in the magnified mitochondria images indicate the relative signal percentages of the top and the bottom cells. Scale bar: 10 μm.

3.7 Conclusion

Over the development of Raman microscopy through last decade, alkynes have arguably become one of the most important classes of Raman imaging probes. The role of alkyne moiety in vibrational microscopy may be analogous to that of GFP to fluorescence imaging. From a fundamental chemistry point view, chemically modifying alkynes and utilizing their rich spectroscopic functions would be highly appealing to push the next frontiers of Raman imaging. Indeed, numerous efforts have been devoted to engineering alkynes for multicolor imaging, for achieving higher sensitivity and for sensing applications⁴⁶. In our work, we established the first general design of photoactivatable alkyne-based Raman probes for live-cell multiplexed imaging and tracking.

We first identified the suitable cyclopropanone caging systems and then performed rational chemical modification of methylation to address the chemical stability issues of the selected scaffold. Next, we engineered the chemical probes with targeting groups and achieved live-cell imaging of multiple organelles including mitochondria, lysosomes, ER and lipid droplets. After further isotope editing and proper combination of the targeting groups with probe cores, we performed three-color photoactivatable imaging and showcased the potential of multiplex subcellular and inter-cellular pulse-chase tracking. Our probes showed superior quantitative imaging capabilities without the complications of photobleaching and the need of post-processing linear unmixing. It is worth pointing out the earlier development of cyclopropanones further substantiates their biocompatibility. They were previously isolated as natural products⁴⁷⁻⁴⁹. The 1-cyclo (**1**, diphenylcyclopropanone) was even approved by

FDA for topical immunotherapy medications (Docket No. FDA-2016-N-3464), underscoring the live-cell utility of the probes.

Further chemical derivatizations should be envisioned to improve the Raman signals after photoactivation, which is essential for imaging low abundance targets such as proteins. For example, the strategies of polymerization^{50,51} and nanoparticle assembly²³ could be explored to enhance the Raman signal of our photoactivatable probes for up to 10^5 fold²³. In addition, the incorporation of enhancing units such as azo groups to the aromatic rings may also enhance the uncaged Raman signals by increasing electron delocalization, and hence the molecular polarizability⁵². Meanwhile, extending the π conjugation would also induce red-shift in the absorption and make the visible-light or two photon activation³³ possible. However, it should be noted that this photoactivation should be decoupled from SRS lasers to prevent artifacts arising from signal read-out step. These new structures may also help expand multiplexity for imaging and tracking applications.

Building upon our current demonstrations, such light-activated multiplex tracking of single cells should ultimately find vast utility in versatile biological systems. For example, going beyond cellular research, this approach could be utilized in tracking the fate of selected and multiplex-profiled cells, or to elucidate the complex cell-to-cell interactions in the native microenvironment in tissues under both physiological and pathological condition^{13,43}.

In addition to engineering probes for higher signals, recent spectroscopy and instrumentation development for SRS, for example, the exciting report of squeezed light with detection sensitivity to below the shot-noise limited regime⁵³, are also narrowing the sensitivity gap toward single molecule level. We therefore envision that these photoactivatable Raman probes, together with previously demonstrated photo-switchable Raman probes, will lay the foundation toward localization-based super-resolution Raman imaging and open new imaging opportunities, just like what photoactivatable GFP has done for PALM microscopy⁸.

3.8 Methods and supplementary figures

General Synthesis Experimental Details

Reagents and solvents from commercial sources were used without further purification unless otherwise stated. All reactions were performed under a N₂ atmosphere unless specified otherwise. All reaction flasks were flame dried. Column chromatography was carried out using SiliaFlash irregular silica gel P60 (Silicycle, 40 - 63 μm, 60 Å). Thin layer chromatography (TLC) was carried out with Millipore silica gel F-254 plates, and plates were visualized using UV light or KMnO₄ stain. The UV handlamp is an Analytik Jena UVP EL Series Lamp (UVLS-24, 4 Watt, 2UV 254/365 nm).

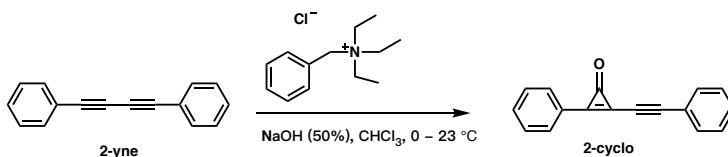
NMR spectra were recorded using a 400 MHz Bruker Avance III HD with Prodigy Cryoprobe or a 400 MHz Bruker Avance Neo. All ¹H NMR spectra are reported in δ units, parts per million (ppm), and were measured relative to the signals for CH₂Cl₂ (5.32 ppm) in deuterated solvent. All ¹³C NMR spectra were measured in deuterated solvents and are reported in ppm relative to the signals for ¹³CD₂Cl₂ (54.00 ppm). Multiplicity and qualifier abbreviations are as follows: s = singlet, d = doublet, t = triplet, q = quartet, m = multiplet, br = broad.

High resolution mass spectra (HRMS) were obtained from an LTQ linear ion trap mass spectrometer with liquid-chromatography (LC) system (Thermo) or LCT Premier XE electrospray TOF mass spectrometer with UPLC (Waters).

Preparative HPLC was performed on an Agilent 1100 Series semi-preparative HPLC apparatus using Eclipse XDB-C18 9.4 x 250 mm column with water (0.1% AcOH) and acetonitrile as mobile phases. UV-Vis absorption spectra were recorded on a Varian Cary 50 UV-Vis Spectrophotometer (Agilent). Analytical HPLC coupled with mass spectrometry (LC-MS) was performed on Agilent 1290 infinity LC system using ZORBAX RRHD Eclipse Plus C18, 95Å, 2.1 x 50 mm, 1.8 μm column with an Agilent 6140 Series Quadrupole

LCMS / LC-MS / MSD / Mass Spectrometer System. The mobile phase is water (0.1% AcOH) and acetonitrile with running method of gradient 5% - 95% acetonitrile (1 ml/min, 0 - 4 min). Mass spectrometry detection region ranges from 100 to 800 AMU.

2-phenyl-3-(phenylethynyl)cycloprop-2-en-1-one (2-cyclo, **3**)



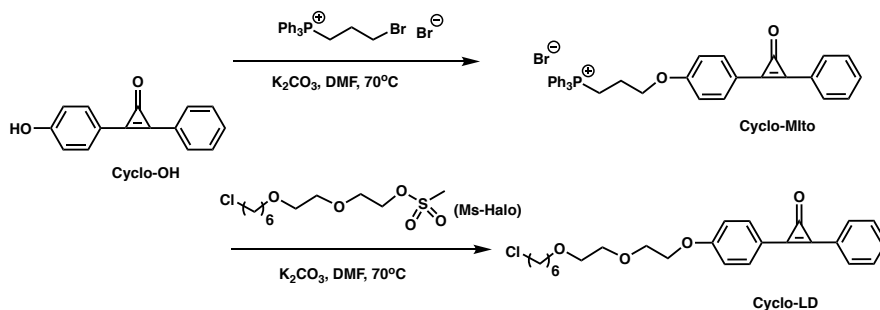
The synthesis procedure of 2-cyclo (**3**) was adapted from literature report¹. To a vigorously stirred mixture of 2-yne (**4**, 202 mg, 1 mmol) and benzyltriethylammonium chloride (114 mg, 0.5 mmol) in chloroform (8 mL), which had been cooled with an ice bath, was added 10 g of 50% aq. NaOH (w/w, 125 mmol) dropwise. Afterwards, the ice bath was removed and the solution was stirred for 40 minutes at 23 °C. The reaction was monitored by TLC (1:3, EtOAc : Hexane). The resulting mixture was then separated, and the aqueous layer extracted with DCM. The combined organic layers were washed with saturated NaHCO₃ and brine, dried over anhydrous Na₂SO₄, and evaporated. The crude product was purified by flash column chromatography with EtOAc : Hexane (1:5) as eluents. 2-cyclo (**4**) was isolated as yellow solid (74 mg, 0.32 mmol, 32%) and unreacted 2-yne (**3**) was also recovered (91 mg, 0.45 mmol, 45%).

¹H NMR (400 MHz, CD₂Cl₂) δ: 7.93 (m, 2H), 7.62 (m, 5H), 7.47 (m, 3H).

¹³C{¹H} NMR (100 MHz, CD₂Cl₂) δ 153.02, 151.18, 137.32, 133.90, 133.25, 131.53, 131.44, 129.89, 129.31, 124.30, 121.25, 108.77, 74.32.

HRMS (FAB⁺, m/z): calcd. for [C₁₇H₁₁O]⁺ (M+H)⁺, 231.0810; found, 231.0838.

(3-(4-(3-oxo-2-phenylcycloprop-1-en-1-yl)phenoxy)propyl)triphenylphosphonium bromide (Cyclo-Mito, **7**) and 2-(4-(2-(2-((6-chlorohexyl)oxy)ethoxy)ethoxy)phenoxy)-3-phenylcycloprop-2-en-1-one (Cyclo-LD, **17**)



Cyclo-OH and Ms-Halo were produced according to literature^{2,3}.

Cyclo-OH (22 mg, 0.1 mmol), K₂CO₃ (28 mg, 0.2 mmol) and (3-Bromopropyl)triphenylphosphonium bromide (139 mg, 0.3 mmol) or Ms-Halo (45 mg, 0.15 mmol) were stirred in 3 ml DMF at 70 °C for 1 hour. Then the reaction solution was filtered and quenched with saturated NH₄Cl solution. The solution was extracted by EtOAc and concentrated. The crude products were dissolved in acetonitrile and subjected to reverse phase prep-HPLC for separation to obtain Cyclo-Mito (**7**, 36 mg, 0.059 mmol, 59%) and Cyclo-LD (**17**, 29 mg, 0.068 mmol, 68%) as pale white solids. The products would decompose to Cyclo-OH on silica gel.

Cyclo-Mito (**7**). ¹H NMR (400 MHz, CD₂Cl₂) δ 7.95 – 7.78 (m, 13H), 7.70 (td, J = 8.0, 3.4 Hz, 6H), 7.57 (ddt, J = 5.7, 4.0, 2.3 Hz, 3H), 7.15 – 7.05 (m, 2H), 4.42 (t, J = 5.8 Hz, 2H), 4.08 – 3.87 (m, 2H), 2.20 (m, 2H)

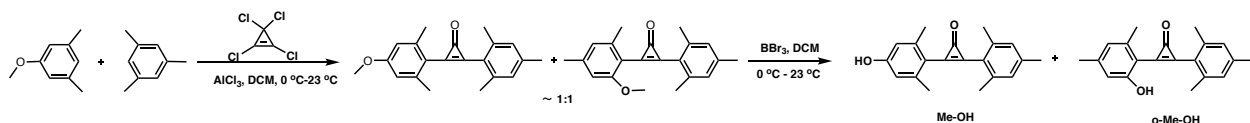
HRMS (ESI, m/z): calcd. for [C₃₆H₃₀O₂P]⁺ (M⁺), 525.1978; found, 525.1960.

Cyclo-LD (**17**). ^1H NMR (400 MHz, CD_2Cl_2) δ 8.01 – 7.90 (m, 4H), 7.59 (dp, $J = 6.2$, 2.0 Hz, 3H), 7.17 – 7.05 (m, 2H), 4.29 – 4.17 (m, 2H), 3.89 – 3.82 (m, 2H), 3.70 – 3.64 (m, 2H), 3.61 – 3.49 (m, 4H), 3.44 (t, $J = 6.6$ Hz, 2H), 1.86 – 1.71 (m, 2H), 1.62 – 1.51 (m, 2H), 1.50 – 1.29 (m, 4H).

$^{13}\text{C}\{^1\text{H}\}$ NMR (100 MHz, CD_2Cl_2) δ 162.78, 155.47, 148.26, 145.02, 134.14, 132.55, 131.52, 129.70, 124.82, 117.43, 115.68, 71.54, 71.28, 70.52, 69.77, 68.35, 45.64, 33.00, 29.94, 27.09, 25.84.

HRMS (ESI, m/z): calcd. for $[\text{C}_{25}\text{H}_{30}\text{O}_4\text{Cl}]^+$ ($\text{M}+\text{H}$) $^+$, 429.1833; found, 429.1845.

2-(4-hydroxy-2,6-dimethylphenyl)-3-mesitylcycloprop-2-en-1-one (Me-1-cyclo-OH or Me-OH or **8**)



Me-OH (**8**) was produced following procedures modified from a previous report². In a flask, AlCl_3 (1.49 g, 11.2 mmol) was charged to 10 ml dry DCM . The flask was then cooled to $0\text{ }^\circ\text{C}$. To the stirring suspension, tetrachlorocyclopropene (500 mg, 2.8 mmol) was added dropwise. The resulting suspension was allowed to stir at $0\text{ }^\circ\text{C}$ for 10 minutes. Then mesitylene (336 mg, 2.8 mmol) was added and this solution was stirred at $0\text{ }^\circ\text{C}$ for 90 minutes. To this stirring suspension, 3,5-Dimethylanisole (381 mg, 2.8 mmol) was added. Then the solution was allowed to warm to $23\text{ }^\circ\text{C}$ and reacted for 1 hour. This reaction was monitored by TLC (1:3, $\text{EtOAc} : \text{Hexane}$). After reaction, at $0\text{ }^\circ\text{C}$ the suspension was quenched slowly with saturated NH_4Cl solution, extracted with DCM , washed with brine and dried over anhydrous Na_2SO_4 . The organic phase was concentrated, and subjected to column chromatography with $\text{EtOAc} : \text{Hexane}$ (1:5) as eluents. The obtained cyclopropenone products (703 mg, 2.3 mmol, 82%) were a mixture of ortho- and para-

substituted isomers (~ 1:1, identified by LC-MS). The two isomers were very close on TLC and column and hard to be separated. The isomers were separated at later step.

The obtained cyclopropenone isomers (306 mg, 1 mmol) were dissolved in 5 ml dry DCM in a flask. The flask was then cooled to 0 °C. To the stirring suspension, 1M BBr₃ in DCM (2.5 ml, 2.5 mmol) was added dropwise. The stirred solution was kept at 0 °C for 1 hour, then allowed to warm to 23 °C and reacted overnight. After reaction, at 0 °C the suspension was quenched slowly with saturated NH₄Cl solution, extracted with DCM, washed with brine and dried over anhydrous Na₂SO₄. The organic phase was concentrated, and subjected to column chromatography with EtOAc : Hexane (1:2) as eluents to obtain Me-OH (7, 132 mg, 0.45 mmol) and o-Me-OH (120 mg, 0.41 mmol) as pale white solids. Note that these two isomers should be carefully separated on a long column, and these solid cyclopropenones have pleasant fragrance similar to that of banana shrub flowers.

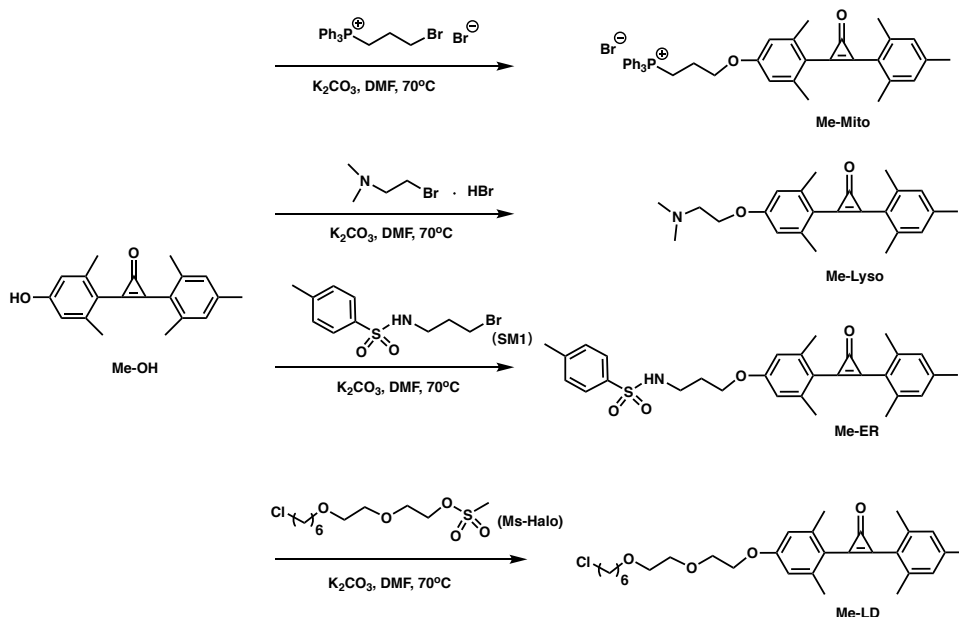
Me-OH (**8**): ¹H NMR (400 MHz, CD₂Cl₂ with CD₃OD as co-solvent) δ 6.90 (d, J = 1.1 Hz, 2H), 6.53 (s, 2H), 4.31 (br, 1H), 2.25-2.22 (s, 3H), 2.21-2.18 (s, 6H), 2.18-2.15 (s, 6H).

¹³C{¹H} NMR (100 MHz, CD₂Cl₂ with CD₃OD as co-solvent) δ 162.10, 160.00, 151.88, 148.49, 143.89, 142.59, 139.48, 129.32, 124.48, 117.37, 115.82, 21.30, 20.91, 20.50.

HRMS (ESI, m/z): calcd. for [C₂₀H₂₁O₂]⁺ (M+H)⁺, 293.1537; found, 293.1539.

o-Me-OH: ¹H NMR (400 MHz, DMSO-d₆) δ 10.27 (br, 1H), 6.99 (s, 2H), 6.67 (s, 1H), 6.62 (s, 1H), 2.44 (s, 3H), 2.33 – 2.23 (m, 12H).

HRMS (ESI, m/z): calcd. for [C₃₆H₃₀O₂P]⁺ (M⁺), 293.1537; found, 293.1537.



(3-(4-(2-mesityl-3-oxocycloprop-1-en-1-yl)-3,5-dimethylphenoxy)propyl)triphenylphosphonium bromide (Me-Mito, **12**)

Me-OH (**8**, 29 mg, 0.1 mmol), K₂CO₃ (28 mg, 0.2 mmol) and (3-Bromopropyl)triphenylphosphonium bromide (139 mg, 0.3 mmol) were stirred in 3 ml DMF at 70 °C for 1 hour. Then the reaction solution was filtered and quenched with saturated NH₄Cl solution. The solution was extracted by EtOAc and concentrated. The crude product was subjected to column chromatography with (MeOH + AcOH) in DCM (10% + 2.5%) as eluents to obtain Me-Mito (**12**, 44 mg, 0.065 mmol, 65%) as pale white solid.

¹H NMR (400 MHz, CD₂Cl₂) δ 7.89 – 7.79 (m, 9H), 7.75 – 7.68 (m, 6H), 6.98 (s, 2H), 6.70 (s, 2H), 4.39 – 4.31 (m, 2H), 3.95 (m, 2H), 2.38 - 2.25 (m, 15H), 2.22 – 2.15 (m, 2H).

¹³C{¹H} NMR (100 MHz, CD₂Cl₂) δ 161.20, 158.11, 151.85, 150.56, 142.77, 142.05, 139.44, 135.71, 134.33, 134.23, 131.06, 130.94, 129.12, 124.59, 119.91, 119.04, 118.18, 114.44, 67.26, 67.09, 23.27, 21.67, 21.26, 20.83, 20.65, 20.12.

HRMS (ESI, m/z): calcd. for $[C_{41}H_{40}O_2P]^+$ (M^+), 595.2761; found, 595.2755.

2-(4-(2-(dimethylamino)ethoxy)-2,6-dimethylphenyl)-3-mesitylcycloprop-2-en-1-one (Me-Lyso, **13**)

Me-OH (**8**, 29 mg, 0.1 mmol), K_2CO_3 (41 mg, 0.3 mmol) and 2-bromo-N,N-dimethylethanamine hydrobromide (46 mg, 0.2 mmol) were stirred in 3 ml DMF at 70 °C for 1 hour. Then the reaction solution was filtered and quenched with saturated NH_4Cl solution. The solution was extracted by EtOAc and concentrated. The crude product was subjected to column chromatography with 7% MeOH in DCM as eluents to obtain Me-Lyso (**13**, 28 mg, 0.076 mmol, 76%) as pale white solid.

1H NMR (400 MHz, CD_2Cl_2) δ 6.98 (s, 2H), 6.70 (s, 2H), 4.11 (t, J = 5.7 Hz, 2H), 2.75 (t, J = 5.7 Hz, 2H), 2.36 – 2.31 (m, 15H), 2.28 (s, 6H).

$^{13}C\{^1H\}$ NMR (100 MHz, CD_2Cl_2) δ 161.84, 158.08, 152.04, 150.29, 142.82, 141.91, 139.36, 129.10, 124.77, 119.51, 114.39, 66.57, 58.53, 46.04, 21.67, 21.31, 20.83.

HRMS (ESI, m/z): calcd. for $[C_{24}H_{29}NO_2]^+$ ($M+H$) $^+$, 364.2272; found, 364.2279.

N-(3-(4-(2-mesityl-3-oxocycloprop-1-en-1-yl)-3,5-dimethylphenoxy)propyl)-4-methylbenzenesulfonamide (Me-ER, **14**)

SM1 was produced according to literature⁴.

Me-OH (**8**, 29 mg, 0.1 mmol), K₂CO₃ (28 mg, 0.2 mmol) and SM1 (88 mg, 0.3 mmol) were stirred in 3 ml DMF at 70 °C for 1 hour. Then the reaction solution was filtered and quenched with saturated NH₄Cl solution. The solution was extracted by EtOAc and concentrated. The crude product was subjected to column chromatography with EtOAc : Hexane (1:1.5) as eluents to obtain Me-ER (**14**, 32 mg, 0.064 mmol, 64%) as pale white solid.

¹H NMR (400 MHz, CD₂Cl₂) δ 7.72 (d, J = 8.2 Hz, 2H), 7.29 (d, J = 8.2 Hz, 2H), 6.98 (s, 2H), 6.63 (s, 2H), 4.94 (t, J = 6.2 Hz, 1H), 4.00 (t, J = 5.6 Hz, 2H), 3.20 – 3.06 (m, 2H), 2.40 (s, 3H), 2.37 – 2.30 (m, 9H), 2.28 (s, 6H), 1.94 (p, J = 6.2 Hz, 2H).

¹³C{¹H} NMR (100 MHz, CD₂Cl₂) δ 161.62, 158.12, 151.92, 150.39, 144.15, 142.78, 141.99, 139.38, 137.48, 130.24, 129.12, 127.53, 124.68, 119.63, 114.33, 65.97, 41.16, 29.64, 21.79, 21.67, 21.29, 20.84.

HRMS (ESI, m/z): calcd. for [C₃₀H₃₄NO₄S]⁺ (M+H)⁺, 504.2204; found, 504.2207.

2-(4-(2-(2-((6-chlorohexyl)oxy)ethoxy)ethoxy)-2,6-dimethylphenyl)-3-mesitylcycloprop-2-en-1-one (Me-LD, **15**)

Me-OH (**8**, 29 mg, 0.1 mmol), K₂CO₃ (41 mg, 0.3 mmol) and Ms-Halo (60 mg, 0.2 mmol) were stirred in 3 ml DMF at 70 °C for 4 hours. Then the reaction solution was filtered and quenched with saturated NH₄Cl solution. The solution was extracted by EtOAc and concentrated. The crude product was subjected to column chromatography with EtOAc : Hexane (1:2) as eluents to obtain Me-LD (**15**, 35 mg, 0.070 mmol, 70%).

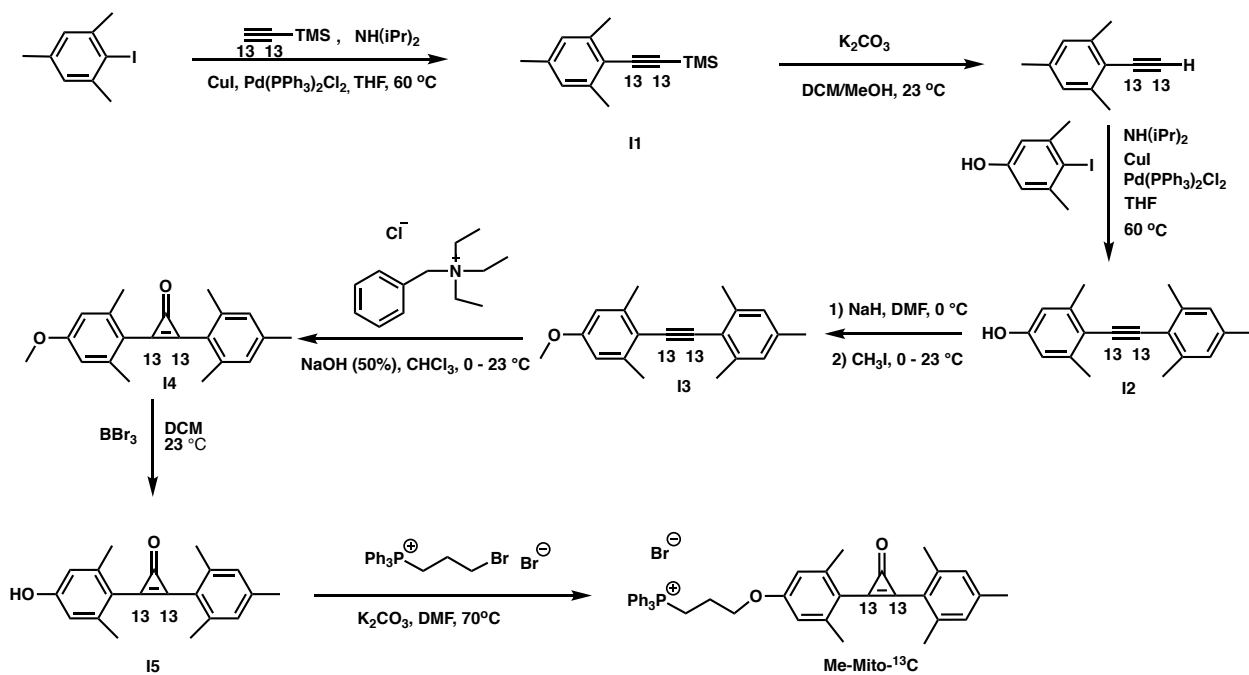
¹H NMR (400 MHz, CD₂Cl₂) δ 6.97 (s, 2H), 6.71 (s, 2H), 4.19 – 4.11 (m, 2H), 3.87 – 3.78 (m, 2H), 3.68 – 3.63 (m, 2H), 3.59 – 3.50 (m, 4H), 3.44 (t, J = 6.6 Hz, 2H), 2.33 (d, J = 2.0

Hz, 9H), 2.28 (s, 6H), 1.76 (dq, $J = 8.1, 6.7$ Hz, 2H), 1.60 – 1.53 (m, 2H), 1.48 – 1.35 (m, 4H).

$^{13}\text{C}\{^1\text{H}\}$ NMR (100 MHz, CD_2Cl_2) δ 161.83, 158.09, 152.01, 150.36, 142.80, 141.93, 139.38, 129.10, 124.74, 119.61, 114.42, 71.70, 71.39, 70.69, 70.03, 68.11, 45.80, 33.17, 30.10, 27.26, 26.00, 21.67, 21.31, 20.83.

HRMS (ESI, m/z): calcd. for $[\text{C}_{30}\text{H}_{40}\text{ClO}_4]^+$ ($\text{M}+\text{H}$) $^+$, 499.2610; found, 499.2620.

(3-(4-(2-mesityl-3-oxocycloprop-1-en-1-yl-1,2- $^{13}\text{C}_2$)-3,5-dimethylphenoxy)propyl)triphenylphosphonium bromide (Me-Mito- ^{13}C , **16**)



2-Iodo-1,3,5-trimethylbenzene (246 mg, 1 mmol), (trimethylsilyl)acetylene- $^{13}\text{C}_2$ (Sigma 603511, 100 mg, 1 mmol), copper(I) iodide (10 mg, 0.05 mmol),

bis(triphenylphosphine)palladium(II) dichloride (35 mg, 0.05 mmol) were dissolved in THF (5 ml). The mixture was degassed and filled with nitrogen. Then diisopropylamine (202 mg, 2 mmol) was added and the black suspension was heated to 60 °C and stirred for 2 hours. After the reaction was finished, the reaction solution was filtered and quenched with 1 M HCl. Then the solution was extracted by EtOAc and hexane. The organic phase was washed with brine, dried over anhydrous Na₂SO₄ and subjected to column chromatography with pure hexane as eluent to obtain **II** (157 mg, 0.72 mmol, 72%) as yellow oil.

II. ¹H NMR (400 MHz, CD₂Cl₂) δ 6.87 (s, 2H), 2.39 (s, 6H), 2.28 (s, 3H), 0.28 (dd, J = 2.3, 0.7 Hz, 9H).

¹³C {¹H} NMR (100 MHz, CD₂Cl₂) δ 141.01, 128.03, 104.46, 103.13, 102.72, 101.38, 21.65, 21.21, 0.48.

To a solution of **II** (109 mg, 0.5 mmol) in DCM-MeOH (1:1, 4 mL) was added K₂CO₃ (276 mg, 2 mmol). After the mixture was stirred at 23 °C for 2 hours, H₂O was added and the mixture was extracted with EtOAc. The organic phase was washed with brine, dried over anhydrous Na₂SO₄ to obtain the product without further purification.

The whole products obtained in the last step, 4-Iodo-2,6-dimethylphenol (124mg, 0.5 mmol), copper(I) iodide (5 mg, 0.026 mmol), bis(triphenylphosphine)palladium(II) dichloride (18 mg, 0.025 mmol) were dissolved in THF (3 ml). The mixture was degassed and filled with nitrogen. Then diisopropylamine (101 mg, 1 mmol) was added and the black suspension was heated to 60 °C and stirred for 2 hours. After the reaction was finished, the reaction solution was filtered and quenched with 1 M HCl. Then the solution was extracted by EtOAc and hexane. The organic phase was washed with brine, dried over anhydrous Na₂SO₄ and subjected to column chromatography with EtOAc : hexane (1:2) as eluent to obtain **I2** (98 mg, 0.37 mmol, 74%, over two steps) as white solids.

^1H NMR (400 MHz, CD_2Cl_2) δ 7.45 – 7.35 (m, 1H), 6.92 (s, 2H), 6.59 (s, 2H), 2.48 (d, J = 3.6 Hz, 12H), 2.29 (s, 3H).

$^{13}\text{C}\{^1\text{H}\}$ NMR (100 MHz, CD_2Cl_2) δ 155.87, 142.56, 140.16, 137.91, 128.16, 114.47, 97.07, 95.30, 95.17, 93.40, 21.99, 21.84, 21.58.

I2 (98 mg, 0.37 mmol) was dissolved in DMF (2 ml) and cooled to 0 °C. NaH (12 mg, 0.5 mmol) was added to the stirred solution. Stirring was maintained for 30 minutes at 0 °C. Then the mixture was added iodomethane (105 mg, 0.74 mmol, dissolved in 1 ml DMF) and allowed to warm up to 23 °C and stirred for 2 hours. Then the mixture was poured over water and extracted with EtOAc. The organic phase was washed with brine, dried over anhydrous Na_2SO_4 to obtain the product **I3** without further purification.

All the product **I3** obtained in the last step was dissolved in chloroform (4 mL) and added with benzyltriethylammonium chloride (68 mg, 0.3 mmol). Then the mixture was cooled with an ice bath, and was added 3 g of 50% NaOH (37.5 mmol) dropwise. After adding NaOH, ice bath was removed and let the solution be stirred for 1 hour at 23 °C. The reaction was monitored by TLC (1:3, EtOAc : Hexane). The resulting mixture was then separated, and the aqueous layer extracted with DCM. The combined organic layers were washed with saturated NaHCO_3 and brine, dried over anhydrous Na_2SO_4 , and evaporated. The crude product was purified by flash column chromatography with EtOAc : Hexane (1:5) as eluents to obtain the product **I4** (65 mg, 0.21 mmol, 57 %, over two steps) as white solid.

I4. ^1H NMR (400 MHz, CD_2Cl_2) δ 6.98 (s, 2H), 6.70 (s, 2H), 3.83 (s, 3H), 2.34 (s, 9H), 2.28 (s, 6H).

^{13}C NMR (100 MHz, CD_2Cl_2) δ 152.16, 151.95, 150.35, 150.13 (The highest four peaks).

The obtained **I4** (65 mg, 0.21 mmol) were dissolved in 2 ml dry DCM in a flask. The flask was then cooled to 0 °C. To the stirring suspension, 1M BBr_3 in DCM (0.5 ml, 0.5 mmol) was added dropwise. The stirred solution was kept at 0 °C for 1 hour, then allowed to warm to 23 °C and reacted overnight. After reaction, at 0 °C the suspension was quenched slowly with saturated NH_4Cl solution, extracted with DCM, washed with brine and dried over anhydrous Na_2SO_4 . The obtained product **I5** was used without further purification.

The product **I5**, K_2CO_3 (56 mg, 0.4 mmol) and (3-Bromopropyl)triphenylphosphonium bromide (279 mg, 0.6 mmol) were stirred in 5 ml DMF at 70 °C for 1 hour. Then the reaction solution was filtered and quenched with saturated NH_4Cl solution. The solution was extracted by EtOAc and concentrated. The crude product was subjected to column chromatography with (MeOH + AcOH) in DCM (10% + 2.5%) as eluents to obtain Me-Mito- ^{13}C (**16**, 75 mg, 0.11 mmol, 52% over two steps) as pale white solid.

^1H NMR (400 MHz, CD_2Cl_2) δ 7.90 – 7.76 (m, 9H), 7.75 – 7.65 (m, 6H), 6.96 (s, 2H), 6.69 (s, 2H), 4.32 (t, $J = 5.9$ Hz, 2H), 4.10 – 3.84 (m, 2H), 2.38 – 2.22 (m, 15H), 2.22 – 2.14 (m, 2H).

^{13}C NMR (100 MHz, CD_2Cl_2) δ 161.25, 151.98, 151.76, 150.57, 150.35, 142.76, 142.00, 139.36, 135.64, 134.33, 134.23, 131.01, 130.88, 129.08, 119.17, 118.31, 114.47, 67.32, 67.15, 23.29, 21.64, 21.22, 20.82, 20.36, 19.84.

HRMS (ESI, m/z): calcd. for $[\text{C}_{39}^{13}\text{C}_2\text{H}_{40}\text{O}_2\text{P}]^+$ (M^+), 597.2828; found, 597.2838.

Stimulated Raman scattering and fluorescence microscopy.

An integrated laser (picoEMERALD, Applied Physics and Electronics, Inc.) was used as a light source for both pump and Stokes beams. It produces 2 ps pump (tunable from 770 nm – 990 nm, bandwidth 0.5 nm, spectral bandwidth $\sim 7 \text{ cm}^{-1}$) and Stokes (1031.2 nm, spectral bandwidth 10 cm^{-1}) beams with 80MHz repetition rate. Stokes beam is modulated at 20 MHz by an internal electro-optic modulator. The spatially and temporally overlapped pump and Stokes beams are introduced into an inverted multiphoton laser scanning microscopy (FV3000, Olympus), and then focused onto the sample by a 25X water objective (XLPLN25XWMP, 1.05 N.A., Olympus). Transmitted pump and Stokes beams are collected by a high N.A. condenser lens (oil immersion, 1.4 N.A., Olympus) and pass through a bandpass filter (893/209 BrightLine, 25 mm, AVR Optics) to filter out Stokes beam. A large area ($10 \times 10 \text{ mm}$) Si photodiode (S3590-09, Hamamatsu) is used to measure the remaining pump beam intensity. 64 V DC voltage was used on the photodiode to increase saturation threshold and reduce response time. The output current is terminated by a 50Ω terminator and pre-filtered by an 19.2-23.6-MHz band-pass filter (BBP-21.4+, Mini-Circuits) to reduce laser and scanning noise. The signal is then demodulated by a lock-in amplifier (SR844, Stanford Research Systems) at the modulation frequency. The in-phase X output is fed back to the Olympus IO interface box (FV30-ANALOG) of the microscope. Image acquisition speed is limited by 30 μs time constant set for the lock-in amplifier. Correspondingly, we use 80 μs pixel dwell time, which gives a speed of 8.5 s frame⁻¹ for a 320-by-320-pixel field of view. Laser powers are monitored through image acquisition by an internal power meter and power fluctuation are controlled within 5% by the laser system. 16-bit grey scale images are acquired by Fluoview software. SRS spectra were acquired by fixing the Stokes beam at 1031.2 nm and scanning the pump beam through the designated wavelength range point by point. 10 mM EdU (H₂O) sample was used as a standard to give RIE of different probes. Fluorescence images were collected using the same Olympus FV3000 confocal microscope with CW laser excitation (405, 488, 561 and 640 nm, Coherent OBIS LX laser) and standard bandpass filter sets. The correlation coefficients (Pearson's R value) between SRS images and fluorescence images were calculated using 'Coloc 2' tool of ImageJ.

Spontaneous Raman spectroscopy.

Spontaneous Raman spectra were acquired using an upright confocal Raman spectrometer (Horiba Raman microscope; Xplora plus). A 532 nm YAG laser is used to illuminate the sample with a power of 12 mW on sample through a 100 x, N.A. 0.9 objective (MPLAN N; Olympus) with 100 μm slit and 500 μm hole. Spectro/Raman shift center was set to be 2000.04 cm^{-1} . With a 1200 grating, Raman shift ranges from 690.81 cm^{-1} to 3141.49 cm^{-1} was acquired to cover whole biological relevant Raman peaks. The acquired spectra were processed by the LabSpec 6 software for baseline correction.

365 nm UV irradiation.

The 365 nm UV light used to activate cyclopropenones comes from a UV handlamp (Analytik Jena UVP EL Series Lamp, UVLS-24, 4 Watt, 2UV 254/365 nm, typically used for TLC monitoring in organic synthesis). The power of 365 nm UV of this handlamp was measured to be 15 mW/cm^2 on samples.

UV-Vis absorption spectra.

UV-Vis absorption spectra were recorded on a Varian Cary 50 UV-Vis Spectrophotometer (Agilent).

(HP)LC-MS for assessing the stability of cyclopropenone probes in physiological condition.

The assessed probe was first dissolved in DMSO and later diluted in 10 mM cysteine (Sigma, 168149, dissolved in PBS) solution or DMEM (Corning, 35-015-CV) medium. Analytical HPLC coupled with mass spectrometry (LC-MS) was performed on Agilent 1290 infinity LC system using ZORBAX RRHD Eclipse Plus C18, 95Å, 2.1 x 50 mm, 1.8 μm column

with Agilent 6140 Series Quadrupole LCMS / LC-MS / MSD / Mass Spectrometer System. The mobile phase is water (0.1% AcOH) and acetonitrile with running method of gradient 5% - 95% acetonitrile (1 ml/min, 4 min for total running time). The mass spectrometry detection region ranges from 100 to 800 AMU. The data shown in the main figures and supplementary figures are the absorption (280.8 nm) intensity traces.

Cell culture.

HeLa cells (ATCC) were cultured in DMEM (Corning, 10-013-CV), supplemented with 10% fetal bovine serum (Corning, 35-015-CV), and 1% penicillin-streptomycin (Sigma-Aldrich). Cultures were incubated in a water-saturated incubator at 37°C with 5% CO₂. Cells were passaged every 3-5 days once confluence reached 80 %. Cultured HeLa cells were seeded onto 14 mm glass-bottom microwell dishes (MatTek Corporation) and grew to 80-90 % confluence before labeling.

Live/dead cell viability assay.

This assay was performed using the LIVE/DEAD viability/cytotoxicity kit for mammalian cells (Molecular Probes L-3224). HeLa cell standards and HeLa cells with dye staining were incubated with 2 μM calcein AM and 4 μM ethidium homodimer-1 (EthD-1) working solution for 20 min at 37 °C before imaging.

Live-cell photo-uncaging organelle imaging.

Mitochondria imaging:

Cells were incubated in 16 μ M Me-Mito (**12**) or Me-Mito- ^{13}C (**16**) with complete DMEM medium for 40 minutes in the incubator. Cells were washed with PBS three times before imaging. For colocalization, 80 nM MitoTracker™ Deep Red (Invitrogen, M22426) was used to stain cells for 25 minutes. For photo-uncaging, 405 nm laser (OBIS LX 405 nm 50 mW Laser, the same 405 nm laser used below) was used to scan the selected field of view for 2 minutes (1.6 mW on samples).

Lysosomes imaging.

Cells were incubated in 30 μ M Me-Lyso (**13**) with complete DMEM medium for 2 hours in the incubator. Cells were washed with PBS three times before imaging. For colocalization, 0.4 x LysoView™ 488 (Biotium, #70067) was used to stain cells for 30 minutes. For photo-uncaging, 405 nm laser was used to scan the selected field of view for 2 minutes (1.6 mW).

ER imaging.

Cells were incubated in 40 μ M Me-ER (**14**) with complete DMEM medium for 2 hours in the incubator. Cells were washed with PBS three times before imaging. For colocalization, 0.5 μ M ER-Tracker™ Red (Invitrogen, E34250) was used to stain cells for 1 hour. For photo-uncaging, 405 nm laser was used to scan the selected field of view for 2 minutes (1.6 mW).

Lipid droplets imaging by Me-LD (15).

Cells were incubated in 20 μ M Me-LD (**15**) with complete DMEM medium for 30 minutes in the incubator. Cells were washed with PBS three times before imaging. For colocalization, 0.5 x LipidSpot™ 610 (Biotium, #70069) was used to stain cells for 20 minutes. For photo-uncaging, 405 nm laser was used to scan the selected field of view for 2 minutes (1.6 mW).

Lipid droplets imaging by Cyclo-LD (17).

Cells were washed with PBS for three times before labeling. Cells were then incubated in 20 μ M Cyclo-LD (17) with PBS for 30 minutes in the incubator. Cells were washed with PBS three times before imaging. For colocalization, 0.5 x LipidSpot™ 610 (Biotium, #70069) was used to stain cells for 20 minutes. For photo-uncaging, 405 nm laser (1.6 mW) was used to scan the selected field of view for 2 minutes.

Two-color tracking with Me-LD (15) and Me-Mito-¹³C (16).

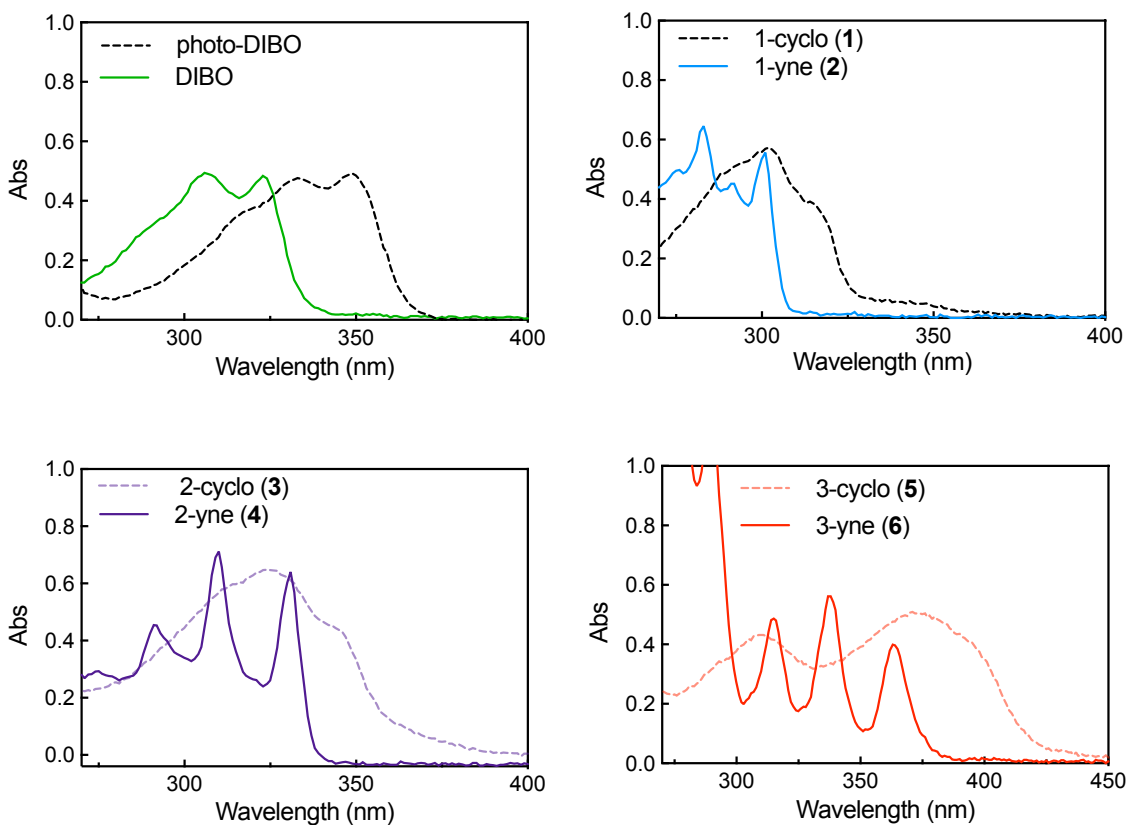
Cells were incubated in 10 μ M Me-LD (15) and 20 μ M Me-Mito-¹³C (16) with complete DMEM medium for 30 minutes in the incubator. Cells were washed with PBS three times before imaging. For selective uncaging, 405 nm laser was used to scan the selected field of view for 15 seconds (0.8 mW).

Three-color targeted photo-uncaging imaging with Cyclo-LD (17), Me-Lyso (13) and Me-Mito-¹³C (16).

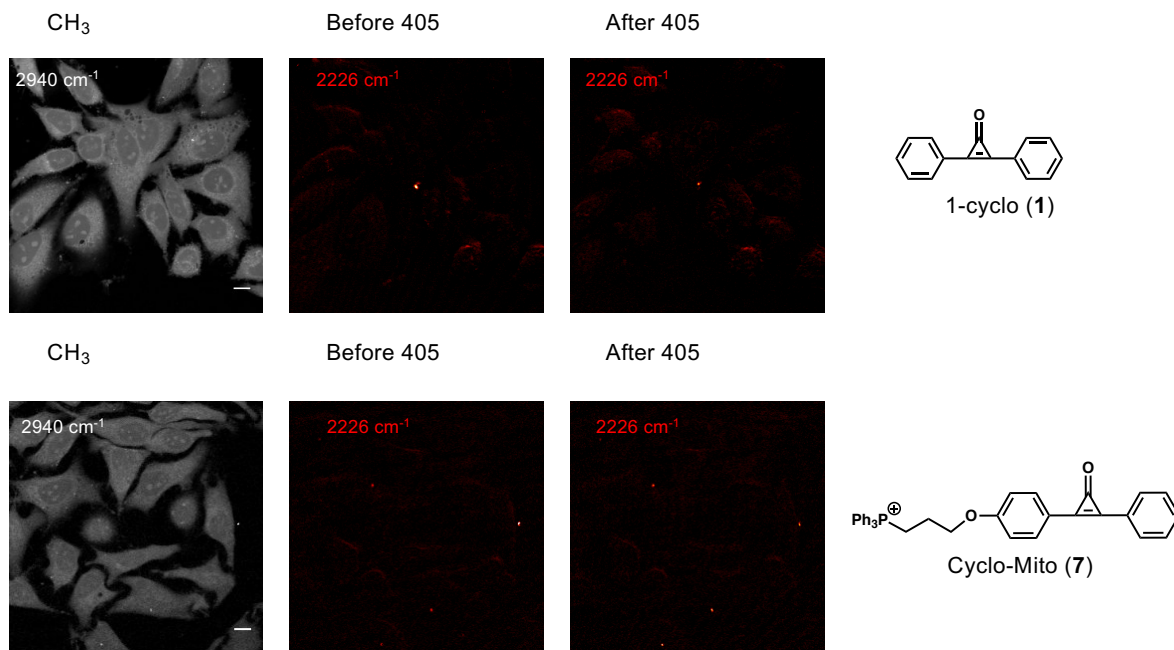
Cells were incubated in 40 μ M Me-Lyso (13) with complete DMEM medium for 4 hours and 20 μ M Me-Mito-¹³C (16) with complete DMEM medium for 30 minutes in the incubator. Cells were washed with PBS three times. Cells were then incubated in 15 μ M Cyclo-LD (17) with PBS for 15 minutes at room temperature. Cells were washed with PBS three times before imaging. For photo-uncaging, 405 nm laser was used to scan the selected field of view for 2 minutes (1.6 mW).

Quantification of SRS laser uncaging.

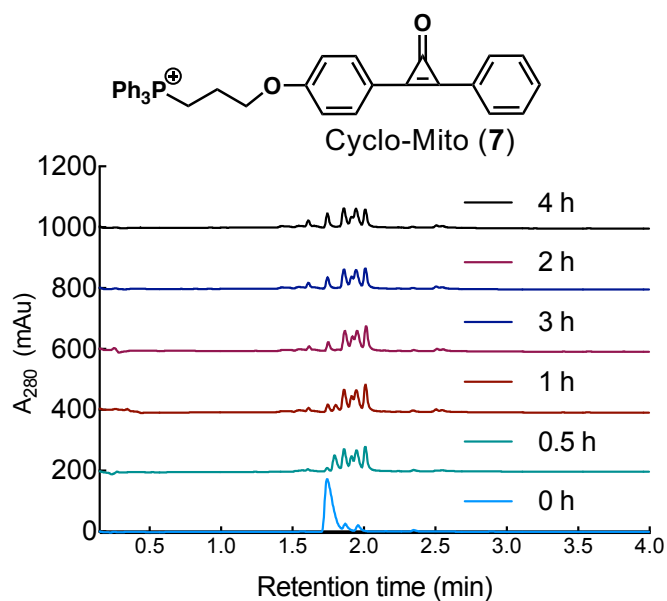
Cells were incubated in 20 μM Me-Mito (**12**) with complete DMEM medium for 30 minutes in the incubator. Cells were washed with PBS three times before imaging. After taking one image at CH_3 channel (2940 cm^{-1}) at low powers (10 mW OPO and 10 mW Stokes, $80\text{ }\mu\text{s}/\text{pixel}$), 10 frames of images at 2205 cm^{-1} were taken at various OPO and Stokes powers sequentially, followed by 405 nm illumination. The image acquired after 405 nm irradiation was assigned as 100% signal frame. The signal of each frame in the 10 images set was divided by the signal of 405 nm irradiated frame (100% signal frame) to obtain its percentage. Our criterion for the powers used were to let the intensity gain of each frame be less than 1.5 %, so we chose 25 mW OPO and 60 mW Stokes for imaging.



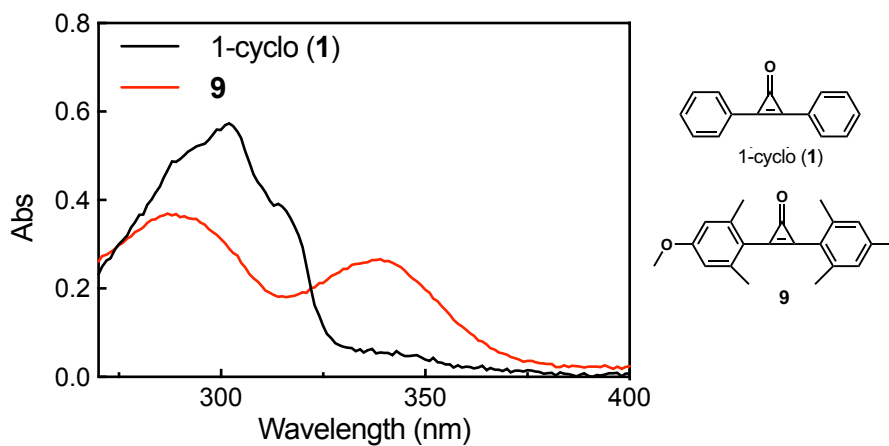
Supplementary Figure 3.1. UV-Vis absorption spectra of 20 μM photo-DIBO, 1-cyclo (1), 2-cyclo (3) and 3-cyclo (5) and their corresponding alkyne products, shown in Fig. 3.1A, in DMSO.



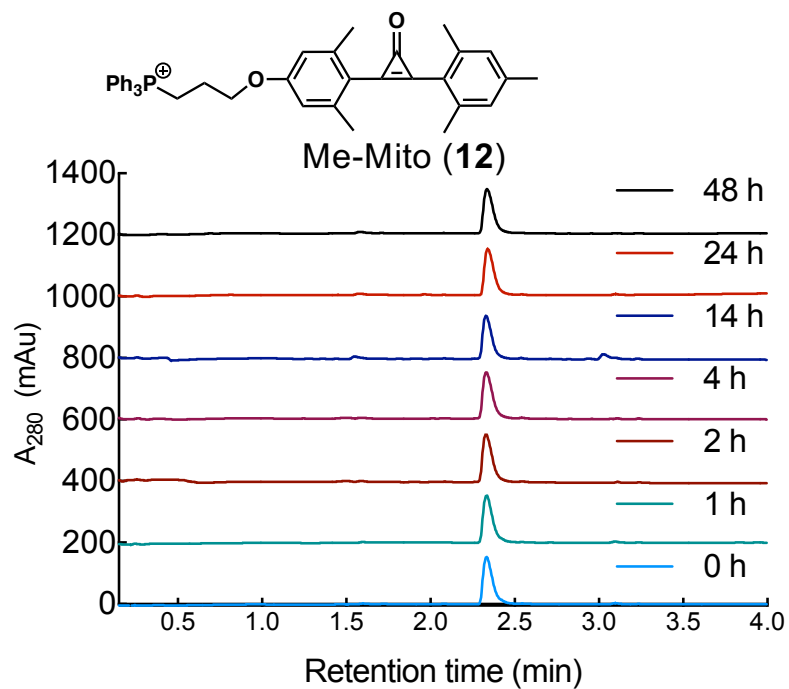
Supplementary Figure 3.2. SRS imaging of live HeLa cells incubated with 1-cyclo (1, 20 μM , 30 minutes of labeling, top) and Cyclo-Mito (7, 20 μM , 30 minutes of labeling, bottom) at the CH_3 (2940 cm^{-1}) channel, and the expected uncaged alkyne channel (2226 cm^{-1}) before and after 405 nm illumination. Scale bar: 10 μm .



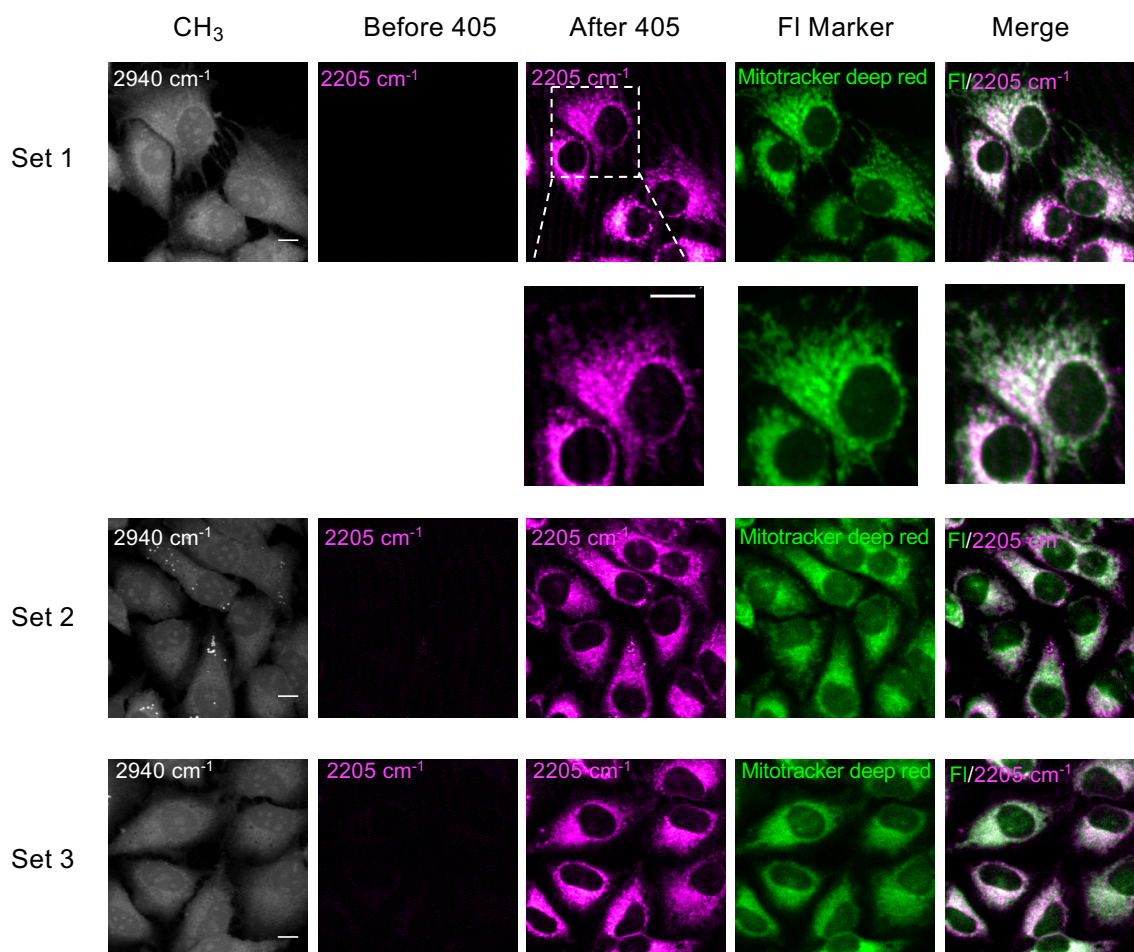
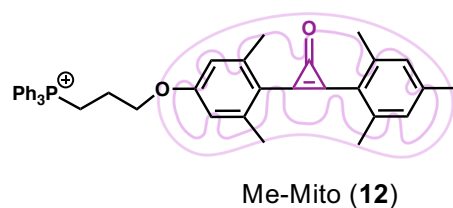
Supplementary Figure 3.3. HPLC trace of Cyclo-Mito (7) after incubating in 10 mM cysteine (PBS) for designated duration at 37 °C.



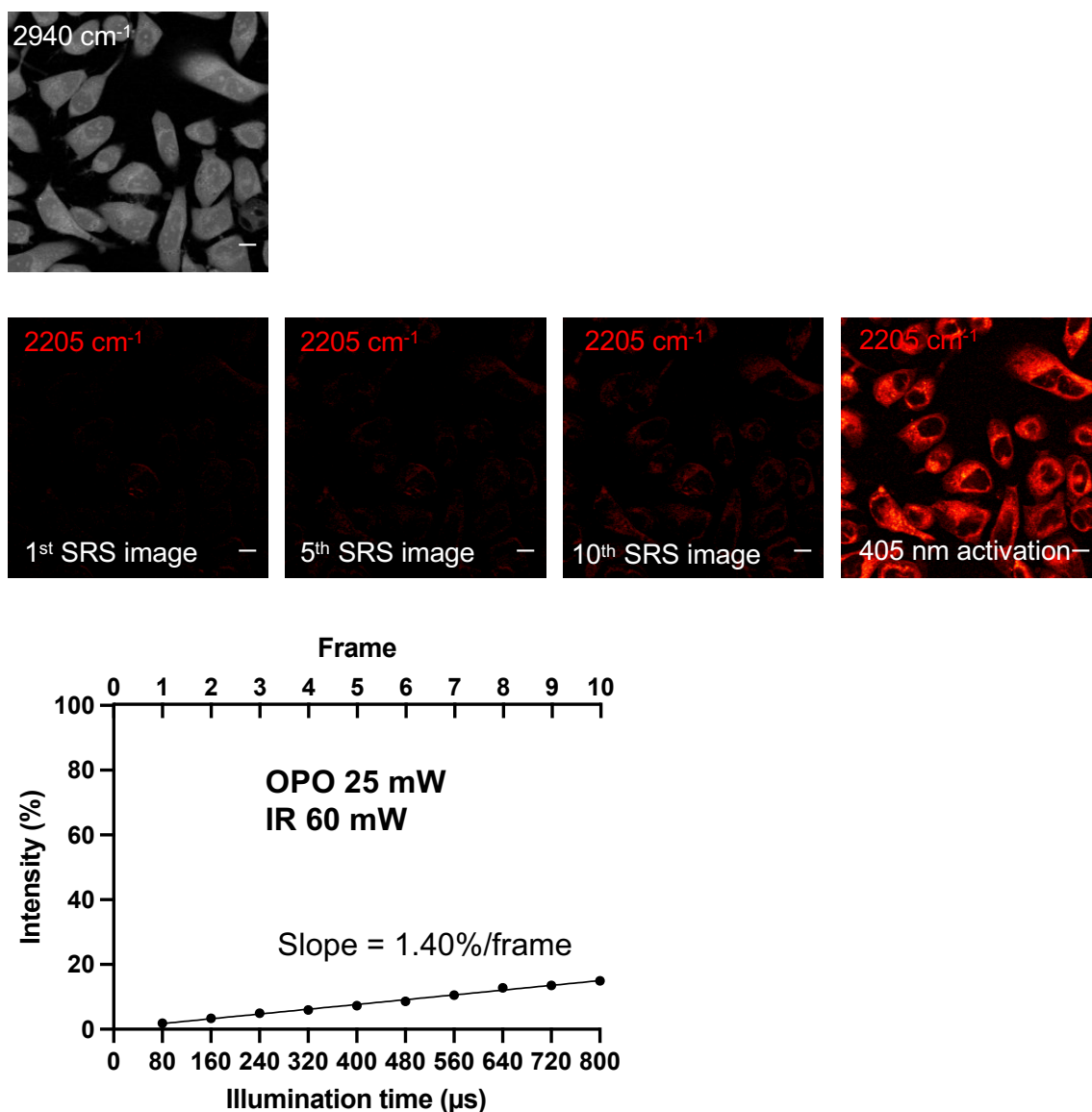
Supplementary Figure 3.4. UV-Vis absorption spectra of 20 uM 1-cyclo (1, black) and 9 (red) in DMSO.



Supplementary Figure 3.5. HPLC trace of Me-Mito (12) after incubating in 10 mM cysteine (PBS) for designated duration at 37 °C.



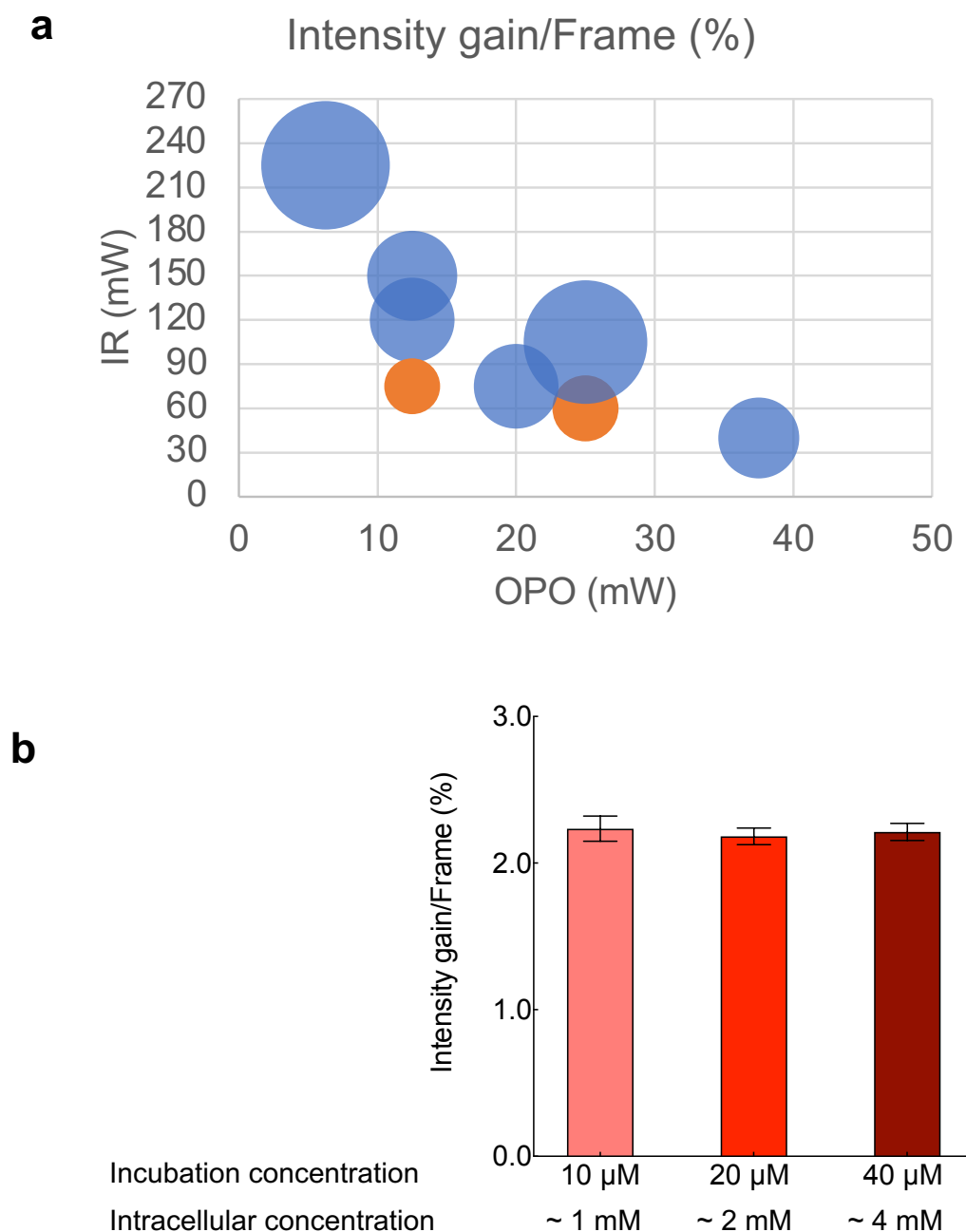
Supplementary Figure 3.6. The magnified images of Figure 3.3a (set 1) and two independent sets of correlative SRS imaging of Me-Mito (12) and fluorescence imaging of Mitotracker deep red in live HeLa cells. The correlation coefficients (Pearson's R value) for set 1, set 2 and set 3 (FI/2225 cm⁻¹ channel) are 0.85, 0.82 and 0.88 respectively. Scale bar: 10 μ m.



Supplementary Figure 3.7. Characterizations of Me-Mito (12) photoactivation by SRS imaging lasers. 10 consecutive frames of SRS images (2205 cm⁻¹, The representative 1st, 5th, 10th images are shown) taken on live HeLa cells (CH₃ SRS imaging at 2940 cm⁻¹ outlines the cell morphology) after incubation with 20 μM Me-Mito (12) for 30 minutes. SRS imaging at 2205 cm⁻¹ after full photoactivation (405 nm activation) is also shown for 100% intensity benchmark for Me-Mito (12) labeling. The relative SRS activated intensity over SRS laser illumination time is plotted in the bottom (the SRS intensity after 405 nm activation is set as 100%). Average frame activation is 1.4% at the chosen condition: OPO and Stokes powers are 25 mW and 60 mW, respectively; and pixel dwell time is 80 μs/pixel for each image frame. Scale bar: 10 μm

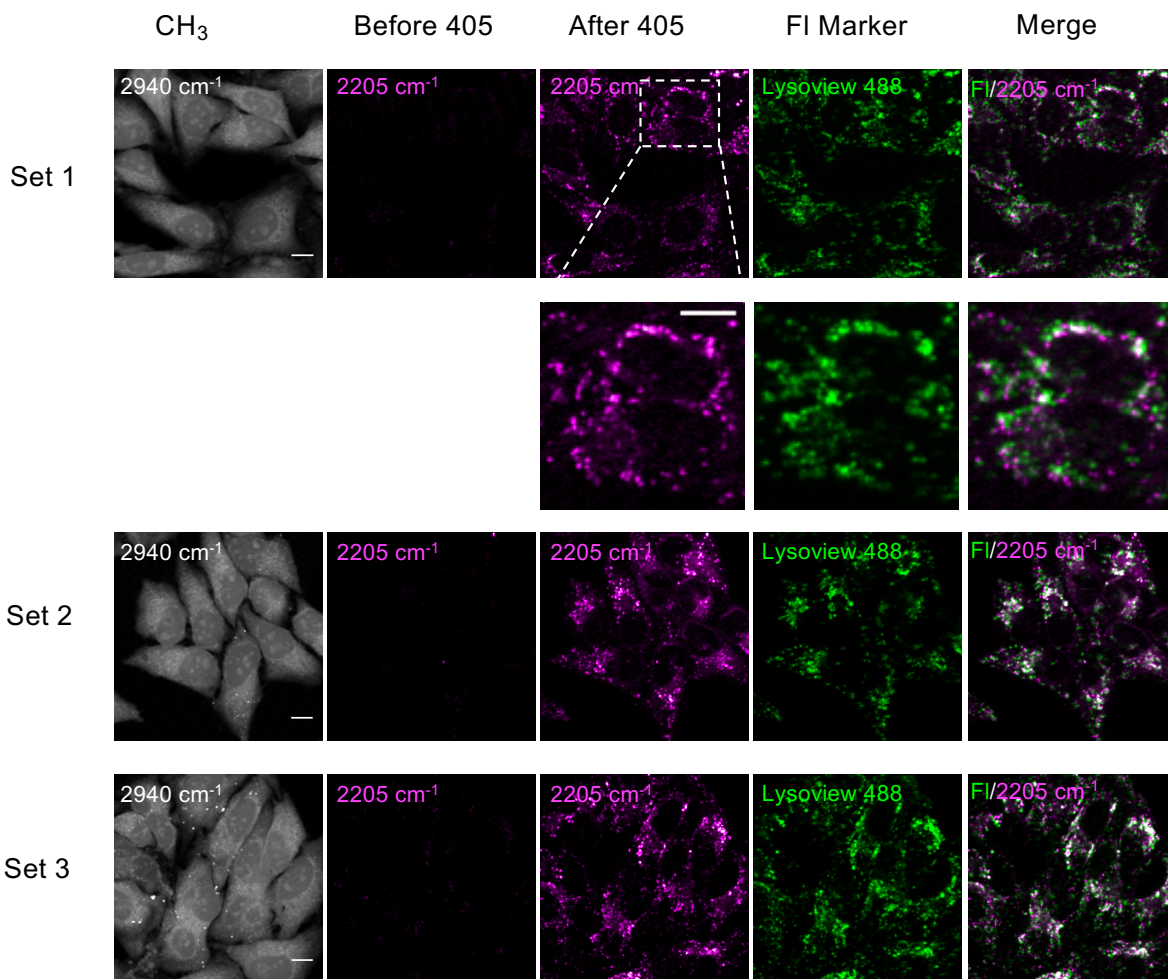
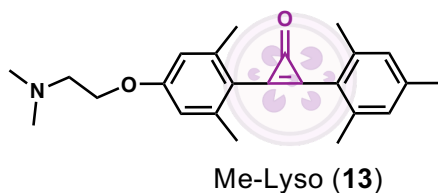
OPO (mW)	Stokes (mW)	Intensity gain (%) / Frame (80 μ s/pixel)
38	40	2.1
25	60	1.4
20	75	2.3
13	120	2.3
6	225	5.3
13	75	1.0
13	150	2.6
25	105	4.9

Supplementary Table 3.1. Intensity gain per frame under different power combinations of the OPO and Stokes lasers with a pixel dwell time of 80 μ s/pixel. Red-colored conditions indicate the selection of our SRS imaging conditions with an average per frame activation less than 1.5%.



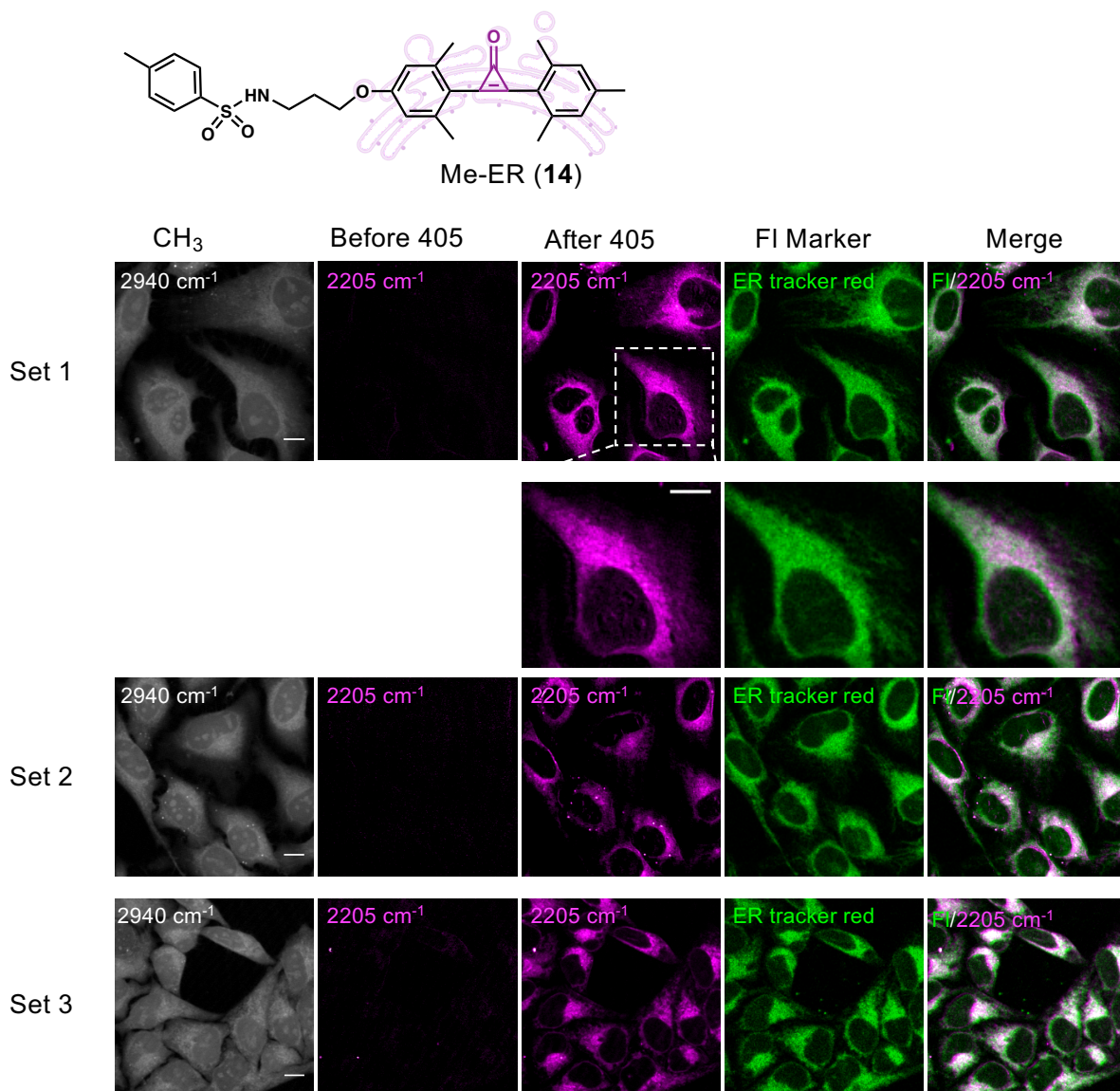
Supplementary Figure 3.8. (a) The plot for intensity gain per frame at different power conditions shown in Supplementary Table 3.1. The size of the cycles is proportional to the intensity gain per frame. (b) SRS Intensity gain per imaging frame (Intensity gain/frame) from time-series SRS imaging is plotted on live HeLa cells incubated with the indicated concentration of Me-Mito (**12**) probe for 30 minutes. The intracellular labeling concentration is calculated by the signal level after final 405 nm activation and benchmarked with the SRS standard curve from the uncaged probe solutions. SRS

laser powers: 40 mW for OPO and 40 mW for Stokes, respectively. $n = 4$ independent experiments. Data shown as mean \pm SEM.



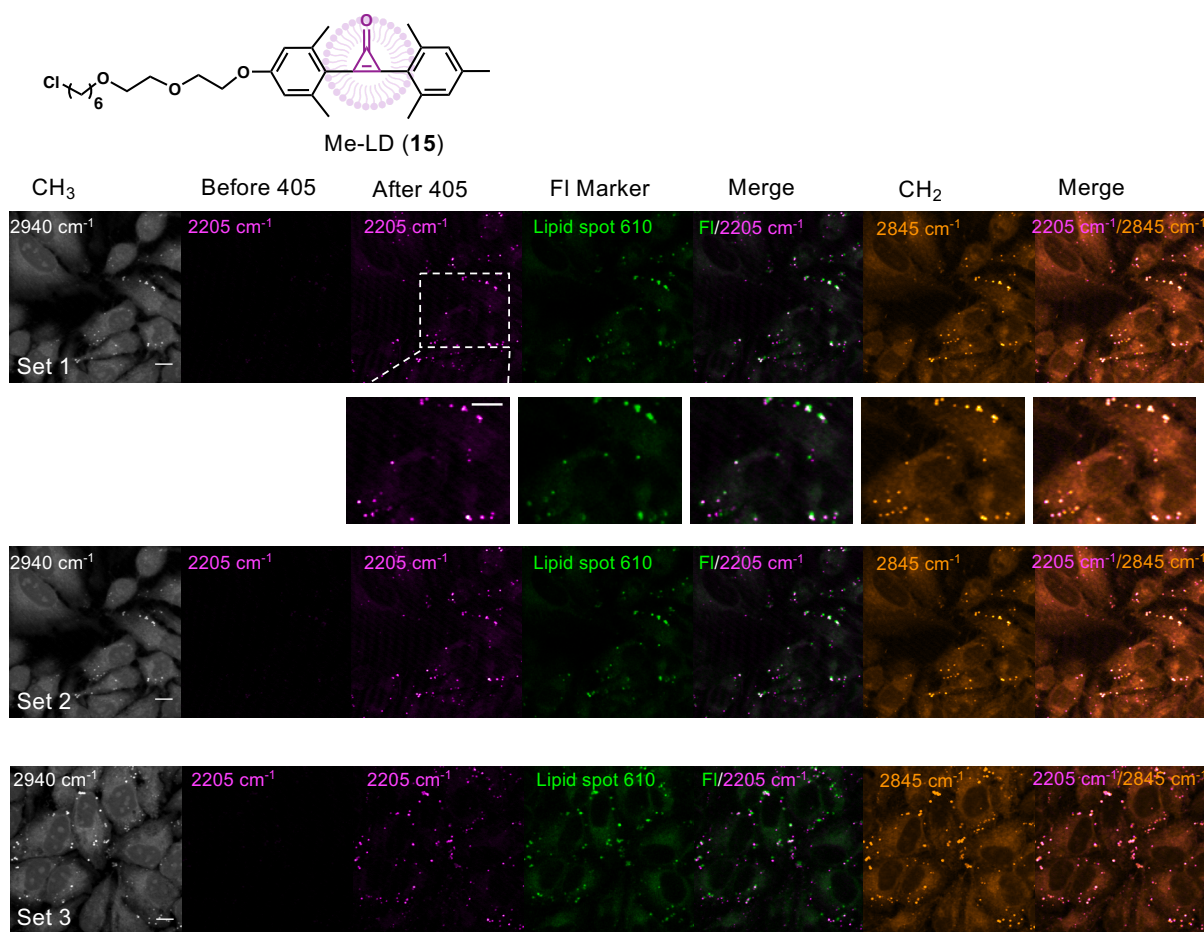
Supplementary Figure 3.9. The magnified images of Figure 3.3b (set 1) and two independent sets of correlative SRS imaging of Me-Lyso (13) and fluorescence imaging of Lysoview 488 in live HeLa cells. The correlation coefficients (Pearson's R value) for set 1, set 2 and set 3 (FI/2205

cm^{-1} channel) are 0.60, 0.67 and 0.62 respectively. We note that, the lowered Pearson's R are mainly due to the active movements of lysosomes in the live cells, from the 3-5 min gap (2 minutes of 405 nm laser illumination + SRS laser tuning time) between acquiring fluorescence and photoactivated SRS images. Scale bar: 10 μm .

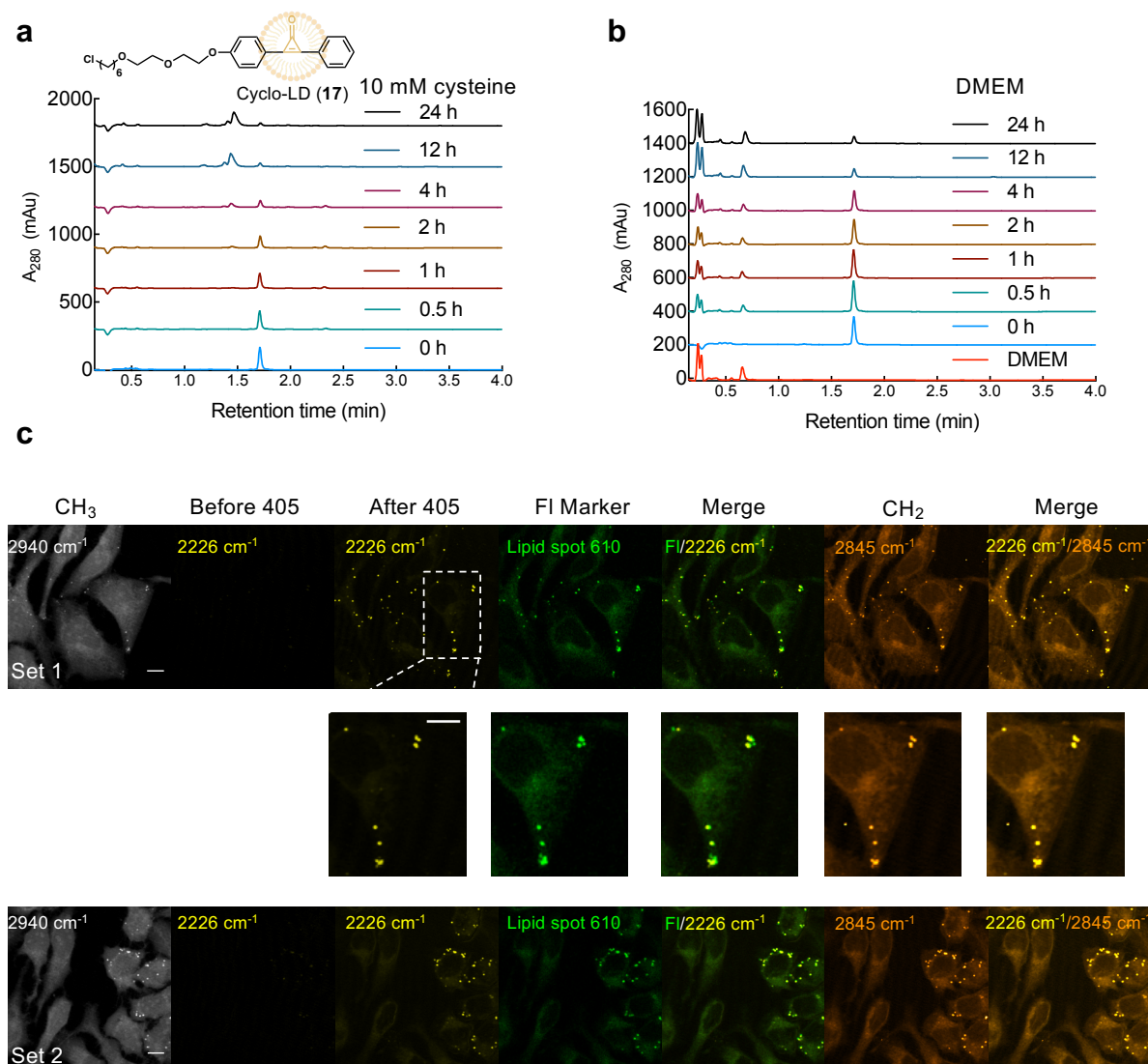


Supplementary Figure 3.10. The magnified images of Figure 3.3c (set 1) and two independent sets of correlative SRS imaging of Me-ER (14) and fluorescence imaging of ER tracker red in

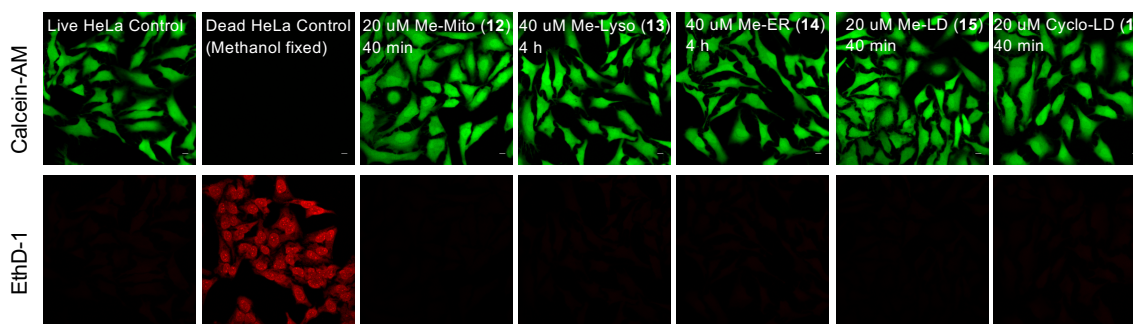
live HeLa cells. The correlation coefficients (Pearson's R value) for set 1, set 2 and set 3 (FI/2205 cm^{-1} channel) are 0.86, 0.80 and 0.90 respectively. Scale bar: 10 μm .



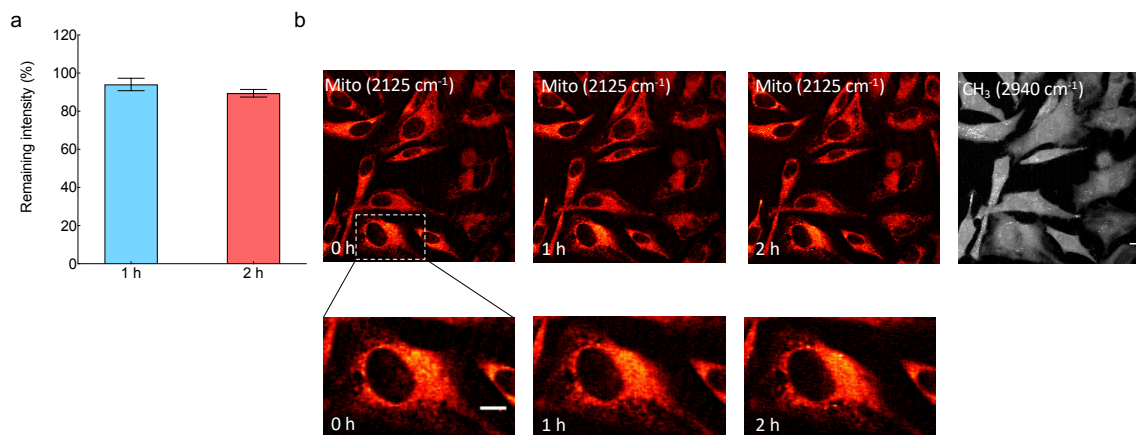
Supplementary Figure 3.11. The magnified images of Figure 3.3d (set 1) and two independent sets of correlative SRS imaging of Me-LD (15) and fluorescence imaging of Lipid spot 610 in live HeLa cells. The correlation coefficients (Pearson's R value) for set 1, set 2 and set 3 (FI/2205 cm^{-1} channel) are 0.54, 0.54 and 0.50 respectively. We note that, the lowered Pearson's R are mainly due to the active movements of lipid droplets in the live cells, from the 3-5 min gap (2 minutes of 405 nm laser illumination + SRS laser tuning time) between acquiring fluorescence and photoactivated SRS images. The colocalization is much improved between the 2205 cm^{-1} channel and the label-free CH₂ lipid channel (2845 cm^{-1}), which are acquired within 1-min time interval. Scale bar: 10 μm .



Supplementary Figure 3.12. (a-b) The stability of Cyclo-LD (17) in 10 mM cysteine in PBS (a), and DMEM (b) at 37 °C. (c) Two independent sets of correlative SRS imaging of Cyclo-LD (17) and fluorescence imaging of Lipid spot 610 in live HeLa cells. The correlation coefficients (Pearson's R value) for set 1 and set 2 (FI/2226 cm⁻¹ channel) are 0.50 and 0.76 respectively, which is again lowered due to active droplet movements. Scale bar: 10 μm.



Supplementary Figure 3.13. Minimum chemical toxicity of cyclopropenone dyes. Control fluorescence images for live/dead cell-viability assay for live HeLa cells (calcein-AM, green, as live cell indicator) and fixed cells (EthD-1, red, as dead cell indicator). The live HeLa cells were labeled with the indicated probe for the indicated time before performing live/dead cell-viability assay. Scale bar: 10 μm .



Supplementary Figure 3.14. Labeling signal and specificity evaluation during 2 hours of time lapse imaging in photoactivated Me-Mito- ^{13}C (16) labeled live HeLa cells. (a) Quantification of retained signals after 1 hour and 2 hours imaging. The values of signals at 0 h were used as 100% signal reference. $n = 6$ independent experiments. Data shown as mean \pm SEM. (b) A series of representative time lapse imaging. The magnified images of the bottom cell (indicated by the dashed white box) are shown. Scale bar: 10 μm .

3.9 Reference

- (1) Silva, J. M.; Silva, E.; Reis, R. L. Light-Triggered Release of Photocaged Therapeutics - Where Are We Now? *J. Control. Release* **2019**, *298* (February), 154–176. <https://doi.org/10.1016/j.jconrel.2019.02.006>.
- (2) Ellis-Davies, G. C. R. Caged Compounds: Photorelease Technology for Control of Cellular Chemistry and Physiology. *Nat. Methods* **2007**, *4* (8), 619–628. <https://doi.org/10.1038/nmeth1072>.
- (3) Kramer, R. H.; Chambers, J. J.; Trauner, D. Photochemical Tools for Remote Control of Ion Channels in Excitable Cells. *Nat. Chem. Biol.* **2005**, *1* (7), 360–365. <https://doi.org/10.1038/nchembio750>.
- (4) Yu, H.; Li, J.; Wu, D.; Qiu, Z.; Zhang, Y. Chemistry and Biological Applications of Photo-Labile Organic Molecules. *Chem. Soc. Rev.* **2010**, *39* (2), 464–473. <https://doi.org/10.1039/b901255a>.
- (5) Patterson, G. H.; Lippincott-Schwartz, J. A Photoactivatable GFP for Selective Photolabeling of Proteins and Cells. *Science* **2002**, *297* (5588), 1873–1877. <https://doi.org/10.1126/science.1074952>.
- (6) Klán, P.; Šolomek, T.; Bochet, C. G.; Blanc, A.; Givens, R.; Rubina, M.; Popik, V.; Kostikov, A.; Wirz, J. Photoremovable Protecting Groups in Chemistry and Biology: Reaction Mechanisms and Efficacy. *Chem. Rev.* **2013**, *113* (1), 119–191. <https://doi.org/10.1021/cr300177k>.
- (7) Belov, V. N.; Mitronova, G. Y.; Bossi, M. L.; Boyarskiy, V. P.; Hebisch, E.; Geisler, C.; Kolmakov, K.; Wurm, C. A.; Willig, K. I.; Hell, S. W. Masked Rhodamine Dyes of Five Principal Colors Revealed by Photolysis of a 2-Diazo-1-Indanone Caging Group: Synthesis, Photophysics, and Light Microscopy Applications. *Chem. - A Eur. J.* **2014**, *20* (41), 13162–13173. <https://doi.org/10.1002/chem.201403316>.
- (8) Betzig, E.; Patterson, G. H.; Sougrat, R.; Lindwasser, O. W.; Olenych, S.; Bonifacino, J. S.; Davidson, M. W.; Lippincott-Schwartz, J.; Hess, H. F. Imaging Intracellular Fluorescent Proteins at Nanometer Resolution. *Science* **2006**, *313* (5793), 1642–1645. <https://doi.org/10.1126/science.1127344>.
- (9) Banala, S.; Maurel, D.; Manley, S.; Johnsson, K. A Caged, Localizable Rhodamine Derivative for Superresolution Microscopy. *ACS Chem. Biol.* **2012**, *7* (2), 289–293. <https://doi.org/10.1021/cb2002889>.
- (10) Grimm, J. B.; Klein, T.; Kopek, B. G.; Shtengel, G.; Hess, H. F.; Sauer, M.; Lavis, L. D. Synthesis of a Far-Red Photoactivatable Silicon-Containing Rhodamine for Super-Resolution Microscopy. *Angew. Chemie - Int. Ed.* **2016**, *55* (5), 1723–1727. <https://doi.org/10.1002/anie.201509649>.
- (11) Hauke, S.; Von Appen, A.; Quidwai, T.; Ries, J.; Wombacher, R. Specific Protein Labeling with Caged Fluorophores for Dual-Color Imaging and Super-Resolution Microscopy in Living Cells. *Chem. Sci.* **2016**, *8* (1), 559–566. <https://doi.org/10.1039/c6sc02088g>.
- (12) Wijesooriya, C. S.; Peterson, J. A.; Shrestha, P.; Gehrman, E. J.; Winter, A. H.; Smith, E. A. A Photoactivatable BODIPY Probe for Localization-Based Super-Resolution Cellular Imaging. *Angew. Chemie - Int. Ed.* **2018**, *57* (39), 12685–12689. <https://doi.org/10.1002/anie.201805827>.

- (13) Shand, F. H. W.; Ueha, S.; Otsuji, M.; Koid, S. S.; Shichino, S.; Tsukui, T.; Kosugi-Kanaya, M.; Abe, J.; Tomura, M.; Ziogas, J.; et al. Tracking of Intertissue Migration Reveals the Origins of Tumor-Infiltrating Monocytes. *Proc. Natl. Acad. Sci. U. S. A.* **2014**, *111* (21), 7771–7776. <https://doi.org/10.1073/pnas.1402914111>.
- (14) Halabi, E. A.; Arasa, J.; Püntener, S.; Collado-Diaz, V.; Halin, C.; Rivera-Fuentes, P. Dual-Activatable Cell Tracker for Controlled and Prolonged Single-Cell Labeling. *ACS Chem. Biol.* **2020**, *15* (6), 1613–1620. <https://doi.org/10.1021/acscchembio.0c00208>.
- (15) Theriot, J. A.; Mitchison, T. J. Actin Microfilament Dynamics in Locomoting Cells. *Nature* **1991**, *352* (6331), 126–131. <https://doi.org/10.1038/352126a0>.
- (16) Lippincott-schwartz, J.; Altan-bonnet, N.; Patterson, G. H. Photobleaching and Photoactivation: Following Protein Dynamics in Living Cells. *Nat. Cell Biol.* **2003**, No. September, S7–S14.
- (17) Politz, J. C. Use of Caged Fluorochromes to Track Macromolecular Movement in Living Cells. *Trends Cell Biol.* **1999**, *9* (7), 284–287. [https://doi.org/10.1016/S0962-8924\(99\)01585-8](https://doi.org/10.1016/S0962-8924(99)01585-8).
- (18) Freudiger, C. W.; Min, W.; Saar, B. G.; Lu, S.; Holtom, G. R.; He, C.; Tsai, J. C.; Kang, J. X.; Xie, S. Label-Free Biomedical Imaging with High Sensitivity by Stimulated Raman Scattering Microscopy. *Science* **2008**, *322* (19), 1857–1860.
- (19) Shen, Y.; Hu, F.; Min, W. Raman Imaging of Small Biomolecules. *Annu. Rev. Biophys.* **2019**, *48* (1), 347–369. <https://doi.org/10.1146/annurev-biophys-052118-115500>.
- (20) Wei, L.; Chen, Z.; Shi, L.; Long, R.; Anzalone, A. V.; Zhang, L.; Hu, F.; Yuste, R.; Cornish, V. W.; Min, W. Super-Multiplex Vibrational Imaging. *Nature* **2017**, *544* (7651), 465–470. <https://doi.org/10.1038/nature22051>.
- (21) Hu, F.; Zeng, C.; Long, R.; Miao, Y.; Wei, L.; Xu, Q.; Min, W. Supermultiplexed Optical Imaging and Barcoding with Engineered Polyynes. *Nat. Methods* **2018**, *15* (3), 194–200. <https://doi.org/10.1038/nmeth.4578>.
- (22) Wei, L.; Hu, F.; Chen, Z.; Shen, Y.; Zhang, L.; Min, W. Live-Cell Bioorthogonal Chemical Imaging: Stimulated Raman Scattering Microscopy of Vibrational Probes. *Acc. Chem. Res.* **2016**, *49* (8), 1494–1502. <https://doi.org/10.1021/acs.accounts.6b00210>.
- (23) Zhao, Z.; Chen, C.; Wei, S.; Xiong, H.; Hu, F.; Miao, Y.; Jin, T.; Min, W. Ultra-Bright Raman Dots for Multiplexed Optical Imaging. *Nat. Commun.* **2021**, *12*, 1305. <https://doi.org/10.1038/s41467-021-21570-0>.
- (24) Miao, Y.; Qian, N.; Shi, L.; Hu, F.; Min, W. 9-Cyanopyronin Probe Palette for Super-Multiplexed Vibrational Imaging. *Nat. Commun.* **2021**, *12*, 4518. <https://doi.org/10.1038/s41467-021-24855-6>.
- (25) Fujioka, H.; Shou, J.; Kojima, R.; Urano, Y.; Ozeki, Y.; Kamiya, M. Multicolor Activatable Raman Probes for Simultaneous Detection of Plural Enzyme Activities. *J. Am. Chem. Soc.* **2020**, *142* (49), 20701–20707. <https://doi.org/10.1021/jacs.0c09200>.
- (26) Ao, J.; Fang, X.; Miao, X.; Ling, J.; Kang, H.; Park, S.; Wu, C.; Ji, M. Switchable Stimulated Raman Scattering Microscopy with Photochromic Vibrational Probes. *Nat. Commun.* **2021**, *12* (1), 1–8. <https://doi.org/10.1038/s41467-021-23407-2>.

- (27) Lee, D.; Qian, C.; Wang, H.; Li, L.; Miao, K.; Du, J.; Shcherbakova, D. M.; Verkhusha, V. V.; Wang, L. V.; Wei, L. Toward Photoswitchable Electronic Pre-Resonance Stimulated Raman Probes. *J. Chem. Phys.* **2021**, *154* (135102), 1–10. <https://doi.org/10.1063/5.0043791>.
- (28) Shou, J.; Ozeki, Y. Photoswitchable Stimulated Raman Scattering Spectroscopy and Microscopy. *Opt. Lett.* **2021**, *46* (9), 2176. <https://doi.org/10.1364/ol.418240>.
- (29) Yamakoshi, H.; Dodo, K.; Palonpon, A.; Ando, J.; Fujita, K.; Kawata, S.; Sodeoka, M. Alkyne-Tag Raman Imaging for Visualization of Mobile Small Molecules in Live Cells. *J. Am. Chem. Soc.* **2012**, *134* (51), 20681–20689. <https://doi.org/10.1021/ja308529n>.
- (30) Chen, Z.; Paley, D. W.; Wei, L.; Weisman, A. L.; Friesner, R. A.; Nuckolls, C.; Min, W. Multicolor Live-Cell Chemical Imaging by Isotopically Edited Alkyne Vibrational Palette. *J. Am. Chem. Soc.* **2014**, *136* (22), 8027–8033. <https://doi.org/10.1021/ja502706q>.
- (31) Ronald Breslow, Robert Haynie, and J. M. The Synthesis of Diphenylcyclopropenone. *J. Am. Chem. Soc.* **1959**, *81* (1), 247–248.
- (32) Poloukhine, A.; Popik, V. V. Highly Efficient Photochemical Generation of a Triple Bond: Synthesis, Properties, and Photodecarbonylation of Cyclopropenones. *J. Org. Chem.* **2003**, *68* (20), 7833–7840. <https://doi.org/10.1021/jo034869m>.
- (33) Urdabayev, N. K.; Poloukhine, A.; Popik, V. V. Two-Photon Induced Photodecarbonylation Reaction of Cyclopropenones. *Chem. Commun.* **2006**, No. 4, 454–456. <https://doi.org/10.1039/b513248g>.
- (34) Poloukhine, A. A.; Mbua, N. E.; Wolfert, M. A.; Boons, G. J.; Popik, V. V. Selective Labeling of Living Cells by a Photo-Triggered Click Reaction. *J. Am. Chem. Soc.* **2009**, *131* (43), 15769–15776. <https://doi.org/10.1021/ja9054096>.
- (35) Nainar, S.; Kubota, M.; McNitt, C.; Tran, C.; Popik, V. V.; Spitale, R. C. Temporal Labeling of Nascent RNA Using Photoclick Chemistry in Live Cells. *J. Am. Chem. Soc.* **2017**, *139* (24), 8090–8093. <https://doi.org/10.1021/jacs.7b03121>.
- (36) Arumugam, S.; Popik, V. V. Sequential “Click” – “Photo-Click” Cross-Linker for Catalyst-Free Ligation of Azide-Tagged Substrates. *J. Org. Chem.* **2014**, *79*, 2702–2708.
- (37) Orski, S. V.; Poloukhine, A. A.; Arumugam, S.; Mao, L.; Popik, V. V.; Locklin, J. High Density Orthogonal Surface Immobilization via Photoactivated Copper-Free Click Chemistry. *J. Am. Chem. Soc.* **2010**, *132* (32), 11024–11026. <https://doi.org/10.1021/ja105066t>.
- (38) Rubin, Y.; Lin, S. S.; Knobler, C. B.; Anthony, J.; Boldi, A. M. Solution-Spray Flash Vacuum Pyrolysis: A New Method for the Synthesis of Linear Polyynes with Odd Numbers of C=C Bonds from Substituted 3,4-Dialkynyl-3-Cyclobutene-1,2-Diones. *J. Am. Chem. Soc.* **1991**, *113*, 6943–6949.
- (39) KT, Potts, JS, B. Chemistry of Cyclopropenones. *Chem. Rev.* **1974**, *74* (2), 189–213.
- (40) Row, R. D.; Shih, H. W.; Alexander, A. T.; Mehl, R. A.; Prescher, J. A. Cyclopropenones for Metabolic Targeting and Sequential Bioorthogonal Labeling. *J. Am. Chem. Soc.* **2017**, *139* (21), 7370–7375. <https://doi.org/10.1021/jacs.7b03010>.
- (41) Ueland, P. M.; Refsum, H.; Stabler, S. P.; Malinow, M. R.; Andersson, A.; Allen, R. H. Total Homocysteine in Plasma or Serum: Methods and Clinical Applications. *Clin.*

- Chem.* **1993**, *39* (9), 1764–1779. <https://doi.org/10.1093/clinchem/39.9.1764>.
- (42) Los, G. V.; Encell, L. P.; Mcdougall, M. G.; Hartzell, D. D.; Karassina, N.; Simpson, D.; Mendez, J.; Zimmerman, K.; Otto, P.; Vidugiris, G.; et al. HaloTag: A Novel Protein Labeling Technology for Cell Imaging and Protein Analysis. *ACS Chem. Biol.* **2008**, *3* (6), 373–382.
- (43) Genshaft, A. S.; Ziegler, C. G. K.; Tzouanas, C. N.; Mead, B. E.; Jaeger, A. M.; Navia, A. W.; King, R. P.; Mana, M. D.; Huang, S.; Mitsialis, V.; et al. Live Cell Tagging Tracking and Isolation for Spatial Transcriptomics Using Photoactivatable Cell Dyes. *Nat. Commun.* **2021**, *12* (4995), 1–15. <https://doi.org/10.1038/s41467-021-25279-y>.
- (44) Guo, Y.; Li, D.; Zhang, S.; Yang, Y.; Liu, J. J.; Wang, X.; Liu, C.; Milkie, D. E.; Moore, R. P.; Tulu, U. S.; et al. Visualizing Intracellular Organelle and Cytoskeletal Interactions at Nanoscale Resolution on Millisecond Timescales. *Cell* **2018**, *175* (5), 1430–1442.e17. <https://doi.org/10.1016/j.cell.2018.09.057>.
- (45) Frei, M. S.; Hoess, P.; Lampe, M.; Nijmeijer, B.; Kueblbeck, M.; Ellenberg, J.; Wadepohl, H.; Ries, J.; Pitsch, S.; Reymond, L.; et al. Photoactivation of Silicon Rhodamines via a Light-Induced Protonation. *Nat. Commun.* **2019**, *10*, 4580. <https://doi.org/10.1038/s41467-019-12480-3>.
- (46) Bakthavatsalam, S.; Dodo, K.; Sodeoka, M. A Decade of Alkyne-Tag Raman Imaging (ATRI): Applications in Biological Systems. *RSC Chem. Biol.* **2021**, *2*, 1415–1429. <https://doi.org/10.1039/d1cb00116g>.
- (47) Bohlmann, F.; Jakupovic, J.; Müller, L.; Schuster, A. Naturally Occurring Cyclopropenone Derivatives. *Angew. Chemie Int. Ed. English* **1981**, *20* (3), 292–293. <https://doi.org/10.1002/anie.198102921>.
- (48) TORU OKUDA, KAZUTERU YOKOSE, TAMOTSU FURUMAI, H. B. M. PENITRICIN, A NEW CLASS OF ANTIBIOTIC PRODUCED BY PENICILLIUM ACULEATUM. *J. Antibiot. (Tokyo)*. **1984**, *37* (7), 718–722. <https://doi.org/10.6009/jjrt.KJ00003576689>.
- (49) Kogen, H.; Kiho, T.; Tago, K.; Miyamoto, S.; Fujioka, T.; Otsuka, N.; Suzuki-Konagai, K.; Takeshi, O. Alutacenoic Acids A and B, Rare Naturally Occurring Cyclopropenone Derivatives Isolated from Fungi : Potent Non-Peptide Factor XIIIa Inhibitors. *J. Am. Chem. Soc.* **2000**, *122*, 1842–1843.
- (50) Li, S.; Chen, T.; Wang, Y.; Liu, L.; Lv, F.; Li, Z.; Huang, Y.; Schanze, K. S.; Wang, S. Conjugated Polymer with Intrinsic Alkyne Units for Synergistically Enhanced Raman Imaging in Living Cells. *Angew. Chemie - Int. Ed.* **2017**, *56* (43), 13455–13458. <https://doi.org/10.1002/anie.201707042>.
- (51) Tian, S.; Li, H.; Li, Z.; Tang, H.; Yin, M.; Chen, Y.; Wang, S.; Gao, Y.; Yang, X.; Meng, F.; et al. Polydiacetylene-Based Ultrastrong Bioorthogonal Raman Probes for Targeted Live-Cell Raman Imaging. *Nat. Commun.* **2020**, *11* (1), 1–9. <https://doi.org/10.1038/s41467-019-13784-0>.
- (52) Tang, Y.; Zhuang, Y.; Zhang, S.; Smith, Z. J.; Li, Y.; Mu, X.; Li, M.; He, C.; Zheng, X.; Pan, F.; et al. Azo-Enhanced Raman Scattering for Enhancing the Sensitivity and Tuning the Frequency of Molecular Vibrations. *ACS Cent. Sci.* **2021**, *7*, 768–780. <https://doi.org/10.1021/acscentsci.1c00117>.
- (53) Casacio, C. A.; Madsen, L. S.; Terrasson, A.; Waleed, M.; Barnscheidt, K.; Hage, B.; Taylor, M. A.; Bowen, W. P. Quantum-Enhanced Nonlinear Microscopy. *Nature*

2021, 594 (7862), 201–206. <https://doi.org/10.1038/s41586-021-03528-w>.

COMPUTATIONAL DESIGN OF
MOLECULAR PROBES FOR
ELECTRONIC PRERESONANCE
RAMAN SCATTERING MICROSCOPY

The content of this chapter has been published in:

Du, J.[#], Tao, X.[#], Begušić, T.*, & Wei, L*. Computational Design of Molecular Probes for Electronic Preresonance Raman Scattering Microscopy. *J. Phys. Chem. B*, 2023, 127, 4979-4988.

[#]*equal contribution.*

4.1 Introduction

Over the last one and a half decades, stimulated Raman scattering (SRS) microscopy has emerged as an important vibrational bioimaging modality complementary to standard fluorescence microscopy. Although SRS has enhanced the otherwise weak spontaneous Raman transition by up to 10^8 -fold through stimulated emission amplification,¹⁻³ current sensitivity of nonresonant probes is still largely limited to micromolar to millimolar range,⁴ restricting probing the rich chemical information on dilute biomolecules *in vivo*, which is usually in the nanomolar to low micromolar range. This sensitivity gap has proven to be successfully tackled by customized Raman probes.⁴ Among numerous Raman probes, some of the most sensitive ones up to date are the pyronin- based electronic preresonance (epr) enhanced Manhattan Raman scattering (MARS) dyes.⁵ When the pump wavelength is tuned to be close to the electronic excitation energy, i.e., under the epr condition, the vibrational mode coupled to the electronic state would be selectively amplified with enhanced SRS signals. By carefully tuning the absorption of the dyes (660–790 nm) to moderately close to the laser wavelength (800–900 nm), SRS intensities of the triple bonds (nitriles or alkynes) when conjugated into the conjugation systems of these dyes have been found to be preresonantly enhanced by up to 10^4 folds (detection limit down to 250 nM) with a well-

maintained high signal-to-background ratio. Since the invention of MARS dyes, numerous exciting imaging applications have been achieved. The MARS dyes enable supermultiplexed (>20 channels) vibrational imaging by taking advantage of the narrow line width of Raman peaks (peak width about 10 cm^{-1} , $\sim 50\text{--}100$ times narrower than fluorescent peaks) from triple bonds in the cell-silent region ($1800\text{--}2800\text{ cm}^{-1}$) where there are no background signals from endogenous molecules.⁵⁻⁷ These ideas inspired the design of multifunctional Raman probes including photo-switchable, photoactivatable, and turn-on enzymatic probes.⁸⁻¹² They also paved the way for all-far-field single-molecule Raman spectroscopy and imaging without plasmonic enhancement by stimulated Raman excited fluorescence (SREF).¹³ Thus, the superb vibrational properties and versatility of epr MARS dyes are widely recognized, making them essential for a wide range of vibrational spectroscopy and imaging. However, these dyes are still the only set of triple-bond bearing epr-SRS dyes until now and the principle of designing such strong Raman probes is still inconclusive. This has largely restricted the development of new epr-SRS scaffolds to further increase the sensitivity and expand the multiplexity, a central topic in the current development of SRS imaging. While the Albrecht A-term preresonance approximation equation was previously adopted to fit the dependence of epr-SRS signals with a single parameter of laser detuning, the treatment ignored the structure dependent factors as it assumed all frequency-independent factors as a constant.⁵ The necessity to rationally explore and design new epr-SRS scaffolds hence sets a high demand for a more systematic theory to understand and predict the dependence of the epr-SRS signals on molecule structures (i.e., a structure–function relationship).

Indeed, our initial screening of molecular candidates for new epr-SRS probes revealed that the structure related factors play a crucial role. For example, a series of pyrrolopyrrole cyanine (PPCy) dyes were originally identified by us to be promising candidates of epr-SRS probes. PPCy dyes are neutral in charge and have two nitrile groups in the conjugation system with adjustable absorption between 680 and 800 nm.¹⁴ The absorption spectrum of one of those dyes, namely the PPCy-10a molecule (Figure 4.1a, blue), almost overlaps with that of MARS2237 (Figure 4.1a, red), one of the well-validated MARS dyes. The absorption

maximum and molar extinction coefficient of these two molecules are also very close, implying that a similar epr-SRS signal should be expected based on the detuning and oscillator strength dependence implied from the full Albrecht A-term preresonance approximation equation.¹⁵ However, as a stark difference to MARS2237, which presented a clear and sharp epr-SRS peak, we barely see any epr-SRS signal from the nitrile groups of PPCy-10a under the same measurement conditions (Figure 4.1a). This observation points out that it is not effective enough to identify novel epr-SRS probes only through the experimentally measured absorption quantities. Instead, it indicates that the epr-SRS process relies heavily on the specific molecular structures. To decipher the structure-dependent factors underlying this vibronic process, we turn to quantum chemistry methods, which provide access to parameters that cannot be obtained from experiments.

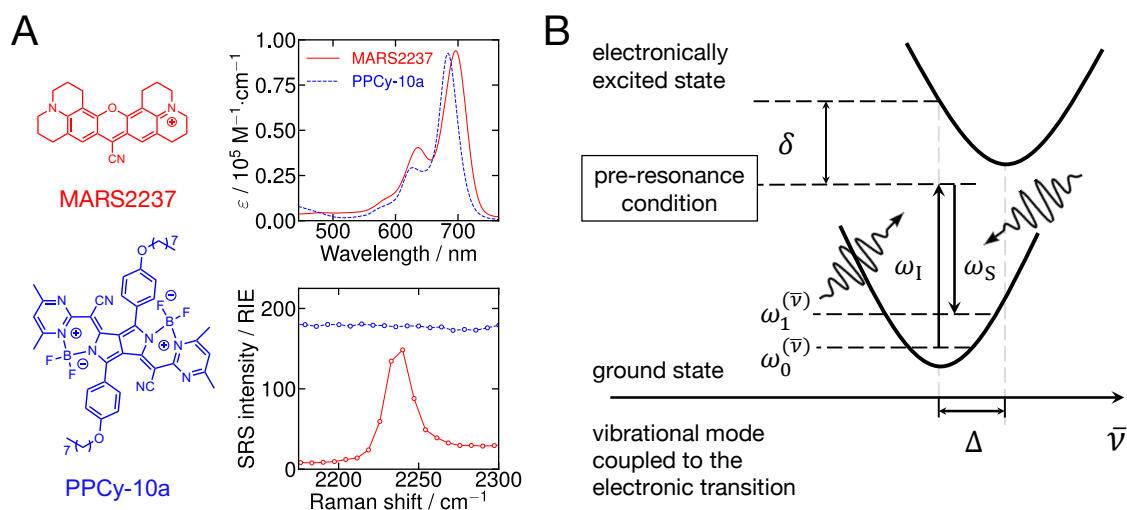


Figure 4.1. (a) Absorption and SRS spectra of MARS2237 (red) and PPCy-10a (blue). SRS intensities are reported relative to EdU (RIE) values. ϵ stands for the molar extinction coefficient. (b) Scheme of the electronic preresonance stimulated Raman scattering (epr-SRS) process, in which the incident (pump) light with frequency ω_I excites the vibrational mode from its ground to the first excited vibrational state. The pump pulse is detuned by δ from the vertical excitation frequency between the ground and first excited electronic states of the molecule. The scattering process is stimulated by a Stokes (probe) pulse of frequency ω_S and proceeds through a coupling between the

vibrational and electronic degrees of freedom, controlled by the dimensionless displacement parameter Δ .

4.2 Theory

Theoretical tools that can accurately and reliably predict Raman intensity could greatly help us understand the key factors involved in epr-SRS. Although established computational methods for simulating resonance and preresonance Raman spectra exist,^{16–25} they have been largely used for simulating the full spectra of individual molecules. Here, we explore an alternative task, in which we compare the intensities of a single peak, corresponding to the nitrile (C≡N) or alkyne (C≡C) bond stretch, in the preresonance Raman spectra of multiple large molecules (50–100 atoms). Theoretically, the SRS signal intensity is^{26,27}

$$I_{0 \rightarrow 1}^{(\bar{\nu})} \propto \sum_{\rho\lambda} \left| \alpha_{0 \rightarrow 1}^{(\bar{\nu})}(\omega_I)_{\rho\lambda} \right|^2 \quad (4.1)$$

where 0 and 1 denote the ground and first excited vibrational states of mode $\bar{\nu}$ in the electronic ground state, $\alpha_{0 \rightarrow 1}^{(\bar{\nu})}(\omega_I)$ is the frequency-dependent polarizability matrix element between these vibrational states, ω_I is the incident light frequency, and ρ and λ are the polarizations of the incident and scattered lights. In eq 4.1, we omit the prefactor that depends on the incident light (pump) frequency and the Stokes pulse intensity because these factors cancel out when the SRS intensity is reported with respect to a standard reference. The conventional frequency-domain approach formulates the polarizability through the Kramers–Heisenberg–Dirac (KHD) equation^{28,29}

$$\alpha_{0 \rightarrow 1}^{(\bar{\nu})}(\omega_I)_{\rho\lambda} = -\frac{1}{\hbar} \sum_n \left[\frac{\langle \psi_1^{(\bar{\nu})} | \hat{\mu}_\rho | \psi_n' \rangle \langle \psi_n' | \hat{\mu}_\lambda | \psi_0^{(\bar{\nu})} \rangle}{\omega_I - \omega_n' + \omega_0^{(\bar{\nu})} + i\gamma} - \frac{\langle \psi_1^{(\bar{\nu})} | \hat{\mu}_\lambda | \psi_n' \rangle \langle \psi_n' | \hat{\mu}_\rho | \psi_0^{(\bar{\nu})} \rangle}{\omega_I + \omega_n' - \omega_0^{(\bar{\nu})} - i\gamma} \right] \quad (4.2)$$

which involves a sum over all vibrational states ψ_n' (with energies $\hbar\omega_n'$) of the excited electronic state that is near-resonance with the incident light $\hbar\omega_0^{(\bar{\nu})}$ and $\hbar\omega_1^{(\bar{\nu})}$ correspond to the energies of the ground and first excited vibrational states of the mode of interest ($\bar{\nu}$),

respectively. $\hat{\mu}_\rho = \hat{\vec{\mu}} \cdot \vec{\epsilon}_s$, $\hat{\mu}_\lambda = \hat{\vec{\mu}} \cdot \vec{\epsilon}_I$ are the projections of transition dipole moment $\hat{\vec{\mu}}$ along the scattered and incident light polarizations, respectively, and γ is the dephasing parameter. In the remainder, we will assume the Condon approximation, $\hat{\vec{\mu}} \equiv \vec{\mu}(\hat{q}) \approx \vec{\mu}(q_{eq})$, in which the coordinate dependence of the transition dipole moment is neglected. q_{eq} denotes the ground-state equilibrium geometry.

The time-domain approach, popularized by Heller and Tannor,^{30,31} offers an efficient alternative to evaluating the above sum-over-states formula. Here, the frequency-dependent polarizability is written as the half-Fourier transform

$$\alpha_{o \rightarrow 1}^{(\bar{v})}(\omega_I)_{\rho\lambda} = \frac{i}{\hbar} \mu_\lambda \mu_\rho \left[\int_0^\infty C(t) \Gamma(t) e^{i\omega_I t} dt + \int_0^\infty C(t) \Gamma(t) e^{-i(\omega_I - \omega^{(\bar{v})}) t} dt \right] \quad (4.3)$$

of the time correlation function

$$C(t) = \left\langle \psi_1^{(\bar{v})} \left| e^{-i\hat{H}_e t/\hbar} \right| \psi_0^{(\bar{v})} \right\rangle e^{i\omega_0^{(\bar{v})} t} \quad (4.4)$$

where H_e is the excited-state Hamiltonian, and we denote $\omega^{(\bar{v})} = \omega_1^{(\bar{v})} - \omega_0^{(\bar{v})}$ for simplicity. $\Gamma(t)$ is the dephasing term in its more general form; for example, $\Gamma(t) = e^{-\gamma t}$ corresponds to the Lorentzian line shape in the KHD expression (eq 4.2). In other words, the computation of $C(t)$ requires the time propagation of a quantum wavepacket $|\psi(t)\rangle = \exp(-i\hat{H}_e t/\hbar) |\psi_0^{(\bar{v})}\rangle$ in the excited electronic state, which is computationally costly for molecular Raman probes with a typical size of 50–100 atoms, even with, for example, trajectory-guided Gaussian wavepacket approaches.^{32,33,42,43,34–41} In fact, the number of ab initio computations in the excited electronic state should be minimized to allow for efficient analysis of relatively large molecules.

The displaced harmonic oscillator (DHO) model¹⁹ offers a practical way to approximate the time propagation in the excited state. Within this model, it is assumed that the ground and excited potential energy surfaces can be sufficiently accurately represented as two harmonic

potentials with equal force constants (with frequencies $\omega^{(v)}$) but different minima. Note that v represents an arbitrary mode, and is distinguished from \bar{v} , the mode of interest that gives the Raman signal. In this case, the time correlation function of eq 4.4 simplifies into

$$C^{DHO}(t) = -\frac{\Delta_{\bar{v}}}{\sqrt{2}}(1 - e^{-i\omega^{(\bar{v})}t}) \prod_v \left[e^{-(1-i\omega^{(v)}t - e^{-i\omega^{(v)}t})\Delta_v^2/2} \right] e^{-i(\delta+\omega_I)t} \quad (4.5)$$

Δ_v is the dimensionless distance between the ground- and excited-state minima along mode v and is expressed within the vertical gradient model²¹ as

$$\Delta_v = \frac{1}{\omega^{(v)}} \sqrt{\frac{f_v^2}{\hbar\omega^{(v)}}} \quad (4.6)$$

where f is the gradient of the excited-state potential energy with respect to the mass-scaled normal mode v (see Figure 4.1b) evaluated at the ground-state equilibrium geometry. The dimensionless displacement parameters Δ_v are directly related to the well-known Huang–Rhys factors $S_v = \Delta_v^2/2$. In eq 4.5, $\delta = \omega_{eg} - \omega_I$ is the difference (detuning) between the vertical excitation frequency ω_{eg} and the incident light frequency. Equation 4.3 is combined with the approximations in eqs 4.5 and 4.6 to provide the major simulation protocol for this study. In addition, because the laser frequency is sufficiently close to the vertical excitation gap, only the resonant part (first term on the right-hand side of eq 4.3) was computed.

Finally, we close the review of the methods by pointing out that two simple but useful expressions can be further derived from eq 4.5 under the preresonance conditions. First, following Heller, Sundberg, and Tannor,^{26,31} a short-time expansion of the time correlation function $C^{DHO}(t)$ leads to

$$C^{ST}(t) = -is_{\bar{v}}te^{-\frac{s^2t^2}{2} - i(\delta+\omega_I)t} \quad (4.7)$$

where $s_v = \frac{\Delta_v\omega^{(v)}}{\sqrt{2}}$ and $s^2 = \sum_v s_v^2$. Substituting eq 4.7 into the first (resonant) term of eq 4.3 yields the short-time expression for the SRS intensity

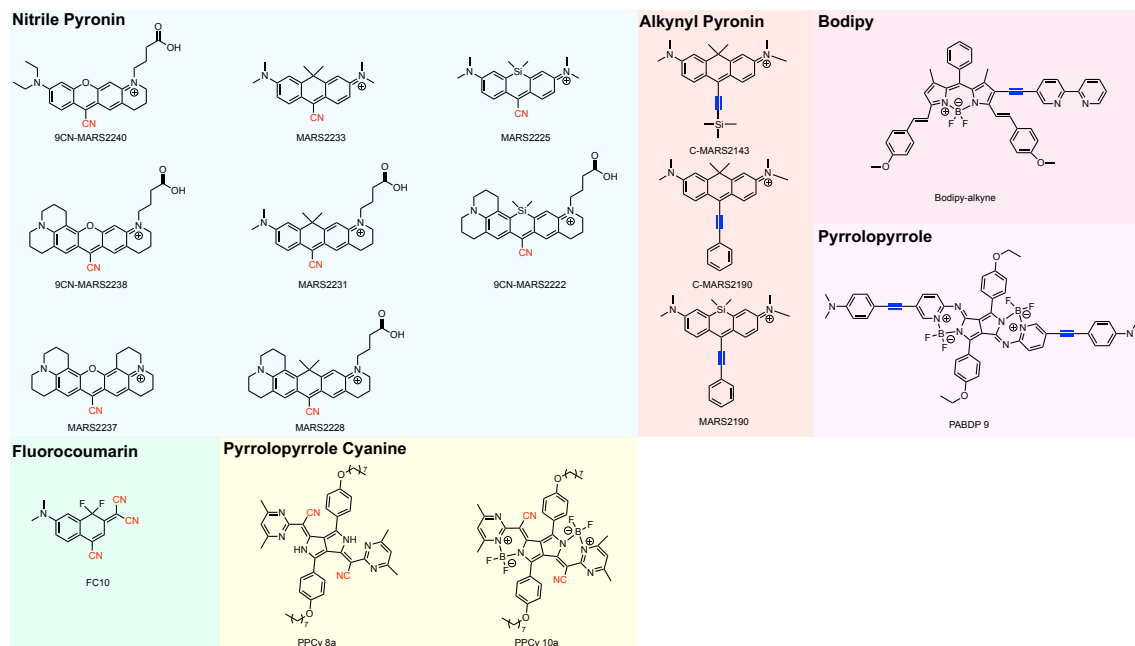
$$I_{0 \rightarrow 1}^{(\bar{\nu}),ST} \propto \frac{\mu^4 s_{\bar{\nu}}^2}{\hbar^2 \delta^4} \left| \int_0^\infty t e^{-\frac{t^2}{2} + i\delta t/s} ds \right|^2 \quad (4.8)$$

where we used $\sum_{\rho\lambda} \mu_\rho^2 \mu_\lambda^2 = \mu^4$ and introduced the dipole strength $\sum_{\rho=x,y,z} \mu_\rho^2 = \mu^2$. Alternatively, the large detuning limit can be applied directly to the KHD formula in the frequency domain, which leads to the well-known Albrecht A-term equation but now with calculable structure-dependent factors^{15,44}

$$I_{0 \rightarrow 1}^{(\bar{\nu}),Albrecht} \propto \frac{4\mu^4 s_{\bar{\nu}}^2}{\hbar^2} \left[\frac{\omega_I^2 + \omega_{eg}^2}{(\omega_I^2 - \omega_{eg}^2)^2} \right]^2 \approx \frac{\mu^4 s_{\bar{\nu}}^2}{\hbar^2 \delta^4} \quad (4.9)$$

The first part of eq 4.9 corresponds to the most common form that includes both resonant and nonresonant terms, whereas the final right-hand side expression is an approximate form assuming $\delta \ll \omega_{eg}$. Although more approximate than eq 4.5, the short-time and Albrecht's expressions provide additional insight into the origins of strong preresonance Raman signals. For example, Albrecht's expression reveals a strong $(1/\delta^4)$ dependence of the Raman intensity on the detuning, which is otherwise hidden in the more accurate equation. However, it neglects the impact of spectator modes, i.e., modes that are not directly excited by the scattering event, which are still accounted for in the short-time expansion formula (eq 4.8) through a collective vibrational parameter s^2 that depends on all mode displacements.

Table 4.1. A Series of Near-Infrared Nitrile and Alkyne Dyes That Fit into the epr Region, Namely, with Intense Absorption in the Range between 660 and 790 nm



4.3 Results and discussion

With the computational approach in hand, we first validate it by comparing the theoretical and experimental SRS intensities of molecules with various scaffolds. For the benchmark, we searched for candidates based on the criteria that the molecules strongly absorb in the epr-SRS region (660–790 nm) and that the nitrile and alkyne groups are directly conjugated to the π -system. Fortunately, there are several molecule scaffolds fitting into our criteria, although not many. In addition to the pyronin (O/C/Si Rhodamine) scaffold presented in MARS dyes and PPCy dyes we introduced earlier, there are other scaffolds such as coumarin⁴⁵, Bodipy⁴⁶ and pyrrolopyrrole⁴⁷ (see Table 4.1). We synthesized the molecules and measured their absorption and epr-SRS signals. The data of some of the MARS dyes were adapted from previous reports.^{5,6} It is noteworthy that we report epr-SRS measurements from two independent laser systems, providing different detuning for the same molecules (see Supplementary Information for details). The pump wavelength is tuned to be around 840 or 860 nm for the triple bond and the corresponding experimental results are shown in Table 4.2. Each laser system used EdU as the reference substance.

Table 4.2. Absorption Maxima and epr-SRS Intensities for the Molecular Probes at Two Pump Laser Frequencies^a

pump laser around 860 (± 3) nm		
epr-SRS probes	absorption maximum/nm	epr-SRS intensity/RIE
9CN-MARS2222	790	940
MARS2228	760	435
MARS2225	760	303
MARS2231	744	240
MARS2237	700	120
9CN-MARS2238	690	108
MARS2233	735	99
9CN-MARS2240	675	86
MARS2190	731	73
Bodipy-alkyne	666	20
pump laser around 840 (± 3) nm		
epr-SRS probes	absorption maximum/nm	epr-SRS intensity/RIE
MARS2228	760	620
MARS2231	744	324
MARS2237	700	150
PADBP-9	699	186
MARS2190	731	132
C-MARS2190	696	16
C-MARS2143	696	15
FC10	694	12
PPCy-8a	690	0
PPCy-10a	692	0

^aThe absorption and Raman scattering are presented for the probes dissolved in DMSO. The Raman intensities are reported in their relative intensities versus EdU (RIE).

Figure 4.2 compares the measured epr-SRS intensities (red bars) of nitrile and alkyne probes with the simulated intensities (blue bars) from the DHO theory described above. Data from two SRS laser systems with different pump wavelengths (around 860 and 840 nm) are shown. A consistent agreement is seen between experiment and theory across magnitudes of SRS intensities on all scaffolds. It is clear that our computational approach remains robust for laser setups with different detunings. Details of the computational quantities involved in the epr-SRS intensity calculations (including vertical excitation wavelength, detuning

frequency, transition dipole strength, Raman mode displacement, Raman mode frequency, and epr-SRS signal strength) are reported in the Supplementary Table 4.1 of the Supplementary Information.

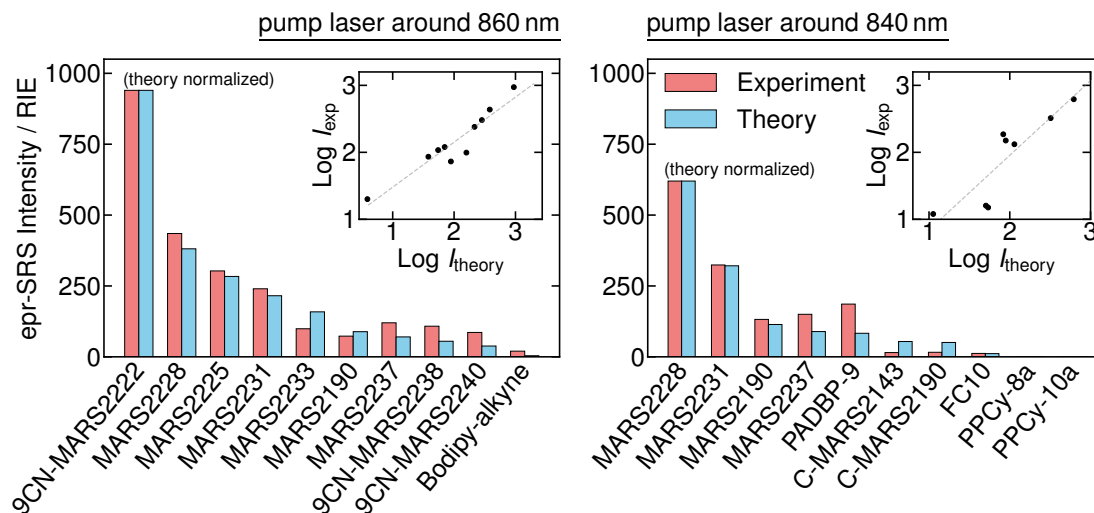


Figure 4.2. Comparing the measured and computed epr-SRS spectral intensities for near-infrared triple bond dyes with pump lasers at around 860 (left) and 840 nm (right). Experimental values are reported in Table 4.2. The theoretical values are obtained with the DHO formula (see eqs 4.3, 4.5, and 4.6). The insets quantitatively compare the intensities on the log₁₀ scale, and a linear regression (dashed gray) of the data gives the slopes of 0.67 (left, $R^2 = 0.95$) and 1.11 (right, $R^2 = 0.88$).

Furthermore, when the comparison is performed at a quantitative level in the inset, the presence of a linear trend in the figure reinforces the ability of our simple theoretical approach to identify high-intensity epr-SRS probes. A linear regression of the data gives a slope of 0.67 or 1.11 rather than 1, illustrating also the limitations of our approach. Admittedly, a number of approximations enter the simulations, including the DHO model for the time-correlation function and (TD)DFT level of electronic structure theory. Most of the calculated values (normalized to the strongest epr-SRS probe in each group) are within or close to the experimental standard error of about 10% (see Supplementary Figure 4.1).

Yet, our calculations deviate more on the intensities of alkyne dyes: they largely overestimate the SRS intensities of the alkynyl pyronin dyes C-MARS2190 and C-MARS2143, while they underestimate the intensity of PADBP-9. Whereas in conventional simulations of a single resonance Raman spectrum the effects of detuning and transition dipole strength are only moderate, e.g., the spectra are typically scaled to the highest peak, here these factors play an important role because different molecules exhibit different detunings and transition dipole strengths. Since the epr-SRS intensity depends strongly on these parameters, even seemingly acceptable quantum-chemical errors can lead to discrepancies between theory and experiment. Furthermore, C-MARS2190 and C-MARS2143 exhibit a strong asymmetry between absorption and emission spectra (see Supplementary Figure 4.6 of the Supplementary Information), which implies that the independent-mode DHO model is not valid for these molecules. In Supplementary Information, we show that mode-coupling (Duschinsky) and non-Condon effects are not much stronger than in several other (nitrile-based) probes. We believe that aggregation effects,⁴⁸ which have already been reported in these molecules,⁴⁹ could be responsible for the distorted absorption and fluorescence spectra, as well as for the discrepancy between theoretical and experimental Raman intensities.

More importantly, the theoretical approach allows us to analyze the effect of the vibrational mode displacement, a key factor that enters the SRS intensity expression but cannot be easily accessed from experiments.^{50,51} To this end, we revisit the opening example of Figure 4.1a. In Figure 4.3 we show the highest occupied molecular orbitals (HOMOs) and lowest unoccupied molecular orbitals (LUMOs) of PPCy-10a and MARS2237, as well as the corresponding parameters related to the vibrational mode displacement between the ground and excited electronic states. The $\pi \rightarrow \pi^*$ electronic transition leads to a strong electron density generation on the C \equiv N vibration for MARS2237 but not for PPCy-10a (Figure 4.3, comparing the HOMO–LUMO difference in the connected dashed-gray boxes). As we see from the $\Delta_{\bar{\nu}}$ values, the C \equiv N bond in MARS2237 has to stretch more to reach the equilibrium position when electronically excited, leading to a stronger SRS signal for this mode. The large difference in the epr-SRS signal strengths for the two probes then

becomes straightforward according to eq 4.5, despite the fact that they exhibit similar characteristic absorption properties.

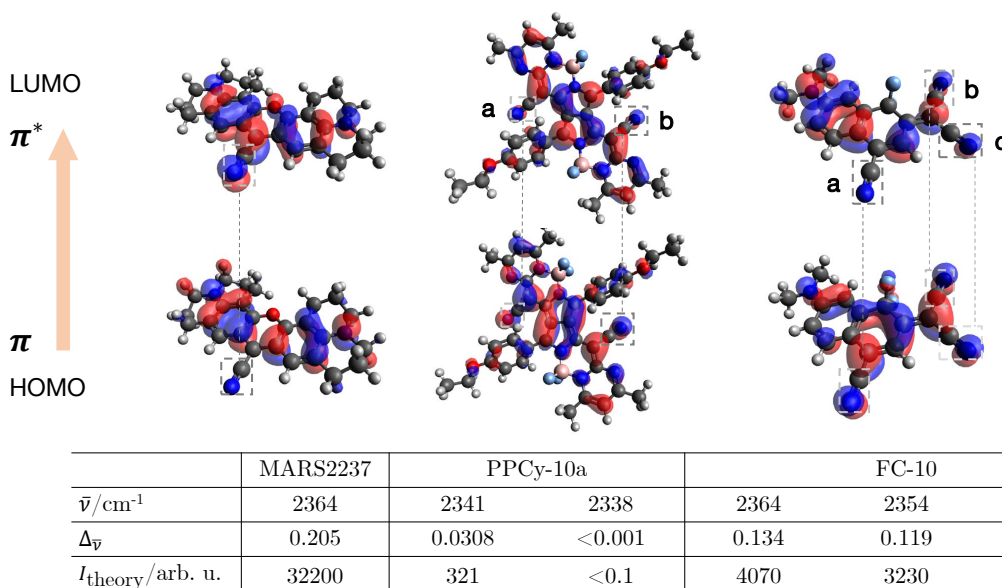


Figure 4.3. Epr-SRS process is strong for vibrational modes that are coupled to the electronic transition. $\pi \rightarrow \pi^*$ electronic transition (as indicated by the HOMO and LUMO orbitals) induces strong electron density generation on the $\text{C}\equiv\text{N}$ bond for MARS2237 but not for PPCy-10a. As a result, MARS2237 exhibits a significantly larger Raman mode displacement ($\Delta_{\bar{\nu}}$), hence the 100 times stronger signal intensity for the epr-SRS Raman peak associated with the $\text{C}\equiv\text{N}$ vibration. The FC-10 molecule, shown in the last column exhibits two relatively strong vibrations even though it contains three nitrile groups, which can be ascribed to the symmetric (Raman active) and antisymmetric (inactive) linear combinations of the stretch vibrations corresponding to the two groups labeled b and c.

Figure 4.3 also reveals that simply adding more nitrile groups does not necessarily increase the overall SRS intensity. The specific comparison of MARS2237 (containing one nitrile) and PPCy-10a (containing two nitriles) is an extreme example. Additionally, in the third column of Figure 4.3, we present the FC-10 molecule, which contains three nitrile groups. Here, in contrast to PPCy-10a, all $\text{C}\equiv\text{N}$ bonds are coupled to the electronic π system of the dye and participate in the electronic transition. However, the coupling is weaker than in

MARS2237, as demonstrated by the values of the dimension-less displacement parameter $\Delta_{\bar{\nu}}$. Interestingly, in the normal mode basis, there are only two modes with nonzero displacement. We explain this by the fact that the two $\text{C}\equiv\text{N}$ bonds labeled “b” and “c” in Figure 4.3 are equally displaced in the excited electronic state. Therefore, their symmetric linear combination forms a normal mode that is displaced and Raman active, whereas their antisymmetric combination is not.

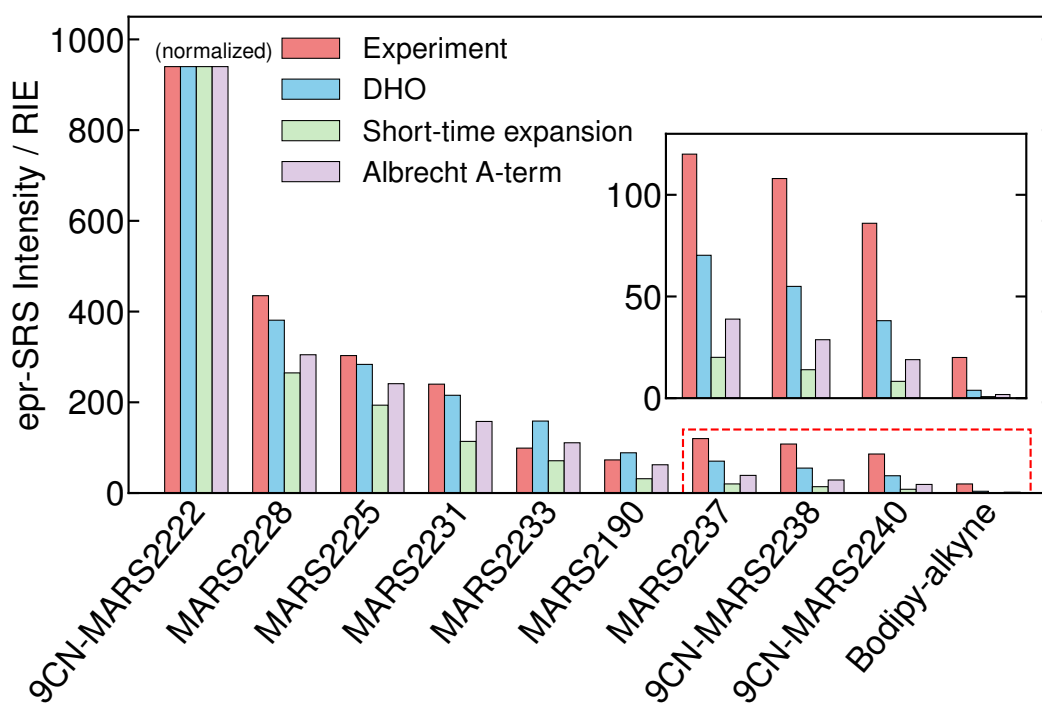
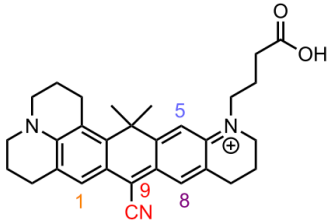


Figure 4.4. Epr-SRS intensities simulated through the two approximate expressions—short-time expansion (eq 4.8) and Albrecht A-term (eq 4.9) formulas—compared with those simulated through the DHO equation (same as in Figure 4.2, 860nm pump) and with the experiment.

Figure 4.4 compares the epr-SRS intensities of several probes simulated with the full DHO expression and two approximate expressions, the short-time expansion (eq 4.8) and Albrecht A-term (eq 4.9) formulas. As expected, both expressions are less accurate than

the DHO method. Since the overall computational cost of the three approaches is almost the same and is contained mostly in the required quantum chemistry calculations, the DHO expression is recommended over the other two when a quantitative agreement is needed. Nevertheless, the qualitative trends in the intensity strength are exactly reproduced. Therefore, we can use these simpler and more interpretable expressions to seek design principles for highly sensitive preresonance Raman probes.

Table 4.3. Predicted epr-SRS Properties for the Proposed Structural Isomers of the Molecular Probe MARS2228 (Labeled 9CN-MARS2228 to Distinguish from Other Isomers)^a

Structure				
Isomers	9CN-MARS2228	1CN-MARS2228	5CN-MARS2228	8CN-MARS2228
$\lambda_{\text{sim}}/\text{nm}$	605	540	520	536
$\omega_{\text{sim}}^{(\bar{\nu})}/\text{cm}^{-1}$	2355	2334	2355	2354
$\mu^2/\text{a.u.}$	37.2	35.8	30.0	35.7
$\Delta_{\bar{\nu}}$	0.175	0.0583	0.0200	0.0595
ξ	0.41	0.29	0.36	0.34
$I_{\text{theory}}/\text{arb. u.}$	2.24e+05	1.96e+04	1.81e+03	2.19e+04

^aThe computational protocol is kept consistent with those described above. For the calculation of epr-SRS intensities (last row), the detuning is fixed at 1572 cm^{-1} (the experimental detuning of 9CN-MARS2228 with 838 nm pump laser, See Supplementary Table 4.1 for details) for all isomers. λ_{sim} denotes the vertical excitation energies of different isomers, as obtained from the quantum chemistry simulations.

Detuning ($\delta = \omega_{eg} - \omega_l$), transition dipole moment (μ), and the Raman mode displacement ($\Delta_{\bar{\nu}}$) are the three factors that are highlighted in the Albrecht A-term formula

(eq 4.9). The epr-SRS intensity increases steeply with an increase in either the transition dipole moment or the reciprocal of the detuning to the fourth order. Molecular probes with strong oscillator strengths are always preferred, while one carefully chooses the detuning, i.e., optimal preresonance regime, to tip the balance between high Raman signal strength and signal-to-background ratio, as discussed in the previous experimental work.⁵ To better illustrate the principles derived from the theoretical analysis, in Table 4.3 we present an example where three structural isomers of (9CN-)MARS2228 are proposed and investigated as potential molecular probe candidates. The isomers, for which the nitrile group is attached at various positions on the conjugated aromatic ring, have not been reported before in the literature and are proposed here. Among the four molecules, the 9CN-substituted one exhibits the lowest-energy absorption maximum, leading to the smallest detuning and, hence, the strongest SRS intensity when the pump laser is consistently fixed at 838 nm. The 9CN-isomer also exhibits the strongest vibrational displacement and can, therefore, be expected to provide a stronger SRS signal even if the detuning is fixed to the same value for different molecules, i.e., even if the pump laser can be freely tuned for each molecule. An example of such calculations is shown in the bottom row of Table 4.3. Combining all of these factors together, it is not surprising that MARS2228 is listed as one of the most sensitive epr-SRS Raman probes to date. And as a prescreening step, our computation may greatly facilitate the development of new epr-SRS scaffolds.

We can similarly analyze the differences between the nitrile- and alkyne-based probes. For example, the alkyne MARS2190 probe exhibits a weaker SRS signal than its nitrile-based structural analog bearing a similar chromophore (Si-pyronin), the MARS2225 probe (see Table 4.1 for structures and Figure 4.2 for intensities). Here, the displacement factors of around 0.146 for MARS2225 and 0.154 for MARS2190 cannot explain this discrepancy. In fact, in this case, we can explain the difference between the nitrile and alkyne dyes through their absorption properties, namely the dipole strength and detuning. Specifically, if we neglect the displacement factor, the ratio of their Raman intensities within the

Albrecht approximation is $I^{MARS2225}/I^{MARS2190} \approx 4.12$, which agrees well with the experimental value of $303/73 \approx 4.15$ (see Table 4.2, pump laser at 860 nm).

The Albrecht A-term equation considers the contribution to the Raman intensity solely from the specific vibrational mode. In contrast, the short-time expansion is useful when analyzing the influence of other (spectator) vibrational modes. More specifically, eq 4.8 can be rewritten as

$$I_{0 \rightarrow 1}^{(\bar{\nu}),ST} = I_{0 \rightarrow 1}^{(\bar{\nu}),Albrecht} \left(\frac{1}{\xi^4} \left| \int_0^\infty t e^{-t^2/2+it/\xi} dt \right|^2 \right) \quad (10)$$

where the second part of the expression depends only on $\xi = s/\delta$, a dimensionless factor that involves the displacement of all modes, including spectator modes.

When ξ approaches zero, the impact of the spectator modes on the Raman intensity becomes negligible, i.e., the ξ -dependent term becomes 1 (see Supplementary Figure 4.2), which corresponds to the relatively large-detuning limit of Albrecht.⁴⁴ On the other hand, $I_{0 \rightarrow 1}^{(\bar{\nu}),ST}/I_{0 \rightarrow 1}^{(\bar{\nu}),Albrecht}$ reaches its optimum at $\xi \approx 0.43$, for which the short-time expansion gives roughly three times stronger intensity than Albrecht equation. That is to say, once the electronic transition properties associated with the Raman mode of interest are optimally tuned, additional fine functionalization of the spectator modes could further enhance the spectral intensity (see Supplementary Information for further discussion). However, as seen from Table 4.3, it is recognized as a mild effect compared with the aforementioned three key factors and is not expected to be the first target in the optimization protocol.

4.4 Conclusion

To conclude, we have demonstrated that theoretical modeling can elucidate the chemical principles behind vastly different epr-SRS signals from different molecular scaffolds. The

computational protocol is both robust and efficient in predicting the epr-SRS intensities and could lead toward a rational design of new epr-SRS scaffolds. Importantly, it allows us to decompose the final SRS intensity into three key factors, namely the (a) detuning, (b) transition dipole strength, and (c) vibrational mode displacement. We showed that the strength of vibronic coupling of the specific chemical bond can be visualized by the electron density distribution during the electronic transition in the epr-SRS setting. In addition, we analyzed the applicability of approximate Albrecht and short-time expressions, which can explicitly separate these parameters. Overall, although not as accurate as the full DHO model, these approximate formulas are still useful because of their interpretability. By combining them with quantum chemistry computations, we could analyze the effect of all relevant molecular properties, including the vibrational mode displacement parameters, which are not necessarily observable in experiments.

This work provides a fundamental step toward a computationally or data-driven methodology of epr-SRS probe design, ensuring efficient utilization of experimental efforts by avoiding traditional trial-and-error procedures. In our simulations, we have observed that the relative values of the transition dipole strength and vibrational mode displacement parameters can be sufficiently accurately modeled from quantum chemistry calculations at the TDDFT level of theory, whereas the detuning cannot. This implies two possible strategies for future work. In a purely computational approach, explicitly correlated electronic structure methods could be used for determining the vertical excitation energy to high accuracy in order to minimize the error in the detuning parameter. Alternatively, in a hybrid, experimental and computational data-driven approach, experimentally available electronic absorption spectra could be used for a range of existing dyes that do not necessarily contain a nitrile or alkyne group. Then, different isomers of such dyes with a nitrile or alkyne substitution could be computationally screened for strong vibrational mode displacement, assuming that the absorption maximum is red-shifted in a predictable way⁶ after the addition of these functional groups. This opens new avenues for designing next-generation highly sensitive epr-SRS palettes, driving the detection limit down to the ultimate single-molecule

level. In either case, our work presents the necessary theoretical and computational basis for future design strategies.

4.5 Methods

Computational Details. Practical implementation of the simulation protocol involves three quantum chemistry calculations for each molecule, namely the (a) ground-state vibrational modes and frequencies (or Hessian), (b) electronic transition dipole moment, and (c) excited state gradient, all evaluated at the ground-state equilibrium geometry (i.e., Franck–Condon point). The excited-state Cartesian forces are then transformed into the normal-mode coordinates obtained from the diagonalization of the mass-scaled Hessian of the ground electronic state. We assumed the validity of the Condon approximation, in which the transition dipole moment is a constant evaluated at a single molecular geometry, in our case the Franck–Condon point. In addition, within the DHO model, the excited state frequencies and normal modes were approximated by those of the ground state, i.e., the changes in the frequencies (mode distortion) and normal modes (Duschinsky effect) between the ground and excited electronic states were neglected.⁵² The DHO and Condon approximations were validated on the electronic absorption spectra of several dyes (see Supplementary Information). We performed the quantum-chemical calculations with the ORCA software package^{53,54} and computed the Raman intensities from the aforementioned analytical expressions in a separate Python code. Further details of ab initio simulations are available in the Supplementary Information.

Raman intensities were computed using mixed computational and experimental data. Namely, to avoid the computational errors in evaluating the vertical excitation gap, we estimated this energy from the experimental spectra. Since most of the probes exhibit absorption spectra that are dominated by the 0–0 transition⁵⁵ (see Supplementary Information), we assumed that the wavelength of maximum intensity, λ_{\max} , corresponds to this transition, i.e., $\lambda_{0-0} \approx \lambda_{\max}$. Then, within the DHO model, we could recover the experimental estimate of the vertical excitation energy as

$$\omega_{eg,exp} = \omega_{0-0} + \frac{1}{2} \sum_v \omega_v \Delta_v^2 \quad (11)$$

Where ω_{0-0} is the 0-0 transition frequency. Computational data was used for all other parameters, including the transition dipole moments (analyzed in the Supplementary Information). After evaluating the time correlation function $C(t)$ within the DHO model (eq 4.5), we used a Gaussian dephasing $\Gamma(t) = e^{-\Theta^2 t^2/2}$ in eq 4.3 to account for the inhomogeneous broadening of the line shape^{18,24} in the solution. Θ was set to 250 cm^{-1} , which was consistent with the broadening used in the electronic absorption spectra simulations.

Experimental Details. There are two independent laser systems of different fundamental wavelengths for measuring epr-SRS signals of the molecules, providing different detuning for the same molecule. One has a fundamental wavelength of 1031.2 nm (2 ps pulse width, 80 MHz repetition rate) and the other one has a fundamental wavelength of 1064.2 nm (6 ps pulse width, 80 MHz repetition rate). The different fundamental wavelengths (used as the Stokes beam) of the two laser systems provide different pump wavelengths for the same molecule. For the Raman peak of triple bond around 2200 cm^{-1} , 1031.2 nm fundamental laser sets the pump wavelength to be around 840 and 1064.2 nm fundamental laser sets the pump wavelength to be around 860 nm. For example, the Raman peak for the nitrile bond of MARS2228 is 2228 cm^{-1} , thus the pump wavelength is either 838.5 nm (when the Stokes beam is 1031.2 nm) or 860.2 nm (when the Stokes beam is 1064.2 nm). Details of the two laser systems are given in the Supplementary Information. A 10 mM aqueous EdU sample is measured under each laser system as a benchmark reference sample to correct the dependence of nonresonant Raman cross section on the wavelength.

4.6 Supplementary Information

Ab Initio Simulation Details

In the quantum-chemical calculations in ORCA, we used an efficient geometry pre-optimization with a tight-binding semi-empirical potential^{56,57} and included the molecule-

solvent interaction (DMSO as solvent in our experiments) through an implicit polarizable continuum model.⁵⁸ Results from density functional theory (DFT) and time-dependent density functional theory (TD-DFT)⁵⁹ schemes at the hybrid functional level (PBE0/cc-pVDZ) are reported. PBE0^{60,61} was tested for the calculation of electronic transition energies and dipole moments of the Rhodamine dyes⁶² and, independently, our benchmark calculations confirm that the Raman intensity predictions are insensitive on whether pure⁶³ or range-separated⁶⁴ density functional is used instead. We also performed benchmark calculations to validate the robustness of the electronic structure calculations with respect to basis set sizes and solvent environments. The convergence criteria of the self-consistent field steps in all reported calculations was set to ‘very tight’, meaning that an energy change lower than 10^{-9} Hartree between the last two iterations was required. It is worthwhile mentioning that in Figure 4.3 and Table 4.3 of the main text, as well as in Supplementary Table 4.1 below, we report the vibrational frequencies without a conventional scaling factor correction, which is why they might differ from the experimental frequencies by about +4%. Such small and systematic errors in the frequency calculations do not significantly alter the simulated Raman intensities, which are the main focus of this work. For efficiency, in PPCy-8a/PPCy-10a, we replaced the octyl groups by the ethyl groups, assuming that the absorption and Raman properties are not strongly influenced by the length of the alkyl chain. The optimized structures and the orbitals were visualized with the Avogadro software.^{65,66}

Supplementary Table 4.1 reports the computational quantities that were used for epr-SRS intensity calculations, including vertical excitation wavelength, detuning frequency, transition dipole strength, Raman mode displacement, Raman mode frequency, and finally the epr-SRS signal strength.

Supplementary Table 4.1. Computational quantities that were used for epr-SRS intensity calculations. From left to right, the columns present the wavelength of the experimental absorption maximum (λ_{max}), vertical excitation wavelength ($\lambda_{eg,exp}$, estimated from λ_{max} using eq 4.10 of the main text), detuning frequency ($\delta = \omega_{eg,exp} - \omega_{pump}$), transition dipole strength ($|\mu|$, as computed with the quantum chemistry method), Raman mode displacement ($\Delta_{\bar{\nu}}$, eq 4.6 of the main text), Raman mode frequency ($\omega^{(\bar{\nu})}$, as computed with the quantum chemistry method), and finally the theoretical epr-SRS signal strength computed using the DHO model (I_{theory}).

$\lambda_{pump} = 860$ nm

epr-SRS probes	λ_{max}/nm	$\lambda_{eg,exp}/\text{nm}$	δ/cm^{-1}	$ \mu /\text{au}$	$\Delta_{\bar{\nu}}$	$\omega^{(\bar{\nu})}/\text{cm}^{-1}$	I_{theory}/RIE
9CN-MARS2222	790	771	1338	6.31	0.146	2348	*940*
MARS2228	760	740	1877	6.10	0.175	2354	381
MARS2225	760	743	1823	6.12	0.146	2352	284
MARS2231	744	726	2152	5.91	0.176	2358	215
MARS2237	700	679	3102	5.55	0.205	2364	70
9CN-MARS2238	690	668	3342	5.50	0.208	2366	55
MARS2233	735	717	2310	5.84	0.174	2359	159
9CN-MARS2240	675	654	3669	5.42	0.209	2368	38
MARS2190	731	716	2335	5.50	0.154	2291	89
Bodipy-alkyne	666	640	3993	6.04	0.063	2314	4

$\lambda_{pump} = 838$ nm

epr-SRS probes	λ_{max}/nm	$\lambda_{eg,exp}/\text{nm}$	δ/cm^{-1}	$ \mu /\text{au}$	$\Delta_{\bar{\nu}}$	$\omega^{(\bar{\nu})}/\text{cm}^{-1}$	I_{theory}/RIE
MARS2228	760	740	1572	6.10	0.175	2354	*620*
MARS2231	744	726	1847	5.91	0.176	2358	321
MARS2237	700	679	2797	5.55	0.205	2364	114
FC10	694	665	3101	4.44	0.134	2364	11
PPCy-8a	690	662	3162	5.21	0.012	2320	0
PPCy-10a	692	657	3289	5.25	0.031	2341	1

$\lambda_{pump} = 842$ nm

epr-SRS probes	λ_{max}/nm	$\lambda_{eg,exp}/\text{nm}$	δ/cm^{-1}	$ \mu /\text{au}$	$\Delta_{\bar{\nu}}$	$\omega^{(\bar{\nu})}/\text{cm}^{-1}$	I_{theory}/RIE
PADBP-9	699	661	3248	7.22	0.148	2310	89
MARS2190	731	716	2086	5.50	0.154	2291	83
C-MARS2190	696	681	2816	5.24	0.184	2297	54
C-MARS2143	696	681	2807	5.43	0.178	2257	51

*Normalized with respect to the experimentally measured epr-SRS intensity. See Figure 4.2 in the main text for details.

epr-SRS spectro-microscope setup

For the laser with a fundamental wavelength of 1031.2 nm: An integrated laser (picoEMERALD, Applied Physics and Electronics, Inc.) is used as a light source for both pump and Stokes beams. It produces 2 ps pump (tunable from 770 nm – 990 nm, bandwidth 0.5 nm, spectral bandwidth $\sim 7 \text{ cm}^{-1}$) and Stokes (also called probe, 1031.2 nm, spectral bandwidth 10 cm^{-1}) beams with 80MHz repetition rate. Stokes beam is modulated at 20 MHz by an internal electro-optic modulator. The spatially and temporally overlapped pump and Stokes beams are introduced into an inverted multiphoton laser scanning microscopy (FV3000, Olympus), and then focused onto the sample by a 25X water objective (XLPLN25XWMP, 1.05 N.A., Olympus). Transmitted pump and Stokes beams are collected by a high N.A. condenser lens (oil immersion, 1.4 N.A., Olympus) and pass through a band-pass filter (893/209 BrightLine, 25 mm, AVR Optics) to filter out Stokes beam. A large area ($10 \times 10 \text{ mm}$) Si photodiode (S3590-09, Hamamatsu) is used to measure the remaining pump beam intensity. 64 V DC voltage is used on the photodiode to increase saturation threshold and reduce response time. The output current is terminated by a 50Ω terminator and pre-filtered by an 19.2-23.6-MHz band-pass filter (BBP-21.4+, Mini-Circuits) to reduce laser and scanning noise. The signal is then demodulated by a lock-in amplifier (SR844, Stanford Research Systems) at the modulation frequency. The in-phase X output is fed back to the Olympus IO interface box (FV30-ANALOG) of the microscope. Image acquisition speed is limited by 30 μs time constant set for the lock-in amplifier. Laser powers are monitored through image acquisition by an internal power meter and power fluctuation are controlled within 5 % by the laser system. 16-bit grey scale images are acquired by Fluoview software. The epr-SRS spectra are acquired by fixing the Stokes beam at 1031.2 nm and scanning the pump beam through the designated wavelength range point by point. 10 mM aqueous EdU sample is used as a standard to give RIE (Relative Intensity to EdU) of different molecule probes. The 1 mM dye solution (DMSO) is used to acquire the epr-SRS spectra. To minimize possible photobleaching, a relatively low power (20 mW on sample for pump laser and 30 mW on sample for Stokes laser) is used.

For the laser with a fundamental wavelength of 1064.2 nm: A similar laser system (picoEMERALD, Applied Physics and Electronics, Inc.) but with a different fundamental

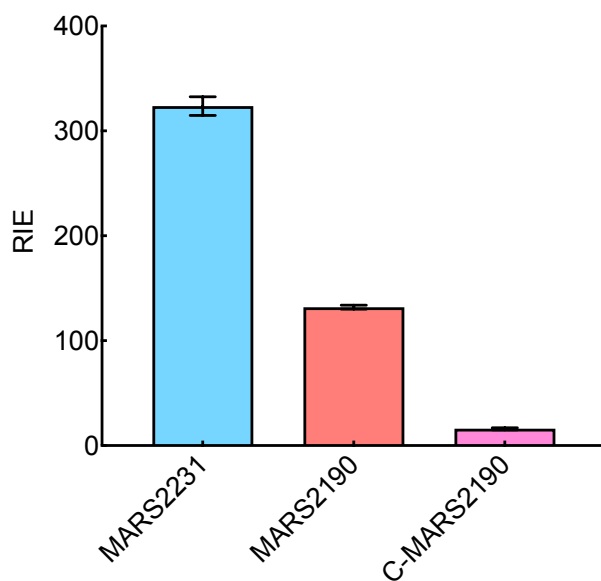
wavelength of 1064.2 nm (80 MHz repetition rate) and 6 ps pulse width was used. The intensity of the Stokes beam was modulated by a built-in EOM at 8 MHz. The other set-up is the same as the previous 1031.2 nm fundamental wavelength laser system.

Absorption and fluorescence spectra measurements

UV-Vis absorption spectra were recorded on a Varian Cary 500 UV-Vis Spectrophotometer (Agilent). The 50 μM dye solution (DMSO) with 1 mm cuvette was used to acquire the absorption spectra. In Supplementary Figure 4.6, 10 μM dye solution (DMSO) with 5 mm cuvette was used to get the absorption spectra. Fluorescence spectra were measured on a Shimadzu RF-6000 spectrofluorophotometer using a quartz microcuvette (Starna 18F-Q-10-GL14-S) with the same dye solution (10 μM DMSO solutions). The obtained spectra were self-normalized.

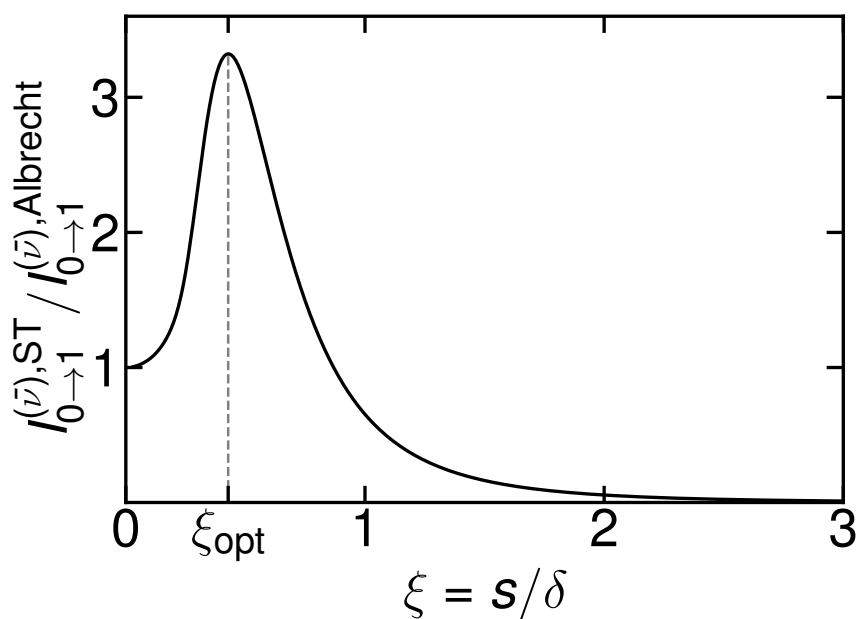
Uncertainty characterization of epr-SRS measurement

To examine the uncertainty of epr-SRS measurements, we performed epr-SRS measurements of replicate samples with the 1031.2 nm fundamental laser system, we randomly chose nitrile dye MARS2231 and alkyne dye MARS2190 and C-MARS2190 for characterization, whose epr-SRS intensity spanned across different levels. The results (Supplementary Figure 4.1) showed that the variation of each measurement is quite small: within 10 %.



Supplementary Figure 4.1. Uncertainty characterization of epr-SRS measurements of three dyes. Data is shown as mean \pm SEM. 4–6 replicates were used for each dye.

Connection between short-time and Albrecht's A- term formulas



Supplementary Figure 4.2. Ratio between short-time and Albrecht A-term Raman intensities as a function of $\xi = s/\delta$.

From eq 4.10 of the main text it follows that

$$\frac{I_{0 \rightarrow 1}^{(\bar{\nu}),ST}}{I_{0 \rightarrow 1}^{(\bar{\nu}),Albrecht}} = \frac{1}{\xi^4} \left| \int_0^\infty t e^{-t^2/2+it/\xi} dt \right|^2 = 1, \quad \xi \rightarrow 0 \quad (\text{S4.1})$$

In other words, the Albrecht expression can be considered as a large detuning ($\delta \gg s$) limit of the short-time formula. As shown in Supplementary Figure 4.2, the dependence of

$\frac{I_{0 \rightarrow 1}^{(\bar{\nu}),ST}}{I_{0 \rightarrow 1}^{(\bar{\nu}),Albrecht}}$ on ξ is not monotonic. Rather, an optimal value at around $\xi_{opt} \approx 0.43$ is found.

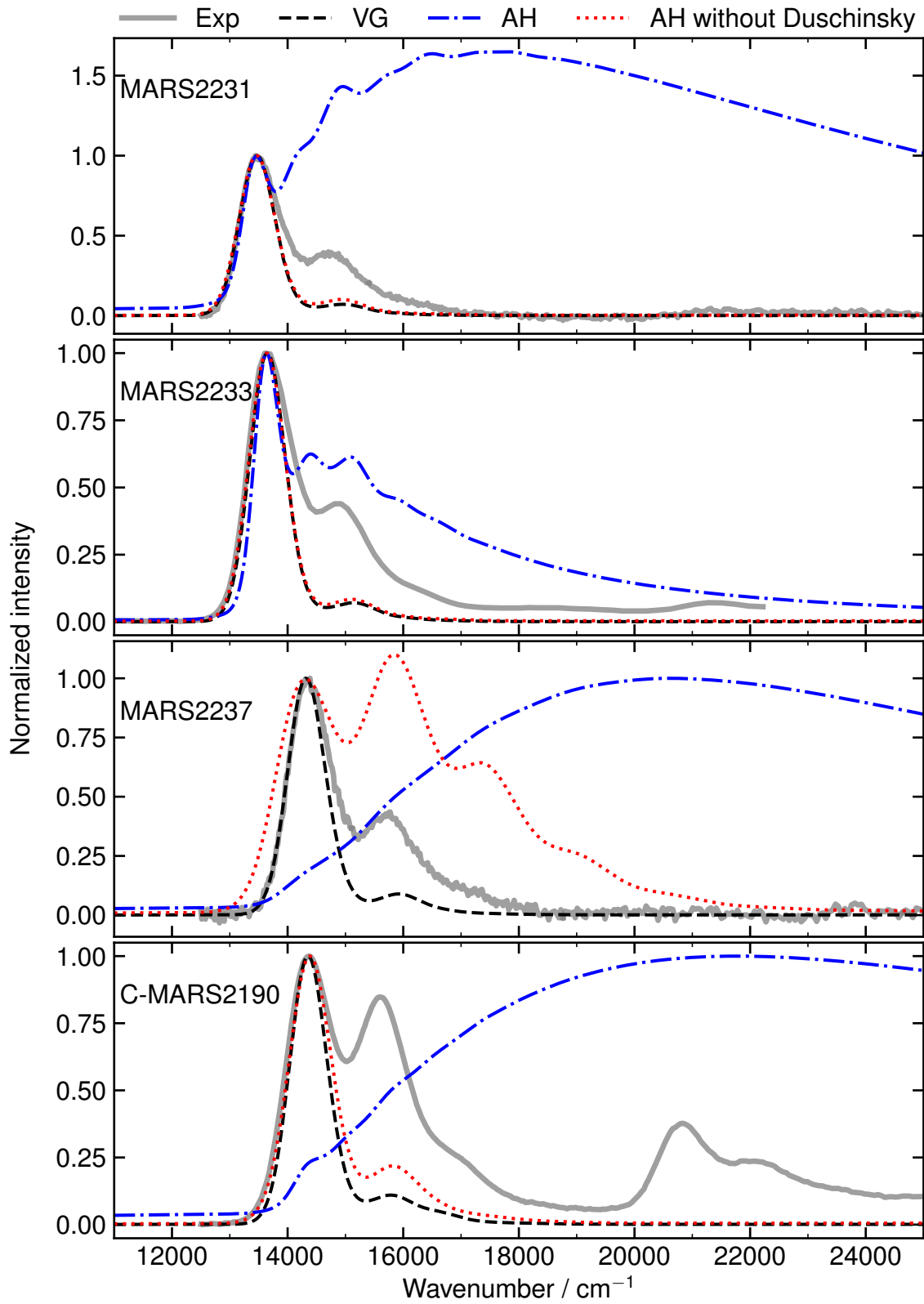
However, we note that s , defined as $s^2 = \sum_{\nu} s_{\nu}^2$, depends also on the Raman mode of interest (labeled $\bar{\nu}$ in the main text) and, specifically, that $s > s_{\bar{\nu}}$. Therefore, if $\xi_{\bar{\nu}} = s_{\bar{\nu}}/\delta > \xi_{opt}$, the displacements of all other modes would ideally be zero to minimize the difference $\xi - \xi_{opt}$. Otherwise, if $\xi_{\bar{\nu}} < \xi_{opt}$, other modes would ideally be displaced as to tune the value of ξ close to the optimal one. Supplementary Table 4.2 lists the values of ξ for molecules presented here.

Supplementary Table 4.2. Values of $\xi = s/\delta$ for epr-SRS probes studied in this work.

epr-SRS probes (860 nm)	ξ	epr-SRS probes (~ 840 nm)	ξ
9CN-MARS2222	0.44	MARS2228	0.41
MARS2228	0.35	MARS2231	0.36
MARS2225	0.33	MARS2237	0.28
MARS2231	0.31	FC10	0.27
MARS2237	0.25	PPCy-8a	0.21
9CN-MARS2238	0.24	PPCy-10a	0.24
MARS2233	0.29	PADBP-9	0.28
9CN-MARS2240	0.22	MARS2190	0.28
MARS2190	0.25	C-MARS2190	0.23
Bodipy-alkyne	0.21	C-MARS2143	0.22

Duschinsky and Herzberg-Teller effects

To analyze the potential Duschinsky and Herzberg-Teller effects, we modeled the absorption spectra of the MARS2231, MARS2233, MARS2237, and C-MARS2190 probes.



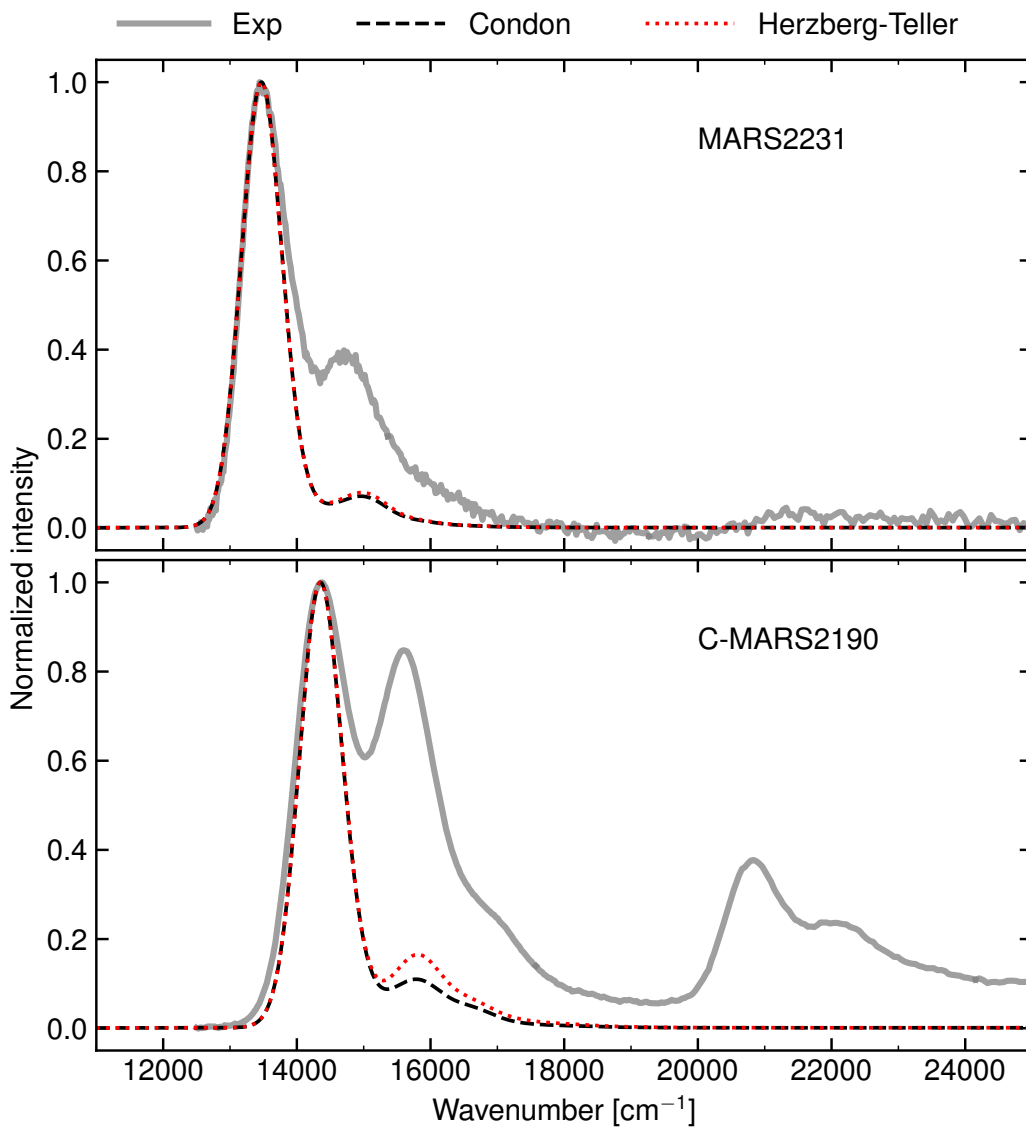
Supplementary Figure 4.3. Experimental and simulated electronic absorption spectra of MARS2231, MARS2233, MARS2237, and C-MARS2190. Simulations were based on the vertical gradient (VG) method, adiabatic Hessian (AH, including Duschinsky rotation) method, and AH method without Duschinsky rotation (by setting Duschinsky matrix J to identity, option USEJ FALSE in Orca). All simulations were performed using the Orca ESD module,⁵³ at room temperature (298.15 K), and within the Condon approximation for the transition dipole moment. To simplify the comparison of the lineshape, the simulated spectra were scaled and shifted to match the experiment at the 0-0 transition. A Gaussian broadening function with $\sigma = 280 \text{ cm}^{-1}$ was used for VG and “AH without Duschinsky” simulations, while $\sigma = 150 \text{ cm}^{-1}$ was used for AH simulations.

First, the absorption spectra were simulated within the vertical gradient (VG) model, which is a version of the DHO model, i.e., uses the same force-constant matrix for the ground and excited electronic states, and within the adiabatic Hessian (AH) model, in which the excited-state geometry is optimized and new vibrational modes and frequencies are evaluated there. Specifically, the VG model neglects any changes in frequencies or normal-mode (Duschinsky) rotation effects, whereas the AH model fully accounts for these effects. Importantly, both of these models neglect anharmonicity of the true potential energy surfaces. Supplementary Figure 4.3 shows that the VG model is more reliable and robust for the studied molecules due to the incorrect overestimation of the Duschinsky coupling between the excited-state modes in the AH model (compare AH with “AH without Duschinsky”). Although the AH approach is more accurate for MARS2233, it yields very inaccurate absorption spectra for the other three molecules. Hence, the results justify our choice of the VG model over the more expensive and less robust AH harmonic model.

Second, we turn to the non-Condon effects due to the dependence of the transition dipole moment on the atomic coordinates. The first-order, Herzberg-Teller correction to the Condon approximation accounts for the linear dependence of the transition dipole moment on the coordinates and is often sufficient to estimate the degree of non-Condon effects. This correction is typically necessary only in weakly allowed or symmetry-forbidden transitions. In Supplementary Figure 4.4, we compare the simulations within Condon and Herzberg-

Teller approximations with the experimental spectrum of MARS2231 and C-MARS2190, demonstrating that the Herzberg-Teller effect is negligible.

Analysis of the 0-0 transition energy



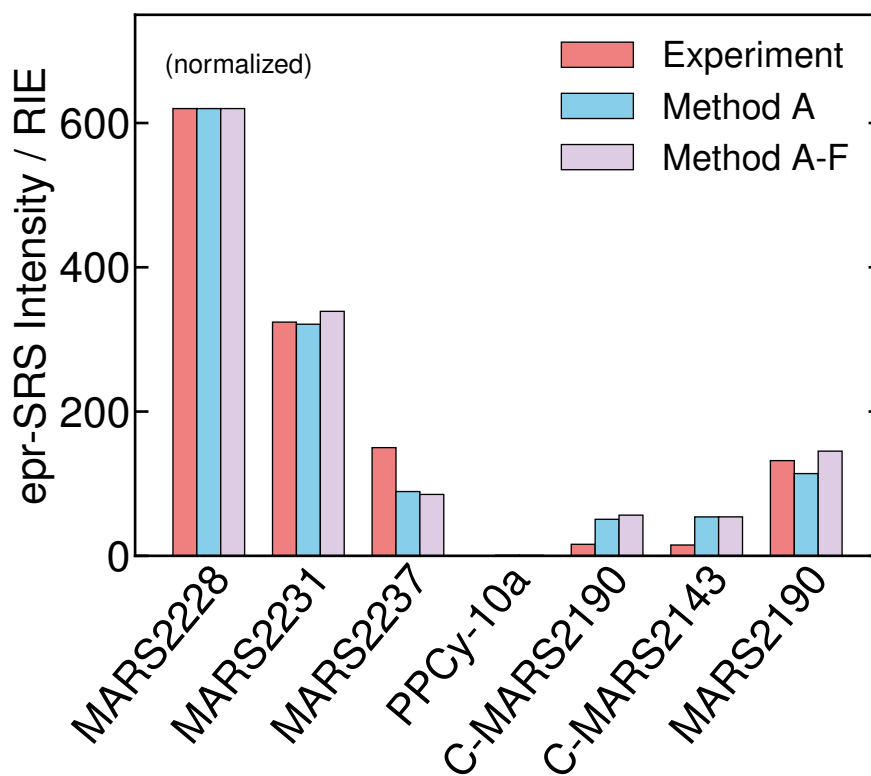
Supplementary Figure 4.4: Experimental and simulated electronic absorption spectra of MARS2231 and C-MARS2190 (only the lowest-energy electronic transition is modeled), where the simulations were based on the VG model and used either Condon or Herzberg-Teller approximation for the transition dipole moment. See Supplementary Figure 4.3 for further details.

Here, we motivate our interpretation of the absorption maximum as the 0-0 vibronic transition, as described in the Computational details of the main text. For molecules with a large Stokes shift, the absorption maximum frequency (ω_{max}) typically coincides with the vertical excitation frequency (ω_{eg}), which, in those cases, is very far from the 0-0 transition frequency (ω_{0-0}). Supplementary Figure 4.6 clearly shows that the molecules considered in this work do not fall into this category, since their Stokes shifts are only modest ($< 900 \text{ cm}^{-1}$). For molecules with such small Stokes shifts, the absorption maximum frequency is much closer to the 0-0 transition frequency than to the vertical excitation frequency. Still, their 0-0 transitions do not necessarily correspond to the respective absorption maxima. A more accurate estimate would be to use the frequency of intersection of absorption and emission spectra, which follows from the theory of vibronic transitions. However, this approach would require not only access to absorption, but also emission spectra. In addition, some prospective probes might not fluoresce due to a fast nonradiative relaxation, which would complicate the determination of the 0-0 transition energy. For these reasons, we decided to use the absorption maximum frequency as a reasonable estimate for the 0-0 transition energy. Here, we show that this specific choice does not significantly affect our results.

For convenience, let us denote by “Method A-F” the approach in which we use the intersection of absorption and fluorescence spectra to determine the 0-0 transition and by “Method A” the approach in which only the absorption maximum is used. Supplementary Table 4.3 shows the detunings computed using these two methods to determine the 0-0 vibronic transition frequency ω_{0-0} and using eq 4.11 of the main text to obtain the DHO-based estimate of the vertical excitation energy. We then used these two sets of detunings to compute the Raman intensities, whose values reflect the fact that the A-F detunings are red-shifted compared to the Method A detunings. However, when comparing to experimental values, all values are scaled to the highest Raman intensity (MARS2228). Supplementary Figure 4.5 shows that both methods result in a similar agreement between theory and experiment. In contrast to Method A-F, Method A allows us to model all molecules on the same footing, including those for which we might not have access to fluorescence spectra.

Supplementary Table 4.3. Comparing epr-SRS intensities from two simulation protocols, one using the absorption maximum frequency (Method A) as the 0-0 transition frequency, the other using the intersection of absorption and fluorescence spectra (Method A-F) as the 0-0 transition.

epr-SRS probes	pump/nm	Method A		Method A-F		I_A/I_{A-F}
		δ/cm^{-1}	$I_A/\text{arb.u.}$	δ/cm^{-1}	$I_{A-F}/\text{arb.u.}$	
MARS2228	838	1572	2.24e+05	1435	3.11e+05	0.72
MARS2231	838	1847	1.16e+05	1651	1.70e+05	0.68
MARS2237	838	2797	3.22e+04	2576	4.27e+04	0.75
PPCy-10a	838	3289	3.21e+02	3062	4.09e+02	0.78
C-MARS2190	842	2816	1.83e+04	2473	2.83e+04	0.65
C-MARS2143	842	2807	1.95e+04	2544	2.71e+04	0.72
MARS2190	842	2086	4.12e+04	1758	7.28e+04	0.57



Supplementary Figure 4.5. Comparing simulated intensities from method A/A-F to the measured values. Both methods result in a similar agreement between theory and experiment.

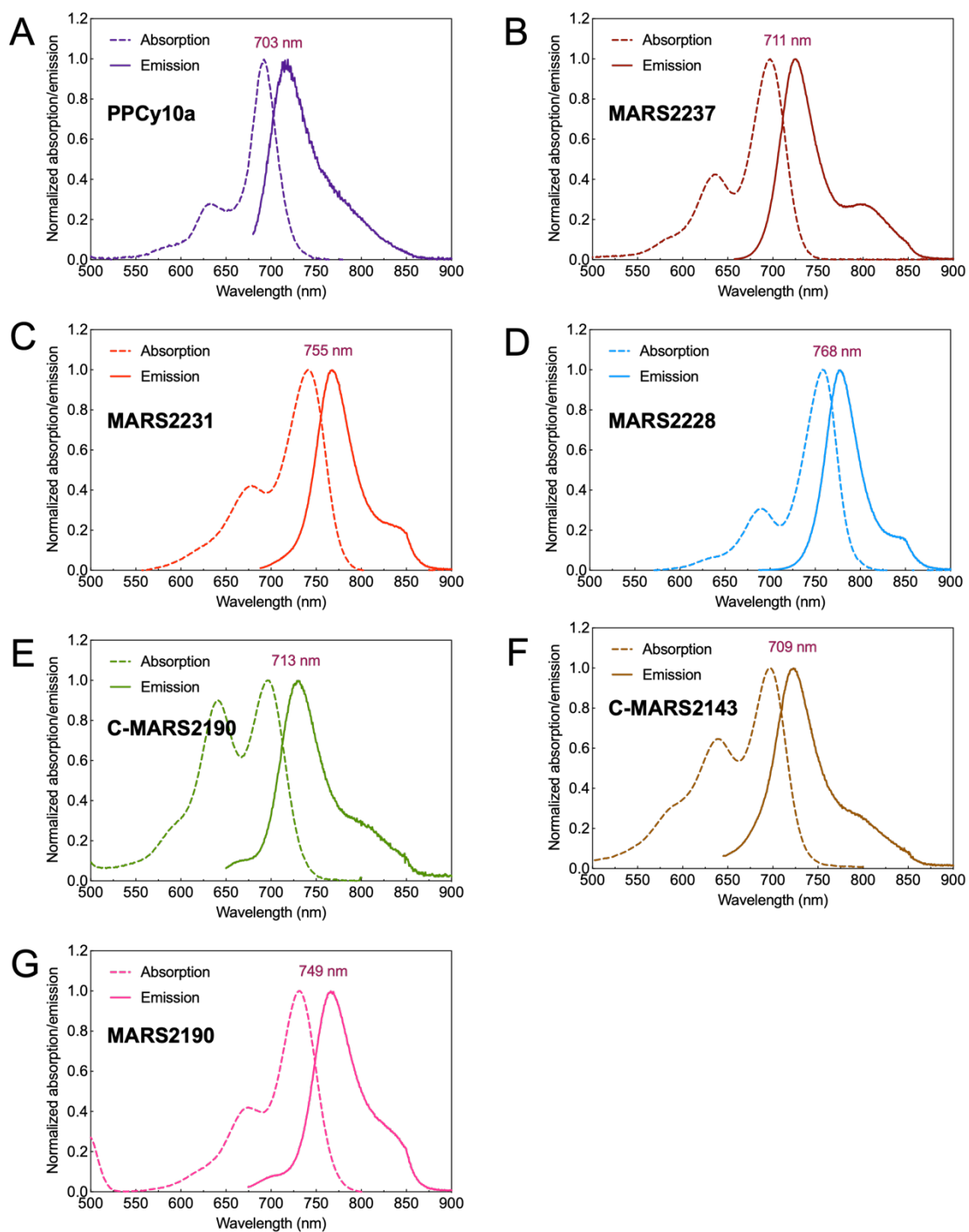
Dipole strengths: Simulation vs. experiment

Experimental dipole strengths were determined according to⁶⁷

$$\mu_{exp}^2 = \frac{3\hbar c \epsilon_0}{\pi} \int_{-\infty}^{\infty} \frac{\sigma(\omega)}{\omega} d\omega \quad (\text{S4.2})$$

where the experimental absorption cross section was obtained from the molar extinction coefficient using $\sigma(\omega) = \frac{\ln(10)\epsilon(\omega)}{N_A}$.

The results (Supplementary Table 4.4) show that the simulated transition dipole moments are reliable as they only differ from the experimental values by approximately a constant factor.



Supplementary Figure 4.6: Normalized absorption and fluorescence spectra of seven representative epr-SRS probes. The intersection wavelength between absorption and emission spectra is labeled on each graph.

Supplementary Table 4.4: Magnitudes of the experimental and simulated transition dipole moments in atomic units.

epr-SRS probes	$ \mu_{\text{exp}} $	$ \mu_{\text{sim}} $
C-MARS2190	3.01	5.24
MARS2190	3.26	5.50
9CN-MARS2238	3.35	5.50
9CN-MARS2240	3.54	5.42
MARS2237	3.79	5.55
MARS2231	3.89	5.91
MARS2228	3.57	6.10
PPCy-10a	3.40	5.25

4.7 Reference

1. Ploetz, E., Laimgruber, S., Berner, S., Zinth, W. & Gilch, P. Femtosecond stimulated Raman microscopy. *Appl. Phys. B Lasers Opt.* **87**, 389–393 (2007).
2. Freudiger, C. W. *et al.* Label-Free Biomedical Imaging with High Sensitivity by Stimulated Raman Scattering Microscopy. *Science* **322**, 1857–1861 (2008).
3. Ozeki, Y., Dake, F., Kajiyama, S., Fukui, K. & Itoh, K. Analysis and experimental assessment of the sensitivity of stimulated Raman scattering microscopy. *Opt. Express* **17**, 3651 (2009).
4. Du, J., Wang, H. & Wei, L. Bringing Vibrational Imaging to Chemical Biology with Molecular Probes. *ACS Chem. Biol.* **17**, 1621–1637 (2022).
5. Wei, L. *et al.* Super-multiplex vibrational imaging. *Nature* **544**, 465–470 (2017).
6. Miao, Y., Qian, N., Shi, L., Hu, F. & Min, W. 9-Cyanopyronin probe palette for super-multiplexed vibrational imaging. *Nat. Commun.* **12**, 4518 (2021).
7. Shi, L. *et al.* Highly-multiplexed volumetric mapping with Raman dye imaging and tissue clearing. *Nat. Biotechnol.* **40**, 364–373 (2022).
8. Lee, D. *et al.* Toward photoswitchable electronic pre-resonance stimulated Raman probes. *J. Chem. Phys.* **154**, 1–10 (2021).
9. Ao, J. *et al.* Switchable stimulated Raman scattering microscopy with photochromic vibrational probes. *Nat. Commun.* **12**, 1–8 (2021).
10. Shou, J. & Ozeki, Y. Photoswitchable stimulated Raman scattering spectroscopy and microscopy. *Opt. Lett.* **46**, 2176 (2021).

11. Fujioka, H. *et al.* Multicolor Activatable Raman Probes for Simultaneous Detection of Plural Enzyme Activities. *J. Am. Chem. Soc.* **142**, 20701–20707 (2020).
12. Kawatani, M. *et al.* 9-Cyano-10-telluriumpyronin Derivatives as Red-light-activatable Raman Probes. *Chem. ASIAN J.* **18**, (2023).
13. Xiong, H. *et al.* Stimulated Raman excited fluorescence spectroscopy and imaging. *Nat. Photonics* **13**, (2019).
14. Fischer, G. M., Isomäki-Krondahl, M., Göttker-Schnetmann, I., Daltrozzo, E. & Zumbusch, A. Pyrrolopyrrole Cyanine Dyes: A New Class of Near-Infrared Dyes and Fluorophores. *Chem. Eur. J.* **15**, 4857–4864 (2009).
15. Asher, S. UV Resonance Raman Studies Of Molecular Structure And Dynamics: Applications In Physical And Biophysical Chemistry. *Annu. Rev. Phys. Chem.* **39**, 537–588 (1988).
16. Kumble, R., Rush, T. S., Blackwood, M. E., Kozlowski, P. M. & Spiro, T. G. Simulation of non-condon enhancement and interference effects in the resonance Raman intensities of metalloporphyrins. *J. Phys. Chem. B* **102**, 7280–7286 (1998).
17. Bailey, S. E., Cohan, J. S. & Zink, J. I. Interference effects of multiple excited states in the resonance Raman spectroscopy of CpCoCOD. *J. Phys. Chem. B* **104**, 10743–10749 (2000).
18. Petrenko, T. & Neese, F. Analysis and prediction of absorption band shapes, fluorescence band shapes, resonance Raman intensities, and excitation profiles using the time-dependent theory of electronic spectroscopy. *J. Chem. Phys.* **127**, (2007).
19. Petrenko, T. & Neese, F. Efficient and automatic calculation of optical band shapes and resonance Raman spectra for larger molecules within the independent mode displaced harmonic oscillator model. *J. Chem. Phys.* **137**, (2012).
20. Egidi, F., Boino, J., Cappell, C. & Barone, V. A Robust and Effective Time-Independent Route to the Calculation of Resonance Raman Spectra of Large Molecules in Condensed Phases with the Inclusion of Duschinsky, Herzberg-Teller, Anharmonic, and Environmental Effects. *J. Chem. Theory Comput.* **10**, 346–363 (2014).
21. Baiardi, A., Bloino, J. & Barone, V. A general time-dependent route to Resonance-Raman spectroscopy including Franck-Condon, Herzberg-Teller and Duschinsky effects. *J. Chem. Phys.* **141**, (2014).
22. Rao, B. J., Gelin, M. F. & Domcke, W. Resonant Femtosecond Stimulated Raman Spectra: Theory and Simulations. *J. Phys. Chem. A* **120**, 3286–3295 (2016).
23. Quincy, T. J., Barclay, M. S., Caricato, M. & Elles, C. G. Probing Dynamics in Higher-Lying Electronic States with Resonance-Enhanced Femtosecond Stimulated Raman Spectroscopy. *J. Phys. Chem. A* **122**, 8308–8319 (2018).
24. de Souza, B., Farias, G., Neese, F. & Izsák, R. Efficient simulation of overtones and combination bands in resonant Raman spectra. *J. Chem. Phys.* **150**, (2019).
25. Mattiat, J. & Lubert, S. Time Domain Simulation of (Resonance) Raman Spectra of Liquids in the Short Time Approximation. *J. Chem. Theory Comput.* **17**, 344–356 (2021).
26. Tannor, D. J. Introduction to Quantum Mechanics: A Time-Dependent Perspective. University Science Books. Chapter 14 (2006).
27. Schatz, G. C. & Ratner, M. A. *Quantum mechanics in chemistry*. (Courier

- Corporation, 2002).
28. Kramers, H. A. & Heisenberg, W. On the dispersal of radiation by atoms. *ZEITSCHRIFT FÜR Phys.* **31**, 681–708 (1925).
 29. Dirac, P. A. M. The quantum theory of dispersion. *Proc. R. Soc. LONDON Ser. A-CONTAINING Pap. A Math. Phys. CHARACTER* **114**, 710–728 (1927).
 30. LEE, S. Y. & HELLER, E. J. TIME-DEPENDENT THEORY OF RAMAN-SCATTERING. *J. Chem. Phys.* **71**, 4777–4788 (1979).
 31. HELLER, E. J., SUNDBERG, R. L. & TANNOR, D. SIMPLE ASPECTS OF RAMAN-SCATTERING. *J. Phys. Chem.* **86**, 1822–1833 (1982).
 32. Rohrdanz, M. A. & Cina, J. A. Probing intermolecular communication via lattice phonons with time-resolved coherent anti-Stokes Raman scattering. *Mol. Phys.* **104**, 1161–1178 (2006).
 33. Makhov, D. V & Shalashilin, D. V. Simulation of the effect of vibrational pre-excitation on the dynamics of pyrrole photo-dissociation. *J. Chem. Phys.* **154**, (2021).
 34. Worth, G. A. & Lasorne, B. Gaussian Wave Packets and the DD-vMCG Approach. in *Quantum Chemistry and Dynamics of Excited States* 413–433 (2020). doi:<https://doi.org/10.1002/9781119417774.ch13>
 35. Conte, R. & Ceotto, M. Semiclassical Molecular Dynamics for Spectroscopic Calculations. in *Quantum Chemistry and Dynamics of Excited States* 595–628 (2020). doi:<https://doi.org/10.1002/9781119417774.ch19>
 36. Bonfanti, M., Petersen, J., Eisenbrandt, P., Burghardt, I. & Pollak, E. Computation of the $S_1 \leftarrow S_0$ Vibronic Absorption Spectrum of Formaldehyde by Variational Gaussian Wavepacket and Semiclassical IVR Methods. *J. Chem. Theory Comput.* **14**, 5310–5323 (2018).
 37. Werther, M. & Grossmann, F. Apoptosis of moving nonorthogonal basis functions in many-particle quantum dynamics. *Phys. Rev. B* **101**, (2020).
 38. Werther, M., Choudhury, S. L. & Grossmann, F. Coherent state based solutions of the time-dependent Schrodinger equation: hierarchy of approximations to the variational principle. *Int. Rev. Phys. Chem.* **40**, 81–125 (2021).
 39. Curchod, B. F. E. & Martínez, T. J. Ab Initio Nonadiabatic Quantum Molecular Dynamics. *Chem. Rev.* **118**, 3305–3336 (2018).
 40. Prlj, A. *et al.* Semiclassical Approach to Photophysics Beyond Kasha’s Rule and Vibronic Spectroscopy Beyond the Condon Approximation. The Case of Azulene. *J. Chem. Theory Comput.* **16**, 2617–2626 (2020).
 41. Vaníček, J. & Begušić, T. Chapter 6 - Ab Initio Semiclassical Evaluation of Vibrationally Resolved Electronic Spectra With Thawed Gaussians. in (eds. Marquardt, R. & Quack, M. B. T.-M. S. and Q. D.) 199–229 (Elsevier, 2021). doi:<https://doi.org/10.1016/B978-0-12-817234-6.00011-8>
 42. Begusic, T. & Vaníček, J. Efficient Semiclassical Dynamics for Vibronic Spectroscopy beyond Harmonic, Condon, and Zero-Temperature Approximations. *Chimia (Aarau)*. **75**, 261–266 (2021).
 43. Begusic, T., Tapavicza, E. & Vaníček, J. Applicability of the Thawed Gaussian Wavepacket Dynamics to the Calculation of Vibronic Spectra of Molecules with Double-Well Potential Energy Surfaces. *J. Chem. Theory Comput.* **18**, 3065–3074 (2022).

44. Albrecht, A. C. On the theory of Raman intensities. *J. Chem. Phys.* **34**, 1476–1484 (1961).
45. Matikonda, S. S., Ivanic, J., Gomez, M., Hammersley, G. & Schnermann, M. J. Core remodeling leads to long wavelength fluoro-coumarins. *Chem. Sci.* **11**, 7302–7307 (2020).
46. Majumdar, P. *et al.* Cyclometalated Ir(III) complexes with styryl-BODIPY ligands showing near IR absorption/emission: preparation, study of photophysical properties and application as photodynamic/luminescence imaging materials. *J. Mater. Chem. B* **2**, 2838–2854 (2014).
47. Zhou, Y. *et al.* Pyrrolopyrrole aza boron dipyrromethene based two-photon fluorescent probes for subcellular imaging. *J. Mater. Chem. B* **6**, 5570–5581 (2018).
48. Hestand, N. J. & Spano, F. C. Expanded Theory of H- and J-Molecular Aggregates: The Effects of Vibronic Coupling and Intermolecular Charge Transfer. *Chem. Rev.* **118**, 7069–7163 (2018).
49. Pastierik, T., Šebej, P., Medalová, J., Štacko, P. & Klán, P. Near-infrared fluorescent 9-phenylethynylpyronin analogues for bioimaging. *J. Org. Chem.* **79**, 3374–3382 (2014).
50. Lee, J., Crampton, K. T., Tallarida, N. & Apkarian, V. A. Visualizing vibrational normal modes of a single molecule with atomically confined light. *Nature* **568**, 78–82 (2019).
51. Xu, J. *et al.* Determining structural and chemical heterogeneities of surface species at the single-bond limit. *Science* **371**, 818–822 (2021).
52. Hassing, S. & Mortenson, O. S. The roles of vibronic coupling and the Duschinsky effect in resonance Raman scattering. *J. Mol. Spectrosc.* **87**, 1–17 (1981).
53. Neese, F., Wennmohs, F., Becker, U. & Riplinger, C. The ORCA quantum chemistry program package. *J. Chem. Phys.* **152**, (2020).
54. Neese, F. Software update: the ORCA program system, version 4.0. *WILEY Interdiscip. Rev. Mol. Sci.* **8**, (2018).
55. Kostjukov, V. V. Excitation of rhodamine 800 in aqueous media: a theoretical investigation. *J. Mol. Model.* **28**, (2022).
56. Grimme, S., Bannwarth, C. & Shushkov, P. A Robust and Accurate Tight-Binding Quantum Chemical Method for Structures, Vibrational Frequencies, and Noncovalent Interactions of Large Molecular Systems Parametrized for All spd-Block Elements (Z = 1–86). *J. Chem. Theory Comput.* **13**, 1989–2009 (2017).
57. Bannwarth, C., Ehlert, S. & Grimme, S. GFN2-xTB—An Accurate and Broadly Parametrized Self-Consistent Tight-Binding Quantum Chemical Method with Multipole Electrostatics and Density-Dependent Dispersion Contributions. *J. Chem. Theory Comput.* **15**, 1652–1671 (2019).
58. Barone, V. & Cossi, M. Quantum Calculation of Molecular Energies and Energy Gradients in Solution by a Conductor Solvent Model. *J. Phys. Chem. A* **102**, 1995–2001 (1998).
59. Petersilka, M., Gossmann, U. J. & Gross, E. K. U. Excitation energies from time-dependent density-functional theory. *Phys. Rev. Lett.* **76**, 1212–1215 (1996).
60. Perdew, J. P. Density-functional approximation for the correlation energy of the inhomogeneous electron gas. *Phys. Rev. B* **33**, 8822 (1986).

61. Adamo, C. & Barone, V. Toward reliable density functional methods without adjustable parameters: The PBE0 model. *J. Chem. Phys.* **110**, 6158–6170 (1999).
62. Zhou, P. Why the lowest electronic excitations of rhodamines are overestimated by time-dependent density functional theory. *Int. J. Quantum Chem.* **118**, e25780 (2018).
63. Becke, A. D. Density-functional exchange-energy approximation with correct asymptotic behavior. *Phys. Rev. A* **38**, 3098 (1988).
64. Iikura, H., Tsuneda, T., Yanai, T. & Hirao, K. A long-range correction scheme for generalized-gradient-approximation exchange functionals. *J. Chem. Phys.* **115**, 3540–3544 (2001).
65. Hanwell, M. D. *et al.* Avogadro: an advanced semantic chemical editor, visualization, and analysis platform. *J. Cheminform.* **4**, 17 (2012).
66. Avogadro: an open-source molecular builder and visualization tool. Version 1.93.0. <http://avogadro.cc/>.
67. Lewis, J. E. & Maroncelli, M. On the (uninteresting) dependence of the absorption and emission transition moments of coumarin 153 on solvent. *Chem. Phys. Lett.* **282**, 197–203 (1998).

SECOND GENERATION ELECTRONIC PRERESONANCE RAMAN IMAGING PROBES

5.1 Introduction

Raman imaging detects the inherent vibration motion of chemical bonds and shows unique advantages for imaging biomolecules. The chemical bond derived contrast ensures imaging abundant biomolecules tagged with just triple bonds (e.g. $C\equiv C$, $C\equiv N$) or even isotopes (e.g. deuterium) but not bulkier fluorophore^{1,2}. The spectroscopy-based feature of Raman is especially beneficial for sensing cellular environment in a non-invasive manner³⁻⁵. Raman imaging also holds high promise for highly multiplexed imaging for its much narrower Raman peak linewidth (50-100 times narrower than fluorescence peaks). However, the bottleneck for Raman imaging is always the sensitivity. The cross section of spontaneous Raman scattering of common non-resonant molecule is at least 12 orders of magnitude smaller than the fluorescence cross section of typical fluorophores. Since the last one and half decade, tremendous advances in both instrumentation and molecule design have pushed the sensitivity of Raman imaging close to what is offered by fluorescence. Stimulated Raman scattering (SRS) microscopy improved the sensitivity of Raman scattering by up to 10^8 -fold, resulting in millimolar or sub-millimolar detection limit⁶⁻⁸. The recent discovery of electronic preresonance (epr) MARS dyes provides another 10^3 to 10^4 enhancement by coupling triple bonds to near infrared chromophores displaying absorption close to the laser wavelength (~ 900 nm)^{9,10}, largely decreasing detection limit to as low as 250 nM. This striking signal enhancement renders highly-efficient super-multiplexed (> 16 color) Raman imaging in the cell silent region ($1800 - 2800$ cm^{-1})^{9,11}.

Although with these breakthroughs, there is still a sensitivity gap between MARS dyes and the ultimate single molecule detection (detection limit < 8 nM)⁹ (Supplementary Figure 5.1). Improving the sensitivity of epr-SRS dyes is highly demanded to allow broader range of applications (e.g. super-multiplexed super-resolution imaging). Recently we did a systematic study of various epr-SRS dye scaffolds and disclosed the structure-function relationship for epr enhancement¹²:

$$I_{epr}^{(\bar{\nu})} \propto \frac{\mu^4 S_{\bar{\nu}}^2}{\delta^4}$$

where μ is transition dipole moment (μ is related to the more common parameter extinction coefficient ϵ : $\mu^2 \propto \int_{-\infty}^{+\infty} \frac{\epsilon(\omega)}{\omega} d\omega$, ω : frequency), $\Delta_{\bar{\nu}}$ is Raman mode displacement and δ is detuning ($\delta = \omega_{eg} - \omega_l$, the difference between vertical excitation frequency ω_{eg} and the incident light frequency ω_l). Larger transition dipole moment (translate to stronger absorption or higher extinction coefficient), larger displacement and smaller detuning leads to larger Raman intensity. Considering that the background arising from electronic excitation increases more steeply with smaller detuning, the detuning is ideally not smaller than $1.5 \Gamma_e$ (Γ_e is the homogeneous line width of the electronic transition, $\sim 700 \text{ cm}^{-1}$). While the transition dipole moment and detuning can be measured by absorption, the displacement can only be accessed by quantum computation¹². This equation lays the theoretical foundation for improving epr-SRS probes.

Here, we adopted structure-function relationship to design and screen stronger epr-SRS probes based on the alkynyl pyronin or nitrile pyronin scaffold. By functionalizing both phenyl ring and Si, therefore benefiting from larger displacement, larger transition dipole

moment as well as smaller detuning, optimized alkyne pyronin has 3.7 times signal enhancement compared with non-functionalized parent molecule. With slightly extending the conjugation and sulfonic acid functionalization to reduce aggregation, optimized nitrile pyronin has 2.7 folds signal enhancement compared with previous strongest nitrile dyes. This study provides the first rational design and optimization of epr-SRS dyes and should guide the future development of epr-SRS dye to finally bridge the sensitivity gap between Raman and fluorescence.

5.2 Results

The current MARS palette has two skeletons: alkynyl and nitrile pyronin. Although the current work horse of epr-SRS dyes is nitrile pyronin dyes^{11,13-17}, we started from optimizing alkynyl pyronin scaffold as alkynes allow more derivatizations by substituting the capped phenyl ring while nitrile is a terminal group and lacks modification on one side. On the basis of the parent molecule (alkynyl Si pyronin **1**), we explored the effect of different substitution groups that compatible with the synthesis routes (Lithium-halogen exchange, see supplementary information) on the phenyl ring (Figure 5.1a). The substituted dye derivatives are ranked by their absorption wavelength in Figure 5.1a. It shows that electronic donation groups (EDG) lead to hypsochromic shift in absorption while electronic withdrawing groups (EWG) introduce bathochromic shift, which can be fairly correlated with their Hammett constants (Supplementary Figure 5.2). More interestingly, the EWG substituted phenyl ring couple the alkyne to the chromophore stronger, representing by higher Raman mode displacement $\Delta_{\bar{\nu}}$ of the alkyne. In contrast, EDG weaken the coupling of the alkyne to the chromophore core. For another important factor, the absorption strength ϵ , the substitution groups have various effects which are unlikely to predict. We follow the common way of characterizing the Raman signal of alkynes using the relative intensities versus EdU (RIE). Among all the phenyl ring modified derivatives, the meta fluorine substituted compound **10** appears to be the hit which has more than 1.6 times sensitivity in its alkyne peak compared to its parent molecule **1** (210 vs 130 in RIE, Figure 5.1b). This can be explained by its redder

absorption (10 nm redder), higher displacement (1.15 times larger, 0.176 vs 0.154) and relatively large extinction coefficient.

In addition to the Raman signal, we are also interested in the peak frequency as peak shift is beneficial to multiplexing. Interestingly, the peak frequency also highly depends on the substitution groups (Figure 5.1c). EDGs shift the frequency to the lower region and EWGs have the opposite trend. Similar to the absorption, the frequency also has linear correlation with the Hammett constants (Supplementary Figure 5.3). The tuning of frequency can be as large as 52 cm^{-1} (2154 cm^{-1} of **4** vs 2206 cm^{-1} of **7**). This straightforward dependence of Raman peak frequency on substitution group gives us an accurate and quantitative tool to design multiplex probes. When combined with isotope ^{13}C labeling^{18,19} ($\text{C}\equiv\text{C}$, $^{13}\text{C}\equiv\text{C}$, $\text{C}\equiv\text{C}^{13}$ and $^{13}\text{C}\equiv^{13}\text{C}$), the multiplexity can be further expanded by several times.

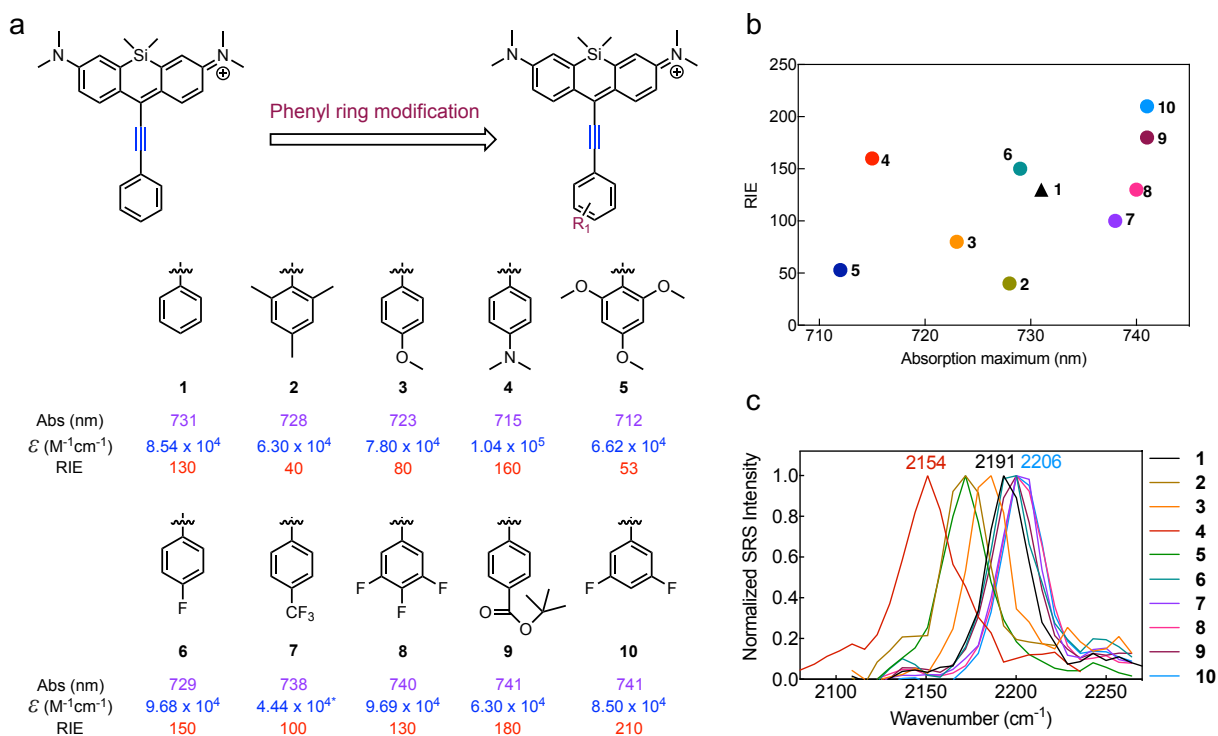


Figure 5.1: Phenyl ring modification on alkynyl pyronin. (a) The parent dye **1** with another 9 derivatives having phenyl modifications. The three key factors are listed under their structures. The measurements were taken in DMSO. (b) The plots of RIE and absorption maximum of phenyl ring substituted derivatives. (c) The normalized SRS spectra of phenyl ring substituted derivatives. *The absorption spectrum of **7** indicates a large portion of dyes exists as aggregates in DMSO.

Going beyond phenyl ring modification, the centered Si represents another site for modification but is rarely explored before. The widely used Si rhodamine dyes always have dimethylsilyl group in the scaffold, but a recent study showcased that the silyl modification can finely tune the photophysics of the dyes²⁰. The commercially available dichlorosilanes provide rapid access for silyl modification on the Si pyronin scaffold (Figure 5.2a). Most silyl modifications that are compatible with the synthesis procedure are hydrocarbon chains and halogen substituted hydrocarbon chains. These modifications appear to have minor effects on the performance of the dyes. Alkyl modification leaves the absorption unchanged (**11 - 14**), chloropropyl (**15**) and trifluoropropyl group (**16**) on the Si slightly redshift the absorption (< 5 nm). Divinyl (**17**) and diphenyl (**18**) modifications redshift the absorption a bit more (4 - 12 nm). However, the silyl modifications have larger influence on the extinction coefficients, with chloropropyl (**15**) and trifluoropropyl group (**16**) showing the largest (> 20 % than **1**) extinction coefficients. It is also noteworthy mentioning that these halogen bearing groups also improve the synthesis yield probably due to lowering the electron density of the electron-rich ketone electrophiles²¹. The overall SRS intensity is lower for those dyes with significant lower extinction coefficients compared with the parent dye **1** while chloropropyl (**15**) and trifluoropropyl group (**16**) substituted dyes have comparable signals (Figure 5.2b).

The frequency of the all the dyes is unperturbed by the available silicon modification (Figure 5.2c).

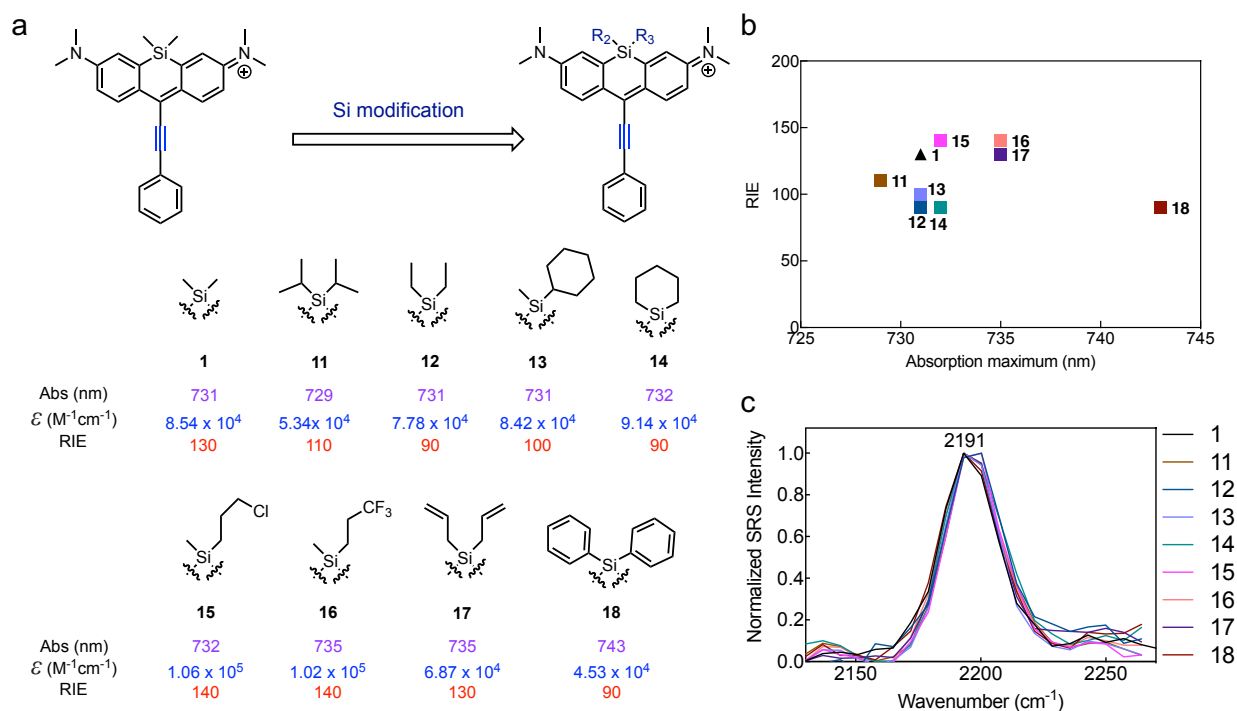


Figure 5.2: Silyl modification on alkyne pyronin. (a) The parent dye **1** with another 8 derivatives having silyl modifications. The three key factors are listed under their structures. (b) The plots of RIE and absorption maximum of silyl ring substituted derivatives. (c) The normalized SRS spectra of silyl substituted derivatives. All measurements were taken in DMSO.

Based on the results of previous phenyl and silyl modification, we next sought to explore derivatives combining both modification (Figure 5.3a). Taking advantage of the meta fluorine substituted hit **10** and the higher extinction coefficient brought by the trifluoropropyl group, the dual-modified dye **19** presents much higher alkyne Raman intensity: 3.7 times higher than the parent dye **1** (Figure 5.3a & 5.3b). The all three key factors of determining epr-SRS signals: larger extinction coefficient (+ 36%), larger Raman displacement $\Delta_{\bar{\nu}}$ (+

22%) and smaller detuning δ (- 18%) altogether account for the large enhancement. For the higher reactivity of trifluoropropyl substituted ketone intermediate, steric phenyl acetylene with substitution groups in the ortho position can be conjugated to the pyronin core. Dye **20** and **21** were successfully synthesized and they produce similar enhanced Raman signals (Figure 5.3a & 5.3b). Their alkyne Raman peak frequency follows the rule obtained from phenyl ring substitution (Figure 5.1c): EWGs shift the peak to higher frequency (Figure 5.3c). To prove this strategy as general for pyronin alkyne, we also synthesized redder alkyne pyronin with more side rings (Supplementary Figure 5.4). Larger dye skeleton tends to aggregate more with lower extinction coefficients, but phenyl and silyl modification still improve the Raman signal. However, for all the alkynyl pyronin dyes, their Raman signals were completely quenched in water for the formation of H aggregates. Further modification to improve the solubility and reduce aggregations is needed for biological use^{22,23}.

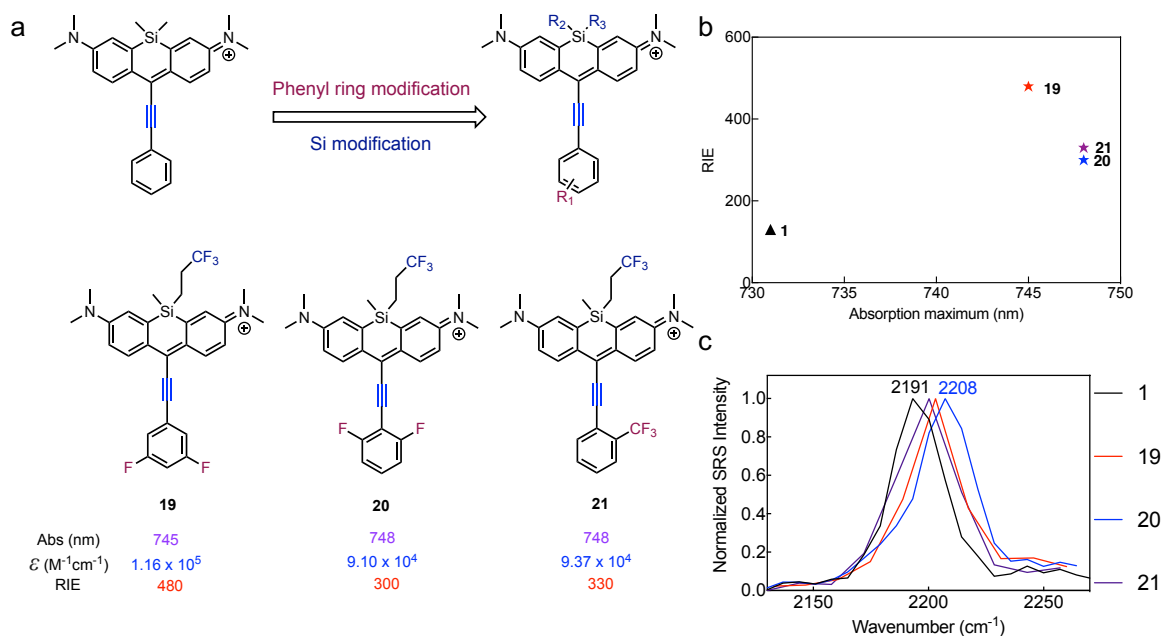


Figure 5.3: Both phenyl and silyl modification on alkynyl pyronin. (a) Three alkynyl pyronin dyes **19 - 21** with trifluoropropyl group on silicon and EWGs on the phenyl ring. The three key factors are listed under their structures. (b) The plots of RIE and absorption maximum of phenyl ring substituted derivatives. (c) The normalized SRS spectra of phenyl ring substituted derivatives. All measurements were taken in DMSO.

Learning from optimizing alkynyl pyronins, we further applied the learned strategy to optimize nitril pyronin dyes. The lack of phenyl modification for nitrile dyes reduces the dimension of structure modification, but the compatibility of nitrile pyronin in aqueous environment makes improving nitrile pyronin dyes more worthwhile for biological imaging. We again started with nitrile Si pyronin dye **25** as the parent molecule and subjected **25** for silyl modification (Figure 5.4). From the results of silyl modification of alkynyl pyronins (Figure 5.2), we specifically functionalize silyl with trifluoropropyl and chloropropyl groups, hoping to improve the extinction coefficient and therefore improve the signals. The complete characterization of the dyes is listed in Table 5.1. Indeed, trifluoropropyl (**26**) and chloropropyl (**27**) group functionalized silyls give slightly higher extinction coefficients (Table 5.1), but comparable nitrile Raman signal in DMSO (Figure 5.4b). In PBS, **25** has slightly higher signals than the silyl derivatives **26** and **27** (Figure 5.4c), probably for its higher hydrophilicity. Since there is still some space to redshift the absorption of the dyes for smaller detuning, we expanded the side ring of the pyronin core. Each side ring gives ~15 nm bathochromic shift in the absorption of nitrile Si pyronins (Table 5.1). For the non-symmetric structures (**28 - 32**), silyl modifications give lower absorption strength and lower Raman signals (**29/30** vs **28**, Table 5.1 and Figure 5.4b & 5.4c) while trifluoropropyl group slightly enhance the performance of ethylated dye (**32** vs **31**, Table 5.1 and Figure 5.4b & 5.4c). For the structure with more side rings (**34 & 35**), trifluoropropyl group largely increase the extinction coefficient with 1.6 times Raman signal in PBS (**34** vs **33**, Table 5.1 and Figure 5.4c).

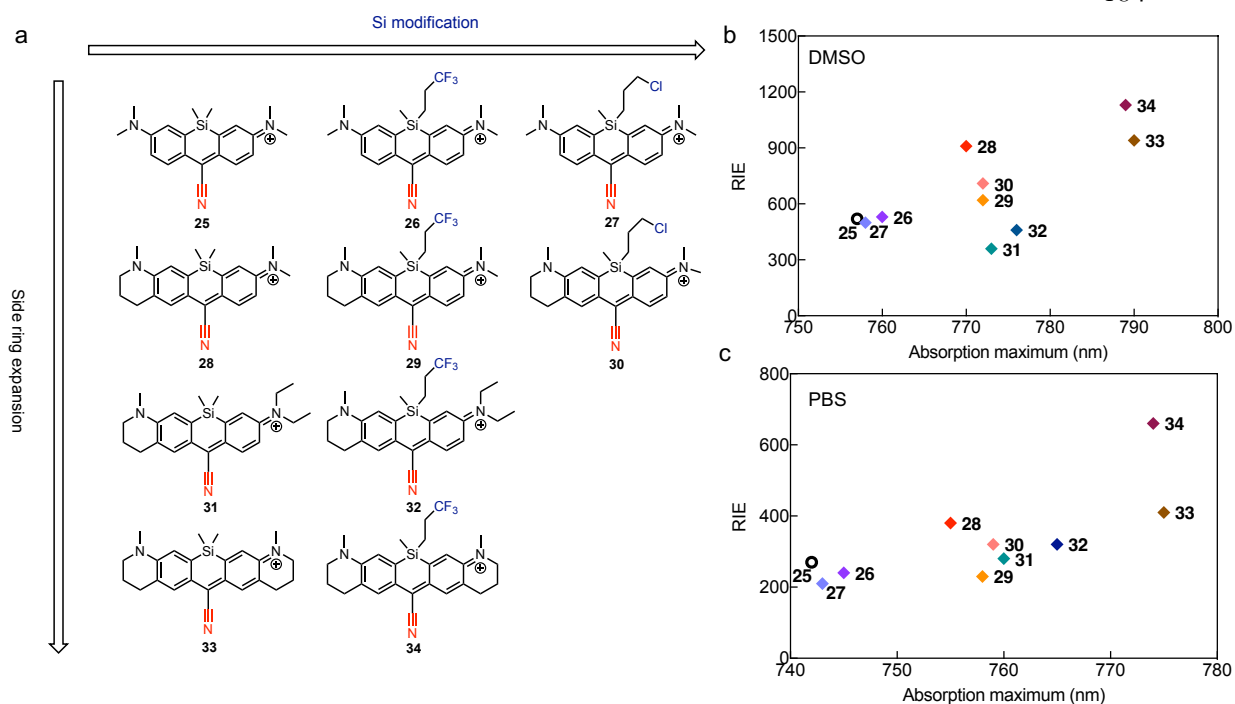


Figure 5.4: Nitrile silicon pyronin derivatives. (a) The structures of nitrile silicon pyronin derivatives. (b) The plots of RIE and absorption maximum of nitrile silicon pyronin derivatives in DMSO. (c) The plots of RIE and absorption maximum of nitrile silicon pyronin derivatives in PBS (with 10% DMSO).

Table 5.1: The photophysical properties of nitrile silicon pyronin derivatives.

Dye	Abs (nm) ^a	ϵ (M ⁻¹ cm ⁻¹) ^a	RIE ^a	Raman peak (cm ⁻¹) ^a	Abs (nm) ^b	ϵ (M ⁻¹ cm ⁻¹) ^b	RIE ^b	Raman peak (cm ⁻¹) ^b
25	757	1.16×10^5	520	2227	742	1.06×10^5	270	2234
26	760	1.39×10^5	530	2227	745	1.26×10^5	240	2234
27	758	1.31×10^5	500	2227	743	1.14×10^5	210	2234
28	770	7.42×10^4	910	2226	755	8.98×10^4	380	2233
29	772	6.71×10^4	710	2226	758	5.59×10^4	230	2233
30	772	6.00×10^4	620	2226	759	7.52×10^4	320	2233
31	773	6.00×10^4	360	2226	760	5.18×10^4	280	2233
32	776	6.71×10^4	460	2226	765	7.38×10^4	320	2233
33	790	7.62×10^4	940	2224	775	6.31×10^4	410	2231
34	789	1.29×10^5	1130	2224	774	9.75×10^4	660	2231

a: measured in DMSO; b: measured in PBS (with 10% DMSO).

We then shifted to nitrile C pyronin optimization. Unlike the commercially available dichlorosilanes for rapid synthesis of silyl modified structures, there lacks the corresponding reagents for center carbon modification. Although the center C modification with substituted pinacol ester intermediates is possible with reported method²⁴, we skipped center carbon modification. We instead focused on tuning the absorption wavelength of the nitrile C pyronin dyes. The carbon pyronin is bluer than the silicon pyronin, thus allows more derivatizations for shifting the absorption with expanded side rings or extending conjugation length with more double bonds. Based on the structure of MARS2231 (absorption maximum at 744/728 nm (DMSO/PBS), Supplementary Figure 5.5), we added one more double bond in the side ring and substitute the quinoline structure with methyl groups for improved stability, a common motif in dye chemistry²⁵ (Figure 5.5a). The complete characterization of the C pyronin dyes is listed in Table 5.2. Extending the conjugation system with additional double bond results in ~ 25 nm bathochromic shift (**35** with absorption maximum of 769/754 nm in DMSO/PBS vs MARS2231), larger than that induced by expanded side rings. This smaller detuning multiplied Raman intensity by 3 times (Table 5.2 and Supplementary Figure 5.5). However, the signal enhancement of **35** in PBS is lower for the diminished absorption strength. This is again caused by the formation of aggregation, evidenced by the rising of the shoulder peak around 700 nm in absorption. The introduced double bond makes the dye more planar and have a higher tendency to form aggregations. Functionalizing the hydrophobic dyes with sulfo groups is a validated method for reducing aggregates and improving performance in water²⁶⁻²⁸. We applied this strategy by sulfonating the 4-methyl group and obtained dye **36**. The introduced sulfonate group has minimal effect on the photophysics of the dye in DMSO (**36** vs **35**, Figure 5.5b and Table 5.2), but significantly reduces aggregation, improves extinction coefficient and enhances the signals by 32% in PBS (**36** vs **35**, Figure 5.5c and Table 5.2). Meanwhile we expanded one side ring and obtained redder dye **37** and **38**. Both of them break the sensitivity records for epr-SRS dyes with **37** achieving RIE of 1690 in DMSO and **38** achieving RIE of 640 in PBS (Figure 5.5b & 5.5c). Adding more methyl groups on the expanded ring results in dye **39** and **40**, which we believe have even better signals for slightly redder absorption and higher extinction coefficients.

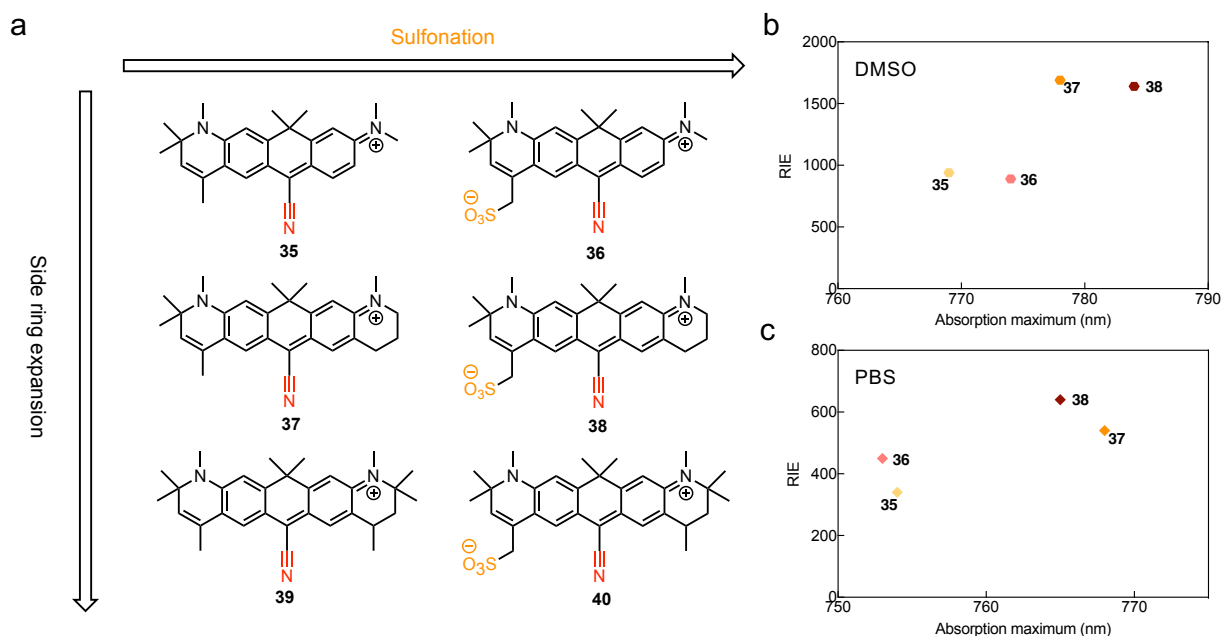


Figure 5.5: Nitrile carbon pyronin derivatives. (a) The structures of nitrile carbon pyronin derivatives. (b) The plots of RIE and absorption maximum of nitrile carbon pyronin derivatives in DMSO. (c) The plots of RIE and absorption maximum of nitrile carbon pyronin derivatives in PBS (with 10% DMSO).

Table 5.2: The photophysical properties of nitrile carbon pyronin derivatives.

Dye	Abs (nm) ^a	ϵ ($M^{-1}cm^{-1}$) ^a	RIE ^a	Raman peak (cm^{-1}) ^a	Abs (nm) ^b	ϵ ($M^{-1}cm^{-1}$) ^b	RIE ^b	Raman peak (cm^{-1}) ^b
35	769	7.41×10^4	940	2230	754	4.78×10^4	340	2237
36	774	7.21×10^4	890	2232	753	6.90×10^4	450	2237
37	778	1.33×10^5	1690	2230	768	5.85×10^4	540	2237
38	784	1.13×10^5	1640	2232	765	7.33×10^4	640	2237
39	781	7.61×10^4			770	2.71×10^4		
40	786	9.88×10^4			767	7.71×10^4		

a: measured in DMSO; b: measured in PBS (with 10% DMSO).

Among nitrile pyronin dyes, our previous theoretical study revealed that oxygen core dye has larger displacement than carbon and silicon core dyes¹². However, their bluer absorption limits their Raman signals. From this perspective, we sought to optimize oxygen core dye by extending the conjugation length and shift the absorption. We hence added two double bonds in the side rings and successfully obtained dye **42** with 42 nm bathochromic shift and about 2.7 x Raman signal compared with the parent dye **41** (Supplementary Figure 5.6). Although dye **42** had the same issue of Raman signal quenching due to aggregation as alkyne pyronin dyes in PBS, we believe introducing two or more sulfo groups can solve this problem and the investigation is undergoing.

	Detuning (δ)	Transition dipole moment (μ)	Raman mode displacement (Δ_{ν})
• Phenyl ring modification	S	L	L
• Silyl modification	S	L	N
• Side ring expansion or conjugation extension	L	L	N

Figure 5.6: The effects of chemical modification on the three physical parameters that determine the Raman signals of epr-SRS probes. L: large; S: small; N: no.

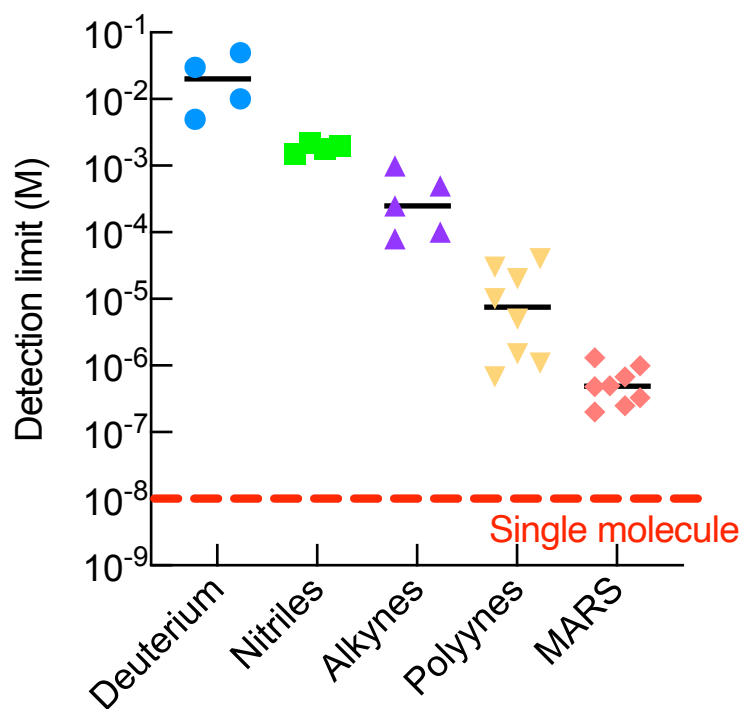
5.3 Discussion

Improving the sensitivity of Raman probe is a long-term goal of vibrational spectroscopy and imaging. With the guidance of theoretical chemistry, we now have a systematic method to evaluate the Raman signal of epr-SRS probes from three key physical factors of δ , μ and Δ_{ν} . In this study, we correlate the chemical modification with the physical factors for the first time, providing an exemplified platform for optimizing structures for higher

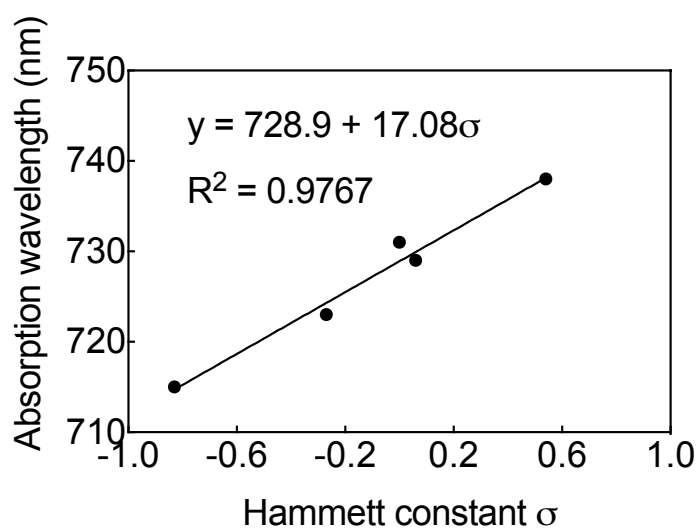
sensitivity with breaking the sensitivity records of epr-SRS dyes for both alkynyl pyronin and nitrile pyronin scaffolds. From derivatizing alkynyl pyronins, we summarize the effects of chemical modification on the physical parameters δ , μ and $\Delta\bar{\nu}$ (Figure 5.6). For the design of dye structures, the detuning and Raman mode displacement can be accurately predicted before synthesizing the molecule, but we lack a precise method for predicting the transition dipole moment or oscillation strength. For the practical use of epr-SRS probes, we always aim for higher transition dipole moment and larger displacement but with reasonably small detuning for high signal to background ratio. A common issue associated with near-infrared dyes is the formation of H aggregates in water. An underlying requirement for modified dye skeleton especially for bulkier near-infrared dyes is low tendency to form aggregation. This always require non-trivial synthesis efforts for introducing hydrophilic or charged groups^{22,28}.

This study further proves that understanding structure-function-relationship lays the foundation for rational design of improved probes. Our theory should be applicable to other vibrational imaging modality, such as the bond-selective fluorescence-detected infrared-excited (BonFIRE)²⁹ and fluorescence detected photothermal microscopy^{30,31}. Since the application of fluorophores for bioimaging, brilliant chemists have been creating a wide range of crafted synthetic and biological fluorophores for several decades. However, the elaboration of vibrational imaging probes just starts. We hope the efforts from the chemistry community can make up for the sensitivity need of single molecule vibrational imaging, a long-sought-after goal in photonics.

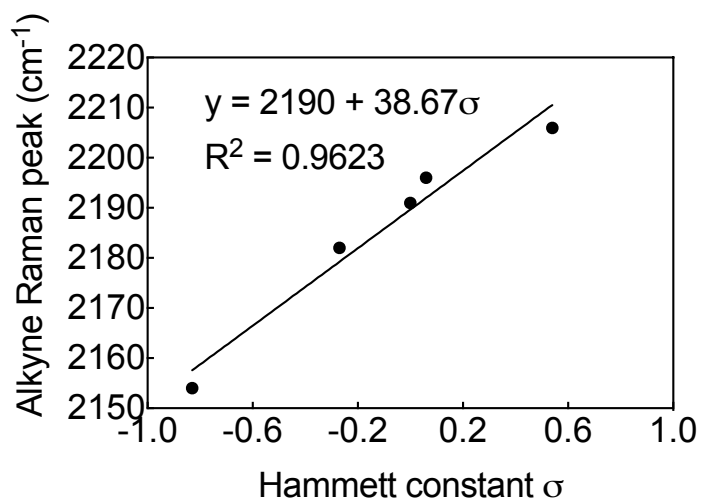
5.4 Supplementary information



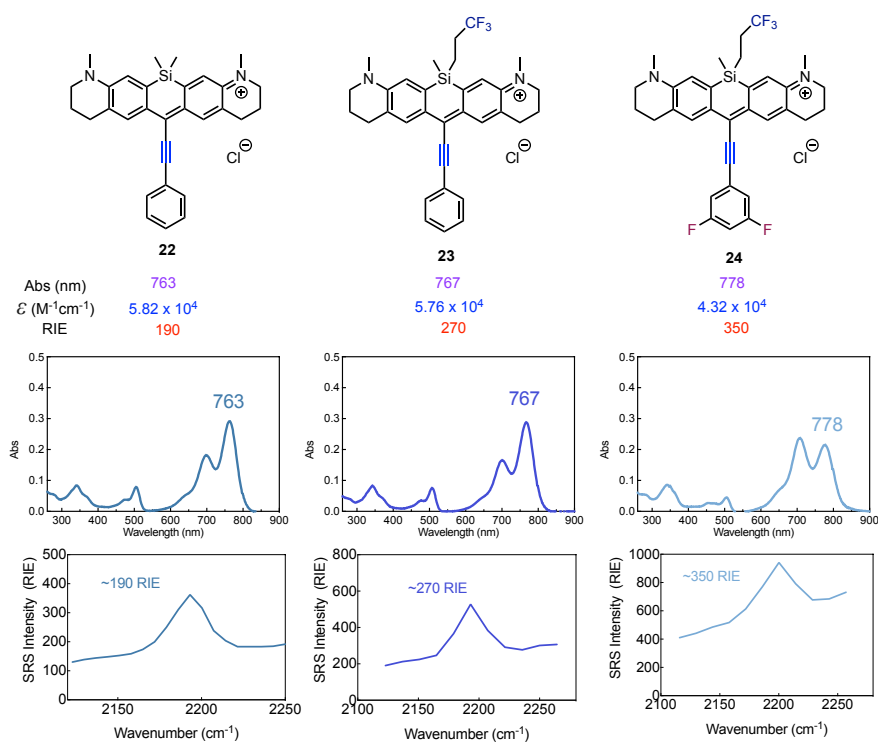
Supplementary Figure 5.1: The SRS detection limit of current probes.



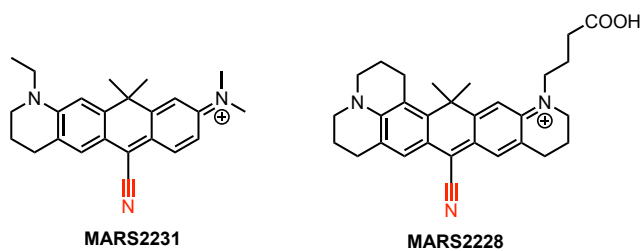
Supplementary Figure 5.2: The linear fitting between absorption maximum and the available Hammett constants of the substitution groups on the phenyl ring³¹. Dye 1, 3, 4, 6, 7 are listed.



Supplementary Figure 5.3: The linear fitting between the alkyne Raman peak frequency and the available Hammett constants of the substitution groups on the phenyl ring³¹. Dye 1, 3, 4, 6, 7 are listed.

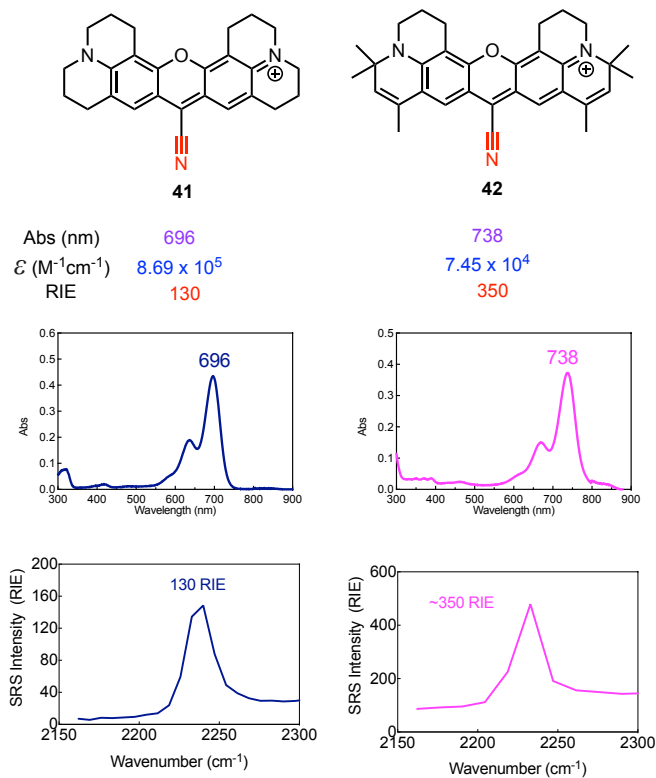


Supplementary Figure 5.4: Redder alkynyl pyronin dyes 22, 23 and 24 with expanded side rings and corresponding modifications on the phenyl ring and silyl. The characterization and raw data are shown in the same row of the molecule. All measurements were taken in DMSO.



Dye	Abs (nm) ^a	ϵ ($M^{-1}cm^{-1}$) ^a	RIE ^a	Raman peak (cm^{-1}) ^a	Abs (nm) ^b	ϵ ($M^{-1}cm^{-1}$) ^b	RIE ^b	Raman peak (cm^{-1}) ^b
MARS2231	744	1.40×10^5	325	2231	728	1.12×10^5	200	2237
MARS2228	757	1.20×10^5	620	2228	743	1.02×10^5	280	2234

Supplementary Figure 5.5. The structures of the parent MARS dyes for nitrile carbon pyronin molecules. The complete photophysical parameters are listed below. a: measured in DMSO; b: measured in PBS (with 10% DMSO).



Supplementary Figure 5.6: Redder nitrile oxygen pyronin dyes 42 and its parent molecule 41. The characterization and raw data are shown in the same row of the molecule. All measurements were taken in DMSO.

Experimental Details

Reagents and solvents from commercial sources were used without further purification unless otherwise stated. All reactions were performed under a N₂ atmosphere unless specified otherwise. All reaction flasks were flame dried. Column chromatography was carried out using SiliaFlash irregular silica gel P60 (Silicycle, 40 - 63 μm, 60 Å). Thin layer chromatography (TLC) was carried out with Millipore silica gel F-254 plates, and plates were visualized using UV light or KMnO₄ stain. The UV handlamp is an Analytik Jena UVP EL Series Lamp (UVLS-24, 4 Watt, 2UV 254/365 nm).

NMR spectra were recorded using a 400 MHz Bruker Avance III HD with Prodigy Cryoprobe or a 400 MHz Bruker Avance Neo. All ¹H NMR spectra are reported in δ units, parts per million (ppm), and were measured relative to the signals for CH₂Cl₂ (5.32 ppm) in deuterated solvent. All ¹³C NMR spectra were measured in deuterated solvents and are reported in ppm relative to the signals for ¹³CD₂Cl₂ (54.00 ppm). Multiplicity and qualifier abbreviations are as follows: s = singlet, d = doublet, t = triplet, q = quartet, m = multiplet, br = broad.

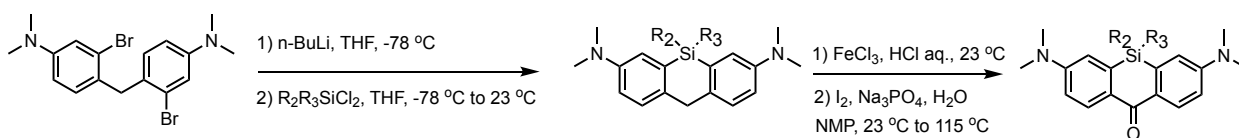
High resolution mass spectra (HRMS) were obtained from an LTQ linear ion trap mass spectrometer with liquid-chromatography (LC) system (Thermo) or LCT Premier XE electrospray TOF mass spectrometer with UPLC (Waters).

Preparative HPLC was performed on an Agilent 1100 Series semi-preparative HPLC apparatus using Eclipse XDB-C18 9.4 x 250 mm column with water (0.1% AcOH) and acetonitrile as mobile phases. UV-Vis absorption spectra were recorded on a Varian Cary 50 UV-Vis Spectrophotometer (Agilent). Analytical HPLC coupled with mass spectrometry (LC-MS) was performed on Agilent 1290 infinity LC system using ZORBAX RRHD

Eclipse Plus C18, 95Å, 2.1 x 50 mm, 1.8 μm column with an Agilent 6140 Series Quadrupole LCMS / LC-MS / MSD / Mass Spectrometer System. The mobile phase is water (0.1% AcOH) and acetonitrile with running method of gradient 5% - 95% acetonitrile (1 ml/min, 0 - 4 min). Mass spectrometry detection region ranges from 100 to 800 AMU.

Synthesis Details:

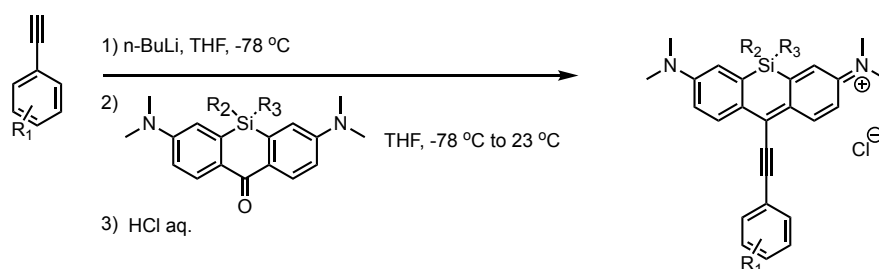
General synthesis procedures for alkyne Si pyronin



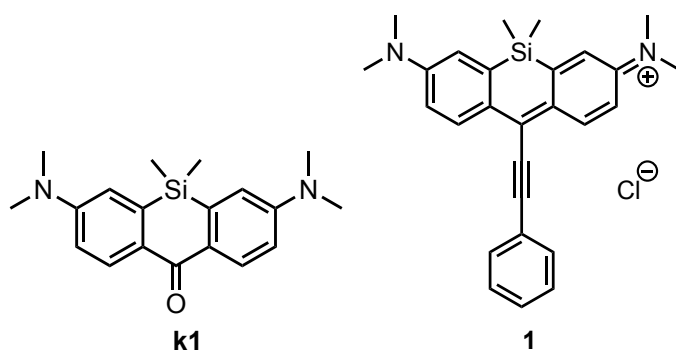
n-Butyllithium (1.6 M solution in hexane, 3.6 mL, 5.8 mmol) was added dropwise into a solution of 4,4'-methylenebis(3-bromo-N,N-dimethylaniline) (1.0 g, 2.4 mmol) in dry tetrahydrofuran (25 mL) when cooling in dry ice bath (-78 °C). The reaction mixture was allowed to stir for 30 min at -78 °C. The corresponding silane (R₂R₃SiCl₂, 3.6 mmol) was then added dropwise into the reaction solution at -78 °C. The dry ice bath was then removed, and the mixture was allowed to stir at 23 °C. The reaction was stirred for 2-6 h before quenched by dropwise addition of aq. HCl (3 mL, 1 M). The solution was then carefully neutralized with saturated aq. NaHCO₃ (keep the pH below 8.0). The mixture was extracted with DCM (3 × 20 mL) and dried over NaSO₄, and concentrated. The obtained crude solid mixture was purified by flash column chromatography with ethyl acetate and hexane as eluents. On TLC plates, the product band was initially colorless and turned to be blue or violet by oxidation with oxygen and showed strong fluorescence under 365 nm UV lamp.

The crude product from the last step was dissolved in 10 ml DCM and mixed with 5 ml aq. FeCl₃ (0.5 M in 1 M HCl) and stirred for 2 h at 23 °C. The organic phase was then separated

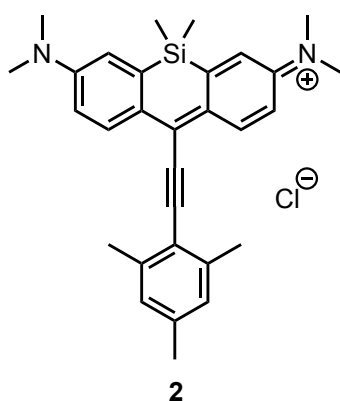
and washed with brine. The organic phase was dried over NaSO₄ and concentrated, and dissolved in N-Methyl-2-pyrrolidinone (NMP, 10 mL). I₂ (0.61 g, 2.4 mmol), Na₃PO₄ (0.79 g, 4.8 mmol) and H₂O (0.43 ml, 24 mmol) were added and the reaction mixture was allowed to heat to 110 °C and stirred for 1 hours. At this time, another batch of Na₃PO₄ (0.79 g, 4.8 mmol) and H₂O (0.43 ml, 24 mmol) was added and the solution and stirred at 110 °C for another 1 h. After cooling to room temperature, the reaction was filtered and diluted with brine (20 ml). The mixture was extracted with EtOAc : hexane (1:1). The organic phase was washed with water for three times and then brine for two times to remove NMP and dried over NaSO₄. The organic phase was then concentrated and purified by flash column chromatography with hexane: DCM: EtOAc (4:1:0.5) to afford the product. The xanthenone ketone product shows intense yellow fluorescence under 365 nm UV lamp.



n-Butyllithium (1.6 M solution in hexane, 0.188 mL, 0.3 mmol) was added dropwise by syringe to a solution of substituted phenylacetylene (0.3 mmol) in dry tetrahydrofuran (5 mL) when cooling in dry ice bath (-78 °C). The mixture was stirred for 30 min at -78 °C, and xanthenone (0.05 mmol) was added. The reaction mixture was then allowed to stir at 23 °C for 4 h. The reaction was quenched by dropwise addition of aq. HCl (1 mL, 1 M), and the mixture was extracted with dichloromethane (3 × 5 mL). The combined organic phase was dried over anhydrous NaSO₄, and the solvent was removed in vacuo. The mixture was purified by flash column chromatography with MeOH: DCM (0.05 : 1) to afford the green products.



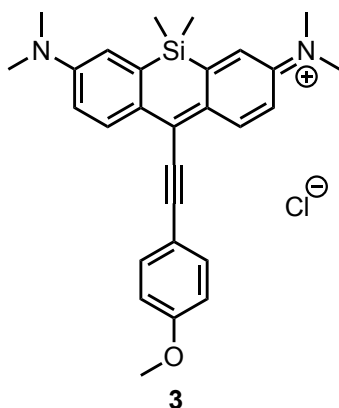
k1 and **1** were synthesized according to previous report³².



Yield: 27%

^1H NMR (400 MHz, CDCl_3) δ 8.59 (d, $J = 9.5$ Hz, 2H), 7.14 (d, $J = 2.8$ Hz, 2H), 7.03 – 6.98 (s, 2H), 6.89 (dd, $J = 9.5, 2.8$ Hz, 2H), 3.44 (s, 12H), 2.61 (s, 6H), 2.36 (s, 3H), 0.58 (s, 6H).

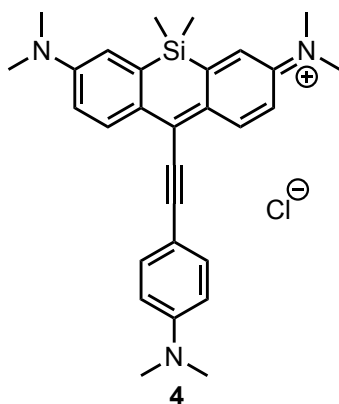
^{13}C NMR (101 MHz, CDCl_3) δ 154.18, 149.74, 146.52, 142.31, 141.84, 140.85, 129.04, 128.77, 120.23, 118.67, 114.52, 112.74, 97.66, 41.31, 21.96, 21.79, -0.76.



Yield: 65%

$^1\text{H NMR}$ (400 MHz, CDCl_3) δ 8.47 (d, $J = 9.5$ Hz, 2H), 7.73 – 7.65 (m, 2H), 7.05 (d, $J = 2.8$ Hz, 2H), 7.02 – 6.93 (m, 4H), 3.88 (s, 3H), 3.41 (s, 12H), 0.53 (s, 6H).

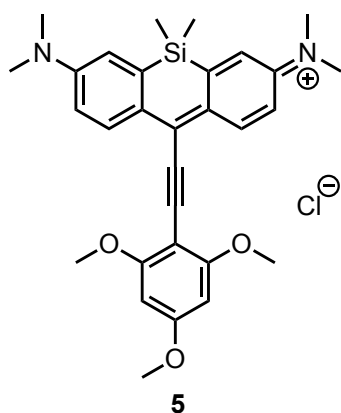
$^{13}\text{C NMR}$ (101 MHz, CDCl_3) δ 162.45, 154.13, 149.51, 146.13, 140.76, 134.88, 128.75, 119.80, 115.51, 114.98, 114.79, 113.26, 90.44, 55.80, 41.26, -0.74.



Yield: (72%)

$^1\text{H NMR}$ (400 MHz, CDCl_3) δ 8.45 (d, $J = 9.4$ Hz, 2H), 7.64 – 7.55 (m, 2H), 6.97 (d, $J = 2.8$ Hz, 2H), 6.92 (dd, $J = 9.4, 2.9$ Hz, 2H), 6.78 – 6.70 (m, 2H), 3.36 (s, 12H), 3.12 (s, 6H), 0.50 (s, 6H).

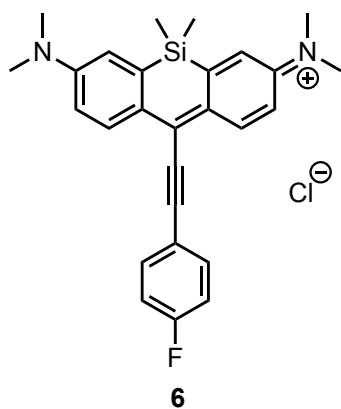
$^{13}\text{C NMR}$ (101 MHz, CDCl_3) δ 153.67, 152.69, 150.45, 145.26, 140.14, 135.41, 128.45, 122.84, 118.84, 114.50, 112.15, 107.08, 94.64, 41.01, 40.30, -0.75.



Yield: 70%

$^1\text{H NMR}$ (400 MHz, CDCl_3) δ 8.77 (d, $J = 9.4$ Hz, 2H), 7.01 (d, $J = 2.7$ Hz, 2H), 6.95 (dd, $J = 9.4, 2.7$ Hz, 2H), 6.18 (s, 2H), 4.05 (s, 6H), 3.93 (s, 3H), 3.41 (s, 12H), 0.53 (s, 6H).

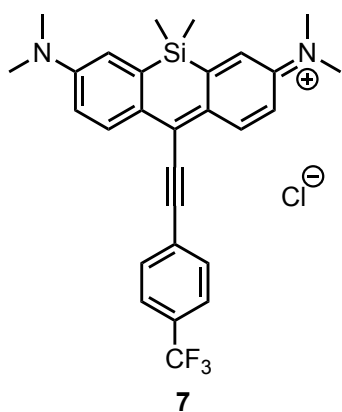
$^{13}\text{C NMR}$ (101 MHz, CDCl_3) δ 166.10, 164.71, 153.86, 151.42, 145.68, 141.42, 128.69, 118.99, 114.60, 114.21, 101.61, 94.10, 91.00, 56.84, 56.12, 41.18, -0.73.



yield: 43%

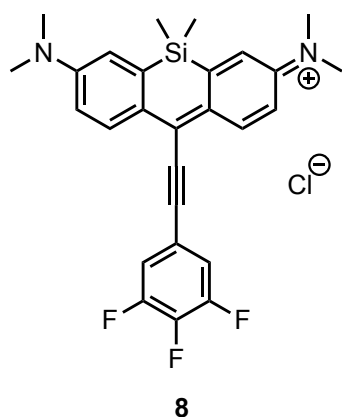
$^1\text{H NMR}$ (400 MHz, CDCl_3) δ 8.46 (d, $J = 9.6$ Hz, 2H), 7.80 – 7.72 (m, 2H), 7.22 – 7.15 (m, 2H), 7.11 (d, $J = 2.7$ Hz, 2H), 6.99 (dd, $J = 9.5, 2.8$ Hz, 2H), 3.45 (s, 12H), 0.56 (s, 6H)

$^{13}\text{C NMR}$ (101 MHz, CDCl_3) δ 154.29, 148.29, 146.43, 140.87, 135.00, 134.90, 128.93, 120.31, 116.83, 116.60, 114.98, 111.61, 89.57, 41.67, -0.69.



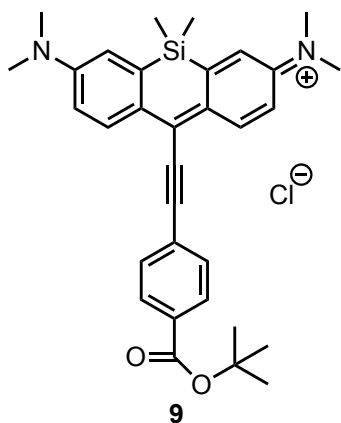
Yield: 30%

$^1\text{H NMR}$ (400 MHz, CDCl_3) δ 8.44 (d, $J = 8.6$ Hz, 2H), 7.85 (d, $J = 8.0$ Hz, 2H), 7.72 (d, $J = 7.8$ Hz, 2H), 7.12 (s, 2H), 7.00 (d, $J = 9.2$ Hz, 2H), 3.46 (s, 12H), 0.56 (s, 6H).



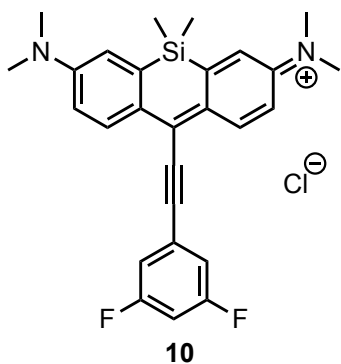
Yield: 32%

$^1\text{H NMR}$ (400 MHz, CD_2Cl_2) δ 8.43 (d, $J = 9.5$ Hz, 2H), 7.45 (t, $J = 6.9$ Hz, 2H), 7.11 (d, $J = 2.8$ Hz, 2H), 6.96 (dd, $J = 9.6, 2.8$ Hz, 2H), 3.40 (s, 12H), 0.55 (s, 6H).



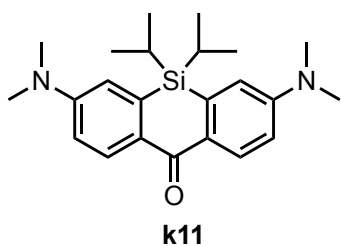
Yield: 21%

$^1\text{H NMR}$ (400 MHz, CD_2Cl_2) δ 8.53 (d, $J = 9.6$ Hz, 2H), 8.12 – 8.07 (m, 2H), 7.81 (d, $J = 8.4$ Hz, 2H), 7.11 (d, $J = 2.8$ Hz, 2H), 6.96 (dd, $J = 9.6, 2.8$ Hz, 2H), 3.40 (s, 12H), 1.61 (s, 9H), 0.56 (s, 6H).



Yield: 36%

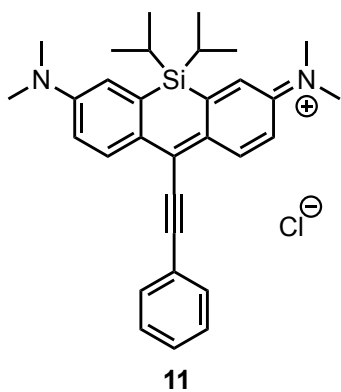
$^1\text{H NMR}$ (400 MHz, CD_2Cl_2) δ 8.45 (d, $J = 9.5$ Hz, 2H), 7.33 – 7.29 (m, 2H), 7.13 (d, $J = 2.8$ Hz, 2H), 7.04 (tt, $J = 9.0, 2.4$ Hz, 1H), 6.96 (dd, $J = 9.5, 2.8$ Hz, 2H), 3.41 (s, 12H), 0.56 (s, 6H).



Yield (46%)

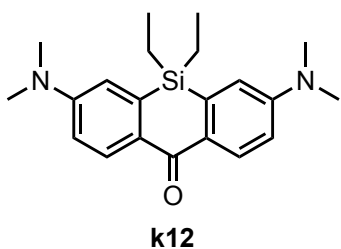
$^1\text{H NMR}$ (400 MHz, CDCl_3) δ 8.42 (d, $J = 8.9$ Hz, 2H), 6.90 – 6.78 (m, 4H), 3.09 (s, 12H), 1.45 (p, $J = 7.4$ Hz, 2H), 1.02 (d, $J = 7.4$ Hz, 12H).

$^{13}\text{C NMR}$ (101 MHz, CDCl_3) δ 185.82, 151.04, 137.48, 131.84, 131.47, 115.18, 113.35, 40.32, 18.06, 12.41.



Yield (34%)

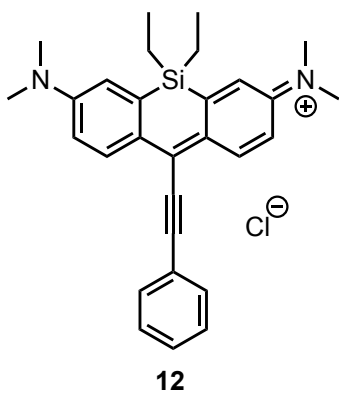
$^1\text{H NMR}$ (400 MHz, CD_2Cl_2) δ 8.61 (d, $J = 9.5$ Hz, 2H), 7.81 – 7.77 (m, 2H), 7.60 – 7.49 (m, 3H), 7.03 (d, $J = 2.8$ Hz, 2H), 6.99 (dd, $J = 9.5, 2.8$ Hz, 2H), 3.38 (s, 12H), 1.50 (p, $J = 7.4$ Hz, 2H), 1.04 (d, $J = 7.4$ Hz, 12H).



Yield (42%)

^1H NMR (400 MHz, CDCl_3) δ 8.41 (d, $J = 9.0$ Hz, 2H), 6.86 (dd, $J = 9.0, 2.8$ Hz, 2H), 6.81 (d, $J = 2.8$ Hz, 2H), 3.09 (s, 12H), 1.00 – 0.95 (m, 4H), 0.94 – 0.87 (m, 6H).

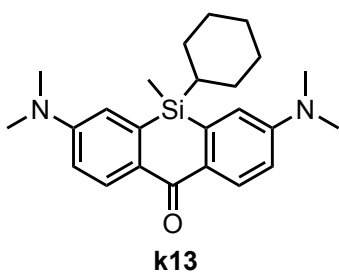
^{13}C NMR (101 MHz, CDCl_3) δ 185.66, 151.31, 138.57, 131.81, 131.12, 114.77, 113.42, 40.31, 7.69, 5.84.



Yield (45%)

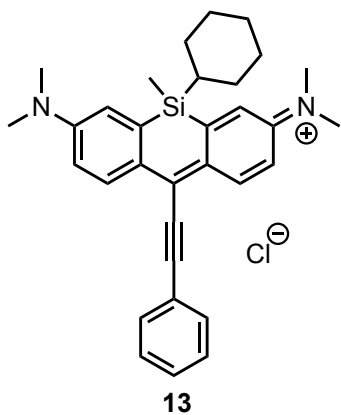
^1H NMR (400 MHz, CDCl_3) δ 8.52 (d, $J = 9.5$ Hz, 2H), 7.76 – 7.70 (m, 2H), 7.54 – 7.43 (m, 3H), 7.05 (d, $J = 2.8$ Hz, 2H), 6.99 (dd, $J = 9.5, 2.8$ Hz, 2H), 3.46 (s, 12H), 1.04 (q, $J = 7.7$ Hz, 4H), 0.90 (t, $J = 7.7$ Hz, 6H).

^{13}C NMR (101 MHz, CDCl_3) δ 154.09, 148.92, 144.53, 141.10, 132.57, 131.27, 129.68, 129.13, 121.35, 120.01, 114.96, 112.96, 89.70, 41.30, 7.35, 6.06.



Yield (35%)

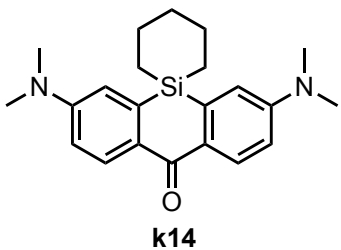
^1H NMR (400 MHz, CD_2Cl_2) δ 8.26 (d, $J = 9.0$ Hz, 2H), 6.83 (dd, $J = 9.0, 2.8$ Hz, 2H), 6.78 (d, $J = 2.7$ Hz, 2H), 3.09 (s, 12H), 1.67 – 1.59 (m, 5H), 1.20 – 0.87 (m, 6H), 0.52 (s, 3H).



Yield (37%)

^1H NMR (400 MHz, CD_2Cl_2) δ 8.57 (d, $J = 9.5$ Hz, 2H), 7.81 – 7.76 (m, 2H), 7.60 – 7.49 (m, 3H), 7.01 (d, $J = 2.8$ Hz, 2H), 6.97 (dd, $J = 9.4, 2.8$ Hz, 2H), 3.39 (s, 12H), 1.71 – 1.60 (m, 5H), 1.26 – 0.95 (m, 6H), 0.60 (s, 3H).

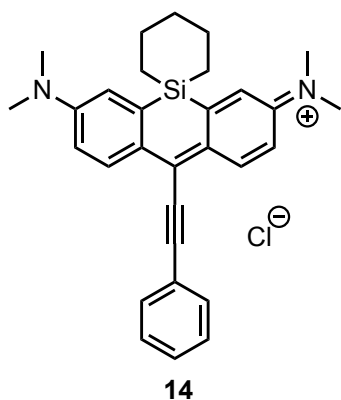
^{13}C NMR (101 MHz, CD_2Cl_2) δ 154.29, 149.53, 145.48, 141.31, 132.84, 131.68, 129.82, 129.44, 121.63, 120.48, 114.93, 113.25, 89.90, 41.31, 28.09, 27.58, 27.03, 26.85, -6.11.



Yield (41%)

^1H NMR (400 MHz, CDCl_3) δ 8.41 (d, $J = 9.0$ Hz, 2H), 7.00 (d, $J = 3.4$ Hz, 2H), 6.86 (ddd, $J = 9.0, 2.9, 1.3$ Hz, 2H), 3.11 (s, 12H), 2.05 (dddd, $J = 11.6, 8.6, 5.9, 4.0$ Hz, 4H), 1.72 (qd, $J = 7.3, 4.1$ Hz, 2H), 1.07 – 1.02 (m, 4H).

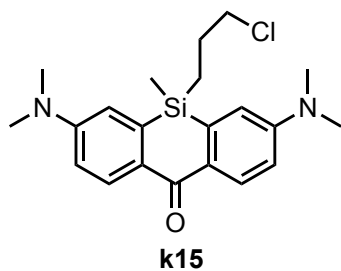
^{13}C NMR (101 MHz, CDCl_3) δ 185.39, 151.19, 140.39, 131.88, 115.49, 113.55, 40.41, 29.82, 25.12, 13.30.



Yield (37%)

^1H NMR (400 MHz, CD_2Cl_2) δ 8.57 (d, $J = 9.5$ Hz, 2H), 7.80 – 7.75 (m, 2H), 7.59 – 7.47 (m, 3H), 7.22 (d, $J = 2.8$ Hz, 2H), 6.98 (dd, $J = 9.6, 2.8$ Hz, 2H), 3.41 (s, 12H), 2.03 (dddd, $J = 11.7, 8.6, 5.9, 3.7$ Hz, 4H), 1.76 (t, $J = 5.5$ Hz, 2H), 1.12 – 1.02 (m, 4H).

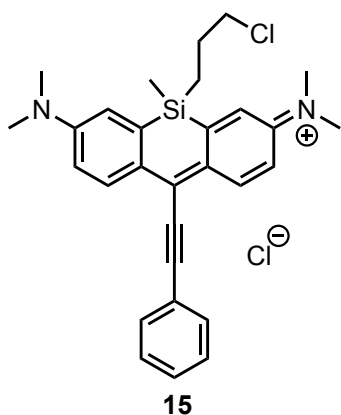
^{13}C NMR (101 MHz, CD_2Cl_2) δ 154.32, 149.27, 146.45, 141.44, 132.86, 131.64, 129.43, 129.40, 121.63, 120.72, 115.01, 113.26, 89.88, 41.17, 29.37, 24.55, 13.15.



Yield (37%)

^1H NMR (400 MHz, CD_2Cl_2) δ 8.29 (d, $J = 9.0$ Hz, 2H), 6.84 (dd, $J = 9.0, 2.8$ Hz, 2H), 6.79 (d, $J = 2.8$ Hz, 2H), 3.38 (t, $J = 6.8$ Hz, 2H), 3.09 (s, 12H), 1.69 – 1.59 (m, 2H), 1.10 – 1.01 (m, 2H), 0.51 (s, 3H).

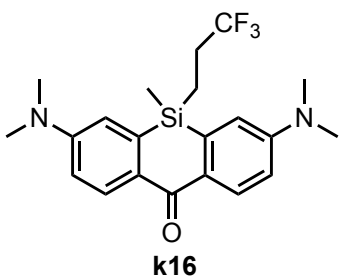
^{13}C NMR (101 MHz, CD_2Cl_2) δ 185.02, 151.94, 139.03, 131.65, 130.24, 114.70, 113.53, 48.20, 40.23, 27.77, 13.71, -3.13.



Yield (68%)

^1H NMR (400 MHz, CD_2Cl_2) δ 8.57 (d, $J = 9.5$ Hz, 2H), 7.79 (dt, $J = 6.7, 1.6$ Hz, 2H), 7.62 – 7.48 (m, 3H), 7.11 (d, $J = 2.8$ Hz, 2H), 6.97 (dd, $J = 9.5, 2.8$ Hz, 2H), 3.44 (t, $J = 6.7$ Hz, 2H), 3.40 (s, 12H), 1.70 – 1.61 (m, 2H), 1.22 – 1.15 (m, 2H), 0.63 (s, 3H).

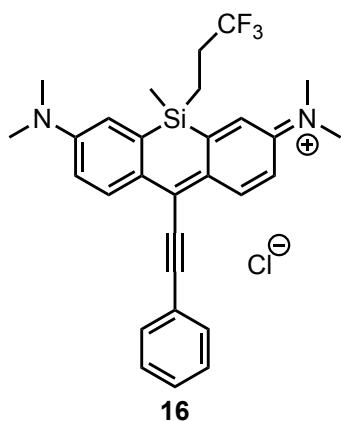
^{13}C NMR (101 MHz, CD_2Cl_2) δ 154.58, 149.22, 145.10, 141.33, 132.86, 131.69, 129.43, 121.62, 120.61, 115.11, 113.38, 89.87, 47.81, 41.40, 27.22, 13.83, -2.99.



Yield (51%)

^1H NMR (400 MHz, CDCl_3) δ 8.41 (d, $J = 9.0$ Hz, 2H), 6.87 (dd, $J = 9.1, 2.8$ Hz, 2H), 6.75 (d, $J = 2.8$ Hz, 2H), 3.11 (s, 12H), 1.90 – 1.76 (m, 2H), 1.19 – 1.11 (m, 2H), 0.55 (s, 3H).

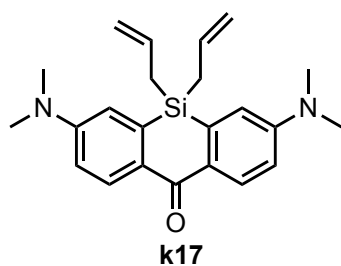
^{13}C NMR (101 MHz, CDCl_3) δ 185.01, 151.60, 137.45, 132.00, 130.34, 114.16, 113.78, 40.25, 28.68 (q, $J = 29.9$ Hz), 8.07, -3.35.



Yield (69%)

^1H NMR (400 MHz, CD_2Cl_2) δ 8.57 (d, $J = 9.6$ Hz, 2H), 7.81 – 7.76 (m, 2H), 7.61 – 7.50 (m, 3H), 7.14 (d, $J = 2.8$ Hz, 2H), 6.99 (dd, $J = 9.5, 2.8$ Hz, 2H), 3.42 (s, 12H), 2.00 – 1.88 (m, 2H), 1.30 – 1.21 (m, 2H), 0.71 (s, 3H).

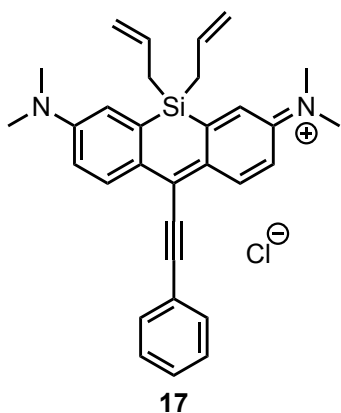
^{13}C NMR (101 MHz, CD_2Cl_2) δ 154.65, 149.06, 143.74, 141.34, 132.88, 131.73, 129.43, 121.57, 120.72, 115.29, 113.58, 89.84, 41.48, 28.47 (q, $J = 30.3$ Hz), 8.79, -3.49.



Yield (33%)

^1H NMR (400 MHz, CD_2Cl_2) δ 8.34 – 8.25 (m, 2H), 6.84 (dt, $J = 4.7, 2.5$ Hz, 4H), 5.89 – 5.74 (m, 2H), 4.92 – 4.81 (m, 4H), 3.08 (s, 12H), 2.03 (dt, $J = 8.0, 1.1$ Hz, 4H).

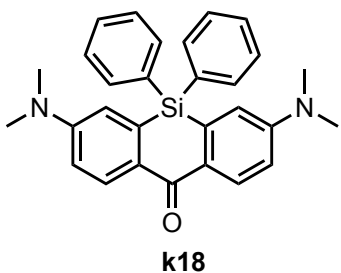
^{13}C NMR (101 MHz, CD_2Cl_2) δ 184.86, 151.70, 137.14, 133.95, 131.66, 130.43, 115.51, 114.66, 113.57, 40.21, 21.76.



Yield (45%)

^1H NMR (400 MHz, CD_2Cl_2) δ 8.58 (d, $J = 9.5$ Hz, 2H), 7.83 – 7.75 (m, 2H), 7.60 – 7.51 (m, 3H), 7.11 (d, $J = 2.9$ Hz, 2H), 6.98 (dd, $J = 9.5, 2.9$ Hz, 2H), 5.80 (ddt, $J = 16.8, 10.1, 7.9$ Hz, 2H), 5.03 – 4.88 (m, 4H), 3.38 (s, 12H), 2.10 (dt, $J = 8.0, 1.2$ Hz, 4H).

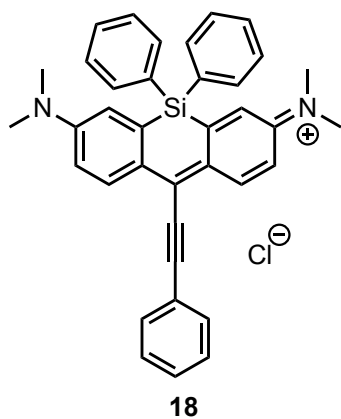
^{13}C NMR (101 MHz, CD_2Cl_2) δ 154.31, 149.12, 142.94, 141.40, 132.86, 132.14, 131.70, 129.57, 129.43, 121.24, 116.20, 115.12, 113.42, 89.84, 41.36, 21.48.



Yield (21%)

^1H NMR (400 MHz, CD_2Cl_2) δ 8.34 (d, $J = 9.0$ Hz, 2H), 7.62 (dd, $J = 8.1, 1.5$ Hz, 3H), 7.45 – 7.31 (m, 6H), 6.87 (dd, $J = 9.0, 2.8$ Hz, 2H), 6.81 (d, $J = 2.8$ Hz, 2H), 2.99 (s, 13H).

^{13}C NMR (101 MHz, CD_2Cl_2) δ 184.94, 151.89, 137.05, 136.31, 134.52, 131.81, 130.65, 130.27, 128.45, 116.46, 113.82, 40.13.

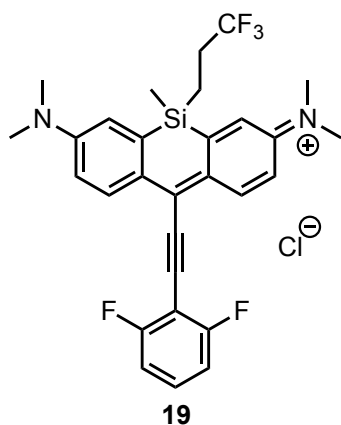


Yield (31%)

$^1\text{H NMR}$ (400 MHz, CD_2Cl_2) δ 8.62 (d, $J = 9.5$ Hz, 2H), 7.83 – 7.77 (m, 2H), 7.64 – 7.48 (m, 10H), 7.40-7.47 (m, 5H), 7.06 (d, $J = 2.8$ Hz, 2H), 7.00 (dd, $J = 9.5, 2.8$ Hz, 2H), 3.30 (s, 12H).

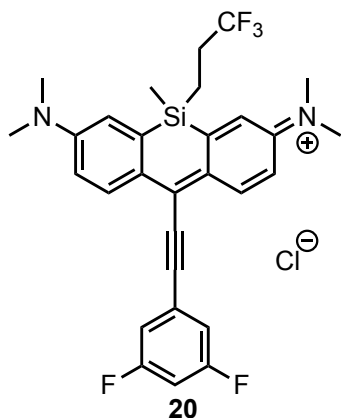
$^{13}\text{C NMR}$ (101 MHz, CD_2Cl_2) δ 154.11, 142.90, 141.19, 136.48, 135.80, 132.52, 131.41, 131.06, 131.00, 129.40, 129.06, 128.72, 121.91, 121.15, 114.92, 113.55, 89.52, 40.89.

$^{13}\text{C NMR}$ (101 MHz, CD_2Cl_2) δ 185.55, 151.69, 139.13, 131.38, 130.67, 115.17, 113.22, 40.22, 28.36, 27.72, 27.07, -6.04.



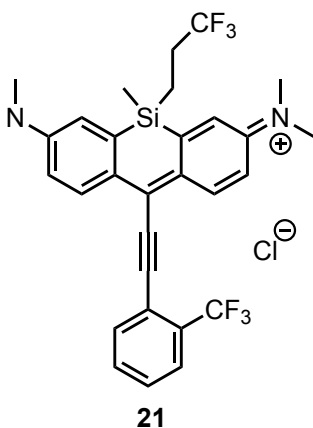
Yield (28%)

$^1\text{H NMR}$ (400 MHz, CD_2Cl_2) δ 8.59 (d, $J = 9.6$ Hz, 2H), 7.61 – 7.50 (m, 1H), 7.23 – 7.08 (m, 4H), 6.99 (dd, $J = 9.5, 2.8$ Hz, 2H), 3.42 (s, 12H), 2.00 – 1.85 (m, 2H), 1.29 – 1.24 (m, 2H), 0.72 (s, 3H).



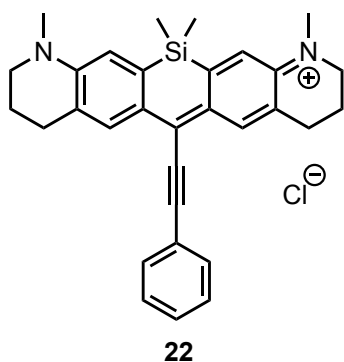
Yield (38%)

$^1\text{H NMR}$ (400 MHz, CD_2Cl_2) δ 8.45 (d, $J = 9.6$ Hz, 2H), 7.32 (m, 2H), 7.23 – 7.14 (m, 3H), 7.10 – 6.91 (m, 4H), 3.42 (s, 6H), 2.05 – 1.90 (m, 2H), 1.30 – 1.22 (m, 2H), 0.73 (s, 3H).



Yield (23%)

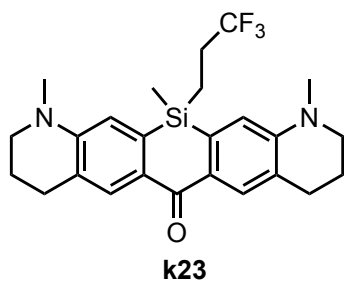
$^1\text{H NMR}$ (400 MHz, CD_2Cl_2) δ 8.54 (d, $J = 9.6$ Hz, 2H), 7.99 (d, $J = 7.6$ Hz, 1H), 7.85 (d, $J = 7.8$ Hz, 1H), 7.79 – 7.60 (m, 2H), 7.17 (d, $J = 2.8$ Hz, 2H), 6.99 (dd, $J = 9.6, 2.8$ Hz, 2H), 3.43 (s, 12H), 2.03 – 1.84 (m, 2H), 1.28 – 1.21 (m, 2H), 0.72 (s, 3H).



Yield (18%)

^1H NMR (400 MHz, CDCl_3) δ 8.11 (d, $J = 1.2$ Hz, 2H), 7.72 – 7.65 (m, 2H), 7.56 – 7.45 (m, 3H), 6.99 (s, 2H), 3.73 (t, $J = 5.8$ Hz, 4H), 3.42 (s, 6H), 2.89 – 2.79 (m, 4H), 2.07 (p, $J = 6.4$ Hz, 4H), 0.52 (s, 6H).

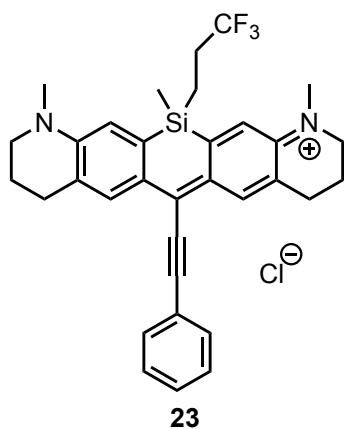
^{13}C NMR (101 MHz, CDCl_3) δ 152.74, 146.90, 146.16, 138.37, 133.00, 131.67, 129.85, 129.83, 126.04, 122.39, 119.96, 112.11, 90.42, 53.68, 41.02, 28.48, 21.92, -0.01.



Yield (30%)

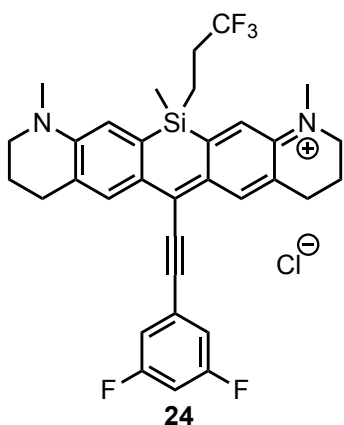
^1H NMR (400 MHz, CD_2Cl_2) δ 7.99 (d, $J = 1.1$ Hz, 2H), 6.59 (s, 2H), 3.37 (dd, $J = 6.2, 5.3$ Hz, 4H), 3.02 (s, 6H), 2.90 – 2.76 (m, 4H), 2.03 – 1.92 (m, 4H), 1.92 – 1.74 (m, 2H), 1.17 – 1.05 (m, 2H), 0.51 (s, 3H).

^{13}C NMR (101 MHz, CD_2Cl_2) δ 184.78, 149.02, 135.85, 130.45, 130.22, 124.81, 112.91, 51.66, 38.96, 28.93 (q, $J = 29.7$ Hz), 28.39, 22.30, 8.17, -3.31.



Yield (42%)

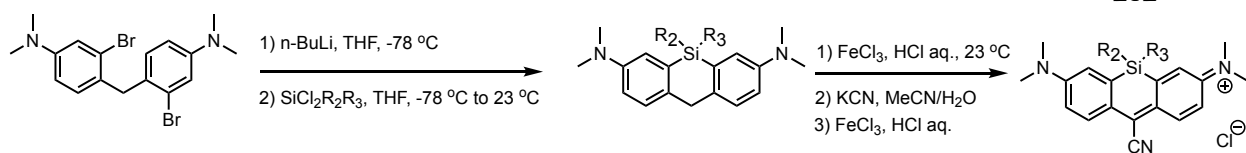
$^1\text{H NMR}$ (400 MHz, CD_2Cl_2) δ 8.19 (d, $J = 1.2$ Hz, 2H), 7.79 – 7.73 (m, 2H), 7.54 (qdd, $J = 8.9, 4.3, 3.0$ Hz, 3H), 6.99 (s, 2H), 3.67 (t, $J = 5.8$ Hz, 6H), 3.36 (s, 6H), 2.92 – 2.80 (m, 4H), 2.07 (p, $J = 6.3$ Hz, 4H), 1.99 – 1.85 (m, 2H), 1.24 – 1.19 (m, 2H), 0.66 (s, 3H).



Yield (27%)

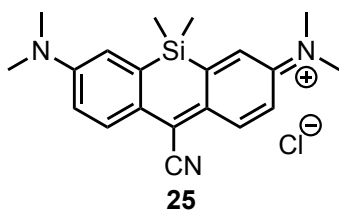
$^1\text{H NMR}$ (400 MHz, CD_2Cl_2) δ 8.07 (s, 2H), 7.32 – 7.22 (m, 2H), 7.10 – 7.00 (m, 3H), 3.69 (t, $J = 5.8$ Hz, 4H), 3.39 (s, 6H), 2.85 (t, $J = 6.2$ Hz, 4H), 2.07 (t, $J = 6.0$ Hz, 4H), 2.00 – 1.84 (m, 2H), 1.29 – 1.17 (m, 2H), 0.68 (s, 3H).

General synthesis procedures for nitrile Si pyronin

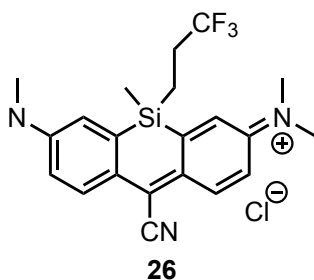


n-Butyllithium (1.6 M solution in hexane, 3.6 mL, 5.8 mmol) was added dropwise into a solution of 4,4'-methylenebis(3-bromo-N,N-dimethylaniline) (1.0 g, 2.4 mmol) in dry tetrahydrofuran (25 mL) when cooling in dry ice bath ($-78\text{ }^{\circ}\text{C}$). The reaction mixture was allowed to stir for 30 min at $-78\text{ }^{\circ}\text{C}$. The corresponding silane ($\text{R}_2\text{R}_3\text{SiCl}_2$, 3.6 mmol) was then added dropwise into the reaction solution at $-78\text{ }^{\circ}\text{C}$. The dry ice bath was then removed, and the mixture was allowed to stir at $23\text{ }^{\circ}\text{C}$. The reaction was stirred for 2-6 h before quenched by dropwise addition of aq. HCl (3 mL, 1 M). The solution was then carefully neutralized with saturated aq. NaHCO_3 (keep the pH below 8.0). The mixture was extracted with DCM ($3 \times 20\text{ mL}$) and dried over NaSO_4 , and concentrated. The obtained crude solid mixture was purified by flash column chromatography with ethyl acetate and hexane as eluents. On TLC plates, the product band was initially colorless and turned to be blue or violet by oxidation with oxygen and showed strong fluorescence under 365 nm UV lamp.

50 mg product from the last step was dissolved in 10 mL DCM and mixed with 5 ml aq. FeCl_3 (0.5 M in 1 M HCl) and stirred for 12 h at $23\text{ }^{\circ}\text{C}$. The organic phase was then separated and washed with brine and concentrated. This freshly-oxidized (Note: the Si xanthenone can also be reduced quickly under air even at $-20\text{ }^{\circ}\text{C}$, so fresh preparation is required) xanthenone was dissolved in 3 ml acetonitrile, aq. KCN (100 mg/mL, 1.5 M) was added dropwise to the xanthenone solution until the blue color disappeared. Right after the blue color disappeared, 2 ml aq. FeCl_3 (0.5 M in 1 M HCl) was added and the reaction was stirred at $23\text{ }^{\circ}\text{C}$ for 15 min. The reaction was then diluted with 10 ml brine. The reaction mixture was extracted with DCM ($10\text{ mL} \times 3$). The combined organic layer was washed with brine and dried over Na_2SO_4 . The solvent was removed in vacuo and the residue was purified by flash column chromatography with MeOH: DCM (0.07 : 1) to afford the green product.



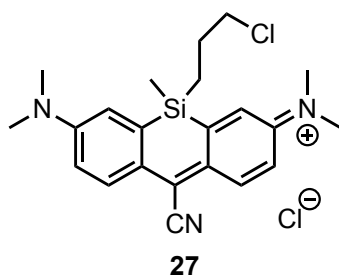
25 was synthesized according to previous report⁹.



Yield (52%)

¹H NMR (400 MHz, CDCl₃ with 1% CD₃OD) δ 8.11 (d, *J* = 9.5 Hz, 2H), 7.47 (d, *J* = 2.7 Hz, 2H), 6.94 (dd, *J* = 9.6, 2.7 Hz, 2H), 3.52 (s, 12H), 2.02 – 1.88 (m, 2H), 1.42 – 1.30 (m, 2H), 0.79 (s, 3H).

¹³C NMR (101 MHz, CDCl₃ with 1% CD₃OD) δ 154.81, 144.20, 140.05, 131.76, 128.15, 123.76, 116.41, 116.00, 42.07, 29.80, 28.21 (q, *J* = 30.1 Hz), 8.28, -3.01.

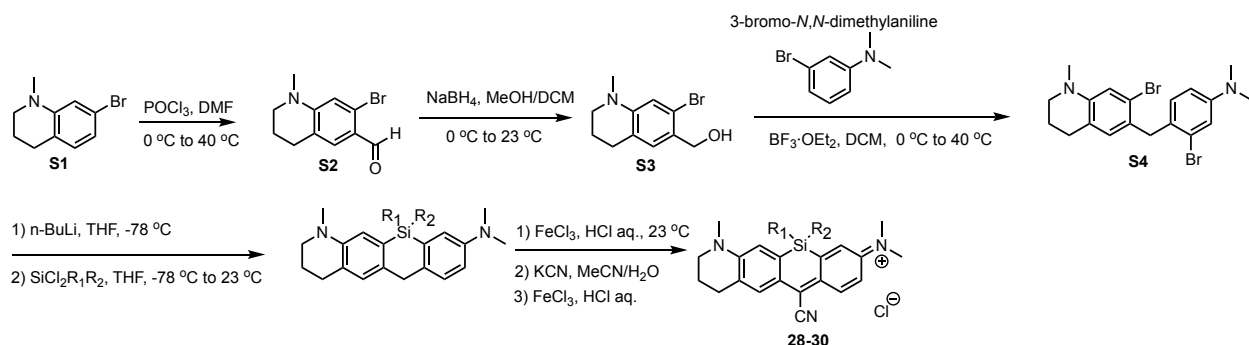


Yield (56%)

¹H NMR (400 MHz, CDCl₃ with 1% CD₃OD) δ 8.09 (dd, *J* = 9.6, 1.2 Hz, 2H), 7.33 (d, *J* = 2.6 Hz, 2H), 6.93 (ddd, *J* = 9.5, 2.7, 1.2 Hz, 2H), 3.48 (s, 12H), 3.43 (t, *J* = 6.5 Hz, 2H), 1.68 – 1.55 (m, 2H), 1.27 – 1.21 (m, 2H), 0.64 (s, 3H).

^{13}C NMR (101 MHz, CDCl_3 with 1% CD_3OD) δ 154.70, 145.15, 140.05, 131.94, 128.12, 123.29, 116.40, 115.90, 47.37, 41.85, 26.83, 13.21, -2.81.

Synthesis of 28-30



7-bromo-1-methyl-1,2,3,4-tetrahydroquinoline (**S1**) was synthesized according to previous report²⁴.

POCl_3 (4.60 g, 2.80 ml, 30 mmol) was added dropwise to a flask filled with DMF (10 mL) when cooled in an ice bath ($0\text{ }^\circ\text{C}$), and stirred for 30 min at $0\text{ }^\circ\text{C}$. Then **I0** (2.26 g, 10 mmol) was then added into the flask and the reaction mixture was allowed to stir for 4 h at $40\text{ }^\circ\text{C}$. When the reaction was cooled to $23\text{ }^\circ\text{C}$, the reaction solution was poured into brine. The mixture was extracted with DCM ($20\text{ mL} \times 3$) and the organic phase was washed with brine (five times) and then dried over Na_2SO_4 . The solvent was removed in vacuo and the residue was purified by column chromatography with hexane : EtOAc (10 : 1) to obtain **S2** (2.08 g, 82%).

S2

^1H NMR (400 MHz, CDCl_3) δ 10.02 (s, 1H), 7.51 (t, $J = 1.1\text{ Hz}$, 1H), 6.64 (s, 1H), 3.37 (t, $J = 5.6\text{ Hz}$, 2H), 3.00 (s, 3H), 2.70 (t, $J = 6.2\text{ Hz}$, 2H), 2.00 – 1.88 (m, 2H).

^{13}C NMR (101 MHz, CDCl_3) δ 190.42, 151.64, 129.46, 128.13, 121.70, 113.25, 51.13, 38.98, 27.27, 21.47.

S2 (1.27 g, 5 mmol) was dissolved in 10 mL MeOH and 5 ml DCM and cooled in an ice bath (0 °C), NaBH₄ (227 mg, 6 mmol) was slowly added into the mixture at 0 °C. The reaction was then allowed to warm to 23 °C and stirred for 2 h. The solvent was then removed in vacuo and water was slowly added to quench the reaction. The mixture was extracted with DCM (20 mL × 3) and the organic phase was washed with brine (three times) and then dried over Na₂SO₄. The solvent was removed in vacuo and the residue was purified by column chromatography with hexane : EtOAc (8 : 1) to obtain **S3** (1.19 g, 93%).

S3

Yield (93%)

¹H NMR (400 MHz, CDCl₃) δ 6.98 (s, 1H), 6.74 (s, 1H), 4.61 (s, 2H), 3.24 (t, *J* = 6.0 Hz, 2H), 2.89 (s, 3H), 2.71 (t, *J* = 6.4 Hz, 2H), 2.02 – 1.90 (m, 2H), 1.84 (br, 1H).

S3 (1.02 g, 4 mmol) and 3-bromo-*N,N*-dimethylaniline (0.80 g, 4 mmol) was dissolved in dichloromethane (15 mL) and cooled in an ice bath (0 °C). BF₃•OEt₂ complex (908 mg, 790 μL, 6.4 mmol) was added to the solution at 0 °C. The reaction mixture was heated to 40 °C and reacted for 8 h. After cooling to 23 °C, saturated NaHCO₃ aqueous solution was added into the reaction solution. The mixture was extracted with DCM (30 mL × 3) and the combined organic phase was washed with brine (three times) and dried over Na₂SO₄. The solvent was removed in vacuo and the residue was purified by column chromatography with hexane : EtOAc (30 : 1) to obtain **S4** (1.08 g, 62%).

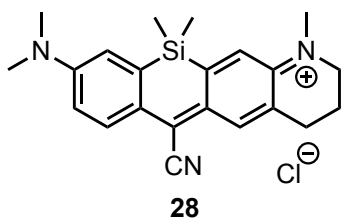
S4

¹H NMR (400 MHz, CD₂Cl₂) δ 6.92 (d, *J* = 2.7 Hz, 1H), 6.83 (d, *J* = 8.5 Hz, 1H), 6.74 (s, 1H), 6.62 – 6.55 (m, 2H), 3.92 (s, 2H), 3.22 – 3.15 (m, 2H), 2.90 (s, 6H), 2.85 (s, 3H), 2.60 (t, *J* = 6.5 Hz, 2H), 1.97 – 1.83 (m, 2H).

¹³C NMR (101 MHz, CD₂Cl₂) δ 150.57, 146.75, 131.01, 130.84, 127.44, 126.56, 125.71, 122.93, 122.90, 116.40, 114.48, 112.15, 51.24, 40.67, 40.06, 39.23, 27.73, 22.61.

n-Butyllithium (1.6 M solution in hexane, 1.56 mL, 2.5 mmol) was added dropwise into a solution of **S4** (438 mg, 1 mmol) in dry tetrahydrofuran (15 mL) when cooling in dry ice bath ($-78\text{ }^{\circ}\text{C}$). The reaction mixture was allowed to stir for 30 min at $-78\text{ }^{\circ}\text{C}$. The corresponding silane (dichlorodimethylsilane or dichloro(3-chloropropyl)methylsilane or dichloro(methyl)(3,3,3-trifluoropropyl)silane, 1.5 mmol) was then added dropwise into the reaction solution at $-78\text{ }^{\circ}\text{C}$. The dry ice bath was then removed, and the mixture was allowed to stir at $23\text{ }^{\circ}\text{C}$. The reaction was stirred for 6 h before quenched by dropwise addition of aq. HCl (3 mL, 1 M). The solution was then carefully neutralized with saturated aq. NaHCO_3 (keep the pH below 8.0). The mixture was extracted with DCM ($3 \times 20\text{ mL}$) and dried over Na_2SO_4 , and concentrated. The obtained crude solid mixture was purified by flash column chromatography with ethyl acetate and hexane as eluents. On TLC plates, the product band was initially colorless and turned to be blue or violet by oxidation with oxygen and showed strong fluorescence under 365 nm UV lamp.

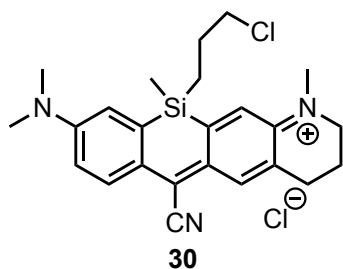
50 mg product from the last step was dissolved in 10 mL DCM and mixed with 5 ml aq. FeCl_3 (0.5 M in 1 M HCl) and stirred for 12 h at $23\text{ }^{\circ}\text{C}$. The organic phase was then separated and washed with brine and concentrated. This freshly-oxidized (Note: the Si xanthenes can also be reduced quickly under air even at $-20\text{ }^{\circ}\text{C}$, so fresh preparation is necessary) xanthenes was dissolved in 3 ml acetonitrile, aq. KCN (100 mg/mL, 1.5 M) was added dropwise to the xanthenes solution until the blue color disappeared. Right after the blue color disappeared, 2 ml aq. FeCl_3 (0.5 M in 1 M HCl) was added and the reaction was stirred at $23\text{ }^{\circ}\text{C}$ for 15 min. The reaction was then diluted with 10 ml brine. The reaction mixture was extracted with DCM ($10\text{ mL} \times 3$). The combined organic layer was washed with brine and dried over Na_2SO_4 . The solvent was removed in vacuo and the residue was purified by flash column chromatography with MeOH: DCM (0.07 : 1) to afford the green product.



Yield (52%)

^1H NMR (400 MHz, CDCl_3) δ 8.04 (d, $J = 9.4$ Hz, 1H), 7.75 (d, $J = 1.3$ Hz, 1H), 7.50 (s, 1H), 7.20 (d, $J = 2.8$ Hz, 1H), 6.87 (dd, $J = 9.5, 2.8$ Hz, 1H), 3.90 (t, $J = 5.8$ Hz, 2H), 3.72 (s, 3H), 3.43 (s, 6H), 2.88 – 2.76 (m, 2H), 2.09 (p, $J = 6.2$ Hz, 4H), 0.62 (s, 6H).

^{13}C NMR (101 MHz, CDCl_3) δ 153.80, 147.31, 145.08, 138.67, 136.93, 130.36, 129.55, 127.62, 126.88, 124.03, 121.71, 116.81, 114.86, 54.14, 42.17, 41.48, 27.15, 20.93, -0.55.

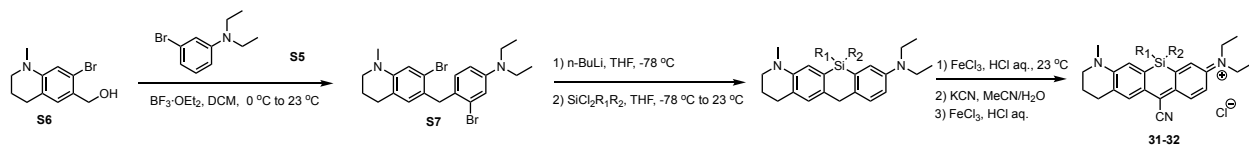


Yield (44%)

^1H NMR (400 MHz, CDCl_3) δ 8.02 (d, $J = 9.4$ Hz, 1H), 7.73 (s, 1H), 7.54 (s, 1H), 7.24 (d, $J = 2.7$ Hz, 1H), 6.88 (dd, $J = 9.4, 2.7$ Hz, 1H), 3.86 (t, $J = 5.8$ Hz, 2H), 3.70 (s, 3H), 3.45 (t, $J = 6.8$ Hz, 2H), 3.43 (s, 6H), 2.82 (t, $J = 6.3$ Hz, 2H), 2.08 (p, $J = 6.2$ Hz, 2H), 1.63 (dp, $J = 12.0, 6.4$ Hz, 2H), 1.36 – 1.20 (m, 2H), 0.67 (s, 3H).

^{13}C NMR (101 MHz, CDCl_3) δ 153.79, 153.65, 145.61, 143.56, 138.77, 136.91, 130.34, 129.57, 127.60, 127.12, 124.21, 122.06, 116.72, 115.05, 54.05, 47.55, 42.18, 41.55, 27.11, 26.96, 20.84, 13.36, -2.40.

Synthesis of 31-32



3-bromo-N,N-diethylaniline (**S5**) was synthesized according to previous report³³.

S6 (1.02 g, 4 mmol) and **S5** (912 mg, 4 mmol) were dissolved in dichloromethane (15 mL) and cooled in an ice bath (0 °C). $\text{BF}_3 \cdot \text{OEt}_2$ complex (908 mg, 790 μL , 6.4 mmol) was added to the solution at 0 °C. The reaction mixture was heated to 40 °C and reacted for 8 h. After cooling to 23 °C, saturated NaHCO_3 aqueous solution was added into the reaction solution. The mixture was extracted with DCM (30 mL \times 3) and the combined organic phase was washed with brine (three times) and dried over Na_2SO_4 . The solvent was removed in vacuo and the residue was purified by column chromatography with hexane : EtOAc (30 : 1) to obtain **S7** (1.04 g, 56%).

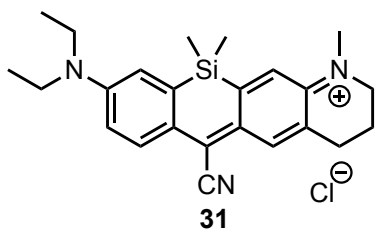
S7

^1H NMR (400 MHz, CDCl_3) δ 6.90 (d, $J = 2.7$ Hz, 1H), 6.85 (d, $J = 8.6$ Hz, 1H), 6.79 (s, 1H), 6.66 (d, $J = 1.0$ Hz, 1H), 6.55 (dd, $J = 8.7, 2.7$ Hz, 1H), 3.97 (s, 2H), 3.32 (q, $J = 7.1$ Hz, 4H), 3.24 – 3.15 (m, 2H), 2.88 (s, 3H), 2.64 (t, $J = 6.5$ Hz, 2H), 1.94 (dtd, $J = 9.0, 6.1, 4.8$ Hz, 2H), 1.17 (t, $J = 7.1$ Hz, 6H).

n-Butyllithium (1.6 M solution in hexane, 1.56 mL, 2.5 mmol) was added dropwise into a solution of **S7** (466 mg, 1 mmol) in dry tetrahydrofuran (15 mL) when cooling in dry ice bath (−78 °C). The reaction mixture was allowed to stir for 30 min at −78 °C. The corresponding silane (dichlorodimethylsilane or dichloro(methyl)(3,3,3-trifluoropropyl)silane, 1.5 mmol) was then added dropwise into the reaction solution at −78 °C. The dry ice bath was then removed, and the mixture was allowed to stir at 23 °C. The reaction was stirred for 6 h before quenched by dropwise addition of aq. HCl (3 mL, 1 M). The solution was then carefully neutralized with saturated aq. NaHCO_3 (keep the pH below 8.0). The mixture was extracted with DCM (3 \times 20 mL) and dried over NaSO_4 , and concentrated. The obtained crude solid mixture was purified by flash column

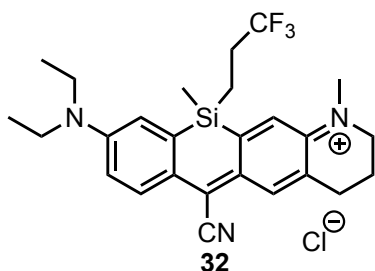
chromatography with ethyl acetate and hexane as eluents. On TLC plates, the product band was initially colorless and turned to be blue or violet by oxidation with oxygen and showed strong fluorescence under 365 nm UV lamp.

50 mg product from the last step was dissolved in 10 mL DCM and mixed with 5 ml aq. FeCl_3 (0.5 M in 1 M HCl) and stirred for 12 h at 23 °C. The organic phase was then separated and washed with brine and concentrated. This freshly-oxidized (Note: the Si xanthenone can also be reduced quickly under air even at -20 °C, so fresh preparation is necessary) xanthenone was dissolved in 3 ml acetonitrile, aq. KCN (100 mg/mL, 1.5 M) was added dropwise to the xanthenone solution until the blue color disappeared. Right after the blue color disappeared, 2 ml aq. FeCl_3 (0.5 M in 1 M HCl) was added and the reaction was stirred at 23 °C for 15 min. the reaction was then diluted with 10 ml brine. The reaction mixture was extracted with DCM (10 mL \times 3). The combined organic layer was washed with brine and dried over Na_2SO_4 . The solvent was removed in vacuo and the residue was purified by flash column chromatography with MeOH: DCM (0.07 : 1) to afford the green product.



Yield (45%)

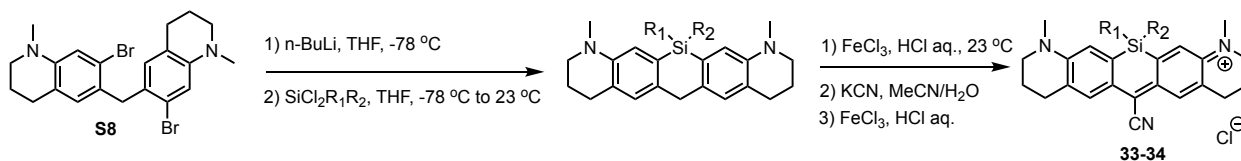
^1H NMR (400 MHz, CDCl_3) δ 8.02 (d, $J = 9.5$ Hz, 1H), 7.72 (s, 1H), 7.41 (s, 1H), 7.15 (d, $J = 2.8$ Hz, 1H), 6.84 (dd, $J = 9.5, 2.8$ Hz, 1H), 3.88 (t, $J = 5.7$ Hz, 2H), 3.72 (q, $J = 7.2$ Hz, 4H), 3.67 (s, 3H), 2.81 (t, $J = 6.4$ Hz, 2H), 2.07 (p, $J = 6.1$ Hz, 2H), 1.34 (t, $J = 7.2$ Hz, 6H), 0.59 (s, 6H).



Yield (43%)

^1H NMR (400 MHz, CDCl_3) δ 8.02 (d, $J = 9.6$ Hz, 1H), 7.71 (d, $J = 10.3$ Hz, 1H), 7.62 (s, 1H), 7.24 (d, $J = 2.8$ Hz, 1H), 6.87 (dd, $J = 9.5, 2.7$ Hz, 1H), 3.84 (s, 2H), 3.79 – 3.72 (m, 4H), 3.72 (s, 3H), 2.81 (t, $J = 6.5$ Hz, 2H), 2.07 (p, $J = 6.1$ Hz, 2H), 2.03 – 1.82 (m, 2H), 1.48 – 1.36 (m, 2H), 1.33 (t, $J = 7.1$ Hz, 6H), 0.77 (s, 3H).

Synthesis of 33-34

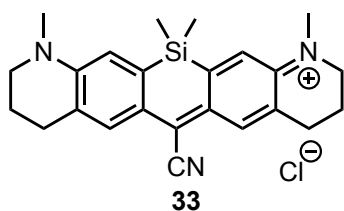


S8 was synthesized according to previous report³⁴.

n-Butyllithium (1.6 M solution in hexane, 1.56 mL, 2.5 mmol) was added dropwise into a solution of **S8** (464 mg, 1 mmol) in dry tetrahydrofuran (15 mL) when cooling in dry ice bath (-78 °C). The reaction mixture was allowed to stir for 30 min at -78 °C. The corresponding silane (dichlorodimethylsilane or dichloro(methyl)(3,3,3-trifluoropropyl)silane, 1.5 mmol) was then added dropwise into the reaction solution at -78 °C. The dry ice bath was then removed, and the mixture was allowed to stir at 23 °C. The reaction was stirred for 6 h before quenched by dropwise addition of aq. HCl (3 mL, 1 M). The solution was then carefully neutralized with saturated aq. NaHCO_3 (keep the pH below 8.0). The mixture was extracted with DCM (3×20 mL) and dried over NaSO_4 , and concentrated. The obtained crude solid mixture was purified by flash column chromatography with ethyl acetate and hexane as eluents. On TLC plates, the product band

was initially colorless and turned to be blue or violet by oxidation with oxygen and showed strong fluorescence under 365 nm UV lamp.

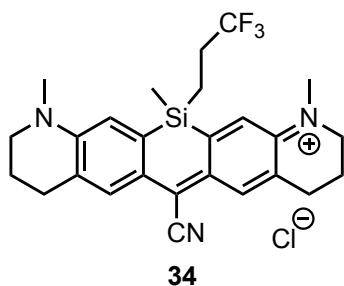
50 mg product from the last step was dissolved in 10 mL DCM and mixed with 5 ml aq. FeCl₃ (0.5 M in 1 M HCl) and stirred for 12 h at 23 °C. The organic phase was then separated and washed with brine and concentrated. This freshly-oxidized (Note: the Si xanthenes can also be reduced quickly under air even at -20 °C, so fresh preparation is necessary) xanthenes were dissolved in 3 ml acetonitrile, aq. KCN (100 mg/mL, 1.5 M) was added dropwise to the xanthenes solution until the blue color disappeared. Right after the blue color disappeared, 2 ml aq. FeCl₃ (0.5 M in 1 M HCl) was added and the reaction was stirred at 23 °C for 15 min. The reaction was then diluted with 10 ml brine. The reaction mixture was extracted with DCM (10 mL × 3). The combined organic layer was washed with brine and dried over Na₂SO₄. The solvent was removed in vacuo and the residue was purified by flash column chromatography with MeOH: DCM (0.07 : 1) to afford the green product.



Yield (55%)

¹H NMR (400 MHz, CDCl₃) δ 7.71 (s, 2H), 7.24 (s, 2H), 3.79 (t, *J* = 5.7 Hz, 4H), 3.55 (s, 6H), 2.81 (t, *J* = 6.2 Hz, 4H), 2.06 (p, *J* = 5.9 Hz, 4H), 0.58 (s, 6H).

¹³C NMR (101 MHz, CDCl₃) δ 152.65, 145.66, 136.28, 129.62, 128.25, 126.63, 122.23, 116.99, 41.33, 27.30, 21.03, 1.12, -0.48.

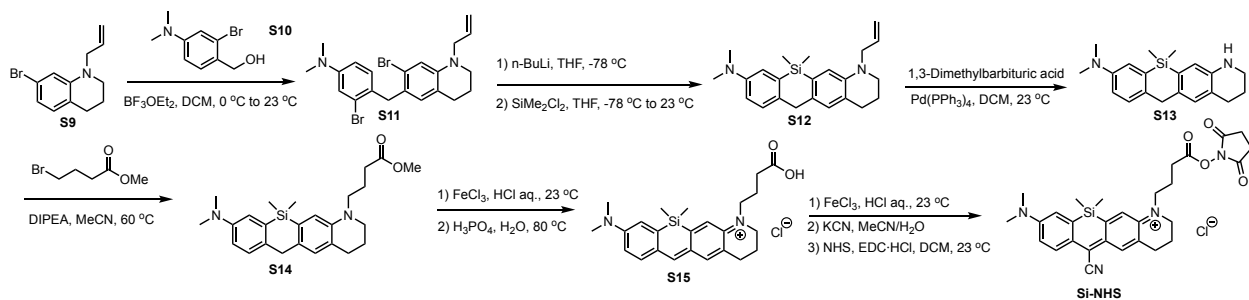


Yield (48%)

^1H NMR (400 MHz, CDCl_3) δ 7.71 (s, 2H), 7.40 (s, 2H), 3.77 (t, $J = 5.8$ Hz, 4H), 3.59 (s, 6H), 2.81 (dd, $J = 7.3, 5.4$ Hz, 4H), 2.13 – 2.03 (m, 4H), 2.01 – 1.85 (m, 2H), 1.39 – 1.32 (m, 2H), 0.78 (s, 3H).

^{13}C NMR (101 MHz, CDCl_3) δ 152.69, 142.99, 136.33, 129.43, 128.43, 126.83, 122.82, 116.89, 41.52, 28.30 (q, $J = 30.3$ Hz), 27.25, 20.91, 8.46, 1.11, -2.77.

Synthesis of Si-NHS



S9¹⁰ and **S10**³³ were synthesized according to previous report.

S9 (1.00 g, 4 mmol) and **S10** (920 mg, 4 mmol) were dissolved in dichloromethane (15 mL) and cooled in an ice bath (0 °C). $\text{BF}_3 \cdot \text{OEt}_2$ complex (908 mg, 790 μL , 6.4 mmol) was added to the solution at 0 °C. The reaction mixture was heated to 40 °C and reacted for 8 h. After cooling to 23 °C, saturated NaHCO_3 aqueous solution was added into the reaction solution. The mixture was extracted with DCM (30 mL \times 3) and the combined organic phase was washed with brine (three times) and dried over Na_2SO_4 . The solvent was removed in vacuo and the residue was purified by column chromatography with hexane : EtOAc (30 : 1) to obtain **S11** (1.15 g, 62%).

S11

^1H NMR (400 MHz, CDCl_3) δ 6.95 (d, $J = 2.7$ Hz, 1H), 6.87 (d, $J = 8.6$ Hz, 1H), 6.74 (s, 1H), 6.64 – 6.58 (m, 2H), 5.84 (ddt, $J = 17.0, 10.0, 4.9$ Hz, 1H), 5.25 – 5.12 (m, 2H), 3.96 (s, 2H), 3.84 (dt, $J = 4.9, 1.7$ Hz, 2H), 3.27 – 3.21 (m, 2H), 2.92 (s, 6H), 2.62 (t, $J = 6.3$ Hz, 2H), 2.00 – 1.86 (m, 2H).

^{13}C NMR (101 MHz, CDCl_3) δ 150.02, 144.88, 133.05, 130.85, 130.81, 127.59, 126.16, 125.65, 122.94, 122.05, 116.40, 116.34, 114.46, 112.06, 53.88, 48.95, 40.71, 39.84, 27.81, 22.21.

n-Butyllithium (1.6 M solution in hexane, 3.12 mL, 5.0 mmol) was added dropwise into a solution of **S11** (928 mg, 2 mmol) in dry tetrahydrofuran (20 mL) when cooling in dry ice bath (-78 °C). The reaction mixture was allowed to stir for 30 min at -78 °C. Dichlorodimethylsilane (388 mg, 362 μL , 3.0 mmol) was then added dropwise into the reaction solution at -78 °C. The dry ice bath was then removed, and the mixture was allowed to stir at 23 °C. The reaction was stirred for 6 h before quenched by dropwise addition of aq. HCl (3 mL, 1 M). The solution was then carefully neutralized with saturated aq. NaHCO_3 (keep the pH below 8.0). The mixture was extracted with DCM (20 mL \times 3) and dried over NaSO_4 , and concentrated. The obtained crude solid mixture was purified by flash column chromatography with hexane : EtOAc : Et_3N (1 : 0.05 : 0.005) as eluents to obtain **S12** (493 mg, 68%).

S12

^1H NMR (400 MHz, CDCl_3) δ 7.16 (d, $J = 8.3$ Hz, 1H), 6.99 (d, $J = 2.8$ Hz, 1H), 6.92 (d, $J = 0.9$ Hz, 1H), 6.80 (s, 1H), 6.73 (dd, $J = 8.4, 2.9$ Hz, 1H), 5.88 (ddt, $J = 17.2, 10.3, 5.2$ Hz, 1H), 5.27 – 5.13 (m, 2H), 3.91 (s, 2H), 3.30 – 3.20 (m, 2H), 2.93 (s, 6H), 2.77 (t, $J = 6.3$ Hz, 2H), 2.02 – 1.89 (m, 2H), 0.42 (s, 6H).

^{13}C NMR (101 MHz, CDCl_3) δ 148.76, 143.37, 136.34, 135.48, 134.23, 134.07, 133.52, 128.81, 128.52, 123.87, 117.75, 116.21, 115.87, 114.21, 54.39, 49.50, 41.32, 39.13, 28.33, 22.56, -2.52.

S12 (363 mg, 1.0 mmol), 1,3-dimethylbarbituric acid (1.25 g, 8.0 mmol) and tetrakis(triphenylphosphine)palladium (231 mg, 0.20 mmol) was dissolved in DCM (20 mL). The solution was degassed with N₂ for 30 min and the reaction was stirred at 23 °C for 12 h. Saturated NaHCO₃ solution was added to quench the solution and the reaction mixture was extracted with DCM (20 mL × 3). The combined organic phase was washed with brine and dried over NaSO₄. The solvent was removed in vacuo and the residue was purified by column chromatography with with hexane : EtOAc : Et₃N (1 : 0.05 : 0.005) as eluents to obtain **S13** (210 mg, 65%).

S13

¹H NMR (400 MHz, CDCl₃) δ 7.17 (d, *J* = 8.4 Hz, 1H), 7.00 (d, *J* = 2.8 Hz, 1H), 6.92 (t, *J* = 1.0 Hz, 1H), 6.75 (dd, *J* = 8.4, 2.8 Hz, 1H), 6.72 (s, 1H), 3.90 (s, 2H), 3.33 – 3.23 (m, 2H), 2.93 (s, 6H), 2.76 (t, *J* = 6.4 Hz, 2H), 1.99 – 1.86 (m, 2H), 0.41 (s, 6H).

¹³C NMR (101 MHz, CDCl₃) δ 148.57, 142.70, 136.37, 135.81, 135.39, 133.69, 129.06, 128.56, 122.85, 119.17, 117.91, 114.39, 42.39, 41.45, 39.40, 27.15, 22.52, -2.60.

S13 (200 mg, 0.62 mmol) was dissolved in acetonitrile (15 mL). N,N-diisopropylethylamine (160 mg, 216 μL, 1.24 mmol), methyl 4-bromobutyrate (898 mg, 628 μL, 4.96 mmol) was added and the reaction was heated at 60 °C for 12h. After cooling to room temperature, water was added to quench the reaction. The reaction mixture was extracted with DCM (20 mL × 3) and the combined organic phase was washed with 1M HCl and brine (three times) and dried over NaSO₄. The solvent was removed in vacuo and the residue was purified by column chromatography with hexane : EtOAc : Et₃N (1 : 0.06 : 0.005) as eluents to obtain **S14** (160 mg, 61%).

S14

¹H NMR (400 MHz, CD₂Cl₂) δ 7.13 (d, *J* = 8.4 Hz, 1H), 6.96 (d, *J* = 2.9 Hz, 1H), 6.86 (s, 1H), 6.80 (s, 1H), 6.70 (dd, *J* = 8.4, 2.9 Hz, 1H), 3.85 (s, 2H), 3.66 (s, 3H), 3.31 (t, *J* = 7.4 Hz, 2H), 3.24 (t, *J* = 5.6 Hz, 2H), 2.91 (s, 6H), 2.72 (t, *J* = 6.4 Hz, 2H), 2.37 (t, *J* = 7.2 Hz, 2H), 1.96 – 1.84 (m, 4H), 0.41 (s, 6H).

^{13}C NMR (101 MHz, CD_2Cl_2) δ 174.02, 149.12, 143.62, 136.53, 135.43, 134.19, 133.66, 129.00, 128.58, 124.11, 117.70, 115.52, 114.14, 51.77, 51.13, 50.01, 41.19, 39.14, 31.71, 28.59, 22.82, 22.04, -2.63.

S14 (150 mg, 0.35 mmol) was dissolved in 10 mL DCM and mixed with 5 ml aq. FeCl_3 (0.5 M in 1 M HCl) and stirred for 12 h at 23 °C. The organic phase was then separated and washed with brine and concentrated. The residue was dissolved in phosphoric acid (10 mL, 85% wt. in water) and water (10 mL) and heated to 80°C. The reaction was stirred for 4 h and cooled to room temperature before adding brine to dilute the reaction mixture. The reaction mixture was extracted with DCM (15 mL \times 3). The combined organic layer was washed with brine (three times) and dried over Na_2SO_4 . The solvent was removed in vacuo and the residue was purified by flash column chromatography with MeOH: DCM (0.07 : 1) to afford **S15** (128 mg, 83%).

S15

^1H NMR (400 MHz, MeOD) δ 7.75 (s, 1H), 7.66 (d, J = 9.1 Hz, 1H), 7.59 (s, 1H), 7.41 (s, 1H), 7.30 – 7.25 (m, 1H), 6.93 (dd, J = 9.2, 2.7 Hz, 1H), 3.74 – 3.66 (m, 4H), 3.36 (s, 6H), 2.79 (t, J = 6.3 Hz, 2H), 2.48 (dd, J = 6.9, 5.6 Hz, 2H), 2.06 – 1.95 (m, 4H), 0.53 (s, 6H).

S15 (50 mg, 0.11 mmol) was dissolved in 10 mL DCM and mixed with 5 ml aq. FeCl_3 (0.5 M in 1 M HCl) and stirred for 6 h at 23 °C. The organic phase was then separated and washed with brine and concentrated. This freshly-oxidized I17 was dissolved in 3 ml acetonitrile, aq. KCN (100 mg/mL, 1.5 M) was added dropwise to the xanthene solution until the blue color disappeared. Right after the blue color disappeared, 2 ml aq. FeCl_3 (0.5 M in 1 M HCl) was added and the reaction was stirred at 23 °C for 15 min. The reaction was then diluted with 10 ml brine. The reaction mixture was extracted with DCM (10 mL \times 3). The combined organic layer was washed with brine and dried over Na_2SO_4 . The solvent was removed in vacuo and the residue was purified by flash column chromatography with MeOH: DCM (0.07 : 1) to afford the green product.

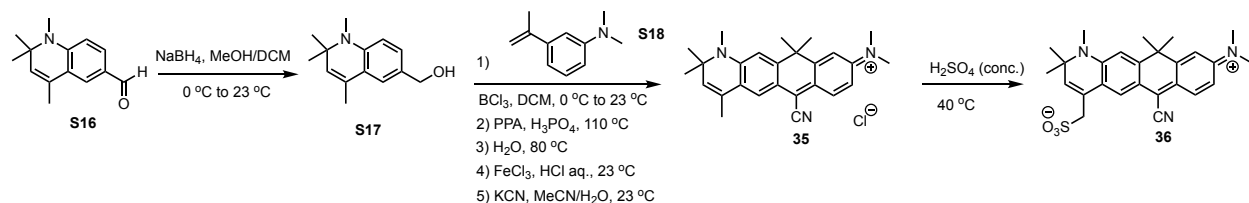
The obtained green solid together with N-hydroxylsuccinimide (NHS, 20 mg, 0.17 mmol) and N-(3-Dimethylaminopropyl)-N'-ethylcarbodiimide hydrochloride (EDC·HCl, 38 mg, 0.20 mmol) was dissolved in DCM (5 mL) and stirred overnight. The reaction was then diluted with 10 mL brine. The reaction mixture was extracted with DCM (10 mL × 3). The combined organic layer was washed with brine and dried over Na₂SO₄. The residue was purified by column chromatography with MeOH: DCM (0.07 : 1) or RP-HPLC (with MeCN and 0.1% TFA aqueous solution) to obtain **Si-NHS** (10 mg, 16%).

Si-NHS

¹H NMR (400 MHz, MeOD) δ 8.10 (d, *J* = 9.4 Hz, 1H), 7.82 (s, 1H), 7.45 (s, 1H), 7.36 (s, 1H), 7.11 (d, *J* = 9.3 Hz, 1H), 3.91 (t, *J* = 7.8 Hz, 2H), 3.82 (d, *J* = 5.3 Hz, 2H), 3.43 (s, 6H), 2.94 – 2.83 (m, 8H), 2.25 – 2.15 (m, 2H), 2.12 – 2.03 (m, 2H), 0.54 (s, 6H).

¹³C NMR (101 MHz, MeOD) δ 171.72, 170.47, 155.82, 154.17, 147.45, 146.52, 140.02, 138.06, 131.83, 130.55, 129.71, 128.96, 128.40, 123.63, 117.49, 116.71, 52.91, 52.57, 41.48, 28.73, 28.18, 26.63, 23.44, 21.97, -1.17.

Synthesis of 35-36



S16³⁵ and **S18**⁹ were synthesized according to previous reports.

S16 (1.08 g, 5 mmol) was dissolved in 10 mL MeOH and 5 mL DCM and cooled in an ice bath (0 °C), NaBH₄ (227 mg, 6 mmol) was slowly added into the mixture at 0 °C. The reaction was then allowed to warm to 23 °C and stirred for 2 h. The solvent was then removed in vacuo and water was slowly added to quench the reaction. The mixture was extracted with DCM (20 mL × 3) and the organic phase was washed with brine (three times) and then dried

over Na₂SO₄. The solvent was removed in vacuo and the residue was purified by column chromatography with hexane : EtOAc (8 : 1) to obtain **S17** (945 mg, 87%).

S17

¹H NMR (400 MHz, CDCl₃) δ 7.16 – 7.04 (m, 2H), 6.50 (s, 1H), 5.32 (s, 1H), 4.56 (d, *J* = 5.0 Hz, 2H), 2.81 (s, 3H), 2.02 – 1.96 (m, 3H), 1.30 (s, 6H).

S17 (217 mg, 1 mmol) and **S18** (161 mg, 1 mmol) were dissolved in 10 mL DCM and cooled in an ice bath (0 °C). BCl₃ (1 M in DCM, 2 mL, 2 mmol) was added dropwise into the solution at 0 °C. The reaction was allowed to warm to 23 °C and stirred for 12 h before a premixed solution of polyphosphoric acid (9.0 g) and H₃PO₄ (9.0 g, 85%) was added. The whole mixture was heated gently to 60 °C until DCM was thoroughly evaporated. The reaction was then heated to 110 °C and stirred vigorously for 4 h. After cooled to 80 °C, the reaction was added with 20 mL H₂O, and kept stirring for another 3 h before pouring into ice. The aqueous solution was carefully neutralized with 50% NaOH solution (keep pH < 8) and extracted with DCM (30 mL × 4). The combined organic phase was washed with brine and concentrated. The residue was dissolved in 20 mL DCM and mixed with 10 ml aq. FeCl₃ (0.5 M in 1 M HCl) and stirred for 2 h at 23 °C. The organic phase was then separated and washed with brine and dried over Na₂SO₄. The solvent was removed in vacuo and the residue was purified by flash column chromatography with MeOH: DCM (0.07 : 1) to afford the blue compound.

This freshly made compound was dissolved in 5 ml acetonitrile, aq. KCN (100 mg/mL, 1.5 M) was added dropwise to the solution until the blue color disappeared. Right after the blue color disappeared, 2 ml aq. FeCl₃ (0.5 M in 1 M HCl) was added and the reaction was stirred at 23 °C for 15 min. The reaction was then diluted with 10 ml brine. The reaction mixture was extracted with DCM (15 mL × 3). The combined organic layer was washed with brine and dried over Na₂SO₄. The solvent was removed in vacuo and the residue was purified by flash column chromatography with MeOH: DCM (0.08 : 1) to afford **35** (85 mg, 20%).

35

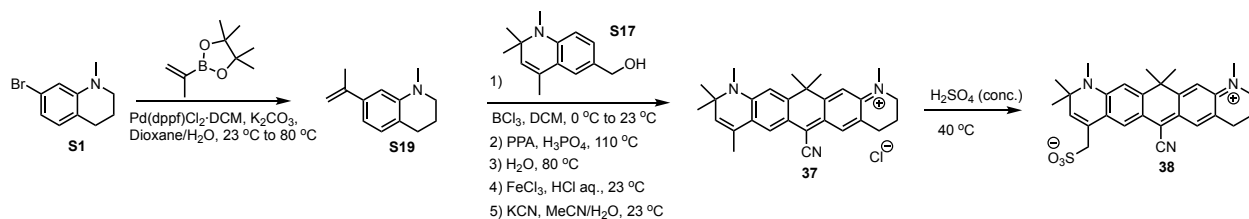
^1H NMR (400 MHz, CDCl_3) δ 7.84 (d, $J = 9.2$ Hz, 1H), 7.51 – 7.44 (m, 1H), 7.39 (s, 1H), 7.16 (d, $J = 2.5$ Hz, 1H), 6.88 (dd, $J = 9.2, 2.4$ Hz, 1H), 5.63 (s, 1H), 3.58 (s, 3H), 3.42 (s, 6H), 2.06 (d, $J = 1.4$ Hz, 3H), 1.84 (s, 6H), 1.56 (s, 6H).

^{13}C NMR (101 MHz, CDCl_3) δ 158.57, 155.96, 154.61, 154.26, 134.60, 132.69, 126.02, 125.72, 125.53, 124.18, 122.64, 119.91, 115.02, 113.84, 113.37, 112.34, 61.99, 42.55, 41.64, 35.40, 34.58, 29.13, 18.23.

35 (42 mg, 0.1 mmol) was dissolved in sulfuric acid (98%, 4 mL) and was heated at 40 °C with vigorous stirring. The reaction was stirred for 12 h before cooling to 0 °C in an ice bath. The reaction was slowly added ice (20 g) and wait until the solution is cooled to 23 °C. The reaction mixture was extracted with DCM (15 mL \times 4). The combined organic layer was washed with brine (five times) until the aqueous phase had no blue color and dried over Na_2SO_4 . The solvent was removed in vacuo and the residue was purified by flash column chromatography with MeOH: DCM (0.1 : 1 to 0.4 : 1) to afford **36** (16 mg, 35%).

36

^1H NMR (400 MHz, CD_2Cl_2) δ 7.92 (d, $J = 1.6$ Hz, 1H), 7.87 (dd, $J = 9.3, 1.5$ Hz, 1H), 7.06 – 6.98 (m, 2H), 6.93 (ddd, $J = 9.3, 2.5, 1.5$ Hz, 1H), 5.94 (s, 1H), 3.97 – 3.82 (m, 2H), 3.32 (s, 6H), 3.28 – 3.18 (m, $J = 1.5$ Hz, 3H), 1.65 (d, $J = 1.5$ Hz, 6H), 1.55 (d, $J = 1.5$ Hz, 6H).

Synthesis of 37-38

S1 (1.13 g, 5 mmol), Pd(dppf)Cl₂·DCM (408 mg, 0.5 mmol) and K₂CO₃ (1.38 g, 10 mmol) were dissolved in 18 mL dioxane and 3 mL water. The mixture was degassed with N₂ for 30 min. Then isopropenylboronic acid pinacol ester (1.26 g, 1.41 mL, 7.5 mmol) was added to the mixture and the solution was further degassed with N₂ for 10 min. The reaction was then stirred at 80 °C for 2 h before another portion of isopropenylboronic acid pinacol ester (840 mg, 0.94 mL, 5 mmol) was added into the solution. The reaction continued to stir at 80 °C for another 6 h before cooled to 23 °C. The reaction mixture was filtered through a short pad of silica and diluted with brine. The solution was extracted with DCM (20 mL × 3) and the organic phase was washed with brine (three times) and then dried over Na₂SO₄. The solvent was removed in vacuo and the residue was purified by column chromatography with hexane : EtOAc (80 : 1) to obtain **S19** (599 mg, 64%).

S19

¹H NMR (400 MHz, CDCl₃) δ 6.93 (d, *J* = 7.7 Hz, 1H), 6.76 – 6.68 (m, 2H), 5.31 (dd, *J* = 1.8, 0.9 Hz, 1H), 5.01 (p, *J* = 1.6 Hz, 1H), 3.27 – 3.19 (m, 2H), 2.93 (s, 3H), 2.77 (t, *J* = 6.5 Hz, 2H), 2.16 – 2.13 (m, 3H), 2.06 – 1.94 (m, 2H).

¹³C NMR (101 MHz, CDCl₃) δ 146.49, 144.35, 140.60, 128.76, 122.63, 114.10, 111.48, 108.50, 51.49, 39.40, 27.66, 22.54, 22.21.

S17 (217 mg, 1 mmol) and **S19** (187 mg, 1 mmol) were dissolved in 10 mL DCM and cooled in an ice bath (0 °C). BCl₃ (1 M in DCM, 2 mL, 2 mmol) was added dropwise into the solution at 0 °C. The reaction was allowed to warm to 23 °C and stirred for 12 h before a premixed solution of polyphosphoric acid (9.0 g) and H₃PO₄ (9.0 g, 85%) was added. The whole mixture was heated gently to 60 °C until DCM was thoroughly evaporated. The reaction was then heated to 110 °C and stirred vigorously for 4 h. After cooled to 80 °C, the reaction was added with 20 mL H₂O, and kept stirring for another 3 h before pouring into ice. The aqueous solution was carefully neutralized with 50% NaOH solution (keep pH < 8) and extracted with DCM (30 mL × 4). The combined organic phase was washed with brine and concentrated.

The residue was dissolved in 20 mL DCM and mixed with 10 ml aq. FeCl₃ (0.5 M in 1 M HCl) and stirred for 2 h at 23 °C. The organic phase was then separated and washed with brine and dried over Na₂SO₄. The solvent was removed in vacuo and the residue was purified by flash column chromatography with MeOH: DCM (0.07 : 1) to afford the blue compound.

This freshly made compound was dissolved in 5 ml acetonitrile, aq. KCN (100 mg/mL, 1.5 M) was added dropwise to the solution until the blue color disappeared. Right after the blue color disappeared, 2 ml aq. FeCl₃ (0.5 M in 1 M HCl) was added and the reaction was stirred at 23 °C for 15 min. The reaction was then diluted with 10 ml brine. The reaction mixture was extracted with DCM (15 mL × 3). The combined organic layer was washed with brine and dried over Na₂SO₄. The solvent was removed in vacuo and the residue was purified by flash column chromatography with MeOH: DCM (0.08 : 1) to afford **37** (80 mg, 18%).

37

¹H NMR (400 MHz, CDCl₃) δ 7.50 (q, *J* = 1.6 Hz, 1H), 7.43 (s, 1H), 7.13 (d, *J* = 3.9 Hz, 2H), 5.55 (s, 1H), 3.75 (t, *J* = 5.7 Hz, 2H), 3.51 (s, 3H), 3.40 (s, 3H), 2.81 (t, *J* = 6.0 Hz, 2H), 2.08 – 1.99 (m, 5H), 1.78 (s, 6H), 1.51 (s, 6H).

¹³C NMR (101 MHz, CDCl₃) δ 157.17, 154.97, 154.44, 153.08, 132.04, 131.81, 125.68, 125.55, 124.81, 123.47, 121.27, 121.03, 115.16, 112.18, 111.97, 111.78, 61.21, 53.24, 42.19, 41.32, 34.58, 34.43, 29.25, 26.86, 20.96, 18.25.

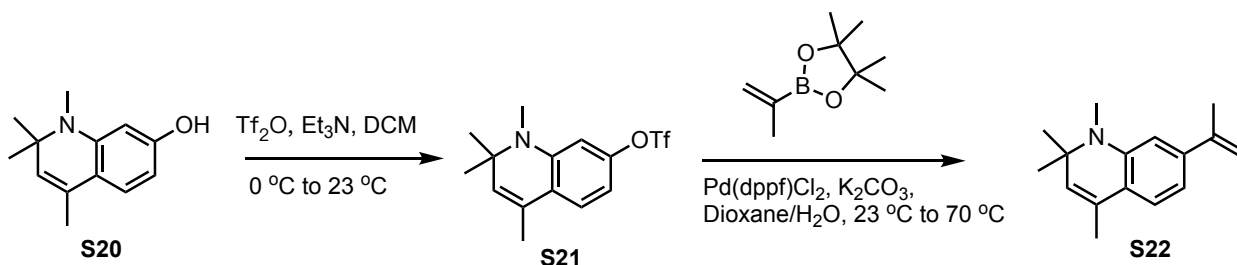
37 (45 mg, 0.1 mmol) was dissolved in sulfuric acid (98%, 4 mL) and was heated at 40 °C with vigorous stirring. The reaction was stirred for 12 h before cooling to 0 °C in an ice bath. The reaction was slowly added ice (20 g) and wait until the solution is cooled to 23 °C. The reaction mixture was extracted with DCM (15 mL × 4). The combined organic layer was washed with brine (five times) until the aqueous phase had no blue color and dried over Na₂SO₄. The solvent was removed in vacuo and the residue was purified by flash column chromatography with MeOH: DCM (0.1 : 1 to 0.4 : 1) to afford **38** (15 mg, 31%).

38

^1H NMR (400 MHz, MeOD) δ 7.78 (s, 1H), 7.45 (d, J = 1.2 Hz, 1H), 7.05 (s, 1H), 6.99 (s, 1H), 5.85 (s, 1H), 3.84 (s, 2H), 3.62 (t, J = 5.8 Hz, 2H), 3.24 (t, J = 4.4 Hz, 3H), 3.20 (p, J = 1.6 Hz, 3H), 2.79 – 2.72 (m, 2H), 1.99 – 1.91 (m, 2H), 1.58 (s, 6H), 1.49 (s, 6H).

^{13}C NMR (101 MHz, MeOD) δ 157.78, 156.14, 155.90, 154.74, 137.97, 132.86, 128.47, 127.46, 126.73, 124.04, 122.88, 122.49, 121.91, 115.81, 112.98, 112.61, 62.61, 54.00, 53.89, 42.96, 40.76, 34.46, 33.97, 28.81, 27.72, 22.02.

Synthesis of 39-40



S20 was synthesized according to previous report²⁵.

S20 (2.03 g, 10 mmol) and triethylamine (3.04 mg, 4.18 mL, 30 mmol) in DCM (20 mL) was cooled in an ice bath ($0\text{ }^\circ\text{C}$). Trifluoromethanesulfonic anhydride (12 mL, 1.0 M solution in DCM, 12 mmol) was added dropwise into the solution at $0\text{ }^\circ\text{C}$. The mixture was allowed to warm to $23\text{ }^\circ\text{C}$ and stirred for 2 h before quenched with 15 mL 1 M HCl. The organic phase was extracted with DCM ($20\text{ mL} \times 3$). The combined organic layer was washed with brine (three times) and dried over Na_2SO_4 . The solvent was removed in vacuo and the residue was purified by flash column chromatography with hexane : EtOAc (10 : 1) to obtain **S21** (2.54 g, 76%).

S21

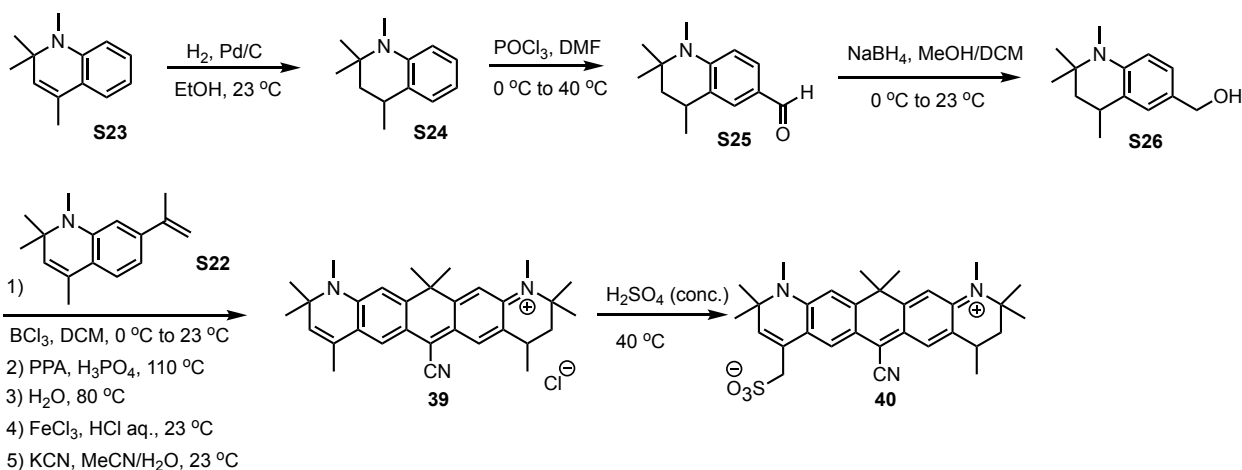
^1H NMR (400 MHz, CDCl_3) δ 7.01 (d, J = 8.3 Hz, 1H), 6.48 (dd, J = 8.3, 2.4 Hz, 1H), 6.30 (d, J = 2.4 Hz, 1H), 5.31 (q, J = 1.4 Hz, 1H), 2.78 (s, 3H), 1.96 (d, J = 1.5 Hz, 3H), 1.33 (s, 6H).

S21 (1.68 g, 5 mmol), Pd(dppf)Cl₂·DCM (408 mg, 0.5 mmol) and K₂CO₃ (1.38 g, 10 mmol) were dissolved in 18 mL dioxane and 3 mL water. The mixture was degassed with N₂ for 30 min. Then isopropenylboronic acid pinacol ester (1.26 g, 1.41 mL, 7.5 mmol) was added to the mixture and the solution was further degassed with N₂ for 10 min. The reaction was then stirred at 80 °C for 2 h before another portion of isopropenylboronic acid pinacol ester (840 mg, 0.94 mL, 5 mmol) was added into the solution. The reaction continued to stir at 80 °C for another 6 h before cooled to 23 °C. The reaction mixture was filtered through a short pad of silica and diluted with brine. The solution was extracted with DCM (20 mL × 3) and the organic phase was washed with brine (three times) and then dried over Na₂SO₄. The solvent was removed in vacuo and the residue was purified by column chromatography with hexane : EtOAc (80 : 1) to obtain **S22** (625 mg, 55%).

S22

¹H NMR (400 MHz, CDCl₃) δ 7.02 (d, *J* = 7.8 Hz, 1H), 6.77 (dd, *J* = 7.8, 1.7 Hz, 1H), 6.63 (d, *J* = 1.8 Hz, 1H), 5.35 (dd, *J* = 1.8, 0.9 Hz, 1H), 5.29 (q, *J* = 1.6 Hz, 1H), 5.03 (p, *J* = 1.5 Hz, 1H), 2.84 (s, 3H), 2.15 (dd, *J* = 1.5, 0.8 Hz, 3H), 1.99 (d, *J* = 1.5 Hz, 3H), 1.31 (s, 6H).

¹³C NMR (101 MHz, CDCl₃) δ 145.11, 144.28, 141.74, 130.20, 128.10, 123.13, 122.91, 113.96, 111.72, 108.02, 56.40, 30.72, 27.32, 22.11, 18.70.



S23 was synthesized according to previous report³⁵.

S23 (2.00 g, 11 mmol) and Pd/C (10 wt. % loading, 567 mg, 0.54 mmol Pd) were dissolved in 40 mL EtOH. Evacuate the reaction flask and backfill with hydrogen three times. The reaction solution was stirred at 23 °C for 10 hours under hydrogen balloon. After the reaction, the solution was filtered and the filtrate was concentrated in vacuo. The residue was purified by column chromatography with pure hexane to obtain **S24** (1.94 g, 96%).

S24

¹H NMR (400 MHz, CDCl₃) δ 7.16 – 7.06 (m, 2H), 6.67 (td, *J* = 7.4, 1.1 Hz, 1H), 6.59 (d, *J* = 9.3 Hz, 0H), 2.91 – 2.82 (m, 1H), 2.82 (s, 6H), 1.79 (dd, *J* = 13.0, 4.5 Hz, 1H), 1.59 – 1.52 (m, 1H), 1.35 (d, *J* = 6.7 Hz, 3H), 1.28 (s, 3H), 1.21 (s, 3H).

¹³C NMR (101 MHz, CDCl₃) δ 146.23, 128.87, 127.06, 125.16, 115.70, 111.22, 54.20, 47.17, 31.58, 29.11, 27.62, 24.72, 19.72.

POCl₃ (4.60 g, 2.80 ml, 30 mmol) was added dropwise to a flask filled with DMF (10 mL) when cooled in an ice bath (0 °C), and stirred for 30 min at 0 °C. Then **S24** (1.89 g, 10 mmol) was then added into the flask and the reaction mixture was allowed to stir for 8 h at 40 °C. When the reaction was cooled to 23 °C, the reaction solution was poured into brine. The mixture was extracted with DCM (20 mL × 3) and the organic phase was washed with brine (five times) and then dried over Na₂SO₄. The solvent was removed in vacuo and the residue was purified by column chromatography with hexane : EtOAc (10 : 1) to obtain **S25** (1.59 g, 73%).

S25

¹H NMR (400 MHz, CDCl₃) δ 9.71 (s, 1H), 7.63 (t, *J* = 1.7 Hz, 1H), 7.58 (dd, *J* = 8.6, 2.1 Hz, 1H), 6.58 (d, *J* = 8.6 Hz, 1H), 2.92 (s, 3H), 2.90 – 2.77 (m, 1H), 1.82 (dd, *J* = 13.1, 4.2 Hz, 1H), 1.53 (t, *J* = 13.1, 1H), 1.39 (d, *J* = 6.6 Hz, 3H), 1.34 (s, 3H), 1.27 (s, 3H).

^{13}C NMR (101 MHz, CDCl_3) δ 190.55, 151.26, 131.51, 128.23, 126.40, 124.84, 110.27, 55.45, 46.06, 32.02, 29.11, 27.20, 25.64, 19.29.

S25 (1.09 g, 5 mmol) was dissolved in 10 mL MeOH and 5 ml DCM and cooled in an ice bath (0 °C), NaBH_4 (227 mg, 6 mmol) was slowly added into the mixture at 0 °C. The reaction was then allowed to warm to 23 °C and stirred for 2 h. The solvent was then removed in vacuo and water was slowly added to quench the reaction. The mixture was extracted with DCM (20 mL \times 3) and the organic phase was washed with brine (three times) and then dried over Na_2SO_4 . The solvent was removed in vacuo and the residue was purified by column chromatography with hexane : EtOAc (8 : 1) to obtain **S26** (932 mg, 85%).

S26

^1H NMR (400 MHz, CDCl_3) δ 7.15 (t, J = 1.6 Hz, 1H), 7.10 (dd, J = 8.3, 2.2 Hz, 1H), 6.56 (d, J = 8.3 Hz, 1H), 4.56 (d, J = 4.1 Hz, 2H), 2.86 (dd, J = 12.6, 6.4 Hz, 1H), 2.81 (s, 3H), 1.79 (dd, J = 13.0, 4.5 Hz, 1H), 1.52 (t, J = 12.8 Hz, 1H), 1.41 (br, 1H), 1.35 (d, J = 6.7 Hz, 3H), 1.28 (s, 3H), 1.19 (s, 3H).

^{13}C NMR (101 MHz, CDCl_3) δ 146.07, 129.01, 127.93, 126.68, 125.06, 111.15, 65.96, 54.28, 47.06, 31.69, 29.10, 27.62, 24.71, 19.71.

S26 (219 mg, 1 mmol) and **S22** (227 mg, 1 mmol) were dissolved in 10 mL DCM and cooled in an ice bath (0 °C). BCl_3 (1 M in DCM, 2 mL, 2 mmol) was added dropwise into the solution at 0 °C. The reaction was allowed to warm to 23 °C and stirred for 12 h before a premixed solution of polyphosphoric acid (9.0 g) and H_3PO_4 (9.0 g, 85%) was added. The whole mixture was heated gently to 60 °C until DCM was thoroughly evaporated. The reaction was then heated to 110 °C and stirred vigorously for 4 h. After cooled to 80 °C, the reaction was added with 20 mL H_2O , and kept stirring for another 3 h before pouring into ice. The aqueous solution was carefully neutralized with 50% NaOH solution (keep pH < 8) and extracted with DCM (30 mL \times 4). The combined organic phase was washed with brine and concentrated. The residue was dissolved in 20 mL DCM and mixed with 10 ml aq. FeCl_3 (0.5 M in 1 M HCl) and stirred for 2 h at 23 °C. The organic phase was then separated and washed with

brine and dried over Na₂SO₄. The solvent was removed in vacuo and the residue was purified by flash column chromatography with MeOH: DCM (0.07 : 1) to afford the blue compound.

This freshly made compound was dissolved in 5 ml acetonitrile, aq. KCN (100 mg/mL, 1.5 M) was added dropwise to the solution until the blue color disappeared. Right after the blue color disappeared, 2 ml aq. FeCl₃ (0.5 M in 1 M HCl) was added and the reaction was stirred at 23 °C for 15 min. The reaction was then diluted with 10 ml brine. The reaction mixture was extracted with DCM (15 mL × 3). The combined organic layer was washed with brine and dried over Na₂SO₄. The solvent was removed in vacuo and the residue was purified by flash column chromatography with MeOH: DCM (0.08 : 1) to afford **39** (61 mg, 12%).

39

¹H NMR (400 MHz, CDCl₃) δ 7.63 (d, *J* = 1.7 Hz, 1H), 7.48 (s, 1H), 7.31 (s, 1H), 7.20 (s, 1H), 5.58 (s, 1H), 5.29 (s, 1H), 3.49 (s, 3H), 3.37 (s, 3H), 2.08 (d, *J* = 1.3 Hz, 3H), 1.93 (dd, *J* = 13.6, 4.1 Hz, 1H), 1.85 (d, *J* = 5.1 Hz, 6H), 1.65 (t, *J* = 13.5 Hz, 1H), 1.54 (s, 6H), 1.49 (s, 3H), 1.45 (d, *J* = 6.5 Hz, 3H), 1.42 (s, 3H).

¹³C NMR (101 MHz, CDCl₃) δ 157.89, 154.69, 154.20, 153.48, 132.21, 130.86, 129.01, 125.66, 125.13, 123.67, 121.64, 120.79, 115.24, 113.10, 112.59, 61.41, 58.89, 44.68, 42.36, 34.81, 34.78, 34.61, 34.53, 29.28, 29.03, 26.60, 25.74, 18.78, 18.33.

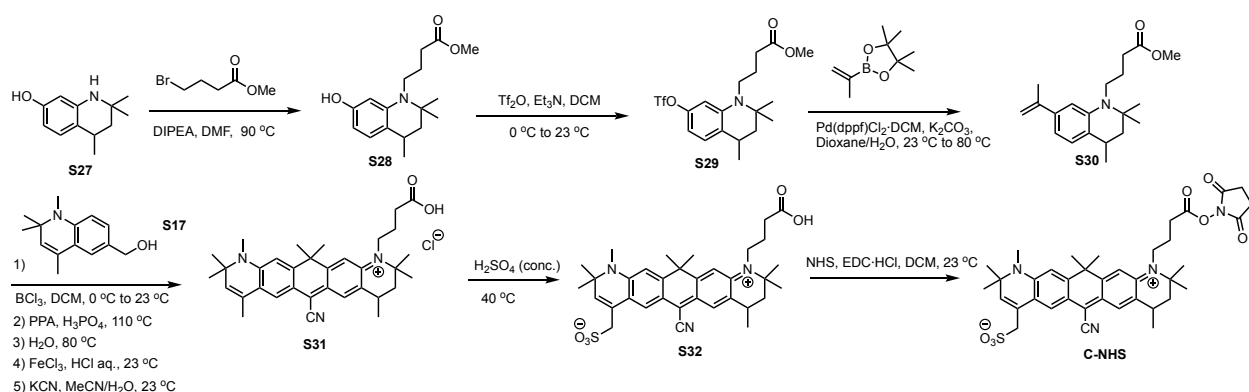
39 (49 mg, 0.1 mmol) was dissolved in sulfuric acid (98%, 4 mL) and was heated at 40 °C with vigorous stirring. The reaction was stirred for 12 h before cooling to 0 °C in an ice bath. The reaction was slowly added ice (20 g) and wait until the solution is cooled to 23 °C. The reaction mixture was extracted with DCM (15 mL × 4). The combined organic layer was washed with brine (five times) until the aqueous phase had no blue color and dried over Na₂SO₄. The solvent was removed in vacuo and the residue was purified by flash column chromatography with MeOH: DCM (0.1 : 1 to 0.4 : 1) to **40** (18 mg, 34%).

40

^1H NMR (400 MHz, 50% MeOD + 50% CD_2Cl_2 , peaks are much broader in this solvent) δ 8.01 (br, 1H), 7.85 – 7.76 (br, 1H), 7.11 – 6.99 (m, 2H), 6.01 (br, 1H), 5.41 (br, 1H), 4.02 (br, 2H), 3.36 (br, 6H), 2.08 – 1.96 (m, 1H), 1.79 – 1.67 (m, 7H), 1.64 (s, 6H), 1.58 – 1.46 (m, 9H).

^{13}C NMR (101 MHz, 50% MeOD + 50% CD_2Cl_2) δ 157.54, 154.93, 154.71, 154.45, 137.15, 131.82, 129.99, 128.33, 127.07, 123.62, 122.71, 122.12, 121.47, 115.32, 112.68, 111.97, 62.24, 59.64, 45.02, 42.30, 34.60, 34.50, 34.04, 33.96, 28.88, 28.78, 27.12, 25.56, 18.78.

Synthesis of C-NHS



S27 was synthesized according to previous report³⁶.

S27 (4.50 g, 23.5 mmol), methyl 4-bromobutyrate (6.39 g, 4.46 mL, 35.3 mmol) and N,N-Diisopropylethylamine (DIPEA, 4.55 g, 6.15 mL, 35.3 mmol) were dissolved in 50 mL DMF. The mixture was heated to 90 °C and stirred for 24 h. After the reaction solution cooled to 23 °C, the mixture was diluted with 150 mL brine. The reaction mixture was extracted with DCM (100 mL \times 3). The combined organic layer was washed with brine (five times) and dried over Na_2SO_4 . The solvent was removed in vacuo and the residue was purified by flash column chromatography with hexane: EtOAc (5 : 1) to obtain **S28** (4.30 g, 63%).

S28

^1H NMR (400 MHz, CDCl_3) δ 6.97 (d, $J = 7.2$ Hz, 1H), 6.15 (dd, $J = 6.2, 2.5$ Hz, 2H), 5.64 (br, 1H), 3.72 (s, 3H), 3.40 – 3.24 (m, 1H), 3.09 – 2.97 (m, 1H), 2.81 (qd, $J = 13.2, 6.7$ Hz, 1H), 2.38 (t, $J = 6.9$, 2H), 2.03 – 1.79 (m, 2H), 1.72 – 1.66 (m, 1H), 1.55 – 1.46 (m, 1H), 1.30 – 1.25 (m, 6H), 1.16 (s, 3H).

^{13}C NMR (101 MHz, CDCl_3) δ 174.29, 155.18, 146.01, 126.70, 120.61, 102.32, 98.82, 54.63, 51.91, 47.28, 44.60, 31.45, 29.66, 26.84, 25.01, 24.12, 20.29.

S28 (2.91 g, 10 mmol) and triethylamine (3.04 mg, 4.18 mL, 30 mmol) in DCM (30 mL) was cooled in an ice bath (0 °C). Trifluoromethanesulfonic anhydride (12 mL, 1.0 M solution in DCM, 12 mmol) was added dropwise into the solution at 0 °C. The mixture was allowed to warm to 23 °C and stirred for 2 h before quenched with 15 mL 1 M HCl. The organic phase was extracted with DCM (30 mL \times 4). The combined organic layer was washed with brine (three times) and dried over Na_2SO_4 . The solvent was removed in vacuo and the residue was purified by flash column chromatography with hexane : EtOAc (20 : 1) to obtain **S29** (3.30 g, 78%).

S29

^1H NMR (400 MHz, CDCl_3) δ 7.10 (dd, $J = 8.4, 1.3$ Hz, 1H), 6.49 (dd, $J = 8.3, 2.4$ Hz, 1H), 6.44 (d, $J = 2.5$ Hz, 1H), 3.71 (s, 3H), 3.43 – 3.30 (m, 1H), 3.13 – 3.02 (m, 1H), 2.88 – 2.76 (m, 1H), 2.39 (t, $J = 6.9$ Hz, 2H), 1.88 (dddd, $J = 12.9, 9.9, 7.0, 5.9$ Hz, 2H), 1.75 (dd, $J = 13.1, 4.6$ Hz, 1H), 1.51 (t, $J = 12.6$ Hz, 1H), 1.34 – 1.26 (m, 6H), 1.19 (s, 3H).

^{13}C NMR (101 MHz, CDCl_3) δ 173.54, 149.41, 146.32, 128.44, 122.10 (q, $J = 30$ Hz), 114.13, 107.04, 103.90, 55.05, 51.76, 46.52, 44.39, 31.25, 29.31, 27.22, 25.59, 23.39, 19.72.

S29 (2.12 g, 5 mmol), $\text{Pd}(\text{dppf})\text{Cl}_2 \cdot \text{DCM}$ (408 mg, 0.5 mmol) and K_2CO_3 (1.38 g, 10 mmol) were dissolved in 18 mL dioxane and 3 mL water. The mixture was degassed with N_2 for 30 min. Then isopropenylboronic acid pinacol ester (1.26 g, 1.41 mL, 7.5 mmol) was added to the mixture and the solution was further degassed with N_2 for 10 min. The reaction was then

stirred at 80 °C for 2 h before another portion of isopropenylboronic acid pinacol ester (840 mg, 0.94 mL, 5 mmol) was added into the solution. The reaction continued to stir at 80 °C for another 12 h before cooled to 23 °C. The reaction mixture was filtered through a short pad of silica and diluted with brine. The solution was extracted with DCM (20 mL × 4) and the organic phase was washed with brine (three times) and then dried over Na₂SO₄. The solvent was removed in vacuo and the residue was purified by column chromatography with hexane : EtOAc (80 : 1) to obtain **S30** (836 mg, 52%).

S30

¹H NMR (400 MHz, CDCl₃) δ 7.10 (d, *J* = 7.9 Hz, 1H), 6.76 (dd, *J* = 7.8, 1.8 Hz, 1H), 6.69 (s, 1H), 5.32 (s, 1H), 5.02 (s, 1H), 3.69 (d, *J* = 1.0 Hz, 3H), 3.40 (ddd, *J* = 15.5, 10.4, 5.4 Hz, 1H), 3.13 (ddd, *J* = 15.3, 10.3, 5.5 Hz, 1H), 2.86 (dt, *J* = 12.4, 6.1 Hz, 1H), 2.39 (t, *J* = 7.0 Hz, 2H), 2.15 (dd, *J* = 1.6, 0.9 Hz, 3H), 1.94 (dtd, *J* = 24.3, 13.8, 6.7 Hz, 2H), 1.73 (dd, *J* = 13.0, 4.7 Hz, 1H), 1.53 (t, *J* = 12.8 Hz, 1H), 1.36 – 1.25 (m, 6H), 1.17 (s, 3H).

¹³C NMR (101 MHz, CDCl₃) δ 173.87, 144.56, 144.38, 140.23, 127.99, 125.68, 113.27, 111.49, 108.86, 54.64, 51.77, 47.22, 44.39, 31.64, 29.60, 27.38, 25.22, 24.30, 22.15, 20.00.

S30 (315 mg, 1 mmol) and **S17** (217 mg, 1 mmol) were dissolved in 10 mL DCM and cooled in an ice bath (0 °C). BCl₃ (1 M in DCM, 2 mL, 2 mmol) was added dropwise into the solution at 0 °C. The reaction was allowed to warm to 23 °C and stirred for 12 h before a premixed solution of polyphosphoric acid (9.0 g) and H₃PO₄ (9.0 g, 85%) was added. The whole mixture was heated gently to 60 °C until DCM was thoroughly evaporated. The reaction was then heated to 110 °C and stirred vigorously for 4 h. After cooled to 80 °C, the reaction was added with 20 mL H₂O, and kept stirring for another 3 h before pouring into ice. The aqueous solution was carefully neutralized with 50% NaOH solution (keep pH < 8) and extracted with DCM (30 mL × 4). The combined organic phase was washed with brine and concentrated. The residue was dissolved in 20 mL DCM and mixed with 10 ml aq. FeCl₃ (0.5 M in 1 M HCl) and stirred for 2 h at 23 °C. The organic phase was then separated and washed with

brine and dried over Na₂SO₄. The solvent was removed in vacuo and the residue was purified by flash column chromatography with MeOH: DCM (0.07 : 1) to afford the blue compound.

This freshly made compound was dissolved in 5 ml acetonitrile, aq. KCN (100 mg/mL, 1.5 M) was added dropwise to the solution until the blue color disappeared. Right after the blue color disappeared, 2 ml aq. FeCl₃ (0.5 M in 1 M HCl) was added and the reaction was stirred at 23 °C for 15 min. The reaction was then diluted with 10 ml brine. The reaction mixture was extracted with DCM (15 mL × 3). The combined organic layer was washed with brine and dried over Na₂SO₄. The solvent was removed in vacuo and the residue was purified by flash column chromatography with MeOH: DCM (0.08 : 1) to afford **S31** (90 mg, 16%).

S31

¹H NMR (400 MHz, CDCl₃) δ 7.65 (s, 2H), 7.47 (s, 1H), 7.13 (s, 1H), 5.58 (s, 1H), 5.28 (s, 1H), 3.74 (t, *J* = 7.8 Hz, 2H), 3.39 (s, 3H), 2.90 (dt, *J* = 12.6, 5.9 Hz, 1H), 2.83 – 2.68 (m, 2H), 2.11 – 2.00 (m, 4H), 1.97 – 1.85 (m, 2H), 1.83 (d, *J* = 3.7 Hz, 6H), 1.65 (t, *J* = 13.5 Hz, 1H), 1.54 (s, 6H), 1.51 (s, 3H), 1.44 (d, *J* = 6.5 Hz, 3H), 1.39 (s, 3H).

S31 (56 mg, 0.1 mmol) was dissolved in sulfuric acid (98%, 4 mL) and was heated at 40 °C with vigorous stirring. The reaction was stirred for 12 h before cooling to 0 °C in an ice bath. The reaction was slowly added ice (20 g) and wait until the solution is cooled to 23 °C. The reaction mixture was extracted with DCM (15 mL × 4). The combined organic layer was washed with brine (five times) until the aqueous phase had no blue color and dried over Na₂SO₄. The solvent was removed in vacuo and the residue was purified by flash column chromatography with MeOH: DCM (0.1 : 1 to 0.4 : 1) to **S32** (20 mg, 33%).

S32

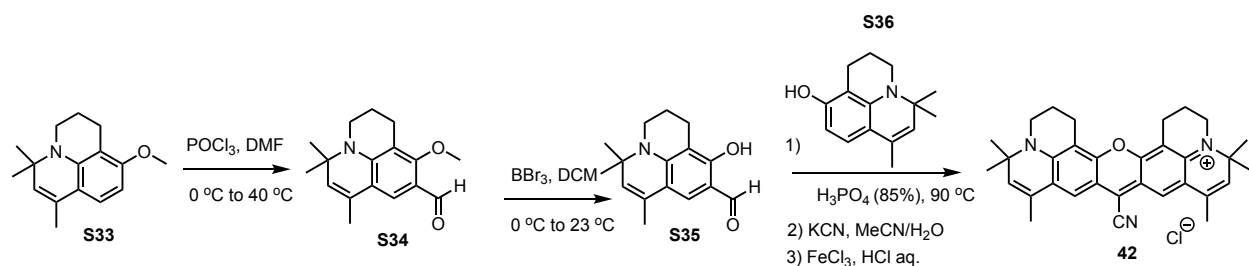
^1H NMR (400 MHz, MeOD) δ 7.93 (s, 1H), 7.72 (d, $J = 1.7$ Hz, 1H), 7.52 (s, 1H), 7.14 (s, 1H), 5.98 (s, 1H), 3.98 (s, 2H), 3.90 – 3.62 (m, 2H), 3.37 (s, 3H), 2.99 (p, $J = 5.2$ Hz, 1H), 2.52 – 2.30 (m, 2H), 2.12 – 1.88 (m, 3H), 1.74 (s, 6H), 1.69 – 1.64 (m, 1H), 1.61 (s, 6H), 1.57 – 1.51 (m, 3H), 1.43 (s, 6H).

S32 (12 mg, 0.02 mmol) together with N-hydroxylsuccinimide (NHS, 5.8 mg, 0.05 mmol) and N-(3-Dimethylaminopropyl)-N'-ethylcarbodiimide hydrochloride (EDC·HCl, 11.6 mg, 0.06 mmol) was dissolved in DCM (10 mL) and stirred overnight. The reaction was concentrated and purified by RP-HPLC (with MeCN and 0.1% TFA aqueous solution) to obtain **C-NHS** (6 mg, 43%).

C-NHS

^1H NMR (400 MHz, MeOD) δ 7.97 (s, 1H), 7.75 (d, $J = 1.7$ Hz, 1H), 7.22 (s, 1H), 7.16 (s, 1H), 6.01 (s, 1H), 4.00 (s, 2H), 3.98 – 3.70 (m, 2H), 3.39 (s, 3H), 3.05 – 2.91 (m, 3H), 2.90 (s, 4H), 2.21 – 2.09 (m, 2H), 2.01 (dd, $J = 13.5, 4.3$ Hz, 1H), 1.71 (d, $J = 6.5$ Hz, 6H), 1.66 (s, 1H), 1.62 (s, 6H), 1.55 (s, 3H), 1.45 (s, 6H).

Synthesis of 42



S33 and **S36** were synthesized according to previous report³⁴.

POCl_3 (4.60 g, 2.80 ml, 30 mmol) was added dropwise to a flask filled with DMF (10 mL) when cooled in an ice bath (0°C), and stirred for 30 min at 0°C . Then **S33** (2.43 g, 10 mmol) was then added into the flask and the reaction mixture was allowed to stir for 4 h at 40°C . When the reaction was cooled to 23°C , the reaction solution was poured into brine. The

mixture was extracted with DCM (20 mL \times 3) and the organic phase was washed with brine (five times) and then dried over Na₂SO₄. The solvent was removed in vacuo and the residue was purified by column chromatography with hexane : EtOAc (10 : 1) to obtain **S34** (2.12 g, 78%).

S34

¹H NMR (400 MHz, CDCl₃) δ 10.00 (s, 1H), 7.41 (s, 1H), 5.22 (q, J = 1.4 Hz, 1H), 3.83 (s, 3H), 3.42 – 3.30 (m, 2H), 2.72 (t, J = 6.4 Hz, 2H), 1.97 (d, J = 1.4 Hz, 3H), 1.94 – 1.84 (m, 2H), 1.36 (s, 6H).

¹³C NMR (101 MHz, CDCl₃) δ 187.49, 162.57, 148.53, 128.41, 127.35, 122.33, 118.26, 116.82, 112.93, 62.84, 57.68, 42.36, 28.40, 21.38, 20.96, 18.98.

S34 (1.08 g, 4 mmol) was dissolved in 20 ml dry DCM when cooled in an ice bath (0 °C). To the stirring suspension, 1M BBr₃ in DCM (8 ml, 8 mmol) was added dropwise. The stirred solution was then allowed to warm to 23 °C and reacted for 2 h. The flask was then cooled at 0 °C again and the reaction was quenched slowly with saturated NH₄Cl solution. The mixture was extracted with DCM (20 mL \times 3), washed with brine and dried over anhydrous Na₂SO₄. The organic phase was concentrated, and subjected to column chromatography with EtOAc : Hexane (8:1) as eluents to obtain **S35** (556 mg, 54%).

S35

¹H NMR (400 MHz, CDCl₃) δ 9.42 (s, 1H), 6.92 (s, 1H), 3.37 – 3.32 (m, 2H), 2.66 (t, J = 6.5 Hz, 2H), 1.95 (d, J = 1.3 Hz, 3H), 1.94 – 1.83 (m, 2H), 1.37 (s, 6H).

¹³C NMR (101 MHz, CDCl₃) δ 191.85, 161.18, 148.65, 127.20, 126.65, 126.47, 115.00, 110.61, 105.92, 57.77, 42.51, 28.57, 20.87, 20.34, 18.83.

S35 (257 mg, 1 mmol) and **S36** (229 mg, 1 mmol) were dissolved in 10 mL 85% H₃PO₄ and flask heated to 90 °C and kept stirring for 8 h. After cooling to room temperature, the reaction mixture was diluted with 25 mL saturated brine. The aqueous phase was extracted with DCM (20 mL \times 3). The combined organic phase was washed with brine (three times), dried over

Na₂SO₄ and concentrated. The residue was purified by column chromatography with MeOH : DCM (0.06 : 1) as eluents to obtain the violet red compound.

50 mg product from the last step was dissolved in 5 ml acetonitrile, aq. KCN (100 mg/mL, 1.5 M) was added dropwise to the xanthen solution until the blue color disappeared. Right after the blue color disappeared, 2 ml aq. FeCl₃ (0.5 M in 1 M HCl) was added and the reaction was stirred at 23 °C for 15 min. The reaction was then diluted with 10 ml brine. The reaction mixture was extracted with DCM (15 mL × 3). The combined organic layer was washed with brine and dried over Na₂SO₄. The solvent was removed in vacuo and the residue was purified by flash column chromatography with MeOH: DCM (0.06 : 1) to afford the product **42** (yield 21%).

42

¹H NMR (400 MHz, CDCl₃) δ 7.27 (s, 2H), 5.65 (d, *J* = 1.6 Hz, 2H), 3.76 – 3.68 (m, 4H), 3.02 (t, *J* = 6.5 Hz, 4H), 2.16 – 2.09 (m, 4H), 2.08 (s, 6H), 1.56 (s, 12H).

¹³C NMR (101 MHz, CDCl₃) δ 152.76, 151.27, 133.90, 125.71, 124.47, 118.98, 117.77, 114.62, 113.09, 107.35, 60.91, 44.39, 28.94, 20.65, 19.82, 18.76.

Epr-SRS spectro-microscopy setup

An integrated laser (picoEMERALD, Applied Physics and Electronics, Inc.) was used as a light source for both pump and Stokes beams. It produces 2 ps pump (tunable from 770 nm – 990 nm, bandwidth 0.5 nm, spectral bandwidth ~ 7 cm⁻¹) and Stokes (1031.2 nm, spectral bandwidth 10 cm⁻¹) beams with 80MHz repetition rate. Stokes beam is modulated at 20 MHz by an internal electro-optic modulator. The spatially and temporally overlapped pump and Stokes beams are introduced into an inverted multiphoton laser scanning microscopy (FV3000, Olympus), and then focused onto the sample by a 25X water objective (XLPLN25XWMP, 1.05 N.A., Olympus). Transmitted pump and Stokes beams are collected by a high N.A. condenser lens (oil immersion, 1.4 N.A., Olympus) and pass through a bandpass filter (893/209 BrightLine, 25 mm, AVR Optics) to filter out Stokes beam. A large

area (10×10 mm) Si photodiode (S3590-09, Hamamatsu) is used to measure the remaining pump beam intensity. 64 V DC voltage was used on the photodiode to increase saturation threshold and reduce response time. The output current is terminated by a 50 Ω terminator and pre-filtered by an 19.2-23.6-MHz band-pass filter (BBP-21.4+, Mini-Circuits) to reduce laser and scanning noise. The signal is then demodulated by a lock-in amplifier (SR844, Stanford Research Systems) at the modulation frequency. The in-phase X output is fed back to the Olympus IO interface box (FV30-ANALOG) of the microscope. Image acquisition speed is limited by 30 μ s time constant set for the lock-in amplifier. Correspondingly, we use 80 μ s pixel dwell time, which gives a speed of 8.5 s frame⁻¹ for a 320-by-320-pixel field of view. Laser powers are monitored through image acquisition by an internal power meter and power fluctuation are controlled within 5% by the laser system. 16-bit grey scale images are acquired by Fluoview software. SRS spectra were acquired by fixing the Stokes beam at 1031.2 nm and scanning the pump beam through the designated wavelength range point by point. 10 mM EdU (H₂O) sample was used as a standard to give RIE of different probes. 1 mM dye in DMSO or 100 μ M dye in PBS : DMSO (90 : 10) solution was used to acquire SRS spectra in DMSO or PBS. 20 mW on sample for pump laser and 30 mW on sample for Stokes laser is typically used for acquiring SRS spectra. For dyes that have maximum absorption longer than 770 nm, 10 mW on sample for pump laser and 30 mW on sample for Stokes laser is used to minimize photobleaching.

UV-Vis absorption spectra.

UV-Vis absorption spectra were recorded on a Varian Cary 50 UV-Vis Spectrophotometer (Agilent). For absorption measurement in DMSO, 50 μ M dye solution with 1 mm cuvette was used. For absorption measurement in PBS, 5 μ M dye solution with 5 mm cuvette was used.

5.5 Reference

1. Du, J., Wang, H. & Wei, L. Bringing Vibrational Imaging to Chemical Biology with

- Molecular Probes. *ACS Chem. Biol.* **17**, 1621–1637 (2022).
- Wei, L. *et al.* Live-cell bioorthogonal chemical imaging: stimulated Raman scattering microscopy of vibrational probes. *Acc. Chem. Res.* **49**, 1494–1502 (2016).
 - Bi, X., Miao, K. & Wei, L. Alkyne-Tagged Raman Probes for Local Environmental Sensing by Hydrogen – Deuterium Exchange. *J. Am. Chem. Soc.* **144**, 8504–8514 (2022).
 - Du, J. *et al.* Raman-guided subcellular pharmaco-metabolomics for metastatic melanoma cells. *Nat. Commun.* **11**, 4830 (2020).
 - Shi, L., Hu, F. & Min, W. Optical mapping of biological water in single live cells by stimulated Raman excited fluorescence microscopy. *Nat. Commun.* **10**, 1–8 (2019).
 - Ploetz, E., Laimgruber, S., Berner, S., Zinth, W. & Gilch, P. Femtosecond stimulated Raman microscopy. *Appl. Phys. B Lasers Opt.* **87**, 389–393 (2007).
 - Freudiger, C. W. *et al.* Label-Free Biomedical Imaging with High Sensitivity by Stimulated Raman Scattering Microscopy. *Science* **322**, 1857–1861 (2008).
 - Ozeki, Y., Dake, F., Kajiyama, S., Fukui, K. & Itoh, K. Analysis and experimental assessment of the sensitivity of stimulated Raman scattering microscopy. *Opt. Express* **17**, 3651 (2009).
 - Wei, L. *et al.* Super-multiplex vibrational imaging. *Nature* **544**, 465–470 (2017).
 - Miao, Y., Qian, N., Shi, L., Hu, F. & Min, W. 9-Cyanopyronin probe palette for super-multiplexed vibrational imaging. *Nat. Commun.* **12**, 4518 (2021).
 - Shi, L. *et al.* Highly-multiplexed volumetric mapping with Raman dye imaging and tissue clearing. *Nat. Biotechnol.* **40**, 364–373 (2022).
 - Du, J., Tao, X., Begušić, T. & Wei, L. Computational Design of Molecular Probes for Electronic Preresonance Raman Scattering Microscopy. *J. Phys. Chem. B* **127**, 4979–4988 (2023).
 - Fujioka, H. *et al.* Multicolor Activatable Raman Probes for Simultaneous Detection of Plural Enzyme Activities. *J. Am. Chem. Soc.* **142**, 20701–20707 (2020).
 - Shi, L. *et al.* Super-Resolution Vibrational Imaging Using Expansion Stimulated Raman Scattering Microscopy. *Adv. Sci.* **9**, 1–12 (2022).
 - Fujioka, H. *et al.* Activatable Raman Probes Utilizing Enzyme-Induced Aggregate Formation for Selective Ex Vivo Imaging. *J. Am. Chem. Soc.* **145**, 8871–8881 (2023).
 - Kawatani, M. *et al.* 9-Cyano-10-telluriumpyronin Derivatives as Red-light-activatable Raman Probes. *Chem. - An Asian J.* **18**, (2023).
 - Chen, Z. *et al.* Multicolor live-cell chemical imaging by isotopically edited alkyne vibrational palette. *J. Am. Chem. Soc.* **136**, 8027–8033 (2014).
 - Du, J. & Wei, L. Multicolor Photoactivatable Raman Probes for Subcellular Imaging and Tracking by Cyclopropanone Caging. *J. Am. Chem. Soc.* (2021). doi:10.1021/jacs.1c09689
 - Rao, D. N., Ji, X. & Miller, S. C. Silicon functionalization expands the repertoire of Si-rhodamine fluorescent probes. *Chem. Sci.* **13**, 6081–6088 (2022).
 - Grimm, J. B., Brown, T. A., Tkachuk, A. N. & Lavis, L. D. General Synthetic Method for Si-Fluoresceins and Si-Rhodamines. *ACS Cent. Sci.* **3**, 975–985 (2017).
 - Jia, S. *et al.* Water-soluble chromenylium dyes for shortwave infrared imaging in mice. *Chem* 1–18 (2023). doi:10.1016/j.chempr.2023.08.021
 - Nishiyama, R. *et al.* Boosting the Brightness of Raman Tags Using Cyanostar

- Macrocycles. *Anal. Chem.* (2023). doi:10.1021/acs.analchem.3c01958
23. Shu, C., Mega, R. S., Andreassen, B. J., Noble, A. & Aggarwal, V. K. Synthesis of Functionalized Cyclopropanes from Carboxylic Acids by a Radical Addition–Polar Cyclization Cascade. *Angew. Chemie* **130**, 15656–15660 (2018).
 24. Koide, Y. *et al.* Development of NIR fluorescent dyes based on Si-rhodamine for in vivo imaging. *J. Am. Chem. Soc.* **134**, 5029–5031 (2012).
 25. Belov, V. N., Bossi, M. L., Fölling, J., Boyarskiy, V. P. & Hell, S. W. Rhodamine spiroamides for multicolor single-molecule switching fluorescent nanoscopy. *Chem. - A Eur. J.* **15**, 10762–10776 (2009).
 26. Kolmakov, K. *et al.* Red-emitting rhodamine dyes for fluorescence microscopy and nanoscopy. *Chem. - A Eur. J.* **16**, 158–166 (2010).
 27. Butkevich, A. N. *et al.* Photoactivatable Fluorescent Dyes with Hydrophilic Caging Groups and Their Use in Multicolor Nanoscopy. *J. Am. Chem. Soc.* **143**, 18388–18393 (2021).
 28. Wang, H. *et al.* Bond-selective fluorescence imaging with single-molecule sensitivity. *Nat. Photonics* **17**, (2023).
 29. Zhang, Y. *et al.* Fluorescence-Detected Mid-Infrared Photothermal Microscopy. *J. Am. Chem. Soc.* **143**, 11490–11499 (2021).
 30. Li, M. *et al.* Fluorescence-Detected Mid-Infrared Photothermal Microscopy. *J. Am. Chem. Soc.* **143**, 10809–10815 (2021).
 31. Hansch, C., Leo, A. & Taft, R. W. A Survey of Hammett Substituent Constants and Resonance and Field Parameters. *Chem. Rev.* **91**, 165–195 (1991).
 32. Pastierik, T., Šebej, P., Medalová, J., Štacko, P. & Klán, P. Near-infrared fluorescent 9-phenylethynylpyronin analogues for bioimaging. *J. Org. Chem.* **79**, 3374–3382 (2014).
 33. Hanaoka, K. *et al.* Synthesis of unsymmetrical Si-rhodamine fluorophores and application to a far-red to near-infrared fluorescence probe for hypoxia. *Chem. Commun.* **54**, 6939–6942 (2018).
 34. Nie, H. *et al.* Reversible and Dynamic Fluorescence Imaging of Cellular Redox Self-Regulation Using Fast-Responsive Near-Infrared Ge-Pyronines. *ACS Appl. Mater. Interfaces* **8**, 8991–8997 (2016).
 35. Tian, K. *et al.* Multiple fluorescence Δ CIIE and Δ rGB codes for sensing volatile organic compounds with a wide range of responses. *Chem. Commun.* **47**, 10052–10054 (2011).
 36. Bai, X., Yang, B., Chen, H., Shen, J. & Yang, D. HKOCl-4: a rhodol-based yellow fluorescent probe for the detection of hypochlorous acid in living cells and tissues. *Org. Chem. Front.* **7**, 993–996 (2020).